Two-Dimensional Numerical Modelling of Wave Propagation in Soil Media

Nawras Hamdan

Submitted for the degree of Doctor of Philosophy

in Geotechnical Engineering

Institute for Infrastructure & Environment

Heriot-Watt University

September 2013

Abstract

Wave propagation in soil media is encountered in many engineering applications. Given that the soil is unbounded, any numerical model of finite size must include absorbing boundary conditions implemented at the artificial boundaries of the domain to allow waves to radiate away to infinity.

In this work, a finite element model is developed under plane strain conditions to simulate the effects of harmonic loading induced waves. The soil can be homogeneous or multi-layered where the soil properties are linear elastic. It may overlay rigid bedrock or half-space. It may also incorporate various discontinuities such as foundations, wave barriers, embankments, tunnels or any other structure.

For the case of soil media over rigid bedrock, lateral wave radiation is ensured through the implementation of the consistent transmitting boundaries, using the Thin Layer Method (TLM), which allow replacing the two semi-infinite media, on the left and right of a central domain of interest, by equivalent nodal forces simulating their effect. Those are deduced from an eigenvalue problem formulated in the two semi-infinite lateral media.

In the case of soil media over half-space, the Thin Layer Method is combined to the Paraxial Boundary Conditions to allow the incoming waves to radiate away to infinity laterally and in-depth. The performance of this coupled model is enhanced by incorporating a buffer layer between the soil medium and the underlain half-space.

For extensive analyses, the eigenvalue problem related to the TLM may become computationally demanding, especially for soil media with multi-wavelength depths. As the TLM involves thin sub-layers, in comparison to the wavelength, the size of the eigenvalue problem increases with increasing depth. A modified version of the TLM is proposed in this work to reduce the computational effort of the related eigenvalue problem.

This dissertation work led to the development of a Fortran computer code capable of simulating wave propagation in two-dimensional soil media models with either structured or unstructured triangular mesh grids. This latter option allows considering soil-structure problems with geometrical complexities, different soil layering configurations and various loading conditions. The pre- and post-processing as well as the analysis stages are all user friendly and easy.

To Peace in Syria.

Acknowledgements

I started this work with very little experience in the Finite Element Method and without any knowledge in FORTRAN coding. During this project I received help, support, constructive discussions and encouragement from my supervisor Prof. Omar Laghrouche. What can I say? Approachability, sincerity, honesty, dedication, commitment, friendship,.... really words are not enough to express my gratitude, appreciation and admiration for my supervisor. Early morning or late day office working hours, Omar was always there to answer my questions. All I can say, I am indebted to you. I learnt from each single meeting or discussion we had. You will be always my inspiration.

I would like to thank the Head of the IIE Prof. P. K. Woodward for his support. Dr A. El-Kacimi is well acknowledged for the time spent in discussions and solving many problems relating to FORTRAN coding. I would like also to express my gratitude and appreciation for the following people who spent time in replying to my emails or talking to me on the phone; Prof. E. Kausel, Prof. J. L. Tassoulas, Prof. B. Yang, Prof. E. Cheever, Prof. P. Avitabile, Prof. D. Kammer, Dr. T. G. Davies, Dr M. Hussein, Dr S. Jones and Dr J. Park. My colleagues Dr G. Kasangaki and P. Shrestha were always there for discussions and for sharing general concerns. Many thanks go to Dr J. Kennedy. My colleagues in the IIE with whom I shared good and bad times. Great people I met in the UK who offered support and encouragement: thanks to Dr. N. Fowdar and his family and thanks to Mr. Stephen Mull and his great family. I will never forget you.

Even from a far distance, thousands of miles away, I can hear your prayers and I can sense your faith and support, my beloved family. You provided continuous support and encouragement during the period of my study which kept my hope and ambition in the highest level. My father always inspired me to pursue my post-graduate studies, this is the best reward I may offer.

Coming home late, frustrated and confused by errors in the code, my son put the smile back on my face and my wife assured me and lifted my spirits up. Thank you both for your patience and understanding when I went to the University in the very early mornings or even in the weekends. Thank you for keeping my life simple and enjoyable during tough times. I would not imagine my life without both of you.

Thank you all so much for everything.

Contents

List of Figures

List of Tables

Abbreviations

TLM: Thin Layer Method
PBC: Paraxial Boundary Conditions
EDT: ElastoDynamics Toolbox
FEM: Finite Element Method
FDM: Finite Difference Method
BEM: Boundary Element Method
FMM: Fast Multipole Method
CQM: Convolution Quadrature Method
FFT: Fast Fourier Transformation
SBFEM: Scaled Boundary Finite Element Method
SBFEE: Scaled Boundary Finite Element Equation
NRBC: Non-Reflecting Boundary Conditions
FT: Fourier Transformation
ABC: Absorbing Boundary Conditions
PML: Perfectly Matched Layer
CALM: Caughey Absorbing Layer Method
DAA: Doubly Asymptotic Approximation
1D: One Dimension
2D: Two Dimensions
3D: Three Dimensions

Publications

Journal papers:

- N. Hamdan, O. Laghrouche, A. El-Kacimi, P.K. Woodward. "*Consistent transmitting boundary conditions with a reduced number of eigenmodes for wave propagation in elastic media*". Computers and Geotechnics: 53 (2013), 9-16.
- N. Hamdan, O. Laghrouche, A. El-Kacimi, P.K. Woodward. "*Combined paraxial-consistent boundary conditions finite element model for simulating wave propagation in elastic half-space media*". Soil Dynamics and Earthquake Engineering, (2013) (accepted).

Conference papers:

- N. Hamdan N, O. Laghrouche, P.K. Woodward. "*A Finite Element Model for Train Induced Vibration from Embankments*". Proceedings of the 12^{th}International Conference and exhibition on Railway Engineering, London, UK, Edited by A. Forde *et al.* (2013).
- N. Hamdan N, O. Laghrouche, P.K. Woodward, A. El-Kacimi. "*A coupled thin layer-paraxial boundary condition model for simulating wave propagation in layered half-space media*". Proceedings of the International Conference on Computational Mechanics (CM13), Durham University, UK, Edited by A. Osman *et al.* (2013).
- N. Hamdan , O. Laghrouche, A. El-Kacimi, P.K. Woodward, G. Medero. "*Investigation of the thin layer method for wave propagation in elastic media*". Proceedings of the 20^{th} UK Conference of the Association of Computational Mechanics in Engineering, University of Manchester, UK, Edited by Z. J. Yang (2012).
- N. Hamdan , O. Laghrouche, A. El-Kacimi, P.K. Woodward, G. Medero. "*Numerical modelling of the dynamic behaviour of a soil deposit overlying bedrock*". Proceedings of the 19^{th} UK Conference of the Association of Computational Mechanics in Engineering, Heriot Watt University, Edinburgh, UK, Edited by O. Laghrouche *et al.* (2011).

Chapter 1

Introduction

Wave propagation phenomenon is encountered in several engineering fields such as soil-structure interaction, seismology, electromagnetics, fluid-structure interaction and in many other areas. The domain in such problems is usually unbounded and for the sake of modelling, the unbounded domain must be represented by a bounded model of finite size. The domain is therefore truncated at some distance and the infinite extent of the model is achieved by imposing special boundary conditions which allow wave radiation towards the far field, with minimal reflection at the artificial boundaries.

A hybrid finite element model is presented in the context of this thesis by coupling the consistent transmitting boundaries, known as the Thin Layer Method (TLM), applied at the lateral boundaries of the domain, and the Paraxial Boundary Conditions (PBC), applied at the bottom boundary of the model, to simulate wave propagation in soil media.

1.1 Motivation

A variety of commercial software packages, either in the frequency domain or in the time domain, are available to engineers and researchers to deal with wave propagation problems in unbounded soil media and for soil-structure interaction problems.

For example, Lysmer *et al.* [1] developed a finite element program, called FLUSH, to deal with seismic soil-structure interaction problems. FLUSH deals with soil layer or layered soil media over rigid bedrock. Plane strain quadrilateral finite elements are used for modelling the bounded domain and the TLM is used at the lateral boundaries to simulate the horizontal semi-infinite extent of the domain. Multiple nonlinear soil properties for equivalent linear analysis can be used. This allows to use a different damping in each element.

More recently, Schevenels *et al.* [2] of KU Leuven, produced an educational toolbox in MAT-

LAB, ElastoDynamics Toolbox EDT version 2.1, which has the capability of dealing with wave propagation in soil media with emphasis focused on site amplification problems. It also deals with the computation of dispersive surface waves in layered soils and the calculation of the forced response of the soil due to the application of harmonic and transient loadings. The TLM and the direct stiffness matrix approach are coupled to solve problems in half-space media.

The motivation of this research project is to model wave propagation in unbounded soil media by producing a numerical code which offers the potential to deal with different types of problems of practical interest to engineers. Indeed, models with structured or unstructured mesh grids can be used to analyse wave propagation in soil media, homogenous or layered, overlaying bedrock or half-space, and capable of containing discontinuities of complex geometries. Furthermore, a more efficient version of the TLM, in terms of computational cost, is proposed in this work by reducing the number of eigenmodes in the original method.

1.2 Outline of the thesis

An introduction and an outline of the dissertation are presented in the current chapter where a statement of the contribution is also given.

A detailed survey on absorbing boundary conditions is presented in Chapter 2. It covers different methods and approaches for treating artificial boundaries. As this research work is related to elastodynamic media, the literature review mainly focuses on this topic.

The TLM is adopted in this research in the frequency domain under plane strain conditions. The theoretical background and mathematical formulation of the method are illustrated in detail in Chapter 3. The TLM is coded in FORTRAN in a numerical programme aiming to simulate wave propagation in soil media overlaying rigid bedrock and extending to infinity in the horizontal direction.

Parametric studies and validation tests are carried out in Chapter 4. The continuity of the surface displacements for symmetrical and non-symmetrical domains is first ensured. Then, the numerical code is validated against the theory of 1D dynamic response of a soil deposit overlaying bedrock in the following sections. The resonance phenomenon and the critical depth concept of a soil layer over rigid bedrock are obtained by the numerical code and the results are compared with theoretical predictions. Simulating wave propagation in layered soil media is addressed theoretically and numerically. Unstructured triangular mesh grids are also used to provide a more practical tool to analyse soil-structure interaction problems in the frequency domain.

The TLM is coupled with the PBC in Chapter 5 to simulate wave propagation in unbounded soil media. This chapter starts by providing a literature review on the PBC as well as a discussion on their efficiency and the potential improvements. The formulation of the PBC is also presented. The stiffness matrix of half-space elements is derived and used, in combination with TLM, to model the half-space effect.

Validation numerical examples are provided in Chapter 6 for dealing with both half-space and layered half-space models. The effect of the half-space depth is first discussed. Improvement of the TLM-PBC coupled model is achieved by incorporating a buffer layer attached at the bottom of the last soil layer with the same material properties of the half-space. The importance of this artificial layer is shown in the application of a rigid foundation over layered half-space. Further stability issues with respect to Poisson's ratio are addressed in the following section. The chapter ends by drawing concluding remarks derived from the presented numerical examples.

The idea of reducing the number of contributing eigenmodes within the context of the TLM is introduced in Chapter 7. Some modifications are first applied to the original approach taking into account the change of the diagonal and modal matrices by reducing the diagonal length and the number of columns, respectively. The effect of various wavenumbers in terms of transmitting energy through the artificial boundary is investigated. The number of contributing eigenmodes is reduced to half, quarter and only three, as suggested in the literature [3] for the last case. Some applications are then presented demonstrating the efficiency of this concept for several problems where the soil is underlain by rigid bedrock.

The benefits of incorporating unstructured mesh grids are exploited in Chapter 8 where a detailed parametric study is conducted using an automatic mesh generator. The flexibility of such mesh grids is shown through the presented numerical examples. Applications are then presented showing the flexibility offered to practitioners to deal with problems with complex geometries where uniform or structured mesh grids are not practical.

Finally, conclusions of the current work are listed in Chapter 9. Potential future research ideas are also highlighted.

1.3 Contribution statement

The main objectives of this thesis are as follow:

- Produce a numerical tool which enables engineers to simulate wave propagation in unbounded soil media with emphasis on dynamic soil-structure interaction problems. The package will allow engineers to employ structured as well as unstructured mesh grids as they may deal with complicated geometries including any type or shape of discontinuity within the model. This is achieved by incorporating the ability to employ unstructured triangular mesh grids generated by an automatic mesh generator.

- Explore the efficiency of the TLM-PBC coupled model for simulating wave propagation problems in unbounded soil media, which is reported in the literature to suffer from poor performance. Improvement is achieved here, especially in the case of layered half-space models, by introducing a buffer layer which separates the location of the PBC from the overlain domain. This technique is then applied to examine the behaviour of rigid foundations over layered half-space media.
- Investigate the effect of reducing the number of contributing eigenmodes within the context of the consistent transmitting boundaries in order to reduce the computational effort. The original solution contains all wavenumbers, we aim to reduce that number and examine the efficiency of the procedure.

Chapter 2

Literature review

2.1 Introduction

Wave propagation occurs in many engineering problems associated with soil-structure interaction, oscillating machines, railway geotechnical engineering and geotechnical earthquake engineering, and other fields. It has been intensively studied numerically through the use of the Finite Element Method (FEM) over the past four decades due to the difficulties in formulating analytical solutions. This is related to several reasons; such as the complex geometry of the problem and the size of the domain especially in the case of wave propagation within unbounded domains. Even with the recent advances in computer systems, solutions to such problems are not practical to achieve without treating the boundaries due to involvement of an infinite number of degrees of freedom. Spurious or reflected waves at the boundaries of a numerical model are one of the challenges to overcome when modelling wave propagation problems. Thus, when modelling such problems an unbounded domain is usually replaced by a bounded domain with special absorbing boundary conditions to allow wave transmission through the infinite extent of the domain. Hence, studying dynamic soil-structure interaction or wave propagation in unbounded soil media using the (FEM) requires artificial boundaries to be placed at the boundaries of the truncated domain. The purpose of the latter absorbing boundaries is to prevent or reduce wave reflections to an acceptable engineering levels and allow wave transmission through the artificial boundaries of the numerical model. The principle objective of these methods is to approximate the radiation and attenuation laws of the waves towards infinity and apply the resulting special conditions on the boundaries. It is worth mentioning that zero reflection is very difficult to achieve. Eventually, the models are reduced in terms of size so that the computational resources required are reasonable.

Different names have been in use for these conditions such as; transmitting boundaries, non-reflecting boundaries, absorbing layer method, silent boundaries and sometimes infinite elements. Let us call the special boundary conditions in this chapter as absorbing boundaries.

Basically absorbing boundary conditions have been classified in the literature into two wide categories; namely the global or nonlocal and local procedures. This classification is followed in this chapter by expanding available methods within this categorization.

A brief summary of the global schemes is introduced in section 2.2. Four main approaches are distinguished, the boundary element method, the consistent transmitting boundary method, the scaled boundary finite element method and, finally, the exact non-reflecting boundary conditions. In section 2.3, local boundary conditions are presented and classified also in four categories namely; absorbing layers methods, high order local absorbing boundary conditions, elementary transmitting boundary conditions and finally the infinite elements. Many papers appear in the literature aiming to review various types of absorbing boundary conditions employed in several disciplines and applications. Further information can be found in references [4, 5, 6, 7].

In Figure 2.1, a general two-dimensional representation of an unbounded soil medium with some discontinuities is depicted. To model the problem, a domain of interest is chosen where the presence of rigid bedrock at the base of the model, or the presence of a half-space, vertical lateral boundaries, homogenous or in-homogenous soil can be encountered. Absorbing boundary conditions would then be applied at the boundaries of the domain corresponding to the adopted assumptions.

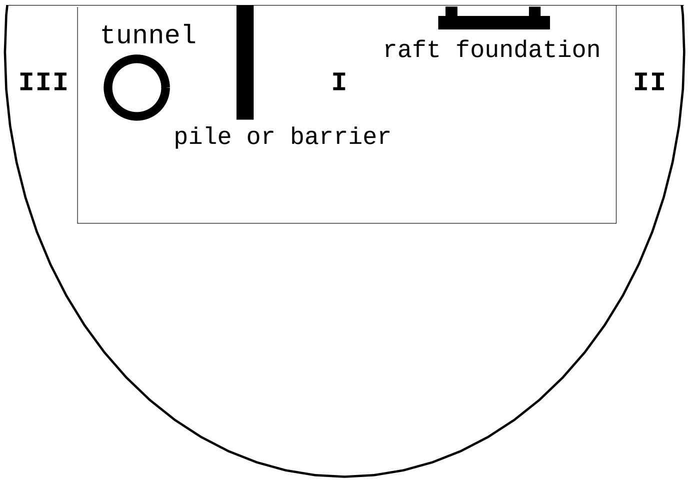

Figure 2.1: Schematic diagram of an unbounded soil domain problem example.

It should be indicated that in the context of the present literature survey, only absorbing boundary conditions related to elastodynamics will be covered. In the following, a review on the available absorbing boundary conditions that can be implemented at the boundaries of the domain is presented in a chronological order.

2.2 Global Absorbing Boundary Conditions (ABC)

The name *global* is gained because all boundary points are usually coupled when adopting the global methods. Generally speaking, these boundaries are known as exact absorbing boundary conditions owing to the fact that the solution at the artificial boundaries could be formulated in an exact sense. The global boundaries are nonlocal in space, or time or in both, and in general these boundaries are considered to perform better, in terms of absorption of the impinging waves, than the local boundary conditions. These methods are known for their superior accuracy compared to the local methods. However, they can be computationally expensive. A review of such methods is presented in the following.

2.2.1 The Boundary Element Method (BEM)

The method gained its name because of discretising the boundary of the problem into elements as it is shown in Figure 2.2.

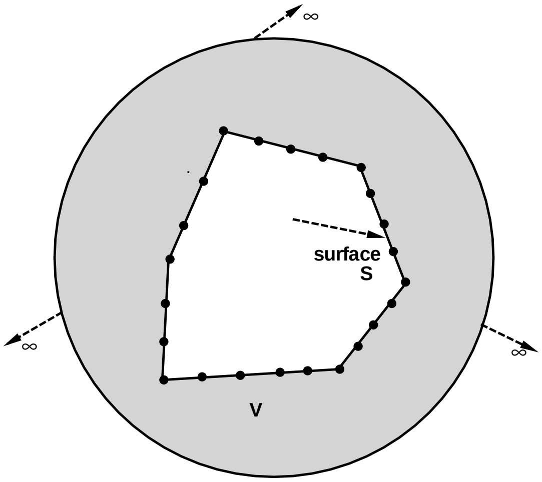

Figure 2.2: Discretisation in the boundary element method for 3D unbounded volume.

The domain of interest is desctretised only at the boundaries leading to a reduction of the spatial dimension by one and consequently in the total number of degrees of freedom. However, a fundamental solution to the governing equations must be available. Difficulties are usually encountered to compute the fundamental solution for anisotropic materials. Nonetheless, the BEM is well suited for modelling unbounded domains if such a solution is available.

The BEM is a numerical technique for solving initial value problems based on an integral equation formulation. The displacement field is obtained by the integral representation in terms of boundary values and the equation is solved numerically. Boundary values are used to determine displacements and tractions at any interior point of interest, as reported in reference [8].

This method was applied to various engineering applications such as; foundation engineering, dynamic soil-structure interaction, wave propagation and vibration isolation, and many other applications. A detailed review of the BEM including its formulation and applications could be found in textbooks such as Brebbia *et al.* [9], Manolis and Davies [10], Hall and Oliveto [11] and in some review articles such as Beskos [12] and Liu *et al.* [13]. It is classified into two categories, direct and indirect approaches. The displacements and tractions are used in the first approach while only displacement quantities are used in the latter. The numerical solution is obtained by solving the integral boundary equation on those elements. Unlike the traditional FEM and Finite Difference Method (FDM) where the discretisation is required in both the surface and the interior of the domain, in the BEM the discretisation is only required on the boundary of the problem, which leads to a reduction in the spatial dimension of the problem by one [10]. In other words, the volume integrals are transformed into surface integrals in 3D case and the surface integrals are reduced into line integrals in the 2D case. Imposing absorbing boundary conditions at the artificial boundaries is crucial in the case of the FEM and FDM while the radiation conditions to infinity is automatically taken into account in the BEM. Elastic or inelastic soil behaviour is possible to consider within the framework of this method in the frequency and time domain analyses. The boundary elements can be represented by interpolating shape functions between the nodes of the elements. Inhomogenous media are usually tackled in the BEM by sub-dividing the medium into homogenous and sub-homogenous regions and then adding together the subdivisions.

The direct integral representation in the time domain of the displacement field u_i of a homogenous, isotropic and linear elastic body of volume V, with surface S, is written as

$$c_{ij}(\xi)\,u_i(\xi,t) = \int_S \left[U_{ij}(x,\xi,t)\,f_i(x,t) - F_{ij}(x,\xi,t)\,u_i(x,t)\right] dS(x)\,. \tag{2.1}$$

The frequency domain representation has the following form

$$c_{ij}(\xi)\,u_i(\xi,\omega) = \int_S \left[U_{ij}(x,\xi,\omega)\,f_i(x,\omega) - F_{ij}(x,\xi,\omega)\,u_i(x,\omega)\right] dS(x)\,, \tag{2.2}$$

where ω denotes the circular frequency, point $x \in S$, point $\xi \in V \cup S$, c_{ij} has the value of Kronecker's δ_{ij} in the case of $\xi \in V$ and the value of $0.5\delta_{ij}$ in the case of $\xi \in S$, f_i is the traction vector, U_{ij} and F_{ij} are the fundamental elastodynamic displacement and traction tensors, respectively. The initial conditions and the body forces are set to zero, and the indices i and j take the values of 1, 2 and 3 in the 3D case. The numerical solution procedures of equations (2.1) and (2.2) are explained in reference [14].

In spite its advantages, the BEM is also characterised by some drawbacks. For example, densely populated system matrices, generally speaking non-symmetrical, are usually obtained from this technique. Furthermore, nonlinearity can be taken into account in the framework of the time domain BEM via incorporating the nonlinear FEM. Only linear response is accounted for in the frequency domain. Another merit of the time domain BEM is that the sparse matrix, due to the bounded support by the Green's function, is inverted only once while in the frequency domain boundary element method a full matrix is required to be inverted at each frequency. As a consequence, the computational cost is reduced.

Several attempts have been proposed to reduce the computational effort of this technique. For example, Fu and Bouchon [15] introduced a method which incorporates the discrete Green's function with the boundary integral volume equation for 2D anti-plane problem. The solution used the average Fresnel-radius approximation to volume integrations to reduce the numerical effort by making the coefficient matrix sparser. The global generalized reflection/transmission matrix propagator method is adopted by Ge and Chen [16] in order to save computer memory and cpu time required for solving the global matrix. The efficiency is further improved later by Ge and Chen [17] through a direct computation of the global matrix propagator where the calculation of the matrix propagator of each individual layer is omitted.

Bouchon *et al.* [18] proposed a sparse approximation of the fully populated matrix to reduce the computational effort and memory required to solve the problem in 2D layered media. Their reduction approach is based on keeping only the high magnitude entries of the fully populated matrix. The development of the Fast Multipole Method (FMM) was able to speed up the solution process by reducing the memory requirement. This method depends on an iterative solution approach for a system of boundary element equations in order to speed-up the matrix-vector multiplication during each iteration without building the whole matrix [13]. Chaillat *et al.* [19] formulated and applied a fast multi-level multipole boundary element methods for 3D elastodynamic problems in the frequency domain. This is extended further by Chaillat *et al.* [20] to multi-domain situations where alluvial basin is considered. An extension to include weakly dissipative viscoelastic media has been carried out recently by Grasso *et al.* [21] where the authors proposed a damping dependent modification to choose the multiple truncation factor. The dense matrices, which require more storage and computing effort, associated with the BEM are tackled by Messner and Schanz [22]. A time stepping scheme, the Convolution Quadrature Method (CQM), is employed in reference [22]. Acceleration of the BEM, in the time domain for elastodynamic problems, is achieved by employing the CQM and Galerkin discretisation. Be-sides the FMM, there exist other approaches to tackle the problem of inefficiency of using only the BEM. Some of these methods in the frequency domain are the pre-corrected Fast Fourier Transformation (FFT), as in reference [23], and the use of hierarchical matrices proposed by Benedetti and Aliabadi [24]. On the other hand, the plane wave time domain methodology in 2D is extended to 3D wave equation in elastodynamics by Takahashi *et al.* [25]. It is worth noting that special integration schemes are used in the BEM to overcome the singularity of the fundamental solution.

2.2.2 The consistent transmitting boundary conditions

The theoretical and mathematical formulations of the consistent transmitting boundary method, or the Thin Layer Method (TLM), are presented in Chapter 3 as this method is adopted throughout this dissertation. It should be noted here that the name *consistent* is used as the exact solution at the artificial boundaries is formulated with the finite elements and the effect of the infinite extent on the bounded domain is replaced by the equivalent transmitting boundary conditions. This section aims at providing an insight into the development of the TLM approach in a chronological order.

The TLM is a semi-discrete numerical technique, developed by Waas [3], to model numerically wave propagation in unbounded layered soil domains. The unbounded medium is divided into three regions, the central or irregular region which is bounded by two lateral regions on the right and the left; the regular regions. The central region is treated by the conventional FEM. This region is usually the region of interest, as it may contain buried structures such as foundations or any other discontinuities.

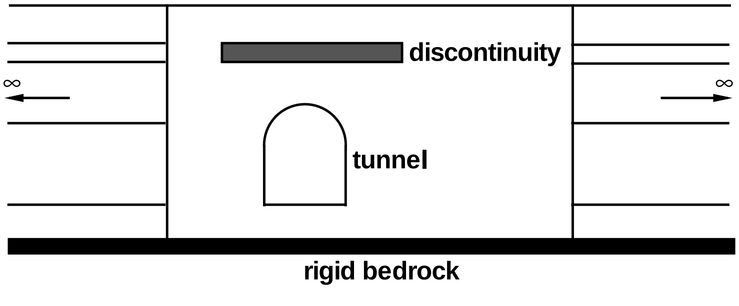

Figure 2.3: Schematic diagram for treating unbounded media by the TLM.

Figure 2.3 illustrates the treatment of the 2D unbounded domain by the TLM technique. A closed-form analytical solution, is adopted for the lateral or the layered regions. The semi-infinite lateral regions are divided into horizontal layers which extend to infinity. The displacement field is assumed to vary linearly with depth and exponentially in the horizontal direction. Some assumptions have been made such as; the soil is resting over rigid bedrock, the soil medium can be homogenous or layered, isotropic, linear elastic or viscoelastic and the material properties of the horizontal layers do not vary within each layer. The thickness of each layer should not exceed one-tenth of the shear wavelength. Waas [3] proposed a numerical technique based on the separation the variables in order to satisfy the wave motion governed by the differential equations in the horizontal direction. The free motion of the layered region consists of a finite number of wave modes obtained by solving an algebraic eigenvalue problem. Having obtained the displacements of the regular regions, the nodal forces on the boundary could be obtained and imposed as external forces. The dynamic stiffness matrices of the semi-infinite regions, which relate the nodal displacements and nodal forces, are then combined with the dynamic stiffness matrix of the irregular region and the unbounded domain can then be analysed. The anti-plane shear, in-plane and axisymmetric cases are dealt with in the previous developments. This has resulted in the development of frequency domain consistent transmitting boundary conditions.

The extension of the above method to the cylindrical transmitting boundaries was carried out by Kausel [26] and Kausel *et al.* [27] to model the three dimensional case of axisymmetric footings by generalising the approach of Waas [3]. The consistent transmitting boundaries of the horizontal layers are obtained. The dynamic stiffness matrices of the consistent transmitting boundaries are expanded into Fourier series and only two terms are considered in the applications provided in reference [26]. Kausel and Roësset [28] attempted to reduce the number of equations involved in the solution and proposed the use of hyperelements, rectangular elements of finite length. This leads to saving in computer storage and increasing the mesh size. These finite elements are based on an arbitrary expansion in one direction and employing closed-form expansion in the other direction. The previous consistent transmitting boundaries are only limited to circular foundations. Tassoulas [29] developed inhomogenous boundary conditions. The solution process starts by computing the practical solution of the inhomogenous boundary conditions then combining them with the semi-discrete modes which satisfy the corresponding homogenous boundary conditions. Plane and axisymmetric elements are developed for inhomogenous boundaries such as the presence of base motion.

Cylindrical coordinates transmitting boundaries are developed by Lin and Tassoulas [30] to handle three dimensional problems of dynamics of foundations of arbitrary geometry. Inhomogeneities in the neighbourhood of the circular foundation could also be considered. Kim *et* *al.* [31] later extended the approach to Cartesian coordinates in 3D. The consistent transmitting boundaries technique is extended to three dimensions by Hanazato *et al.* [32] considering travelling waves, induced by traffic loads, towards the boundaries. The solution leads to an eigenvalue problem of dimension six times the number of considered thin layers in the model.

The consistent transmitting boundary method is a very powerful method as it is based on a semi-analytical finite element method by solving an eigenvalue problem. However, in the entire previous development, it is applicable to vertical boundaries and this may not the case in real engineering problems such as inclined boundaries as in soil and dam embankments. The debuts of inclined consistent transmitting boundary appeared in reference [33] by Park and Tassoulas, where they developed a nonvertical absorbing boundary condition for wave propagation in layered strata media to satisfy these problems. The consistent absorbing boundary method was adopted in their work in the frequency domain under plane strain and antiplane shear strain and it was called the *zigzag* boundary condition.

Another limitation of the TLM is related to the assumption of horizontal layers. This was tackled by Ikeda and Tassoulas [34] via employing the perturbation method which takes into account non-parallel interfaces and also lateral inhomogeneities. Thus, an approximate treatment of the system equation is obtained. In the solution presented in reference [34], only the lowest-order and first-order terms of the perturbation series are included in the approximation.

Recently, Barbosa and Kausel [35] generalized the concept of the TLM to 3D problems where the material is transversely isotropic. The solution is obtained by solving two eigenvalue problems, for Rayleigh and Love waves.

As it is shown, a lot of development has taken place in relation to the TLM owing to its high level of accuracy. The restriction of the TLM for modelling unbounded domains only in the horizontal direction inspired researchers to couple the method with other techniques to allow simulating wave propagation in half-space media. A review of the methods simulating wave propagation in half-space media by coupling the TLM and other techniques is presented in Chapter 5.

2.2.3 The Scaled Boundary Finite Element Method (SBFEM)

The scaled boundary finite element method or the less boundary element method is a rigorous semi-analytical method and is spatially and temporally global. It is relatively a new technique for modelling unbounded domains. The fundamental solution is not required, as it is the case for BEM, within the framework of the SBFEM as it is based on the FEM. It combines the advantages of both BEM and FEM. So the boundaries are only discretised as in the BEM.

It was called first by Song and Wolf [36], for anti-plane motion, the consistent infinitesimal finite-element cell method in the frequency domain where a finite element cell or a bounded cell, with the exterior boundary similar to the interior boundary, is added in the radial direction to the structure-medium interface. The inverse Fourier transform is applied to the consistent infinitesimal finite-element cell, obtained in reference [36], to transform the equation into the time domain. This approach was later extended by Wolf and Song [37] to cover the in-plane motion. The method was renamed in reference [38] to the SBFEM where the solution procedure is based only on the finite element method with boundary discretisation as surface finite elements reducing the dimension of the problem by one.

The discretisation technique associated with the SBFEM is explained in Figure 2.4. Initially, one may choose a scaling centre O, the origin of the Cartesian coordinates, in such a manner that the total boundary S must be visible from the zone of the scaling centre. One dimensional line elements are used to discretise the boundary S. Then, shape functions in the local coordinate η are used to interpolate the geometry of the elements on the boundary, in the same way as in the conventional finite element procedure. A non-dimensional radial coordinate ξ is introduced to scale the boundary (from the scaling centre to a point on the boundary) to describe the geometry of the domain V. The non-dimensional radial coordinate has zero value at the scaling centre and a value of one at the boundary S leading to representing the unbounded domain by $1 \leq \xi < \infty$. The coordinates of the scaled boundary element are represented by the radial and circumferential coordinates η and ξ, respectively.

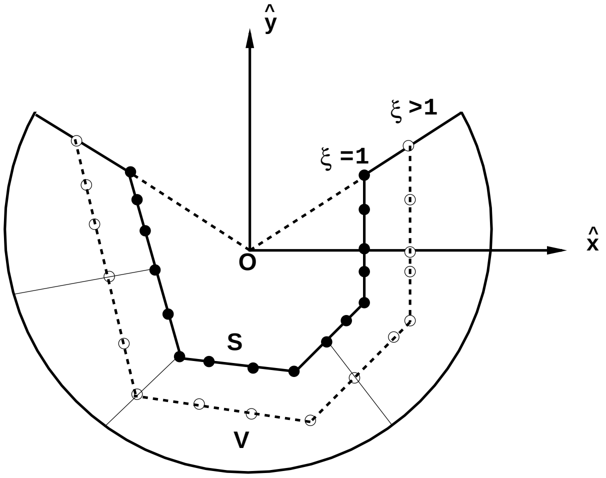

Figure 2.4: Discretisation of the scaled boundary finite element method.

In the SBFEM, the displacement and stress fields on the boundary of any problem are usually expressed by semi-analytical solutions and subsequently the boundary condition at infinity will be expressed analytically. Thereby, shape functions are now used on the circumferential direction to interpolate the displacement field for each radial line connecting the scaling centre and a node on the boundary surface S. Then, the governing differential equations are introduced in the scaled boundary coordinates. The Galerkin's weighted residual method or the principle of virtual work method could be applied to the differential equations, in the circumferential direction η, in order to formulate the Scaled Boundary Finite Element Equation (SBFEE) in displacement in the ordinary coordinates which is an Euler-Cauchy ordinary differential equation. The SBFEE in terms of displacements is derived by Song and Wolf [38] for 2D and 3D as follows

$$\begin{aligned}[\mathbf{E}^0]\xi^2\{u(\xi)\}_{,\xi\xi} \quad & +((s-1)[\mathbf{E}^0]-[\mathbf{E}^1]+[\mathbf{E}^{\mathbf{1}}]^T)\xi\{u(\xi)\}_{,\xi} \\ +((s-2)[\mathbf{E}^{\mathbf{1}}]^T \quad & -[\mathbf{E}^2])\{u(\xi)\}+\omega^2[\mathbf{M}^0]\xi^2\{u(\xi)\}=0, \end{aligned} \tag{2.3}$$

where matrices $\mathbf{E}^0$, $\mathbf{E}^1$, $\mathbf{E}^2$ and $\mathbf{M}$ are assembled by computing the elementary coefficient matrices on the boundary of the domain and ω is the driving frequency. Integer s has a value of either 2 or 3 for 2D and 3D, respectively. The SBFEE in the dynamic stiffness formulation is derived in reference [38] and expressed as

$$\begin{aligned}([\mathbf{S}^\infty(\omega)]+[\mathbf{E}^1]) \quad & [\mathbf{E}^0]^{-1}([\mathbf{S}^\infty(\omega)]+[\mathbf{E}^1]^T)-[\mathbf{E}^2]-(s-2)[\mathbf{S}^\infty(\omega)] \\ -\omega[\mathbf{S}^\infty(\omega)]_{,\omega} \quad & +\omega^2[\mathbf{M}^0]=0. \end{aligned} \tag{2.4}$$

Here, the term $[\mathbf{S}^\infty(\omega)]$ expresses the dynamic stiffness matrix of the unbounded domain which is proven to be symmetrical. For the derivation and the solution procedures of the SBFEE, the reader is directed to references [39] and [40], respectively. Equation (2.3) is solved analytically in reference [41] in the frequency domain in order to avoid the discretisation in the ξ-direction. The analytical solution is obtained by a power series. Consequently, the analytical solution of the dynamic stiffness matrix is also obtained without numerical discretisation resulting in a more attractive version of the SBFEM. Transformation of the SBFEE into the Bessel functions is employed in the case of scalar coefficient matrices in reference [41]. As the number of the degrees of freedom on the boundaries increases the computational effort of the SBFEM becomes significant. Improvements were made by employing the base functions reduction scheme where an asymptotic expansion of the dynamic stiffness matrix is utilized to determine its value at high frequencies ensuring the radiation condition. A more efficient technique is employed by Song [42] where an asymptotic expansion is applied to equation (2.3) to obtain the displacement field at high frequency and subsequently the dynamic stiffness matrix is determined.

Another attempt is also employed to avoid computing the dynamic stiffness matrix. It is achieved by Song and Bazyar [43] where Padé approximations of the dynamic stiffness matrix are formulated directly from the SBFEE. The advantage of these approximations is their rapid convergence in comparison to the power series. Choosing the order of the Padé series is also suggested. Moreover, the reduced set of base functions supplied in reference [42] is also adopted by Song and Bazyar [43]. Opting to increase the efficiency of the method, more recently, a fundamental-solution-less boundary for wave problems is developed by Song and Bazyar [44]. This is due to the time required to compute a set of the base functions which is the most time consuming part of the implementation of the method. In their method, lumped coefficients of the matrices and high order elements are obtained by employing the Gauss-Lobatto-Legendre shape functions with nodal quadrature. In fact, savings in the computer memory and also in the cpu time are achieved by obtaining sparsity of the matrices via applying the partial Schur decomposition.

2.2.4 Exact Non-Reflecting Boundary Conditions (NRBC)

This type of absorbing boundary conditions represents theoretically exact boundaries. However, most of the time an integral transform is involved along the boundary and hence they are not exact anymore. Givoli and Keller [45] employed the technique of reducing the wave equation to derive an exact non-local reflecting circular artificial boundary condition for 2D time-harmonic elastodynamic problems which has the form

$$-T_i(x) = M_{ij}u_j(x) \equiv \Sigma_{n=0}^{\infty} \int_{\Gamma} m_{ij}^{n}\left(x,x'\right) u_i\left(x'\right) dx', \tag{2.5}$$

where m_{ij}^{n} stands for the Kernel and Γ represents the circular artificial boundary. The authors used Helmholtz decomposition to write the displacements in terms of the potentials. Plane strain and stress problems are considered. The artificial boundary condition of expression (2.5) is implemented at the boundaries of the computational domain within the finite element framework. A few years later and by employing the Fourier Transformation, Grote and Keller [46] developed an exact non-reflecting spherical boundary condition, local in time but nonlocal in space, from the boundary conditions of reference [45]. High derivatives of displacements and their time derivatives with respect to the polar coordinates are involved in these boundary conditions. This is tackled by using boundary conditions which involve only the first derivative of the displacements with respect to the polar coordinates.

On the other hand, Grote and Keller [47] derived an exact non-reflecting spherical boundary condition for time-dependent elastic wave equation in 3D. As in the previous exact boundary conditions, they are local in time but nonlocal in space and also involve only the first derivatives of the displacements and inner products with spherical harmonics of the displacement on the artificial boundary. These boundary conditions are incorporated within the FEM and FDM by

Grote [48] where the stability of the non-reflecting boundaries is also discussed through some examples.

2.3 Local Absorbing Boundary Conditions (ABC)

In general, local absorbing boundary conditions are considered to be non demanding in terms of computational cost and simple in terms of their mathematical formulations, but they do not achieve the same level of accuracy compared to that of nonlocal methods. It was named ‘local’ because only spatial and temporal points near the boundary points are considered to be involved in the condition. In other words, the response at any location and time depends on the response at the neighbouring points *spatially local* and at some few previous time steps *temporally local*. Generally speaking, local ABC are preferred for transient wave problems instead of the non-local procedures because of the high computational effort. They are usually approximate and therefore spurious wave will be reflected at the artificial boundaries. Kausel and Tassoulas [49] indicated that “*however these boundaries may absorb the reflected waves they are not perfect absorbers as some echo may occur in the solution in addition to factious waves travelling along those boundaries*”. Hence, to obtain the required level of accuracy, local boundary conditions must be applied far enough from the structure-soil interface and therefore increase the number of degrees of freedom in the domain, and consequently the computational cost. On the other hand, their mathematical formulation is relatively simple compared to the global methods and they are simple to implement in the FEM or FDM. Local ABC are usually formulated in the time domain and therefore non-linearity of the soil within the finite domain can be modelled by implementing non-linear constitutive models, while the far field is still modelled linearly.

The viscous boundary conditions, developed by Lysmer and Kuhlemeyer [50], are the first local absorbing boundary conditions which appeared in the literature to handle elastodynamic problems in the time domain. The idea consists to implement viscous dashpots at the boundaries in order to absorb the energy of the compression and shear waves. The dashpot constants are related to the properties of the adjacent soil where the viscous boundaries are placed. These boundary conditions are very simple and easy to implement and they work in both time and frequency domains. The viscous boundary conditions of reference [50] are perfect absorbers in the case of normal incidence of the incoming waves. However, if the incident waves are not normal to the boundary they only absorb part of the energy. In fact, if a wave hits the boundary at a small angle, large spurious reflections will be encountered. The formulation of the viscous boundaries is given by

$$\sigma = a\rho c_p \frac{\partial u}{\partial t} \qquad \text{and} \qquad \tau = b\rho c_s \frac{\partial v}{\partial t}, \tag{2.6}$$

where σ and τ are the normal and shear stresses on the boundary, ρ is the soil density, c_p and c_s are the dilational and shear wave velocities, u and v are the normal and tangential displacements on the boundary, respectively. Parameters a and b, which had unit values on the original expressions of (2.6), are the absorption parameters which were suggested by White *et al.* [51] to take into account the incident waves directions. They are determined by discretising the domain with finite elements and then finding a linear relationship between the velocities and stresses at the boundary. Due to their simplicity and easiness of implementation in a finite element framework, the viscous boundary conditions have been implemented in commercial finite element packages such as ABAQUS.

Another attempt was made by Ang and Newmark [52], where they proposed a new local boundary condition for the FDM in the time domain which again worked well only in the case of normal incidence of impinging waves. Their boundary conditions are equivalent to the viscous boundary conditions. Engquist and Majda [53] introduced a new group of local boundary conditions based on the FDM. The first order approximation is similar in accuracy to those of Ang-Newmark and Lysmer-Kuhlemeyer absorbers. Better accuracy is achieved by employing the second order approximations and even higher in the case of higher order boundaries where more points in the neighborhood of the boundaries are considered. However, it should be pointed out that higher order local boundaries loose the locality property when increasing the number of points near the boundary. Improvements were suggested by White *et al.* [51].

A new technique was proposed by Smith [54] which is based on cancelling the reflections by averaging two complementary problems where a fixed Dirichlet boundary is assumed for the first problem and a free Neumann boundary for the other. Smith's approach was later modified by Cundall *et al.* [55], and Kunar and Marti [56] to account for multiple reflections. The boundary element method is employed in reference [57] to formulate the dynamic stiffness matrix of the central medium while doubly-asymptotic boundary conditions, dashpots and coupled static springs, are used. These boundary conditions are asymptotically exact for plane waves travelling perpendicularly to the truncated boundaries at both high and low frequencies. However, some errors are induced in the intermediate frequency range. This scheme is local in time but nonlocal in space.

Paraxial boundary conditions, which transmit energy only in one direction, have been derived by Engquist and Majda [53], and Clayton and Engquist [58] for the the scalar and elastic wave equation, respectively. Their boundary conditions are based on the pseudo-differential operators for a general class of differential equations where a set of local approximate absorbing boundary conditions with increasing order are obtained. The outgoing waves were separated from the incoming waves by splitting the differential operator of the wave equation for elastic waves and hence the paraxial boundaries are used to simulate only the outgoing waves leading to a reduction in the reflection at the boundaries. More details are provided in Chapter 5 as these boundaries are also used in the context of this thesis. A transmitting boundary formula was presented by Liao and Wong [59] that could be used in 2D or 3D and for convex artificial boundaries. The extrapolation method, based on polynomial fitting, is used in their work.

Multi-directional boundary conditions for the multi-directional wave equation were constructed by Higdon [60, 61] in both time and space, where the scalar wave equation was approximated by the finite difference rather than finding the analytical solution. This family of absorbing boundary condition is based on the discrete form of the wave equation. Those boundaries, unlike the paraxial boundaries which are most suitable for normal incidence, are considered perfect absorbers for waves propagating at non-zero angle of incidence. Higdon non-reflecting boundary of order j is expressed by

$$\left[\prod_{j=1}^{p}\left((\cos\alpha_j)\frac{\partial}{\partial t} - c\frac{\partial}{\partial x}\right)\right] u = 0, \tag{2.7}$$

where α is the angle of incidence and c is the wave speed. It was demonstrated that for low order of the above equation, good results were obtained for a wide range of angles of incidence. The derived boundaries are found to be perfect absorbers for a plane wave hitting the boundary at a preselected angle of incidence. Absorbing boundary conditions for stratified media are also introduced in reference [62] for acoustic and elastic waves.

Scandrett *et al.* [63] derived an approximate time-dependent absorbing boundary condition employing the finite difference scheme for elastodynamic problems in two dimensional plane strain. The limiting amplitude principle is used to derive the boundary conditions. The boundary conditions of reference [63] are similar to the second order boundary conditions of Engquist and Majda [53]. The difference is that they were derived in the rectangular coordinates while polar coordinates are used in reference [63].

Cohen [64] proposed in his thesis *extended paraxial boundary conditions* and compared the proposed boundaries with the analytical and numerical solutions. In spite of the difference between the viscous and paraxial boundaries, Cohen [64] proved that there is a relationship between these boundaries by the equilibrium equation. The paraxial boundaries are classified as dashpots to be applied at the length of an element rather than attaching dashpots from the boundary nodes to a rigid base and same function is performed by both boundaries. Modifications to the PBC are also suggested in [64], it is worth mentioning that these modifications were available before the publication of references [65, 66].

Bamberger *et al.* [67] introduced modifications to the first order absorbing boundary conditions of reference [64] as the original boundaries are transparent boundaries for both longitudinal and transverse waves at normal angles of incidence. Thus, the modifications extended the transparency boundary conditions to include Rayleigh waves. The new absorbing boundaries are of second order and they are transparent to the three types of waves.

The doubly asymptotic and the mutli-directional transmitting boundaries are combined by Wolf and Song [68], by exploiting their advantages, where the doubly asymptotic is used for modelling the low frequency limit or the static case. These boundary conditions are temporally local and could be spatially either local or nonlocal depending on the implementation of the static stiffness matrix.

In order to overcome the fact that boundary operators in some of the local boundary schemes of order one or more lead to non-symmetric matrices, in addition to the dependency of the accuracy on the static behaviour, Kellezi [69] formulated new local boundary conditions for dynamic analysis in 2D and 3D. These boundaries are considered as doubly asymptotic and as a generalisation of the viscous boundary conditions.

2.3.1 Absorbing layers at the boundaries

In this approach, a finite thickness layer is used as an envelop around the computational domain, as it is shown in Figure (2.5), in order to reduce wave reflections at the boundaries.

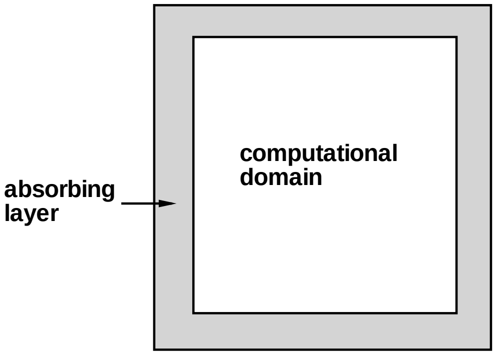

Figure 2.5: Schematic diagram of the absorbing layer method.

This is achieved by incorporating some parameters which either force outgoing waves to slow down or decay. If those parameters are chosen in such a case that minimal or zero reflection will occur, the absorbing layer will be classified as a Perfectly Matched Layer (PML). A PML is a high order absorbing boundary condition applied around the circumference of the interior domain. The principle of the PML is that once the outgoing waves enter the lossy layer, they will be transformed into evanescent waves with minmising the reflections at the boundaries. The main idea of the method is to introduce an absorbing layer with uniform thickness at the boundary which will force the wave to attenuate exponentially according to a pre-defined decay function. PML was originally introduced by Berenger [70] for electromagnetic problems and it is extended later to elastic waves by Hastings *et al.* [71] where the wave energy is converted into shear and compression waves with their energy decaying exponentially. PML was firstly extended from electromagnetic to elastodynamics by Chew and Liu [72] using the FDM in the frequency domain and by stretching the coordinates via a variable change in a manner to convert the plane wave into an attinuative wave in the new complex coordinates. The new stretched coordinates are a result of a complex variable change such as $x = x^{'}(a + \mathrm{i}\alpha)$. In this case, a wave travelling in a lossless medium will be also attinuative in the new coordinates and will have the form $e^{\mathrm{i}kax^{'} - k\alpha x^{'}}$. This type of transmitting boundary is classified by Tsynkov [6] between local and nonlocal schemes. Some nonlocality is gained by an artificial enlargement of the computational domain and there is no global integral relationship along the boundary. Collino and Tsogka [73] introduced the PML in elastodynamics, for heterogenous anisotropic media, for velocity stress formulation by decomposing each component of the unknown to orthogonal and parallel components to the boundary. Further development to extend the formulation of the PML to poroelastic media is achieved by Zeng *et al.* [74]. Moreover, Zheng and Huang [75] developed an anisotropic PML in the Cartesian, cylindrical and spherical coordinates for time harmonic elastodynamic problems. The anisotropic PML could be used in the FEM and the FDM in the time domain. The stability and well-posedness of the PML for elastic anisotropic media is examined by Becache *et al.* [76].

The concept of the PML is extended by Basu and Chopra [77] to time-harmonic, frequency domain, elastodynamics Cartesian coordinates where a displacement-based symmetrical finite element implementation is developed for plane strain and three dimensional wave motion. A year later, Basu and Chopra [78] extended the PML technique and presented displacement-based wave equations, for anti-plane and plane strain cases, and their implementations in the FEM in the time domain to analyse transient problems. The finite element implementation of the anti-plane case is symmetrical but it is not for the plane strain problems.

A further development is introduced by Basu [79] where the author extended his previous work in [78], where implicit time integration was adopted, to implement explicit time integration for the 3D elastic wave equation. This is made first by transforming the frequency domain equations as obtained by Basu and Chopra [77] to the time domain and second by incorporating an explicit time integration scheme with special considerations. Kausel and Barbosa [80] proposed a simple method for obtaining the finite element matrices of the PML in the frequency domain. In their formulation, the stretched functions were applied directly to the mass and stiffness element matrices computed by the conventional FEM. Both anti-plane shear and in-plane cases are considered and the authors stated that it would be applicable to the three-dimensional wave equation.

Semblat *et al.* [81] proposed an absorbing layer method to be implemented at the boundaries of the numerical model to reduce the spurious reflections from the boundaries. Damping properties of the proposed layer are estimated by Rayleigh/Caughey coefficients to express the attenuation properties within the absorbing layer and they called their method *the Caughey Absorbing Layer Method*, CALM. Rayleigh damping is a combination of the stiffness and the mass of the medium as shown in the equation

$$\mathbf{C} = a_0\mathbf{M} + a_1\mathbf{K}, \tag{2.8}$$

where a_0 and a_1 are Rayleigh coefficients, $\mathbf{K}$ is the stiffness matrix and $\mathbf{M}$ is the mass matrix. Caughey damping is expressed in a more general formulation and leads to the Rayleigh formulation if a second order Caughey damping is considered (i.e. m=2)

$$\mathbf{C} = \mathbf{M}\sum_{j=0}^{m-1} a_j \left(\mathbf{M}^{-1}\mathbf{K}\right)^j. \tag{2.9}$$

Typical values of Rayleigh coefficients are between 0.5 and 1.0. Damping ratio can be expressed as

$$\zeta = \frac{a_0}{2\omega} + \frac{a_1\omega}{2}, \tag{2.10}$$

where ω stands for the circular frequency. The frequency of the minimum damping is determined from the Rayleigh coefficients and subsequently the minimum damping relationship is used as

$$2\zeta_{min} = \frac{a_0}{\omega_R} + a_1\omega_R, \tag{2.11}$$

and the predominant frequency is computed by

$$\omega_R = \sqrt{\frac{a_0}{a_1}}. \tag{2.12}$$

Thus, Rayleigh damping coefficients within the absorbing layer are determined. A 2D finite element model in plane strain conditions was considered to examine the efficiency of the proposed method in elastic media. The model was four times the length of the compression wave in both directions. It was therefore found even if the efficiency of the absorbing layer method is lower in comparison to other methods but still efficient enough to reduce the magnitude of the reflected waves. A comparison between the CALM and PML is performed and the accuracy of CALM is equivalent to a third-order PML accuracy. Nonetheless, the thickness of the absorbing layer should be large enough to reduce the reflection and the method leads to an increase in storage memory.

2.3.2 High-order local transmitting boundaries

The accuracy limitation of the local absorbing boundary conditions, as explained at the beginning of section 2.3, is usually questioned. For more accurate results and as an alternative to the low-order local absorbing conditions, high-order local absorbing boundary conditions usually provide better accuracy, however, their implementation is not straightforward. High-order absorbing boundary conditions emerged in the mid-1990s, where the accuracy of the absorbing boundary is better than the low-order absorbing boundaries, however they are not necessarily exact, but asymptotic. The level of the accuracy depends on their order. However, their implementation in a computer code is comparatively difficult. In the following, a brief review of the different high-order local absorbing boundary is presented with emphasising on their accuracy and implementation issues.

A series of arbitrarily high-order absorbing boundary conditions is introduced by Guddati and Tassoulas [82] for the scalar wave equation in the Cartesian coordinates. High-order derivatives are not involved in these boundary conditions, only the second-order derivatives are required. These boundary conditions are based on the continued fraction approximation of the dispersion relationship. The idea is to introduce auxiliary layers adjacent to the boundary.

A technique, based on Higdon transmitting boundaries, for modelling time-dependent waves in unbounded media was proposed by Givoli and Neta [83]. The Higdon transmitting boundary equation was reformulated by introducing special auxiliary variables $\phi_1, \phi_2, \ldots \phi_{j-1}$ to be incorporated in the finite element and the finite difference approaches. The proposed formulations do not require any higher order derivatives and permit the use of any order of Higdon boundaries. In the reformulation process, equation (2.7) is replaced by

$$\left[\prod_{j=1}^{p}\left(\frac{\partial}{\partial x}+\frac{1}{C_j}\frac{\partial}{\partial t}\right)\right]u=0, \tag{2.13}$$

where C_j denotes the parameters to be chosen and which represent phase speeds in the x-direction. The auxiliary functions are introduced on the artificial boundary and the exterior domain. These functions will be used only on the boundary and will be defined on the exterior domain. The auxiliary functions are given by

$$\left(\frac{\partial}{\partial x}+\frac{1}{C_1}\frac{\partial}{\partial t}\right)u=\phi_1. \tag{2.14a}$$

$$\left(\frac{\partial}{\partial x}+\frac{1}{C_2}\frac{\partial}{\partial t}\right)\phi_1=\phi_2. \tag{2.14b}$$

$$\vdots$$

$$\left(\frac{\partial}{\partial x}+\frac{1}{C_j}\frac{\partial}{\partial t}\right)\phi_{j-1}=0. \tag{2.14c}$$

The set of equations (2.14) are equivalent to the original equation if they are used together and only the first derivative of the displacement is involved. To make this set discretisable on the boundary with respect to ϕ, the derivative with respect to x must be eliminated as indicated by Givoli and Neta [83] and a new formulation will be obtained. It is given by

$$\beta_j\frac{\partial u}{\partial t}+\frac{\partial u}{\partial x}=\phi_1. \tag{2.15}$$

$$\beta_0\frac{\partial \phi_j}{\partial t}-\alpha_j\frac{\partial^2 \phi_{j-1}}{\partial t^2}-\frac{\partial^2 \phi_{j-1}}{\partial y^2}+\lambda\phi_{j-1}=\phi_{j+1} \qquad , \qquad j=1,....,j-1. \tag{2.16}$$

$$\alpha_j=\frac{1}{C_j^2}-\frac{1}{C_0^2} \qquad , \qquad \beta_0=\frac{1}{C_1} \qquad , \qquad \beta_j=\frac{1}{C_j}+\frac{1}{C_{j+1}} \qquad , \qquad \lambda=\frac{f^2}{C_0^2}. \tag{2.17}$$

$$\phi_0\equiv u \qquad , \qquad \phi_j\equiv 0. \tag{2.18}$$

A review of seven high-order nonlocal absorbing boundary conditions was provided by Givoli [7]. Those high-order boundary conditions are applicable to the scalar wave equation, Maxwell equations, Helmholtz equation, linearized shallow water equations, linear hyperbolic systems and elastic wave equation. Only the boundary conditions related to the elastic wave equation will be listed in this section.

An exact non-reflecting boundary condition, local in time but nonlocal in space, is derived by Grote and Keller [47] for the 3D elastic wave in spherical surface. Only the first derivative of the solution is involved in this boundary making the implementation simple. In their derivation, they started from the elastic wave equation and then decomposed the displacement field into two types making a justification of the different two speeds of the compression and shear wave speeds in the medium. This boundary condition was combined later in the framework of the FEM and FDM by Grote [48] where the exact boundary conditions performed better than those of reference [50]. These boundaries do not involve high order derivatives.

Although, several high-order local absorbing boundary conditions were developed for the scalar wave equation, Maxwell's equations and Helmholtz wave equation, it is not easy to extend these high order absorbing boundary conditions to dynamic soil-structure interaction problems as reported by Bazyar and Song [84]. This is due to various reasons such as the complicated geometry of the unbounded soil domain, the anisotropic behaviour of the materials and the presence of corners and curved edges of the boundary. Thus, this has been tackled in reference [84] by Padé approximation of the dynamic stiffness matrix of the unbounded domain, obtained by the SBFEM, presented into a recursive formulation in time domain. The dynamic stiffness matrix of the unbounded domain could also be obtained by the BEM.

Another technique is to construct a continued fraction solution of the dynamic stiffness matrix as proposed in reference [84]. It is then followed by introducing auxiliary variables, in order to eliminate the high-order derivatives in the high-order transmitting boundaries, to be employed with the continued fraction solution for the development of a high-order local transmitting boundary condition. The FEM is used in both frequency and time domains. The continued fraction solution is determined directly from the SBFEM leading to frequency independent coefficients and symmetrical matrices. This method is proved to be very efficient for 2D problems, however it may fail for large scale problems which involve large number of degrees of freedom. As a consequence, the method does not converge by increasing the order of the expansion. Ill-conditioned equations and instability issues have been encountered. The advantage of the high-order absorbing boundaries based on the continued fraction is that the coefficient matrices computed for lower orders are not required to be determined again if one is seeking to increase the order of the continued fraction. This is not the case as in Padé series of reference [43]. Improvement of the continued fraction method is also achieved by Birk *et al.* [85] where the numerical procedure is improved by normalising the coefficient matrices of the continued fraction using a matrix-valued scaling factor. A more robust solution is obtained which is also suitable for 3D problems with many degrees of freedom.

Another approach, developed in the 1970s for dealing with acoustic problems, is based on the Doubly Asymptotic Approximation (DAA) of the impedance of the boundary in a such way that the approximations will match asymptotically the boundary integrals at both high and low frequency range, sometimes it is referred as early (short wavelength) and late time (long wavelength), respectively. The development to elastodynamics found its way around 10 years later by Underwood and Geers [57] where a first order DAA for linear soil-structure interaction problems is proposed for linear elastic media and it is applicable to nonlinear behaviour of the soil.

Mathews and Geers [86] used a first order DAA to model nonlinear ground shock where the DAA is placed at some distance from the surface of the structure. To make things more obvious, the DAA relates the scattered force vector to the scattered displacement vector and approximates the relationship for both ranges of frequencies, high and low.

First and second order DAA_1 and DAA_2 are derived by Geers and Lewis [87] for isotropic elastic media for transient elastodynamic problems using operator matching procedure. In their procedure, they first derived the early time and the late time approximation equations. They applied Laplace transform on these approximations. They introduced a trial equation of the DAA_1 and then reformulated this equation in an asymptotic form. To obtain DAA_1, a matching procedure between the transformed equation and the asymptotic equation is employed. Deriving DAA_2 is similar to deriving DAA_1. Qi and Geers [88] employed Biot's equations to derive DAA_1 and DAA_2 for poroelastic media using the operator matching method.

2.3.3 Elementary boundaries (non-transmitting)

In this type of boundaries, either prescribed displacements or stresses are placed at the boundaries of interest. Herein, when displacements are prescribed at the boundaries this will represent a fixed end (for example a fixed end of rod where the displacement is not allowed or fixed base like rigid bedrock). This case is referred as Dirichlet boundary condition and it is recognised as (D) condition. On the other hand, if stresses are prescribed at the boundaries (i.e. displacements are allowed), this represents the analogue of free end (in the case of rod or free surface condition). This is also known as Neumann condition and recognised as (N) condition. Now, if both schemes are combined we will be able to solve problems with more than one degree of freedom per boundary node. Smith [54] attempted to improve the performance of (D,N) boundaries as they behave as perfect reflectors if energy is not transmitted as some energy may be trapped in along those boundaries and eventually will dissipate with the presence of internal damping in the medium. Where an approach was proposed to solve at least twice, one with respect to (D_n,N_t) and the other with respect (D_t,N_n), where the subscripts n and t refer to normal and tangential directions to the boundary at a point of interest, respectively. Smith's refinement was based on the fact that body waves will reflect with same amplitude and phase in the first situation and with the same amplitude but opposite phase in the second reflection. Hence, the process of adding these two solutions together will cancel the reflections. One disadvantage of this scheme is when multiple reflections occur, they could not be fully dealt with by this method and hence the solution deteriorates with time. This scheme is not suitable for the frequency domain analysis.

2.3.4 Infinite elements

The term infinite element indicates an element which has at least one coordinate extending to infinity. Ungless [89] developed in his master dissertation the first infinite element and named it as an infinite finite element but has not been published. A few years later, Bettess [90] published his work on infinite elements for treating fluid-structure interaction. Infinite elements are classified by Bettess as static and dynamic. It is worth mentioning that various infinite elements are used in the literature for dealing with several types of problems such as; heat transfer problems, hydrodynamics and seepage problems. For each individual problem, shape functions associated with the infinite elements are derived by considering the far field behaviour in the problem. As this thesis is only concerned on wave propagation problems in elastodynamics, other applications will not be included here.

Bettess [90] pioneered the infinite elements with Zienkiewicz and other co-workers [91, 92], where he introduced a set of shape functions simulating the infinite extent of the elements. These shape functions are based on the Lagrange polynomials multiplied by a decay function. The mathematical formulations of these shape functions could be found in reference [90]. It is worth mentioning that the decay function depends on an arbitrary distance which gives an indication of the exponential decay, chosen by the analyst. It has an important influence on the results. Hence, Bettess [90] indicated that the infinite element technique could lead to misleading results at that stage, where an application of viscous flow problem in 2D was provided. Bettess and Zienkiewicz [91] introduced the finite/infinite concept in dealing with several problems with unbounded surface waves. It was assumed that the variation of local coordinates in η-direction lays from -1 to 1 as it is shown in Figure 2.6.

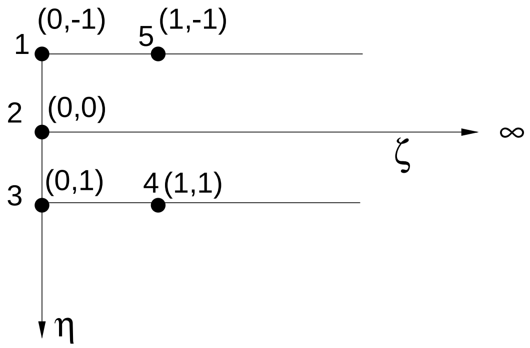

Figure 2.6: Schematic diagram of an infinite element in the local coordinates.

Saini *et al.* [92] employed the developed shape function in reference [91] to study hydrodynamic effects on concrete gravity dams. Chow and Smith [93] developed periodic infinite elements based on the Serendipity family which were shown to be more effective than the Lagrangian elements to deal with problems involving multiple wave types such as in geomechanic and elastodynamic problems. In the formulations presented in reference [93], three types of shape functions were developed namely; extending to infinity in η-direction, ξ-direction and in both directions where the Gauss-Laguerre integration scheme is used when integrating in the infinite direction, while the Gauss-Legendre is used in the finite direction.

The formulation of the infinite element is first achieved by transforming the coordinates x and y. For example, Yang *et al.* [94] used the following formulations

$$x = \sum_{i=1}^{5} N_i^{'} x_i \qquad \text{and} \qquad y = \sum_{i=1}^{5} N_i^{'} y_i. \tag{2.19}$$

The shape functions $N_i^{'}$ are linear in ξ and quadratic in η and are expressed as

$$\begin{aligned} N_1^{'} &= -\frac{1}{2}(\xi-1)(\eta-1)\eta, \\ N_2^{'} &= -(\xi-1)(\eta-1)(\eta+1), \\ N_3^{'} &= -\frac{1}{2}(\xi-1)(\eta+1)\eta, \\ N_4^{'} &= \frac{1}{2}\xi(\eta+1), \\ N_5^{'} &= -\frac{1}{2}\xi(\eta-1). \end{aligned} \tag{2.20}$$

For example, displacement within the element is interpolated from the nodal displacements of the element

$$u = \sum_{i=1}^{3} N_i u_i \qquad \text{and} \qquad v = \sum_{i=1}^{3} N_i v_i, \tag{2.21}$$

where the shape functions N_i are given by

$$\begin{aligned} N_1 &= \frac{\eta(\eta-1)}{2} \times P(\xi), \\ N_2 &= -(\eta-1)(\eta+1) \times P(\xi), \\ N_3 &= \frac{\eta(\eta+1)}{2} \times P(\xi), \end{aligned} \tag{2.22}$$

with $P(\xi)$ being a propagation function which contains the displacement amplitude decay factor α_L due to the geometric attenuation and the wave number k_L of the propagating waves. It is given by

$$P(\xi) = e^{-\alpha_L \xi} \times e^{-ik_L \xi}. \tag{2.23}$$

The propagation factor has a key role in constructing the infinite elements. It is expressed in terms of local coordinates in expression (2.23). It is then expressed in a global sense and the amplitude decay factor is given some values as proposed in reference [94] based on properties of wave propagation. The location of the element is taken into account for the chosen value. For example, in the case of a line source, zero value is suggested for shallow depths arguing that Rayleigh waves do not decay on the free surface. A value of $(1/2R)$, R being the radial distance of the line source and the lateral boundary, is suggested in the regions where body waves are dominant. Values of $(1/2R)$ and $(1/R)$ were proposed for the near surface and well below the free surface elements in the case of a point load. It is very difficult to represent a region with a predefined wavenumber as it is dependant on the velocity. The criteria for choosing the wavenumber is based on the dominance of the type of the wave in a certain region. This means that wavenumber associated with Rayleigh waves is selected for near surface elements while wavenumbers associated with the shear and pressure waves are chosen for elsewhere. Figure 2.7 depicts the problem representation by finite elements in the near field and infinite elements in the far field.

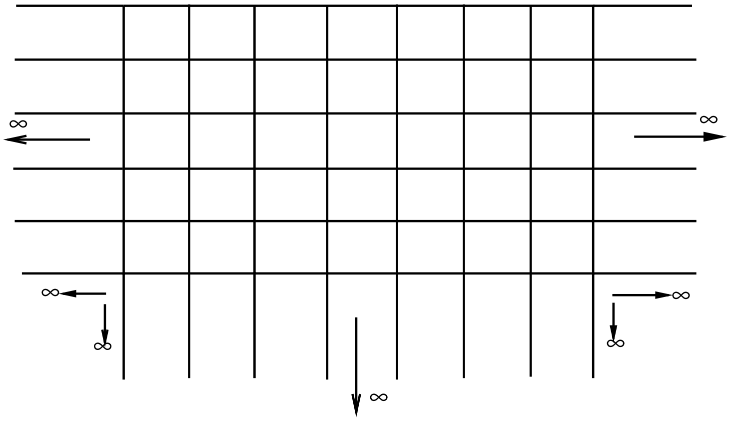

Figure 2.7: Finite/infinite element for unbounded domains.

The variation in ξ-direction was chosen arbitrarily to be 0, 2 and 30. Lagrange interpolation is used in both directions but, a new coordinate is introduced in the ξ-direction to scale the length of the element. Regarding the construction of the shape functions, Lagrange polynomials are used in the η-direction. A special shape function in the new direction is introduced in which an exponential term, a function of the wavenumber, is enforced. Three terms are involved in the new shape function; the first term represents a polynomial with the new coordinate, a decay function which depends on the arbitrarily chosen distance and an exponential term which reflects the propagation of waves with respect to the new coordinate. Sommerfeld radiation condition is therefore satisfied. The formulation of the infinite elements' matrices would be carried out in the same way as in FEM. For the numerical integration, Newton-Cotes formula is used to overcome the large number of sampling points of the Gauss-Legendre method in order to approximate the harmonic function.

When analysing surface water problems, only one wave type is used in reference [91]. This is not the case in elasticity problems where multiple types of waves may be encountered. This is tackled by Chow and Smith [93], for static and periodic problems in geomechanics, where they incorporated two wave types to determine the area where a single wave type will be dominant. Arguing that Rayleigh waves are dominant near the surface and decay very quickly with depth, it would be appropriate to use Rayleigh wavenumber at the lateral boundaries near the surface. On the other hand, body waves will be dominant in depth and therefore body wavenumbers would be used with the infinite elements at the base of the domain. Regarding the numerical integration, Gauss-Legendre integration is used for infinite elements in the direction not extending to infinity while Newton-Cotes scheme is used in the direction extending to infinity.

Medina and Taylor [95] proposed a scheme for computing the element matrices of the infinite elements. It is based on Gauss-Laguerre quadrature in the infinite direction and Gauss-Legendre in the finite direction. An element matrix is first expressed as an integration with respect to the infinite and finite directions and then approximated numerically. The approximated expressions contain the Gauss-Laguerre weights and some integration points which are required to evaluate the expression of the element matrix. Thereafter, Medina and Taylor [95] introduced a criteria which is basically based on element shape functions in order to select the number of integration points. Chuhan and Chongbin [96] extended this approach to problems dealing with foundation dynamics. Galerkin weighted residual method was used first for the derivation of the system dynamic equation and then the infinite elements were constructed. In a more recent attempt, Yang *et al.* [94] introduced the idea of simulating wave propagation in semi-infinite media with problems of ground borne vibrations induced by passing trains on the soil surface and proposed a scheme for estimating the decay factor rather than use arbitrary values. Yang *et al.* [94] proposed guidelines for choosing values for the amplitude decay factor based on the characteristics of the waves within the domain. As Rayleigh waves are dominant near the surface and decay very quickly with depth, the amplitude decay factor could be assigned a very small value, close to zero, for this region. On the other hand, body waves are dominant at greater depths and therefore a higher amplitude decay factor would be chosen.

The concept of coupled finite-infinite elements was extended to cover various types of problems such as dealing with unbounded surface waves [91], fluid wave propagation or dam-reservoir interaction [92], elastodynamic and geomechanic problems [93, 95]. Yang and Hung [97] proposed a 2.5D finite/infinite element approach to deal with ground borne vibrations induced by moving loads. Yang *et al.* [98] conducted an extensive parametric study by adopting a 2D finite-infinite approach for simulating wave propagation in soil media and examined the effect of the loading depth, the shear modulus of the soil, the thickness of the soil layer, damping and the loading in a tunnel.

2.4 Brief summary

A literature review is carried out in this chapter to cover some of the research work related to the development of absorbing boundary conditions for elastodynamic problems. These boundary conditions play a major role in making finite-size computational models, based principally on FEM, efficient in solving wave problems in unbounded media.

These absorbing boundary conditions are classified into local and nonlocal (global) boundary conditions. In summary, while the nonlocal boundary conditions are more accurate, they involve high computational effort in addition to associated difficulties at the implementation level. Whereas the local absorbing boundary conditions are simpler to implement and do not involve high computational cost. However, they are not as accurate as the nonlocal boundary conditions when used on similar models.

Given that the following chapter is based on a modelling approach in the frequency domain, under plane strain condition, the Thin Layer Method is adopted as a method to ensure wave radiation to infinity

Chapter 3

Wave propagation modelling in soil media over bedrock

3.1 Introduction

The Thin Layer Method (TLM) or the consistent transmitting boundary condition method, developed by Waas [3], is adopted in this work to simulate wave propagation in unbounded soil media. The problem is formulated in the frequency domain under plane strain conditions. The domain is divided into three regions. The region of interest usually contains foundations, tunnels, wave barriers or surface structures, which is the focus for analysis. It is called the irregular soil domain. This zone will be treated by the finite element method and it will be discretised into structured or unstructured mesh grids with two degrees of freedom per node. The base of the model is assumed in the current analysis to be horizontal and resting on rigid bedrock. The irregular region is bounded by two lateral regular regions extending to infinity with horizontal layers, each assumed to be homogenous. The finite element model does not include the two lateral semi-infinite regions and therefore efficient boundary conditions should be defined at the boundaries of the computational domain to reduce the computational size and ensure wave radiation to infinity. Figure 3.1a shows a schematic diagram of the considered problem and its idealisation within the context of FEM in Figure 3.1b.

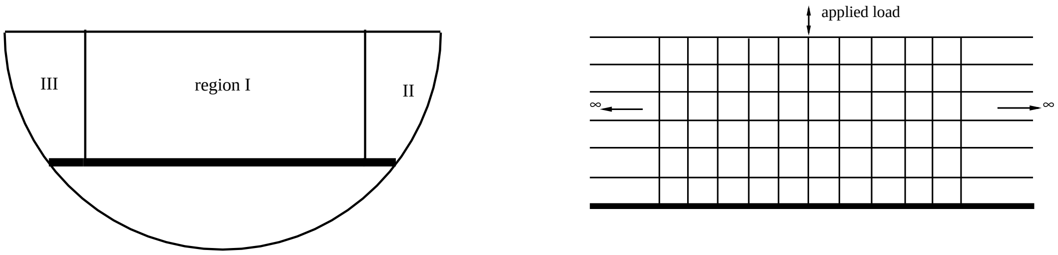

(a) General diagram of 2D soil domain

(b) Finite element treatment

Figure 3.1: Problem representation and idealisation.

3.2 Treatment of the irregular region

The irregular region (I) is modelled by the conventional finite element method. It is divided into finite elements, quadrilateral or triangular, with two degrees of freedom per node, the horizontal and vertical displacements. Each element adjacent to either the left or right vertical boundary shares two nodes with the semi-infinite lateral sub-layers. As the irregular region is assumed to be overlaying rigid bedrock the nodes at the base are fixed. Finite element matrices, mass and stiffness matrices, are computed by the standard finite element method and the global mass and stiffness matrices are obtained by assembling the elementary matrices. Assuming that a harmonic load of frequency ω, is imposed at any location of the model, the dynamic equation of the irregular region is expressed by

$$\left[\mathbf{K} - \omega^2 \mathbf{M}\right] \mathbf{u} = \mathbf{F}, \tag{3.1}$$

where **K** and **M** are the global stiffness and mass matrices, **u** is the nodal displacement vector and **F** denotes to the nodal force vector. The level of discretisation, recommended in reference [3], consists to constraint the element size not to exceed one-tenth of the shear wavelength.

3.3 Treatment of the regular regions

The regular or semi-infinite lateral layered regions (II) and (III), right and left, could not be treated by the FEM. The reason for this is that they extend to infinity and therefore an infinite number of elements and degrees of freedom would be involved; the problem will not be practical to solve. Therefore, a semi-analytical solution is employed in their corresponding model. The region on the left is analogous to the one on the right, the only difference is the location of the nodes, and for this reason the region on the right, as depicted in Figure 3.2, is only considered. It is assumed that material properties of each layer do not vary in the horizontal direction. Each soil layer is divided into sub-layers with thicknesses not exceeding on tenth of the shear wavelength. Within each sub-layer the displacement field is assumed to vary linearly with depth. In the horizontal direction, the displacement field is described by a plane wave propagating in the *x*-direction with a given wavenumber *k*.

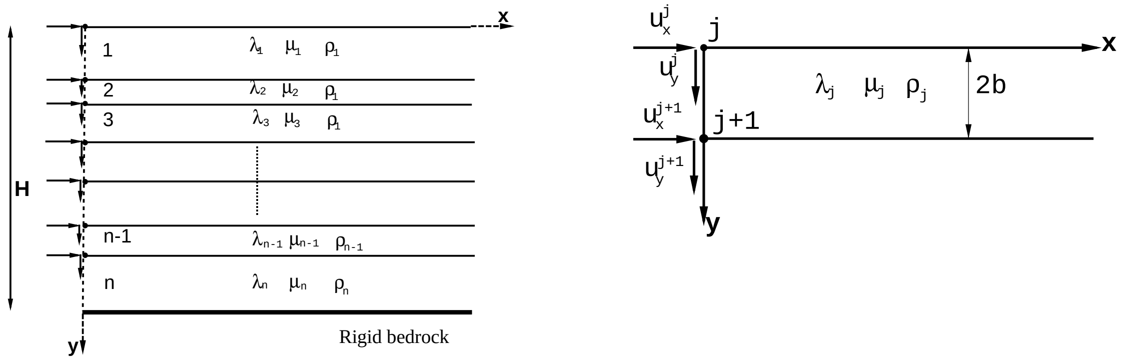

(a) horizontal layers

(b) single layer representation

Figure 3.2: Regular region representation.

The virtual work method, which is most suited for harmonic loading, was employed by Waas [3] to deal with this region where the variables are also separated. The principle of virtual work is based on energy equilibrium. It is achieved when the summation of the virtual work performed by the actual strains and actual forces on the virtual displacements and strains vanishes, otherwise the rate of virtual work should be considered.

Stresses σ and strains ε are related by the stress-strain matrix as in the following expression

$$\begin{Bmatrix} \sigma_{xx} \\ \sigma_{yy} \\ \sigma_{xy} \end{Bmatrix} = \begin{bmatrix} \lambda+2\mu & \lambda & 0 \\ \lambda & \lambda+2\mu & 0 \\ 0 & 0 & \mu \end{bmatrix} \begin{Bmatrix} \varepsilon_{xx} \\ \varepsilon_{yy} \\ \gamma_{xy} \end{Bmatrix}, \tag{3.2}$$

where λ and μ are the Lamé coefficients and they are expressed by

$$\lambda = \frac{E\nu}{(1+\nu)(1-2\nu)} \qquad \text{and} \qquad \mu = \frac{E}{2(1+\nu)}, \tag{3.3}$$

with E being the elasticity modulus of the soil which is complex in the viscoelastic case and ν is Poisson's ratio. Compression and shear wave velocities, c_p and c_s, are calculated respectively from the following expressions

$$c_p = \sqrt{\frac{\lambda + 2\mu}{\rho}} \qquad \text{and} \qquad c_s = \sqrt{\frac{\mu}{\rho}}, \tag{3.4}$$

where ρ represents the soil density. For linear viscoelastic materials, the Lamé coefficients are of complex nature. The fraction of the critical damping, β, is used as a measure for material damping. Therefore, complex Lamé modulii are expressed as

$$\lambda^c = \lambda(1 + \mathrm{i}2\beta) \qquad \text{and} \qquad \mu^c = \mu(1 + \mathrm{i}2\beta).$$

The pressure and shear wave velocities will be also of complex values. All derivations are given for linear elastic soil, however, complex Lamé coefficients, λ^c and μ^c can replace the elastic coefficients, λ and μ for viscoelastic materials.

Strains are expressed in terms of the displacements as follows

$$\left\{ \begin{array}{c} \varepsilon_{xx} \\ \varepsilon_{yy} \\ \gamma_{xy} \end{array} \right\} = \left\{ \begin{array}{c} u_{,x} \\ v_{,y} \\ u_{,y} + v_{,x} \end{array} \right\}, \tag{3.5}$$

where $u_{,x}$, for example, represents the derivative of the displacements field u with respect to x.

The derivation of the consistent transmitting boundary in this thesis is adopted from Laghrouche [99] who employed the principle of virtual work and formulated the consistent transmitting boundaries for 2D soil-structure interaction problems [100]. The principle of virtual displacement indicates that work done by external forces, δW_{ext}, and internal forces, δW_{int}, during an arbitrary virtual displacement is equivalent to the change in strain energy and energy dissipated by internal friction due to the virtual displacement. This is summarised in the following expression

$$\delta W_{ext} + \delta W_{int} = \delta A, \tag{3.6}$$

where δA is the change in the virtual work by the acceleration quantities. However, the work performed by the interior forces on a body is equivalent to the change of the deformation on that body with an opposite sign, $\delta W_{int} = -\delta Ed$, and therefore

$$\delta Ed + \delta A = \delta W_{ext}. \tag{3.7}$$

In other words, the virtual work of a system of equilibrium forces vanishes on virtual displacements. Next, we will compute these quantities, balance the equation for a single sub-layer j and assemble for all sub-layers.

3.3.1 Virtual change of strain energy

For any sub-layer j, the change in the strain energy can be written as

$$
\begin{aligned}
\delta Ed &= \int_v \{\sigma^T\}\{\delta\varepsilon\}\, dV \\
&= \int_0^\infty \int_0^{2b} \int_0^1 (\delta\varepsilon_{xx}\sigma_{xx} + \delta\varepsilon_{yy}\sigma_{yy} + \delta\gamma_{xy}\sigma_{xy})\, dx\, dy\, dz. \qquad (3.8)
\end{aligned}
$$

The term $\{\sigma^T\}\{\delta\varepsilon\}$ represents the change in the strain energy in addition to the loss in energy over the entire volume of the sub-layer due to the internal friction. If we consider a unit length in z-direction, the z term in the integration will yield to a unit value. Using the stress-strain and the strain-displacement relations described in equations (3.2) and (3.5), the variation of the strain energy can be rearranged in a new form

$$
\begin{aligned}
\delta Ed &= \int_0^\infty \int_0^{2b} \{\delta u_{,x}[(\lambda+2\mu)\, u_{,x} + \lambda v_{,y}] + \delta v_{,y}[\lambda u_{,x} + (\lambda+2\mu)\, v_{,y}] \\
&+ \delta\,(u_{,y} + v_{,x})\,\mu\,(u_{,y} + v_{,x})\} dx\, dy. \qquad (3.9)
\end{aligned}
$$

As mentioned above, the displacement is assumed to vary linearly with respect to depth so if we introduce linear shape functions in the y-direction such that

$$
\{U_p\} = \begin{bmatrix} N(y) & 0 \\ 0 & N(y) \end{bmatrix} \begin{Bmatrix} u_j \\ u_{j+1} \\ v_j \\ v_{j+1} \end{Bmatrix} \quad , \qquad N(y) = \begin{bmatrix} 1 - \frac{y}{2b} & \frac{y}{2b} \end{bmatrix}, \qquad (3.10)
$$

where U_p is the displacement vector at any point within the sub-layer. If we let

$$
U = \begin{Bmatrix} u_j \\ u_{j+1} \end{Bmatrix} \qquad \text{and} \qquad V = \begin{Bmatrix} v_j \\ v_{j+1} \end{Bmatrix}. \qquad (3.11)
$$

Substituting in equation (3.9) we obtain

$$
\begin{aligned}
\delta Ed &= \int_0^\infty \int_0^{2b} \{\delta U_{,x}^T N^T (\lambda+2\mu) N U_{,x} + \delta U_{,x}^T N^T \lambda N_{,y} V + \delta V^T N_{,y}^T \lambda N U_{,x} \\
&+ \delta V^T N_{,y}^T (\lambda+2\mu) N_{,y} V + \delta U^T N_{,y}^T \mu N_{,y} U + \delta U^T N_{,y}^T \mu V_{,x} \qquad (3.12) \\
&+ \delta V_{,x}^T N^T \mu N_{,y} U + \delta V_{,x}^T N^T \mu N V_{,x}\} dx\, dy.
\end{aligned}
$$

Using the integration by part scheme, the previous equation will yield to

$$\begin{aligned}
\delta Ed &= \left[\delta U^T \int_0^{2b} N^T[(\lambda+2\mu)NU_{,x}+\lambda N_{,y}V]dy\right]_0^\infty + \left[\delta V^T \int_0^{2b} N^T[\mu(N_{,y}U+NV_{,x}]dy\right]_0^\infty \\
&- \int_0^\infty \delta U^T \left[(\lambda+2\mu)\int_0^{2b} N^T N dy\right] U_{,xx}dx - \int_0^\infty \delta V^T \left[\mu \int_0^{2b} N^T N dy\right] V_{,xx}dx \\
&+ \int_0^\infty \delta U^T \left[\mu \int_0^{2b} N_{,y}^T N dy\right] V_{,x}dx - \int_0^\infty \delta U^T \left[\lambda \int_0^{2b} N^T N_{,y}dy\right] V_{,x}dx \\
&+ \int_0^\infty \delta V^T \left[\lambda \int_0^{2b} N_{,y}^T N dy\right] U_{,x}dx - \int_0^\infty \delta V^T \left[\mu \int_0^{2b} N^T N_{,y}dy\right] U_{,x}dx \\
&+ \int_0^\infty \delta U^T \left[\mu \int_0^{2b} N_{,y}^T N_{,y}dy\right] U dx + \int_0^\infty \delta V^T \left[(\lambda+2\mu)\int_0^{2b} N_{y}^T N_{,y}dy\right] V dx.
\end{aligned} \tag{3.13}$$

The first and second terms in equation (3.13) can be written in a new expression with considering the stress-strain relationship described earlier in (3.2)

$$\left[\delta U^T \int_0^{2b} N^T[(\lambda+2\mu)NU_{,x}+\lambda N_{,y}V]dy\right]_0^\infty = \left[\delta U^T \int_0^{2b} N^T \sigma_{xx} dy\right]_0^\infty . \tag{3.14}$$

$$\left[\delta V^T \int_0^{2b} N^T[\mu(N_{,y}U+NV_{,x}]dy\right]_0^\infty = \left[\delta V^T \int_0^{2b} N^T \sigma_{xy} dy\right]_0^\infty . \tag{3.15}$$

When x approaches infinity, σ_{xx} and σ_{xy} will vanish while for x=0, expressions (3.14) & (3.15) should be kept for further developments.

3.3.2 Virtual work by the acceleration quantities

The acceleration quantities or inertial forces are proportional to the actual displacement when considering a harmonic loading. The virtual work of the acceleration quantities is expressed as

$$\delta A = \int_0^\infty \int_0^{2b} (\rho \ddot{u}\delta u + \rho \ddot{v}\delta v)\,dx\,dy, \tag{3.16}$$

and therefore

$$\delta A = \int_0^\infty \{\delta U^T \left(\rho \int_0^{2b} N^T N dy\right)\ddot{U} + \delta V^T \left(\rho \int_0^{2b} N^T N dy\right)\ddot{V}\}dx. \tag{3.17}$$

Combining equation (3.10) with equation (3.17) we obtain the following matrices

$$\mathbf{A_0} = \begin{bmatrix} \mu \int_0^{2b} N_{,y}^T N_{,y}\,dy & 0 \\ 0 & (\lambda+2\mu)\int_0^{2b} N_{,y}^T N_{,y}\,dy \end{bmatrix}, \tag{3.18a}$$

$$\mathbf{A_1} = \begin{bmatrix} 0 & \lambda \int_0^{2b} N^T N_{,y} dy - \mu \int_0^{2b} N_{,y}^T N dy \\ -\lambda \int_0^{2b} N_{,y}^T N dy + \mu \int_0^{2b} N^T N_{,y} dy & 0 \end{bmatrix}, \qquad (3.18b)$$

$$\mathbf{A_2} = \begin{bmatrix} (\lambda + 2\mu) \int_0^{2b} N^T N dy & 0 \\ 0 & \mu \int_0^{2b} N^T N dy \end{bmatrix}, \qquad (3.18c)$$

$$\mathbf{A_3} = \begin{bmatrix} 0 & \lambda \int_0^{2b} N^T N_{,y} dy \\ \mu \int_0^{2b} N^T N_{,y} dy & 0 \end{bmatrix}, \qquad (3.18d)$$

$$\mathbf{M_0} = \begin{bmatrix} \rho \int_0^{2b} N^T N dy & 0 \\ 0 & \rho \int_0^{2b} N^T N dy \end{bmatrix}. \qquad (3.18e)$$

Computing the integrals inside the matrices in expressions (3.18) will explicitly show that these matrices are function of Lamé coefficients as well as the thickness of each individual sub-layer, except for matrix $\mathbf{A}_3$ which depends only on the material properties. Matrix $\mathbf{M}_0$ will vary with both the thickness and density of the layer. These matrices are 4×4, matrices $\mathbf{A}_0$, $\mathbf{A}_2$, $\mathbf{A}_3$ and $\mathbf{M}_0$ are symmetrical while $\mathbf{A}_1$ is antisymmetrical. After integration, they are expressed as follows

$$\mathbf{A_0} = \frac{1}{2b} \begin{bmatrix} \mu & 0 & -\mu & 0 \\ 0 & \lambda + 2\mu & 0 & -(\lambda + 2\mu) \\ -\mu & 0 & \mu & 0 \\ 0 & -(\lambda + 2\mu) & 0 & \lambda + 2\mu \end{bmatrix}, \qquad (3.19a)$$

$$\mathbf{A_1} = \frac{1}{2} \begin{bmatrix} 0 & -\lambda + \mu & 0 & \lambda + \mu \\ -\mu + \lambda & 0 & \lambda + \mu & 0 \\ 0 & -\lambda - \mu & 0 & \lambda - \mu \\ -\lambda - \mu & 0 & -\lambda + \mu & 0 \end{bmatrix}, \qquad (3.19b)$$

$$\mathbf{A_2} = \frac{b}{3}\begin{bmatrix} 2(\lambda+2\mu) & 0 & \lambda+2\mu & 0 \\ 0 & 2\mu & 0 & \mu \\ \lambda+2\mu & 0 & 2(\lambda+2\mu) & 0 \\ 0 & \mu & 0 & 2\mu \end{bmatrix}, \tag{3.19c}$$

$$\mathbf{A_3} = \frac{1}{2}\begin{bmatrix} 0 & \lambda & 0 & -\lambda \\ \mu & 0 & -\mu & 0 \\ 0 & \lambda & 0 & -\lambda \\ \mu & 0 & -\mu & 0 \end{bmatrix}, \tag{3.19d}$$

$$\mathbf{M_0} = \frac{\rho b}{3}\begin{bmatrix} 2 & 0 & 1 & 0 \\ 0 & 2 & 0 & 1 \\ 1 & 0 & 2 & 0 \\ 0 & 1 & 0 & 2 \end{bmatrix}. \tag{3.19e}$$

Back substituting these matrices into the left-hand side of the virtual work equation (3.7), the equation for sub-layer j would be

$$\begin{aligned} \delta Ed + \delta A &= \int_0^\infty \delta u^T \left(-\mathbf{A_2} u_{,xx} - \mathbf{A_1} u_{,x} + \mathbf{A_0} u + \mathbf{M_0} \ddot{u}\right) dx \\ &+ \delta u_{x=0}^T \left(\mathbf{A_2} u_{,x} + \mathbf{A_3} u\right)_{x=0}. \end{aligned} \tag{3.20}$$

Assembling for all sub-layers gives

$$\begin{aligned} \delta Ed^* + \delta A^* &= \int_0^\infty \delta u^{*T} \left(-\mathbf{A_2^*} u^*_{,xx} - \mathbf{A_1^*} u^*_{,x} + \mathbf{A_0^*} u^* + \mathbf{M_0^*} \ddot{u}^*\right) dx \\ &+ \left(\delta u^{*T}_{x=0} \mathbf{A_2^*} u^*_{,x} + \mathbf{A_3^*} u^*\right)_{x=0}. \end{aligned} \tag{3.21}$$

The superscript symbol * refers to the global system. A typical assembling process, for example matrix $\mathbf{A_1^*}$, is shown in Figure 3.3.

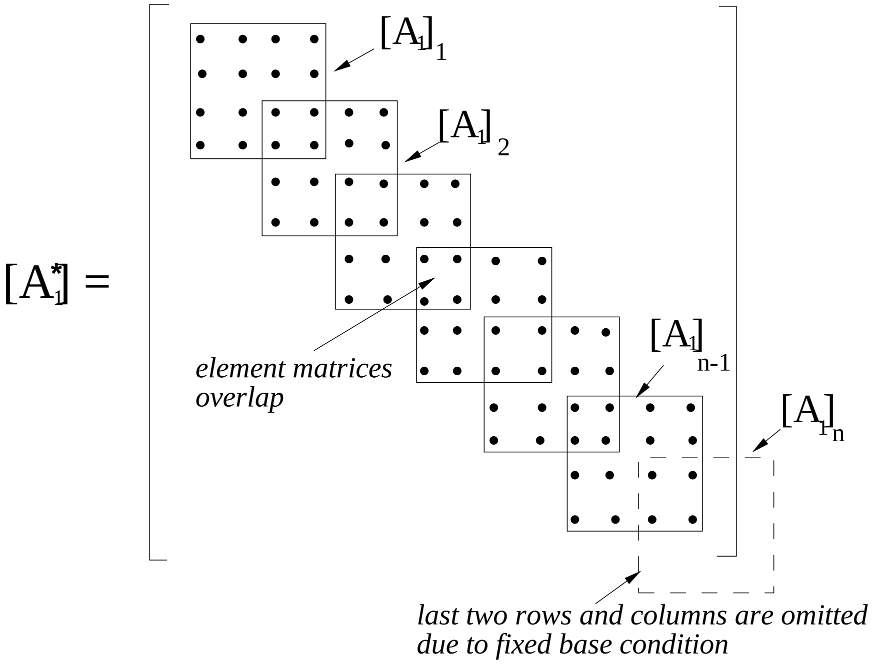

Figure 3.3: The structure of global matrices.

The index outside the square brackets refers to the sub-layer number. As the layered region is assumed to be overlaying rigid bedrock, the last two degrees of freedom corresponding to the last node at the base are discarded as it is fixed. As a result, the dimension of the layered system matrices is $2n \times 2n$ where n is the number of sub-layers. All matrices are complex, except $\mathbf{M_0}$, for viscoelastic materials.

3.3.3 Virtual work of external forces

The work performed by the external forces on the central domain is expressed as

$$\delta W_{ext} = \vec{F}\,\delta\vec{u}, \tag{3.22}$$

where

$$F = \begin{Bmatrix} F_{1x} \\ F_{2x} \\ F_{1y} \\ F_{2y} \end{Bmatrix} \quad \text{and} \quad \delta u = \begin{Bmatrix} \delta u_1 \\ \delta u_2 \\ \delta v_1 \\ \delta v_2 \end{Bmatrix}. \tag{3.23}$$

Therefore,

$$\delta W_{ext} = \delta U^T F_x + \delta V^T F_y = \delta u_{x=0}^T F. \tag{3.24}$$

For the global system

$$\delta W_{ext}^* = \{\delta u^*\}_{x=0}^T F^*. \tag{3.25}$$

Substituting in the virtual work equation of expression (3.15)

$$\int_0^{\infty} \{\delta u^*\}^T (-\mathbf{A_2^*} u^*_{,xx} - \mathbf{A_1^*} u^*_{,x} + \mathbf{A_0^*} u^* + \mathbf{M_0^*} \ddot{u}^*) dx$$

$$+\{\delta u^*\}^T_{x=0} \left(\mathbf{A_2^*} u^*_{,x} + \mathbf{A_3^*} u^*\right)_{x=0} = \{\delta u^*\}^T_{x=0} \mathbf{F}^*. \tag{3.26}$$

This equation is satisfied if both

$$-\mathbf{A_2^*} u^*_{,xx} - \mathbf{A_1^*} u^*_{,x} + \mathbf{A_0^*} u^* + \mathbf{M_0^*} \ddot{u}^* = 0, \tag{3.27}$$

and

$$\left[\mathbf{A_2^*} u^*_{,x} + \mathbf{A_3^*} u^*\right]_{x=0} = \mathbf{F}^*, \tag{3.28}$$

are satisfied. Equation (3.27) will lead to a second order eigenvalue problem and nodal forces will be determined from equation (3.28) as will be shown later. The external forces are assumed to be harmonic and therefore the displacements are also harmonic in time. Therefore it is possible to write

$$\{u^*\} = \{u_0^*\} e^{\mathrm{i}(\omega t - kx)}, \tag{3.29}$$

where ω is the frequency of the forcing load and k is the wavenumber. Substituting (3.29) into (3.27) leads to

$$\left[k^2 \mathbf{A_2^*} + \mathrm{i} k \mathbf{A_1^*} + \mathbf{A_0^*} - \omega^2 \mathbf{M_0^*}\right] u_0^* = 0. \tag{3.30}$$

Equation (3.30) is a second order eigenvalue problem in k and represents $2n$ homogeneous equations. For a nontrivial solution, the determinant of the system matrix must be equal to zero. One method to solve the quadratic eigenvalue problem is by reducing it into a first order problem, hence the dimension of the problem will be increased to $4n$ and consequently $4n$ eigenvalues, k_s, with their corresponding eignevectors, $\mathbf{U}_s$, are obtained. It is shown that for each eigenvalue k_s of the form $\kappa_1 + \mathrm{i}\kappa_2$ there is a corresponding eigenvalue of the form $\kappa_1 - \mathrm{i}\kappa_2$. This leads to the fact that half of the modes decay with $x > 0$, $\kappa_2 < 0$, and therefore represent waves travelling in the positive x-direction, and the other half decaying with $x < 0$, $\kappa_2 > 0$, representing waves travelling in the negative x-direction. The eigenvalues or wavenumbers are retained in the diagonal matrix $\mathbf{H}$, a $2n \times 2n$ matrix, which has the form

$$\mathbf{H} = \begin{bmatrix} k_1 & & \\ & \ddots & \\ & & k_{2n} \end{bmatrix}. \tag{3.31}$$

The displacement field is therefore written as a combination of all eigenmodes such that

$$\{u^*\} = \sum_{s=1}^{2n} a_s \{u_s\} e^{\mathrm{i}(\omega t - k_s x)}, \tag{3.32}$$

where$\{u_s\}$ is the eigenvector associated with the eigenvalue k_s, a_s is the mode shape participation factor.

The displacement field of the right region could be written as

$$\mathbf{U_R} = \sum_{s=1}^{2n} a_s \{u_s\} = a\mathbf{U}, \tag{3.33}$$

with $\mathbf{U_R}$ and a_s being vectors of dimension of $2n$. The mode shapes are contained in the matrix $\mathbf{U}$ of dimension $2n \times 2n$. Let us now derive the nodal forces on the boundary of the right side region, recalling equation (3.28) and performing the first derivative of equation (3.32) the force vector could be written as

$$F^* = \sum_{s=1}^{2n} a_s e^{\mathrm{i}(\omega t - k_s x)} \left[-\mathrm{i}k_s \mathbf{A}_2^* + \mathbf{A}_3^*\right]. \tag{3.34}$$

The derivative of expression (3.28) could be rearranged, by calling the diagonal matrix $\mathbf{H}$ which contains the eigenvalues and their corresponding eigenvectors in $\mathbf{V}$, as follows

$$u^*_{,x} = -\mathrm{i}\mathbf{VH} \left\{ \begin{array}{c} a_1 e^{\mathrm{i}(\omega t - k_1 x)} \\ a_2 e^{\mathrm{i}(\omega t - k_2 x)} \\ a_3 e^{\mathrm{i}(\omega t - k_3 x)} \\ . \\ . \\ . \\ a_{2n} e^{\mathrm{i}(\omega t - k_{2n} x)} \end{array} \right\}. \tag{3.35}$$

However, from equation (3.32) we can write

$$\left\{ \begin{array}{c} a_1 e^{\mathrm{i}(\omega t - k_1 x)} \\ a_2 e^{\mathrm{i}(\omega t - k_2 x)} \\ a_3 e^{\mathrm{i}(\omega t - k_3 x)} \\ . \\ . \\ . \\ a_{2n} e^{\mathrm{i}(\omega t - k_{2n} x)} \end{array} \right\} = \mathbf{V}^{-1} u^*. \tag{3.36}$$

The force vector acting on the lateral boundary of the domain can be deduced by employing the stress and strain compatibility conditions and thereafter substituting equation (3.35) and (3.36) into (3.34) to obtain a $2n$ column force vector

$$\mathbf{F}^* = -\left[\mathrm{i}\mathbf{A}_2^* \mathbf{VHV}^{-1} + \mathbf{A}_3^*\right] u^*_{x=0}. \tag{3.37}$$

Matrix **V** contains the $2n$ eigenvectors columnwise as follows

$$\mathbf{V} = \begin{bmatrix} \mathbf{U}_1 & \ldots & \mathbf{U}_{2n} \end{bmatrix}. \tag{3.38}$$

Nodal forces are contained in vector $\mathbf{F}^*$. The displacement field is therefore written as a combination of all mode shapes which leads to nodal forces on the right and left sides of the central domain, respectively. Let us consider the right side boundary, its nodal forces vector is expressed as

$$\mathbf{F_R} = -\mathbf{R}\mathbf{U_R} \qquad \text{with} \qquad \mathbf{R} = \mathrm{i}\mathbf{A}_2^*\mathbf{V}\mathbf{H}\mathbf{V}^{-1} + \mathbf{A}_3^*, \tag{3.39}$$

where $\mathbf{U_R}$ is the nodal displacement vector of the right hand side vertical boundary. In the same way, the nodal force vector of the left hand side vertical boundary is obtained. The corresponding nodal displacement vector is $\mathbf{U_L}$

$$\mathbf{F_L} = -\mathbf{L}\mathbf{U_L} \qquad \text{with} \qquad \mathbf{L} = -\mathrm{i}\mathbf{A}_2^*\mathbf{V}^{'}\mathbf{H}^{'}\mathbf{V}^{'-1} - \mathbf{A}_3^*, \tag{3.40}$$

with $\mathbf{H}^{'}$ contains the $2n$ computed wavenumbers with $\kappa_2 > 0$ and $\mathbf{V}^{'}$ contains the corresponding $2n$ eigenmodes columnwise. The nodal displacement vectors of both lateral boundaries are part of the global displacement vector **U**. Matrices **R** and **L** are deduced form the eigenvalues and eigenmodes. The modal dynamic stiffness matrices of the transmitting boundary **R** and **L** relate the nodal displacements and the nodal forces at the right and left boundaries, respectively. These matrices are of dimension $2n \times 2n$ and represent the effect of the semi-infinite extent of the right and left lateral regular regions. Given that the displacements $\mathbf{U_R}$ and $\mathbf{U_L}$ are unknown, the associated forces will be combined with the ones of the irregular region to formulate the system equation.

3.4 The finite element model

The consistent transmitting boundary conditions are derived in section 3.3 and the unbounded domain is replaced by a bounded domain on which these transmitting conditions are applied. Therefore, the sought finite element model consists of combining the irregular region defined in section 3.2 bounded by the lateral boundaries of the domain and rigid bedrock at the bottom, as depicted in Figure 3.4. Having obtained the consistent nodal forces on the lateral boundaries, $\mathbf{F_R}$ and $\mathbf{F_L}$, and as they are a function of the nodal displacements, we can recall the dynamic stiffness of the central domain, from (3.1), and assemble these vectors as follows

$$\left[\mathbf{K} - \omega^2\mathbf{M} + \mathbf{R} + \mathbf{L}\right]\mathbf{u} = \mathbf{F}. \tag{3.41}$$

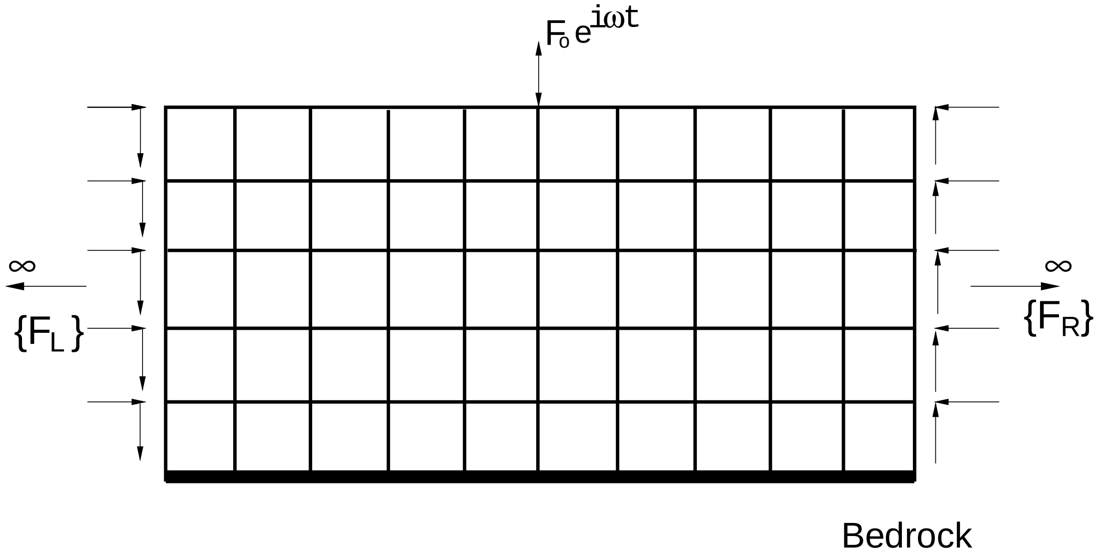

Figure 3.4: The finite element model.

As the external load is harmonic the displacement field is also harmonic, equation (3.41) will yield to

$$\left[\mathbf{K} - \omega^2 \mathbf{M} + \mathbf{R} + \mathbf{L}\right] \mathbf{u_0} = \mathbf{F}_0, \tag{3.42}$$

with $\mathbf{u_0}$ and $\mathbf{F}_0$ are amplitudes of $\mathbf{u}$ and $\mathbf{F}$, respectively and the time variable is omitted by considering a steady state problem. The system of equations (3.42) is linear and a direct solver such as the Gauss elimination approach is used to solve the problem. The solution of the linear system of equation (3.42) gives the horizontal and vertical displacements at each node of the meshed region as complex numbers, $u = a_h + \mathrm{i}b_h$ and $v = a_v + \mathrm{i}b_v$, respectively. Their amplitudes $|u| = \sqrt{a_h^2 + b_h^2}$ and $|v| = \sqrt{a_v^2 + b_v^2}$ are used in the analysis to represent the results in a non-dimensional form by dividing the displacements by a factor $a = 1$m. Nonetheless, another expression, normalised area, is used for exploiting the results in Chapters 4 and 7. It is evaluated by computing the area under the relevant displacement curve, vertical or horizontal, at the soil surface and normalised by a unit area for a non-dimensional representation. In addition to that, the absolute relative error norm is used to quantify the difference between the displacements at each node for different cases. It is given by

$$\varepsilon(\%) = \| \frac{v_1^j - v_2^j}{v_1^j} \| \times 100, \tag{3.43}$$

where j denotes to the node number, 1 and 2 refer to displacement curves associated with those cases. In other words, the error is computed in the same location for different displacement curve.

3.5 Concluding remarks

In this chapter, a finite element model is developed to solve steady state wave propagation problems in soils media in two dimensions under plane strain conditions. The soil medium, assumed to overlay rigid bedrock, is divided into three regions. The central domain or irregular region, which is of interest, is meshed into finite elements. The two lateral domains or regular regions extending to infinity are replaced by equivalent nodal forces they apply on the irregular region. These nodal forces are computed through the solution of a second order eigenvalue problem, which is reduced to a first order with doubling its size. The obtained FEM model allows numerical modelling of wave propagation is soil media over rigid bedrock and subjected to harmonic loads. The nodal displacements, especially at the soil surface, will be used in the post processing stage of the results for validation and parametric study purposes.

Chapter 4

Wave propagation in soil media over bedrock: validation & applications

4.1 Introduction

This chapter aims to validate the implemented numerical model, developed in Chapter 3, for the simulation of wave propagation in soil media. The soil medium is assumed to be resting on horizontal rigid bedrock. The ability of the numerical model to simulate wave propagation and predict the dynamic behaviour of soil media will be examined. Several cases where the analytical solution is available are considered. For other cases, judgement is used to justify the results.

4.2 Effectiveness of the consistent transmitting boundary conditions

In order to examine the effectiveness of the implemented consistent transmitting boundary conditions, the response of a soil domain is analysed with and without incorporating the lateral forces to simulate the semi-infinite extent of the domain. Therefore, a soil domain of $6\lambda_R$ and $2\lambda_R$, in length and depth respectively, is subjected in this example to a vertical harmonic load of 1kN in magnitude at the soil surface with a frequency of 20Hz. The soil layer has the following properties; density of 1700kg/m^3, elasticity modulus of 100MPa, Poisson's ratio of 0.3 and a damping ratio of 5%. The computational domain is meshed into 4-node quadrilateral elements. As the Rayleigh wavelength is 6.98m the element size is taken about 0.7m. Figure 4.1 shows a comparison between the vertical (left) and horizontal displacement (right) at the soil surface in both cases of treated and untreated lateral boundaries (with and without the consistent transmitting boundary conditions, respectively). The results are presented in a non-dimensional form by normalising with respect to the unit displacements a. The results clearly show that when the vertical boundaries are treated, to allow the waves to radiate away into infinity, the surface displacement curves are smooth and wavy. However, when the lateral boundaries are not treated, the incoming waves are reflected leading to spurious oscillations.

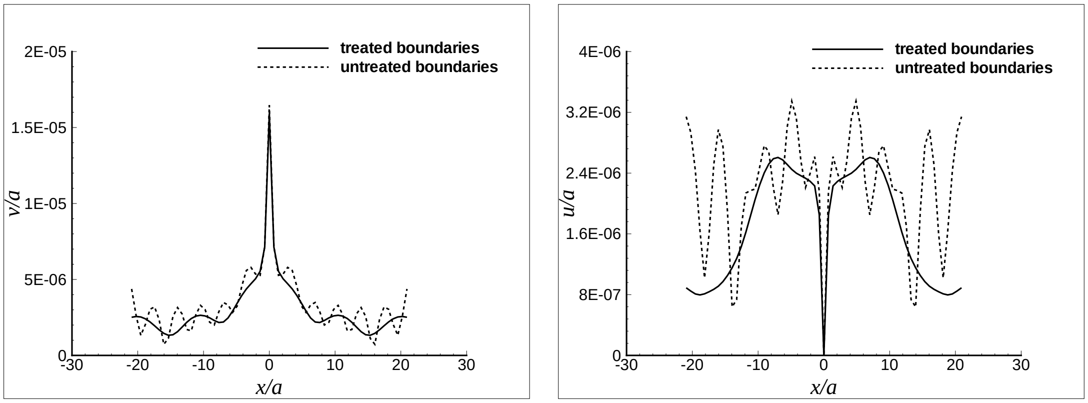

Figure 4.1: Effectiveness of the consistent transmitting boundaries.

It is obvious from this example that treatment of the two lateral boundaries of the soil model is necessary when dealing with wave propagation modelling so that the waves radiate away to infinity with no or very little reflection.

Next, the continuity of the surface displacements is investigated when the length of the soil model is increased. It is anticipated that the soil behaviour remains unchanged for any length of the domain since the consistent transmitting boundaries should simulate the infinite extent of the domain. Both undamped and damped cases are dealt with.

4.2.1 Undamped case

The matrices of the eigenvalue problem of expression (3.30) could be real or complex depending on damping. Therefore, damped and undamped soil models lead to different eigenvalues (wavenumbers, k) and eigenvectors. In the case of undamped soil model, wavenumbers could be purely real or even take the zero value, while the damped case does not produce such values (see section 6.3).

The developed finite element model is used to analyse the previously considered example in the frequency domain by changing the length of the domain from $1\lambda_R$ to $10\lambda_R$. The Rayleigh wavelength is meshed into 10 elements in the vertical and horizontal directions as recommended by Laghrouche [99]. Other researchers considered 8 elements per Rayleigh wavelength, however 10 elements produces a smoother wave pattern. Herein, a fixed depth of $2\lambda_R$ of the soil layer and a fixed applied frequency of 20Hz are again used, and the length of the domain is varied to check the continuity of the soil response. The efficiency of the method is also examined by computing the relative error at the nodes of the surface for two successive lengths of the domain.

First, the length of the model is considered to be $1\lambda_R$ then $2\lambda_R$ while keeping the depth constant. When comparing the surface displacements it is clear that this approach is very effective as the continuity of the displacements is ensured with the relative error being less than 0.25% as shown in Figure 4.2.

The length of the model is increased to $4\lambda_R$ and a comparison with $2\lambda_R$ length is drawn. Waves propagate through the boundaries and very little reflection is encountered, the symmetry of the displacement is clear and again the error does not exceed 0.9%. It could be seen that the highest percentage of error is encountered close to the vertical boundaries of the domain, nonetheless it is so small and insignificant.

The same trend is shown when the length of the domain is increased to $8\lambda_R$ and $10\lambda_R$. The relative error is less than 1.5% as shown in Figure 4.2. Looking at the results, it could be concluded that the consistent transmitting boundaries are very effective to simulate wave propagation in undamped soil media.

Surface horizontal displacements and their corresponding errors when extending the length of the computational domain are depicted in Figure 4.3. At the point of application of the load, the horizontal displacement is zero and therefore the error percentage at this point is not representative and hence its corresponding error is not included in the results.

It is obvious from the results corresponding to the horizontal displacements that the consistent transmitting boundaries perform well as the continuity of the displacements is ensured and the relative errors remain very low.

4.2.2 Damped case

The numerical tests carried out for the undamped case are reconsidered here with a damping ratio of 5%. The results shown in Figures 4.4 and 4.5, for the vertical and horizontal displacements, respectively, lead to similar conclusions drawn for the undamped case. Indeed, the relative error remains very low and the maximum error is about 1.8%, which is an acceptable engineering accuracy.

Figure 4.6 shows an example of contour plots of the vertical and horizontal displacements for the case of length $10\lambda_R$. It is obvious that both displacements are symmetrical with respect to the line of action of the vertical loading at the surface. In fact, as will be shown next, this symmetry is maintained even for non-symmetrical domains.

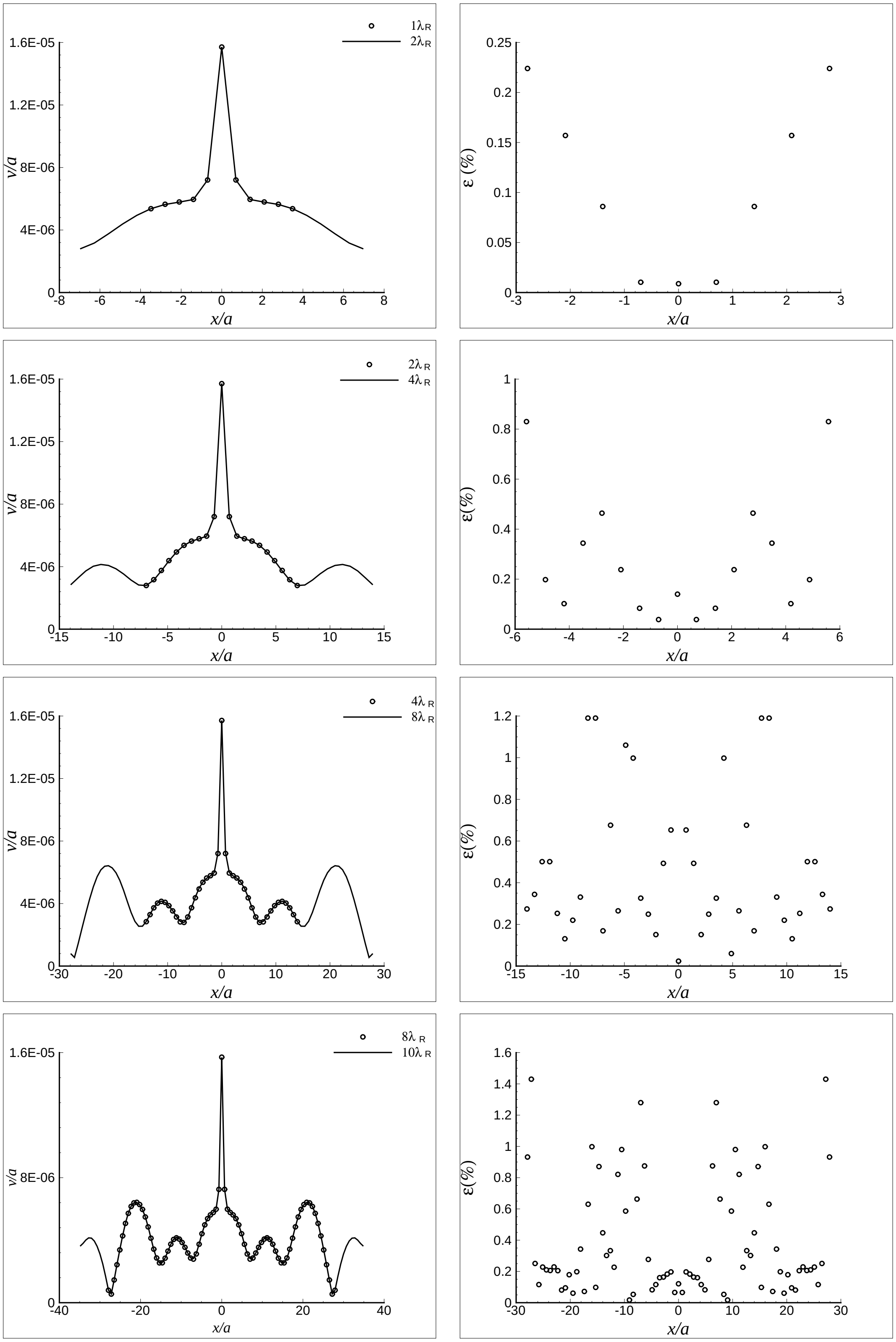

Figure 4.2: Vertical surface displacements and corresponding errors: undamped soil.

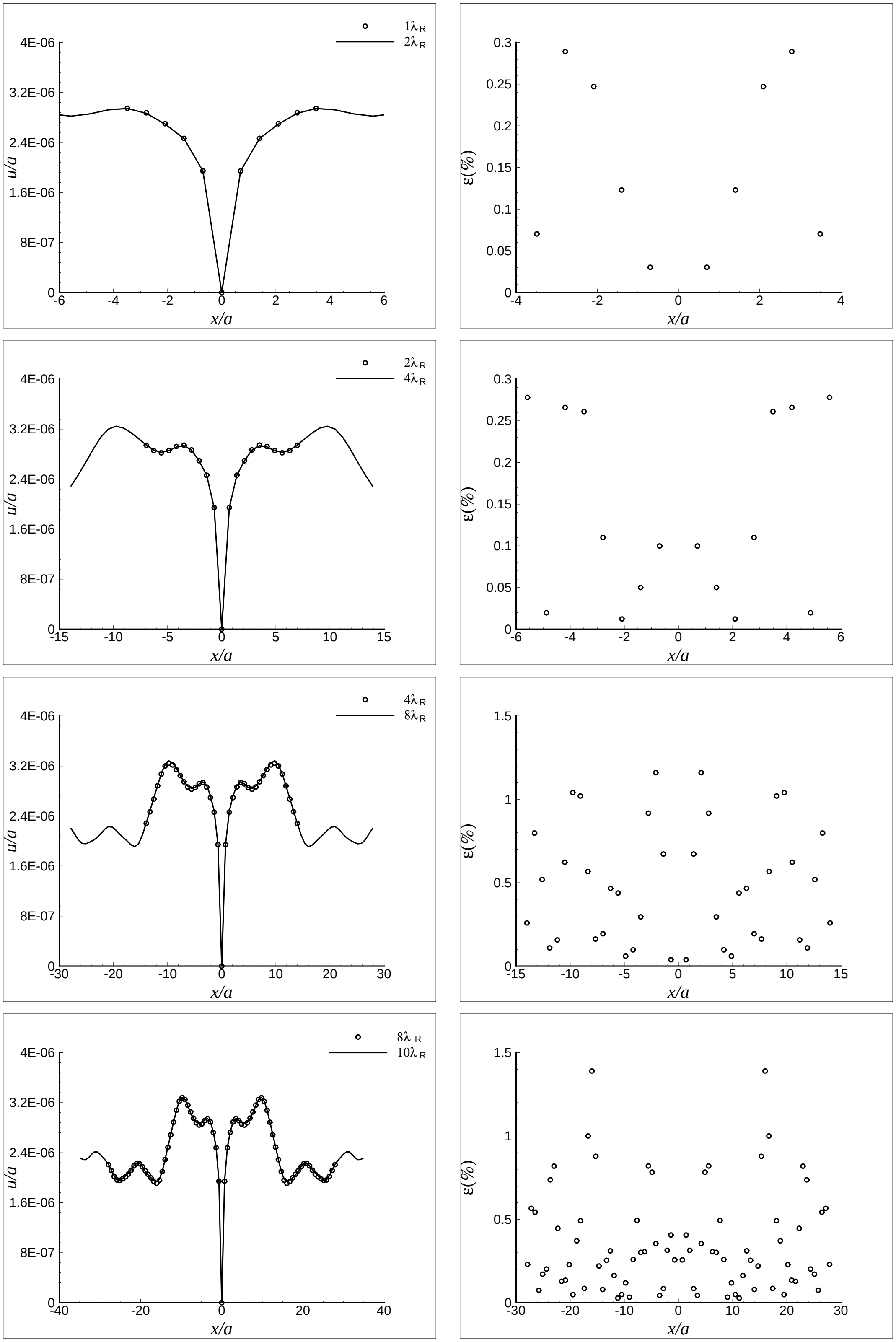

Figure 4.3: Horizontal surface displacements and corresponding errors: undamped soil.

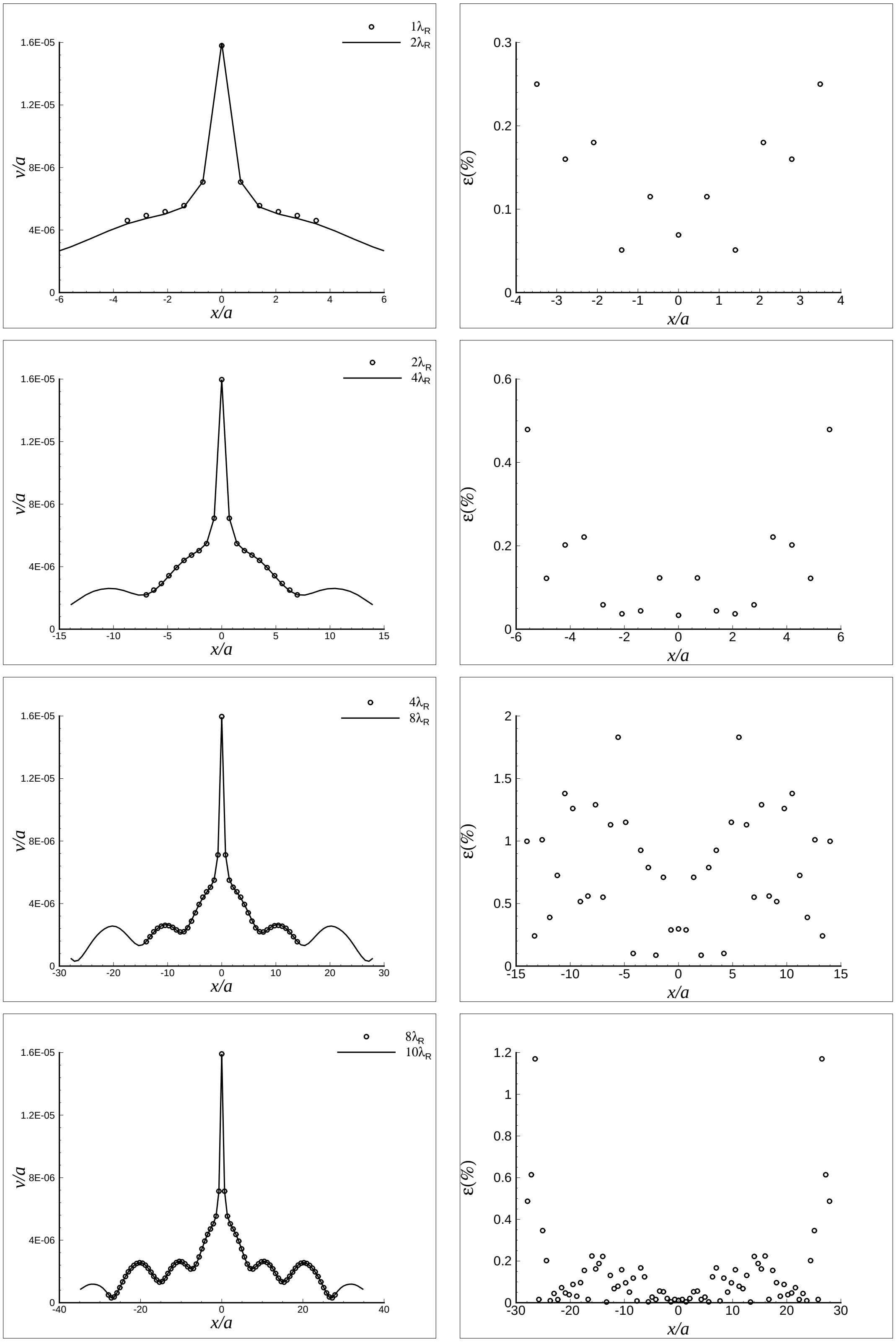

Figure 4.4: Vertical surface displacements and corresponding errors: damped soil.

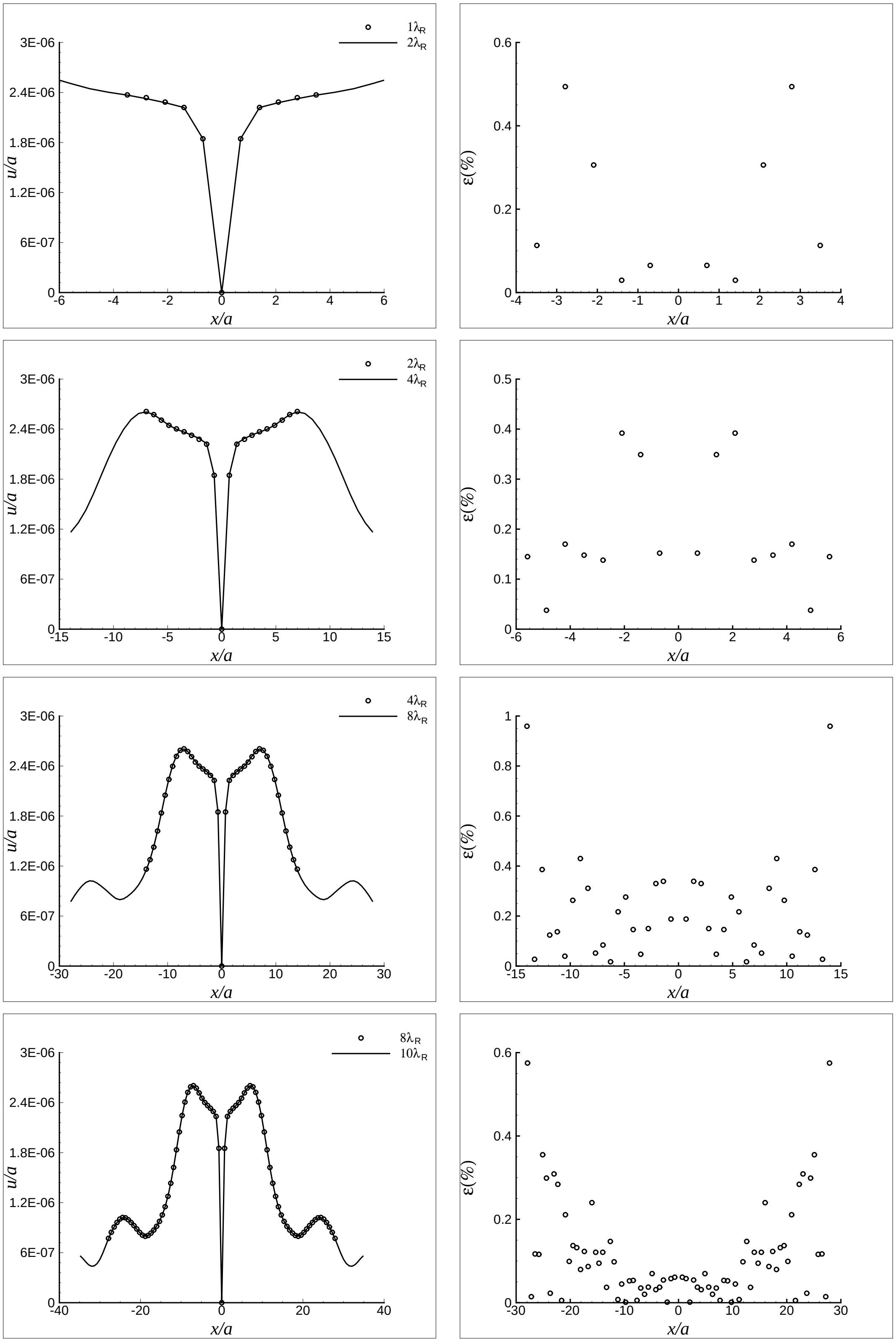

Figure 4.5: Horizontal surface displacements and corresponding errors: damped soil.

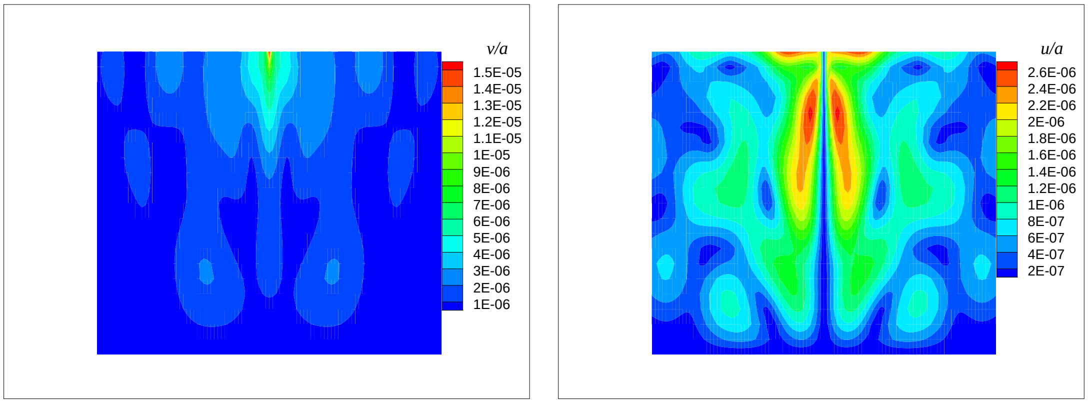

Figure 4.6: Vertical and horizontal displacement contour plots: case of $10\lambda_R$.

4.3 Non-symmetrical problem

In the configurations of section 4.2, the vertical load is applied such that the model is symmetrical with respect to the line of action of the applied vertical load. Here, we assume that the load is applied not necessarily in a symmetric manner and the efficiency of the numerical model is examined by ensuring the continuity of the displacements at the surface. This is carried out to show that good results are obtained by the numerical code even when the applied load is close to the lateral boundary of the domain where the energy transmits through the boundary.

4.3.1 Undamped case

In the current numerical tests, various non-symmetrical cases with no damping are considered such that there is no symmetry in the model with respect to the line of action of the vertical load. A first case consists of applying a vertical load at the top of the right lateral boundary of a domain of $4\lambda_R$ length and $2\lambda_R$ depth. The same model is reconsidered where the domain length is increased by $1\lambda_R$ to the right of the applied load such that the length becomes $5\lambda_R$. The top graphs of Figure 4.7 show the vertical displacements for both cases and the corresponding relative errors. It is clearly shown that the results are in very good agreement and the errors are very low, except at the extreme nodes at the surface. Moreover, the results for the case of length $5\lambda_R$ show symmetry with respect to the vertical load despite the fact that the problem is not symmetrical. In fact, this shows that the transmitting boundary conditions are effective in radiating the waves to infinity and are capable to simulate the semi-infinite extent of the model in the lateral direction. The length of the domain is further increased to $6\lambda_R$, $8\lambda_R$ and $10\lambda_R$. Further comparisons of the vertical displacements and evaluation of the relative errors (Figure 4.7) confirm the above stated conclusions. Here, only vertical surface displacements are analysed. In fact analysis of the horizontal displacements leads to the same conclusions. Moreover, a horizontal load could be used instead of a vertical one.

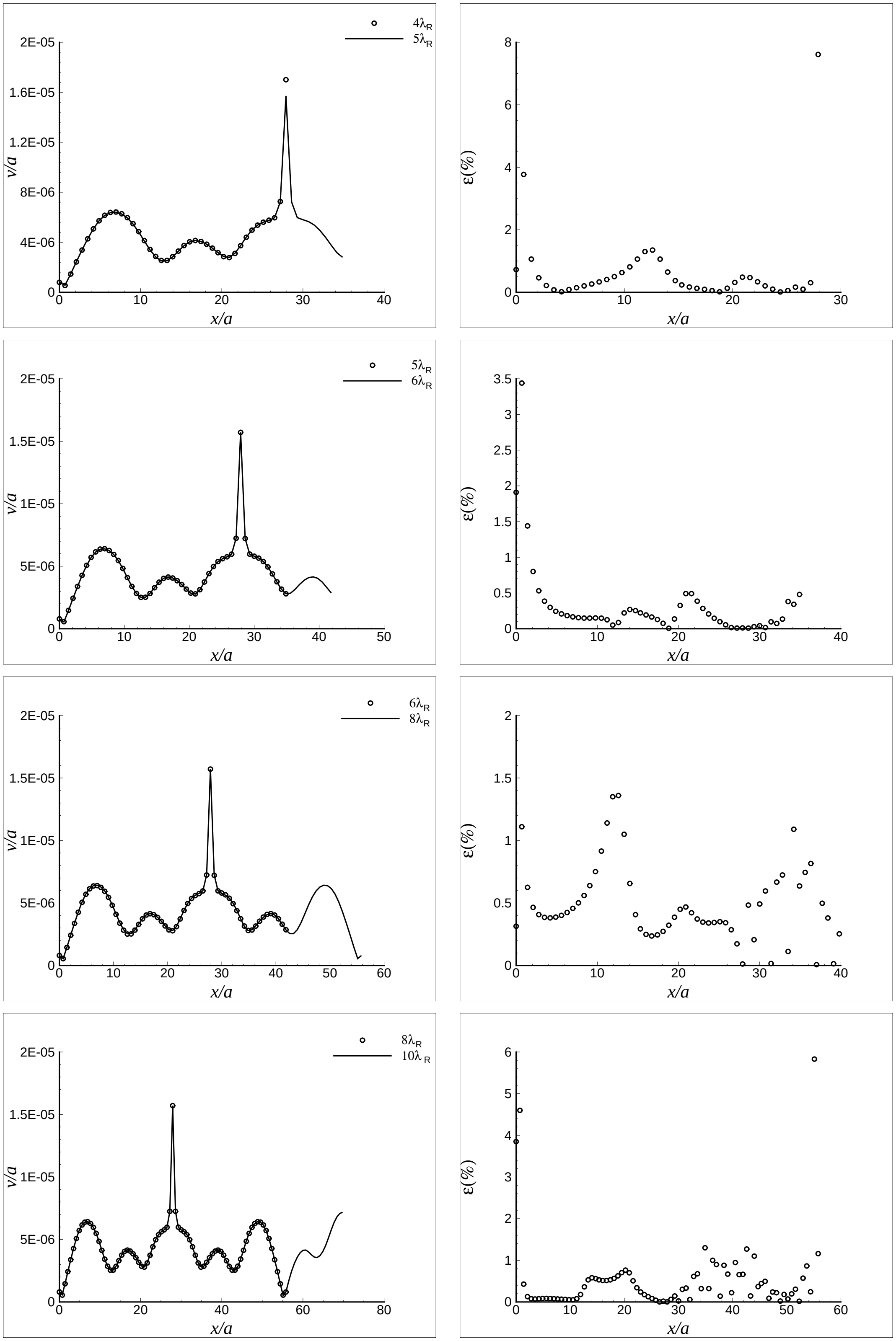

Figure 4.7: Vertical surface displacements and corresponding errors in the undamped soil for a non-symmetrical problem.

4.3.2 Damped case

A damping ratio of 5% is introduced for all considered examples of the undamped case. In the same way, the results are summarised in Figure 4.8 for the surface vertical displacements and relative errors, when the domain length is increased from $4\lambda_R$ to $10\lambda_R$. Again, the results show that the consistent transmitting boundaries are very effective in radiating the waves away to infinity through the lateral boundaries. The relative errors are very low and they are even lower in certain cases in comparison to the undamped case. The largest relative errors are again encountered at the extreme nodes of the domain surface but they are still very acceptable in terms of engineering accuracy.

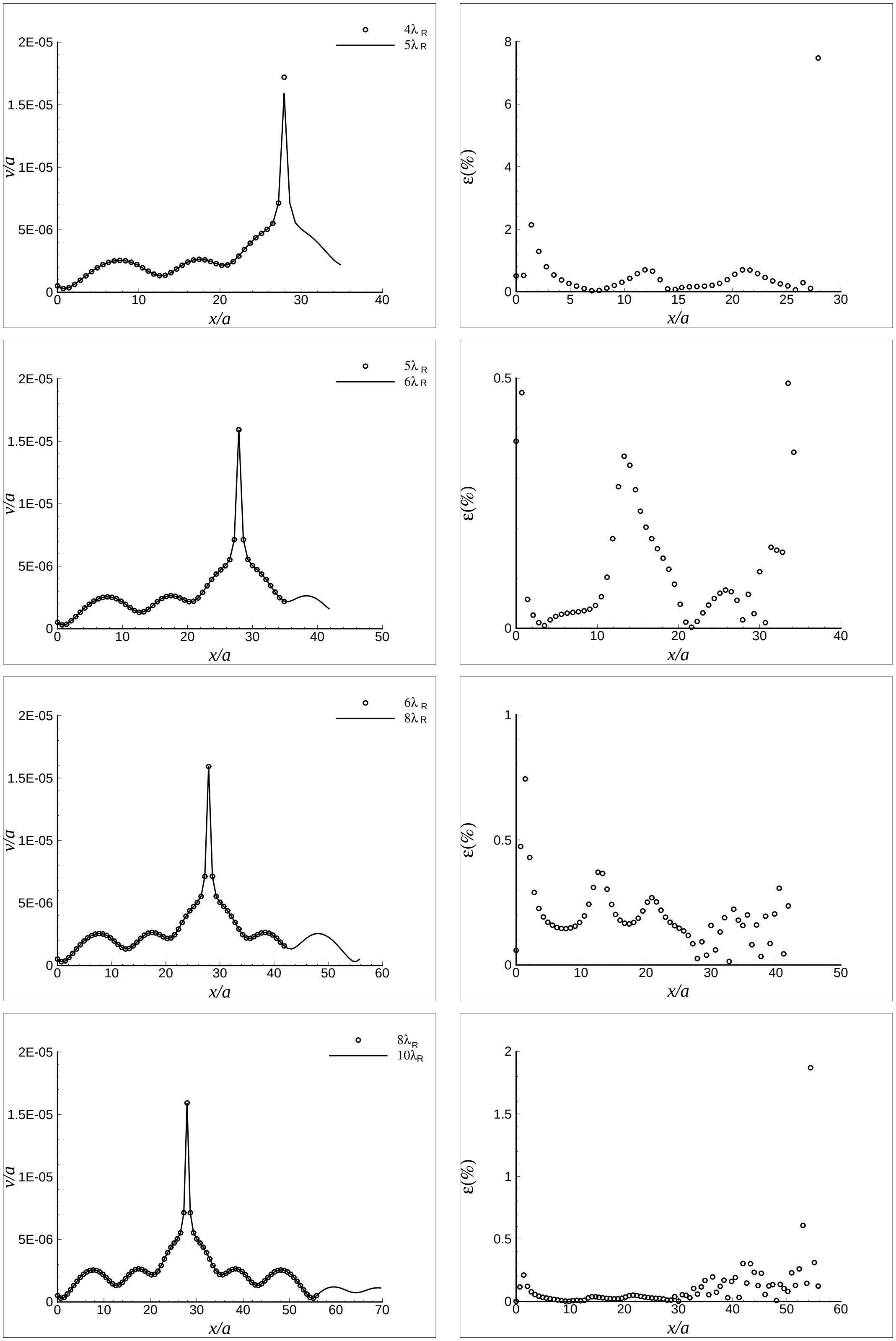

Figure 4.8: Vertical surface displacements and corresponding errors in the damped soil for a non-symmetrical problem.

4.4 Dynamic behaviour of a soil layer over rigid bedrock: critical frequencies

A rational approach is employed in sections 4.2 and 4.3 to provide a judgment on the numerical results. This section is aimed at simulating the dynamic response of a homogeneous soil layer over horizontal rigid bedrock, as an analytical solution for the natural frequencies is available. It is based on a one-dimensional wave propagation theory. It will be first presented and then the numerical results will be checked against this solution.

If a homogenous soil layer, of depth H, is subjected to a horizontal or vertical harmonic load, the natural frequencies of the horizontal and vertical responses of the soil layer can be determined from the following expressions

$$f_n^h = (2n-1)\frac{c_s}{4H}, n = 1, 2, 3, ..., \tag{4.1}$$

$$f_n^v = (2n-1)\frac{c_p}{4H}, n = 1, 2, 3, ... \tag{4.2}$$

where c_p and c_s are the compression and shear wave velocities respectively, f_n^h and f_n^v are the natural frequencies of the horizontal and vertical responses and n is an integer. The superscripts h and v refer, respectively, to the horizontal and vertical responses.

Consider an isotropic, linear elastic soil medium underlain by rigid bedrock as shown in Figure 4.9. A harmonic load applied at the top surface generates compression and shear waves which propagate vertically within the soil layer, consequently causing displacements and deformations in the soil deposit. An incident horizontal harmonic load, for example, generates a vertically propagating shear wave in the soil layer. Once the propagating shear wave hits the fixed base it reflects back into the domain with the same amplitude. However, the reflected wave doubles its amplitude once hitting the free surface. The solution for the horizontal displacement can be written as

$$u(y,t) = Ae^{i(\omega t + k_s y)} + Be^{i(\omega t - k_s y)}, \tag{4.3}$$

where ω is the circular frequency of the harmonic load, $k_s = \frac{\omega}{c_s}$ is the horizontal wavenumber and A and B are the amplitudes of the travelling waves upwards and downwards, respectively. Boundary conditions in this case are zero displacements at the base and zero shear stresses at the soil surface (free surface), and as consequence zero shear strains as well. A standing wave with amplitude $2\cos k_s y$ can be described by the previous equation. This leads to define the transfer function or the amplification factor $F_1(\omega)$ given by the ratio of the displacements between the surface and the base. It is given by

$$F_1(\omega) = \frac{1}{\cos k_s H}. \tag{4.4}$$

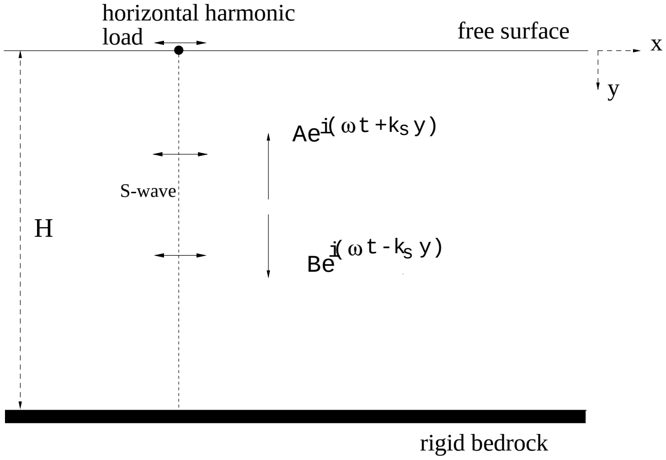

Figure 4.9: Linear elastic soil deposit over bedrock.

Equation (4.4) represents the analytical transfer function for undamped soil layer subjected to horizontal excitation. Similarly, if the soil layer is subjected to a vertical harmonic load, the associated transfer function could be derived and the compression wavenumber k_p replaces k_s in expression (4.4).

To understand the soil response due to the harmonic load, let us plot the magnitude of the transfer function against the frequency considering a soil medium of 10m depth with the same material properties presented in section 4.2. The natural frequencies for both the horizontal and vertical loading can be determined from equations (4.1) and (4.2). The top graphs of Figure 4.10 show the magnitude of the transfer function of the vertical and horizontal undamped response of the soil layer, under vertical and horizontal harmonic loads. The results show that resonance happens at certain frequencies, natural frequencies, where the response goes to infinity due to the absence of damping. These frequencies are function of the properties and the depth of the soil layer. However, this is not the case for practical applications where the presence of damping leads to energy dissipation. The transfer function for viscoelastic materials is derived by introducing a damping ratio, β, in equation (4.3). The transfer function for the damped soil layer subjected to horizontal excitation is expressed as

$$F_2(\omega) = \frac{1}{\sqrt{\cos^2 k_s H + (\beta k_s H)^2)}}. \tag{4.5}$$

Again, the compression wavenumber k_p replaces k_s in expression (4.5) to obtain the transfer function in the case of vertical excitation. More details about the derivation of the transfer functions may be found in text books such as Kramer [101].

When evaluating the damped response of the same soil layer by considering 5% damping ratio we obtain the bottom graphs of Figure 4.10 in the vertical and horizontal directions. Although amplifications happen at natural frequencies, resonance is more pronounced at the lower natural frequencies, especially at the fundamental one. It is obvious that the magnitude of the transfer function $F_2(\omega)$ reduces significantly for increasing frequency, thanks to the presence of damping, unlike in the undamped case where all natural frequencies lead to infinite amplification.
Next the dynamic response of the considered soil layer is investigated numerically to evaluate its natural frequencies and compare them to those obtained theoretically.

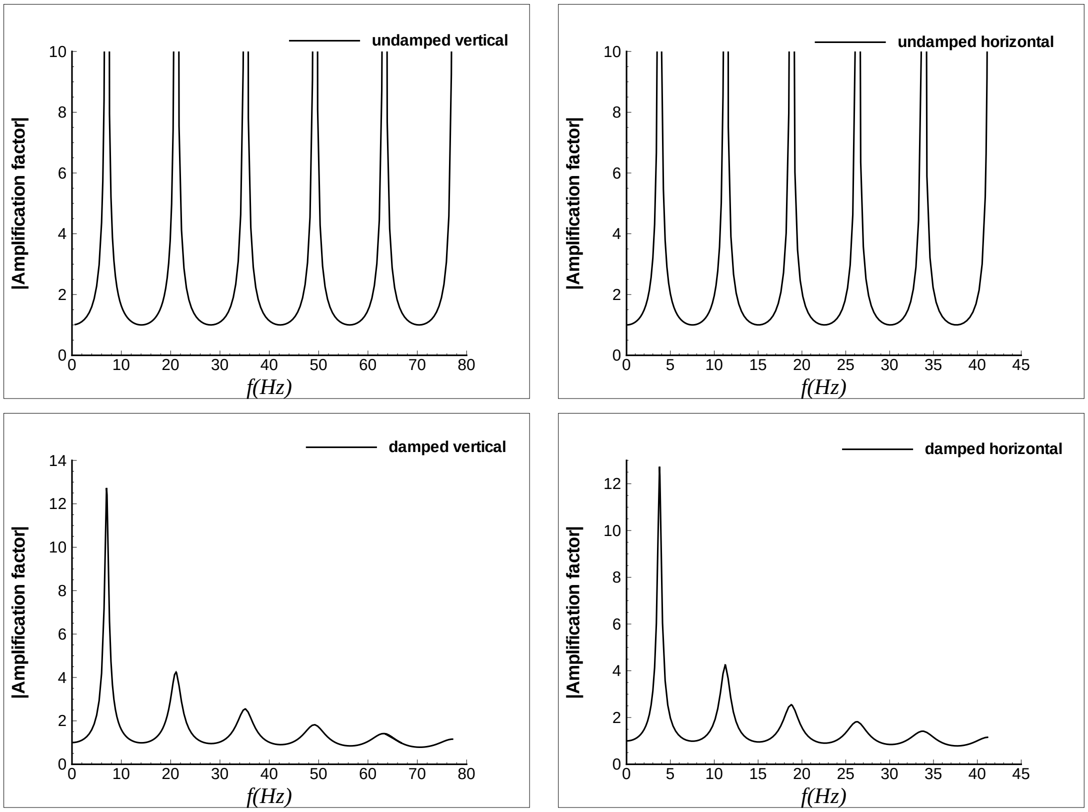

Figure 4.10: Theoretical amplification factors for vertical (left) and horizontal (horizontal) excitations for undamped and damped homogenous soil layer over bedrock.

4.4.1 Undamped response

The dynamic response of a soil layer overlaying bedrock is analysed numerically here by the developed finite element model. The same soil layer considered in section 4.4 is used in the numerical simulations to examine the capability of the model to capture its dynamic response in

n	f_n^v(Hz)	f_n^h(Hz)
1	7.04	3.8
2	21.1	11.3
3	35.2	18.8
4	49.2	26.3
5	63.3	33.8

Table 4.1: Natural frequencies of the horizontal and vertical response of the soil layer.

terms of the natural frequencies of the horizontal and vertical displacements. Those frequencies are calculated using expressions (4.1) and (4.2) and are shown in Table 4.1.
First, let us consider a vertical harmonic load applied at the soil surface with a range of frequencies including the first two natural frequencies of the soil domain. As usual, the domain is meshed into finite elements with size not exceeding one-tenth of the Rayleigh wavelength. The top left graph of Figure 4.11 shows the vertical surface displacements for the frequencies 3, 7 and 10Hz. For the case of 3Hz, apart from a disturbance around the point of application of the load, the rest of the soil surface shows no displacements. At 7Hz, however, significant displacements take place along the whole surface. This frequency is very close to the fundamental frequency of the soil medium, which is 7.04Hz, and hence resonance was expected. Then at 10Hz, while noticeable displacements occur, those are a lot smaller in comparison to those corresponding to the frequency of 7Hz.

Similar numerical experiments are carried out with higher frequencies. The bottom left graph of Figure 4.11 shows the vertical displacements corresponding to 15, 21 and 25Hz. Once again, the displacements occurring for the 21Hz case are more important than those corresponding to 15 and 25Hz. In fact, at around 21Hz resonance takes place again which corresponds to the second natural frequency.

To show this in a more obvious way, for each frequency ranging between 1 and 25Hz, the area A under the surface displacement curve is calculated and plotted in Figure 4.12 (left). The area A is normalised here with respect to a unit area A_0 for a non-dimensional representation. Other authors such as Yang *et al.* [98] multiplied, for example, the vertical displacement by the shear modulus and plotted it against the frequency. Figure 4.12 (left) clearly shows that resonance occurs at the frequencies around 7 and 21Hz, which are very close to the predicted frequencies of 7.04 and 21.1Hz by expression (4.2).

For the case of natural frequencies of the horizontal loading, the same approach is followed. The soil layer is subjected to a surface horizontal load with frequency ranging from 0.5 to 20Hz. The surface displacements for selected frequencies are shown in the right graphs of Figure 4.11. Once again, the displacements seem to be higher at certain frequencies.

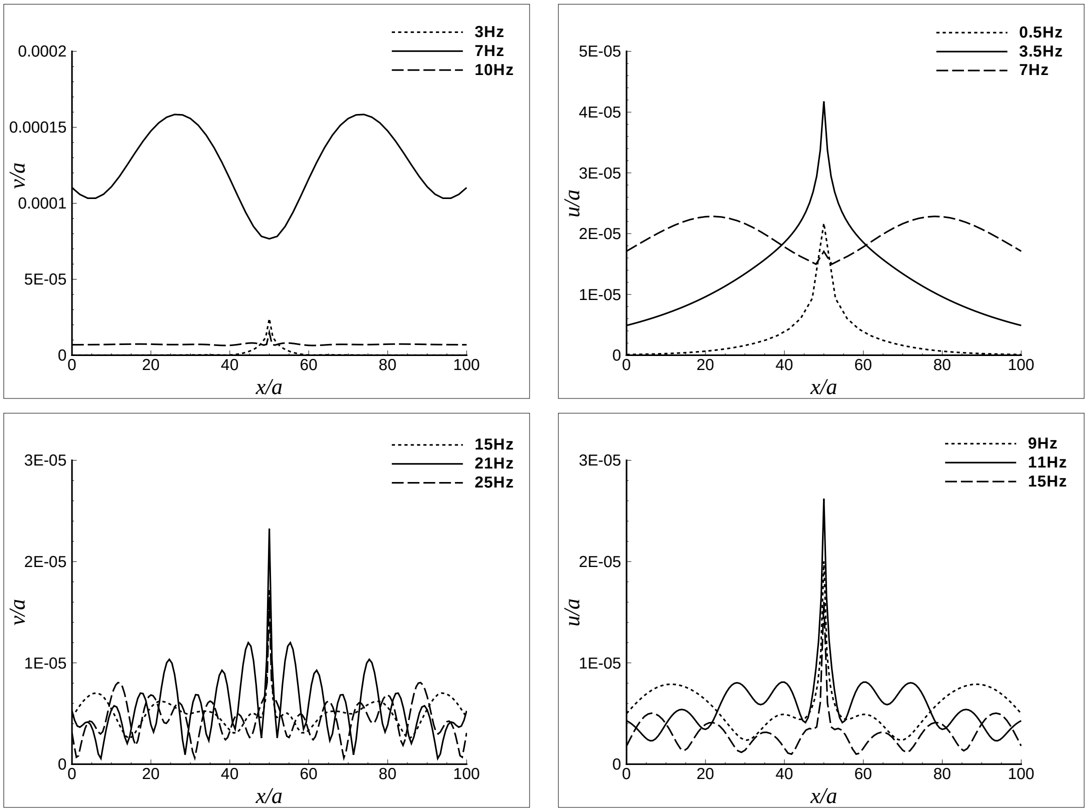

Figure 4.11: Undamped vertical (left) and horizontal (right) displacements at the surface for various applied frequencies.

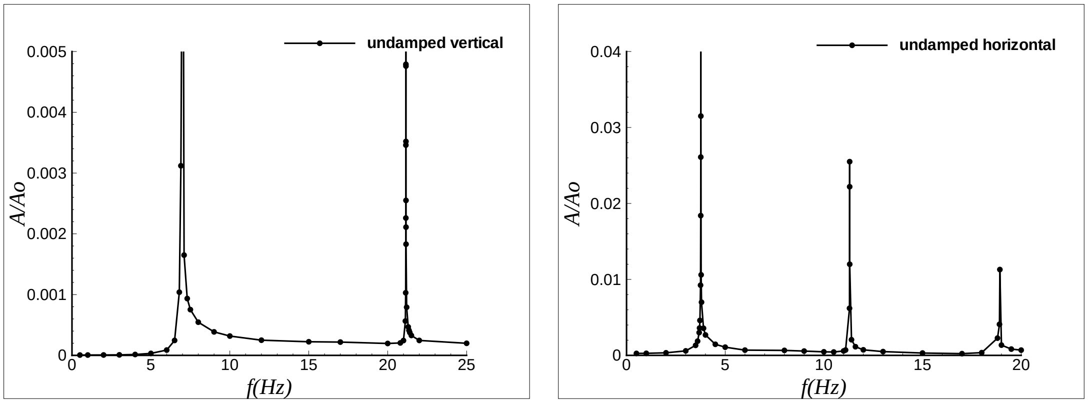

Figure 4.12: Soil response amplification for vertical and horizontal excitations under undamped condition for homogenous soil layer over bedrock.

To show the resonance behaviour, the normalised area A/A_0 is evaluated for each loading frequency and the results are plotted in Figure 4.12 (right). Once again, it is obvious that resonance occurs at the frequencies around 4, 11 and 19Hz. Those frequencies are in very good agreement with the values predicted by expression (4.1), which are 3.8, 11.3 and 18.8Hz (Table 4.1). The above numerical tests validate further the developed numerical model and show its ability to capture the dynamic behaviour of soil media overlaying bedrock. Since previous numerical simulations considered both undamped and damped cases of the soil, complementary numerical tests are carried out with the introduction of a damping.

4.4.2 Damped response

The same cases analysed in the previous section are reconsidered here with the introduction of a damping ratio of 5%. The results are presented in Figure 4.13 for the vertical and horizontal loading. The left graphs represent the response of the soil layer due to a vertical harmonic load while the right graphs show the response associated with the horizontal loading. The same behaviour is shown as in the undamped case except that the level of displacement is less pronounced in the presence of damping. A steady displacement, i.e. steady wave, is encountered in the undamped case, while the pattern of the displacement is damped as we move away from the point of application of the load. This is related to the effect of damping in the soil which is an important property when considering dynamic analysis. Figure 4.14 shows the fundamental frequencies for vertical and horizontal displacements, respectively, to be around 7Hz and 3.5Hz. These values are in good agreement with the theoretical values of Table 4.1.

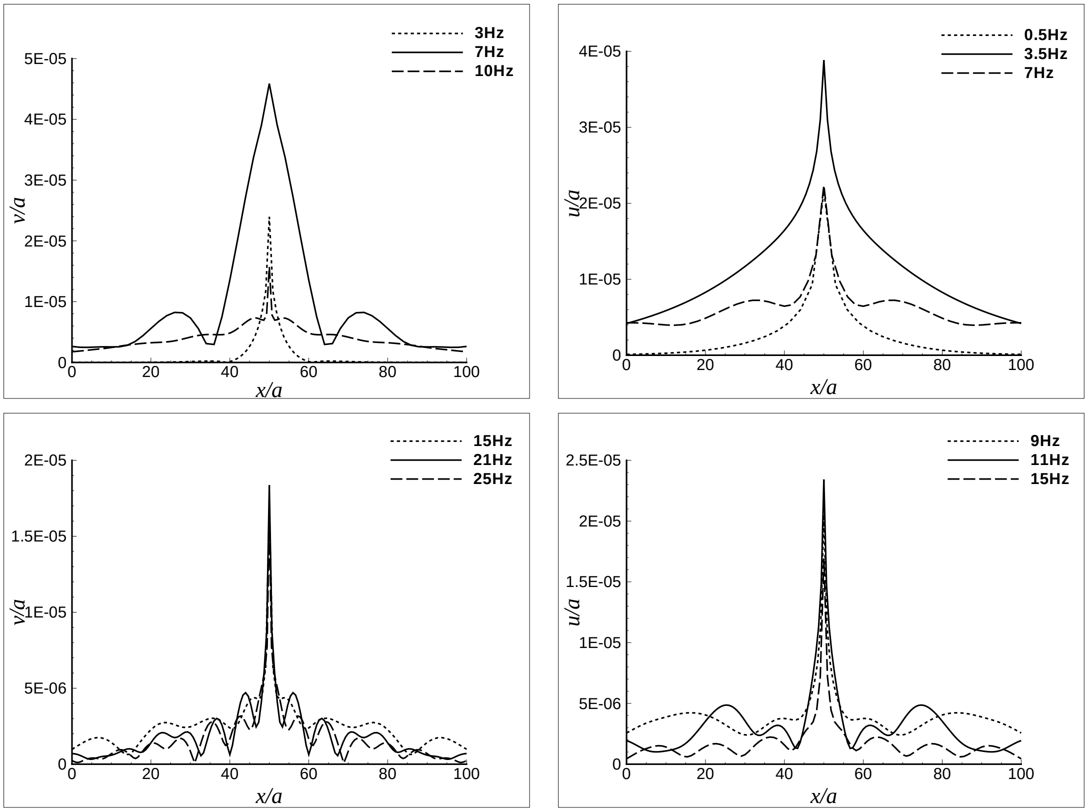

Figure 4.13: Damped vertical (left) and horizontal (right) displacements at the surface for various applied frequencies.

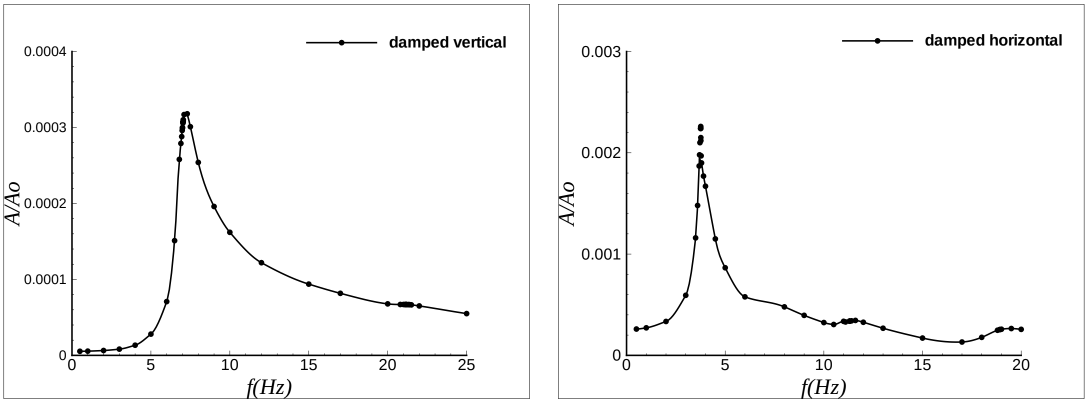

Figure 4.14: Soil response amplification for vertical and horizontal excitations under damped condition for homogenous soil layer over bedrock.

4.5 Dynamic behaviour of a soil layer over rigid bedrock: critical depths

The depth of a soil layer over rigid bedrock has a significant effect on its dynamic behaviour when it coincides with a critical value as it also leads to resonance. Such cases include; machine foundations where ground vibrations can be a major concern for neighbouring structures and people. The case of a moving load such as a train over soil layer overlaying bedrock is another example. In the following sections, analytical and numerical analysis are presented to investigate the effect of these critical depths.

4.5.1 Vertical loading

The critical depth formula associated with a vertical loading with a fixed frequency f acting on a soil layer is deduced from expression (4.2) as

$$H_n^v = \frac{c_p}{4f}(2n-1). \tag{4.6}$$

Let us consider a vertical load of a magnitude 1kN with a frequency of 5Hz acting at the surface of a soil layer with the same material characteristics of previous examples (sections 4.2, 4.3 and 4.4). The length of the domain is taken to be $8\lambda_R$ and its depth varied between $0.1\lambda_R$ and $4\lambda_R$ with λ_R being around 27.9m, in this case. The harmonic load is assumed to be applied on the left boundary of the domain to make the results more readable. The effect of the soil layer depth is shown in Figure 4.15. In the case of shallow depths, $0.1\lambda_R$ and $0.2\lambda_R$, the waves do not seem to propagate. Propagation starts when increasing the depth of the soil layer and it is more pronounced with depths greater than $0.5\lambda_R$. In fact, resonance occurs when approaching a depth of $0.5\lambda_R$, which coincides with the first critical depth of the soil layer for the vertical loading case determined from expression (4.6). Actually, if we consider the depth of $0.5\lambda_R$ of the soil layer and compute the fundamental frequency of the vertical loading it will be around 5Hz. As it is shown in Figure 4.15, waves do not propagate if the depth of the soil layer is less than the first critical depth. From other cases of larger depths, we can see resonance happens at the second critical depth of $1.51\lambda_R$.

4.5.2 Horizontal loading

This time a horizontal surface load is considered with a frequency of 5Hz. The effect of the soil layer depth is examined for a series of numerical examples for surface wave propagation. Similar to the vertical load case, the critical depth formula associated with horizontal loading with a fixed frequency f acting on a soil layer is deduced from expression (4.1) as

$$H_n^h = \frac{c_s}{4f}(2n-1). \tag{4.7}$$

As in the case of vertical excitation, waves do not propagate when the depth of the soil layer is less than the first critical depth associated with the horizontal loading, as in Figure 4.16 (top left). The magnitude of the horizontal displacement increased with increasing the depth of the soil layer and waves start to propagate for depths greater than $0.29\lambda_R$. The first critical depth associated with horizontal loading is computed from expression (4.7) to be around $0.27\lambda_R$ and the second critical depth is around $0.8\lambda_R$.

To compare the soil surface response for varying soil layer depth, the area underneath the displacement curve is evaluated with a numerical integration approach and normalised with respect to a unit area. These are shown in Figure 4.17 (bottom) against the normalised depth of the soil layer. The top plots of Figure 4.17 present the theoretical prediction of amplification in the horizontal and vertical directions against the normalized depth, with respect to the Rayleigh wavelength of the soil layer. Amplification occurs at certain depths which are the critical depths as depicted in the previous figure. It is clear that the numerical results predict very well resonance and that the numerical critical depths coincide well with the theoretical values. In practice, it is very important to avoid those depths or to change the applied frequency if possible when designing machine foundations or when running a moving load. The same trend is found in the damped case but it is not included in this dissertation.

So in summary, the developed numerical model captures the dynamic behaviour of soil media over rigid bedrock, in the case of a fixed frequency, where the depth of the bedrock varies. Indeed when the depth coincides with critical values determined by expressions (4.6) and (4.7) for vertical and horizontal loadings, respectively, the soil layer shows resonance.

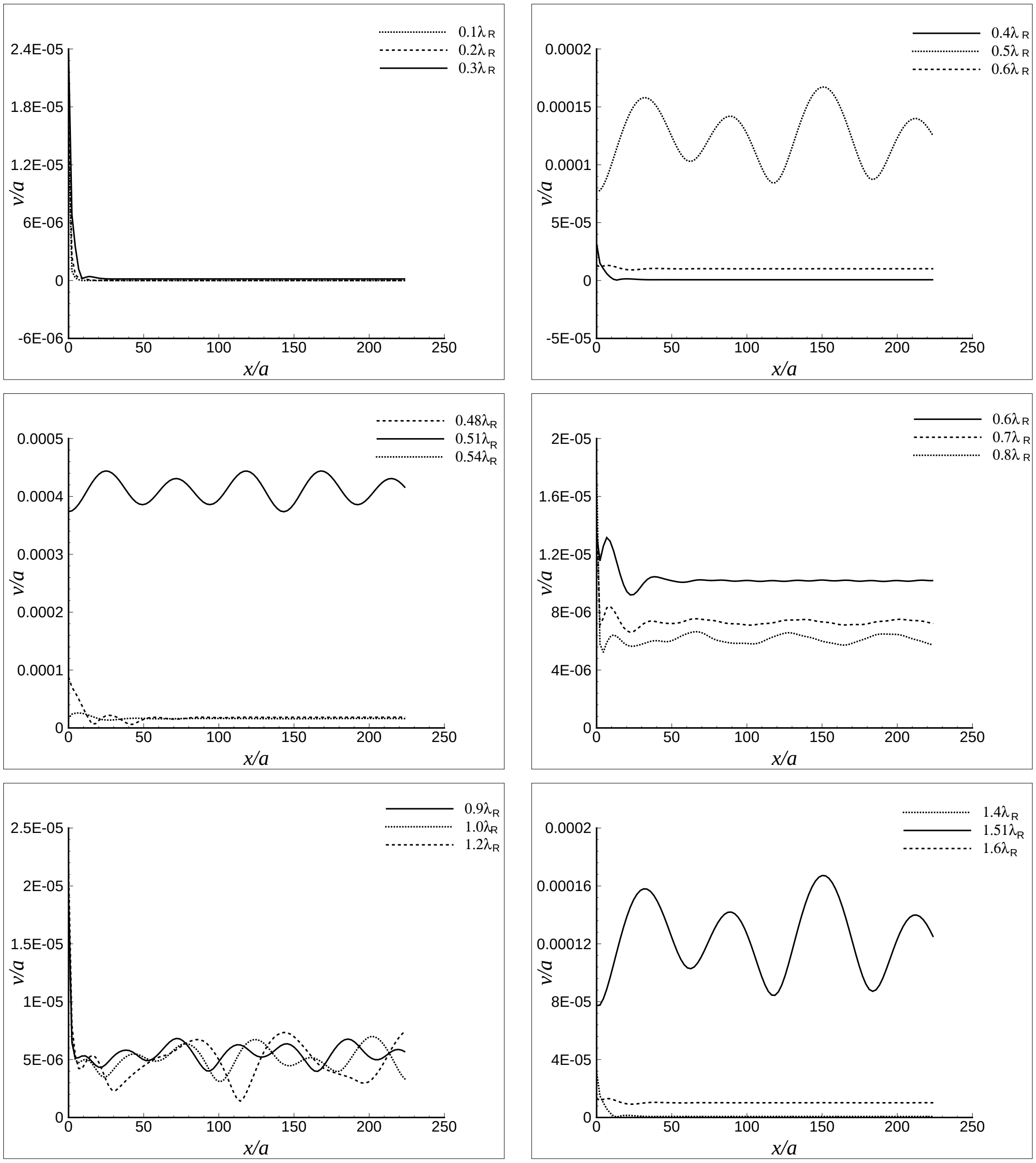

Figure 4.15: Effect of soil layer depth in the undamped case for vertical excitation.

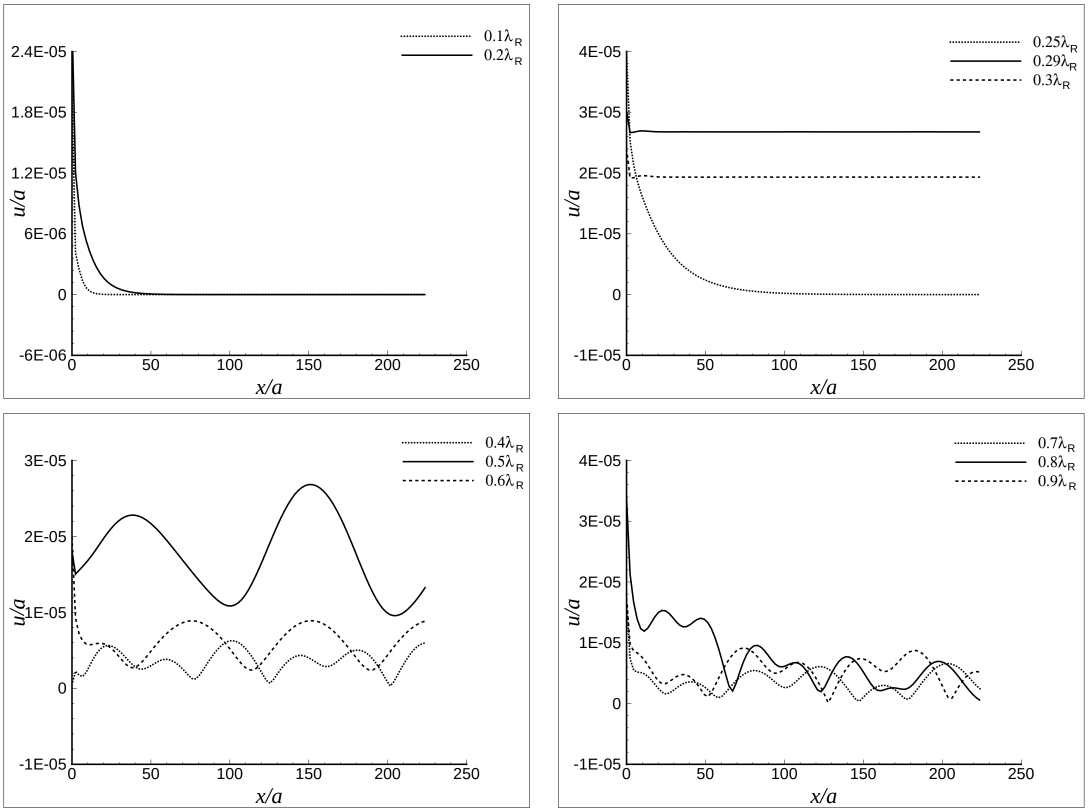

Figure 4.16: Effect of soil layer depth in the undamped case for horizontal excitation.

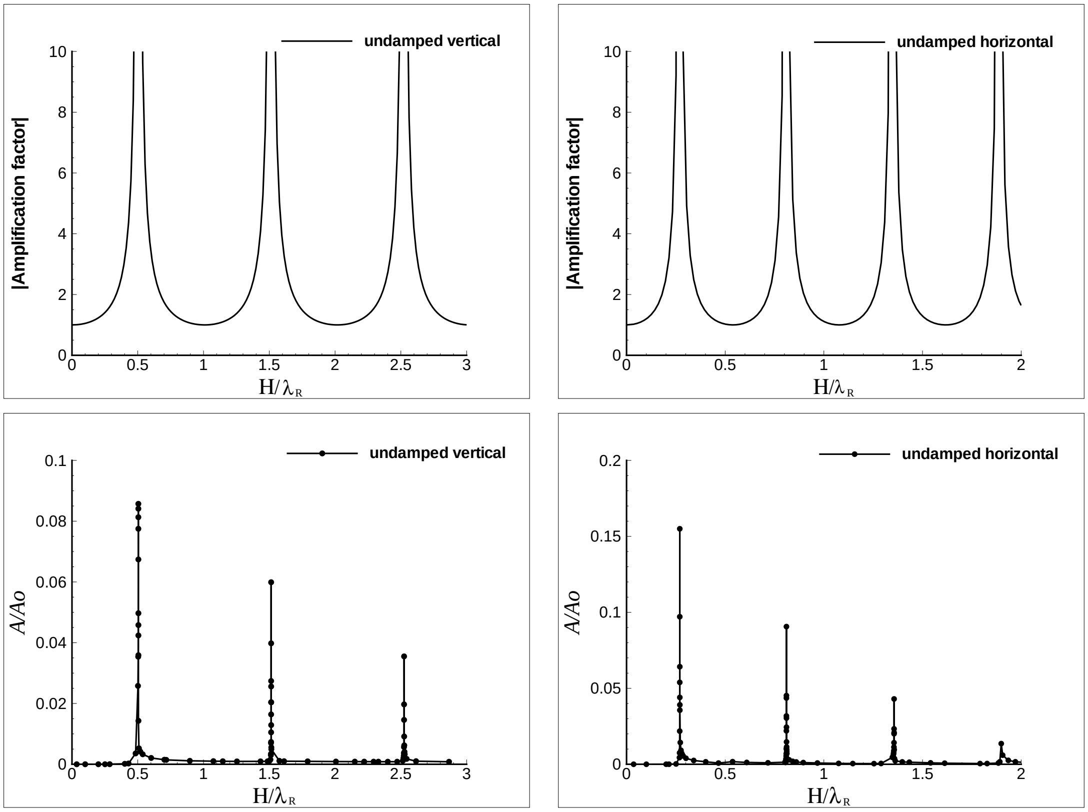

Figure 4.17: Critical depth amplification for vertical and horizontal loading: theoretical (top) and numerical (bottom).

4.6 Dynamic behaviour of layered soil media over rigid bedrock

Up to this point, the soil medium is assumed to be a homogenous single layer. In spite of this assumption being very helpful to simulate wave propagation in soil media, it is unusual in engineering practice to encounter such a situation. Soil properties usually vary with depth, especially the stiffness, which could be due to the geological history of the soil, for example. Moreover, soil layers usually deposit over each other with time and consolidate leading to forming stiffer materials with depth, in general. Next, the response of two-layer and multi-layered soil profiles are examined in the following sections.

4.6.1 Dynamic behaviour of a two-layer soil profile

In this section, the developed numerical model is employed to simulate wave propagation in a two-layer soil profile consisting of a soft soil layer overlaying a stiff deposit. The material properties of the soft soil layer are; 20MPa, 1550kg/m^3 and 0.3 for elasticity modulus, density and Poisson's ratio, respectively, with no damping. Whereas Young's modulus, soil density and Poisson's ratio for the stiff soil are assigned as 100MPa, 2000kg/m^3 and 0.25. For the layers' thicknesses, let us assume for simplicity that H_1=H_2=5m. The two-layer medium is subjected to a vertical surface load of 1kN with a frequency of 20Hz. To ensure that the consistent transmitting boundaries allow the waves to radiate away towards infinity, the same approach used for homogenous media is followed. The length of the domain is increased from $2\lambda_R$ to $8\lambda_R$ while the total depth is kept, as mentioned above, unchanged at 10m. Horizontal and vertical surface displacements are displayed in Figure 4.18 for different lengths of the domain. It is clearly shown that the results are in very good agreement and that the consistent transmitting boundaries allow the waves to radiate away at both lateral vertical boundaries. Comparison between successive cases of length show low relative errors which do not exceed 2% and 3% for the horizontal and vertical displacements, respectively.

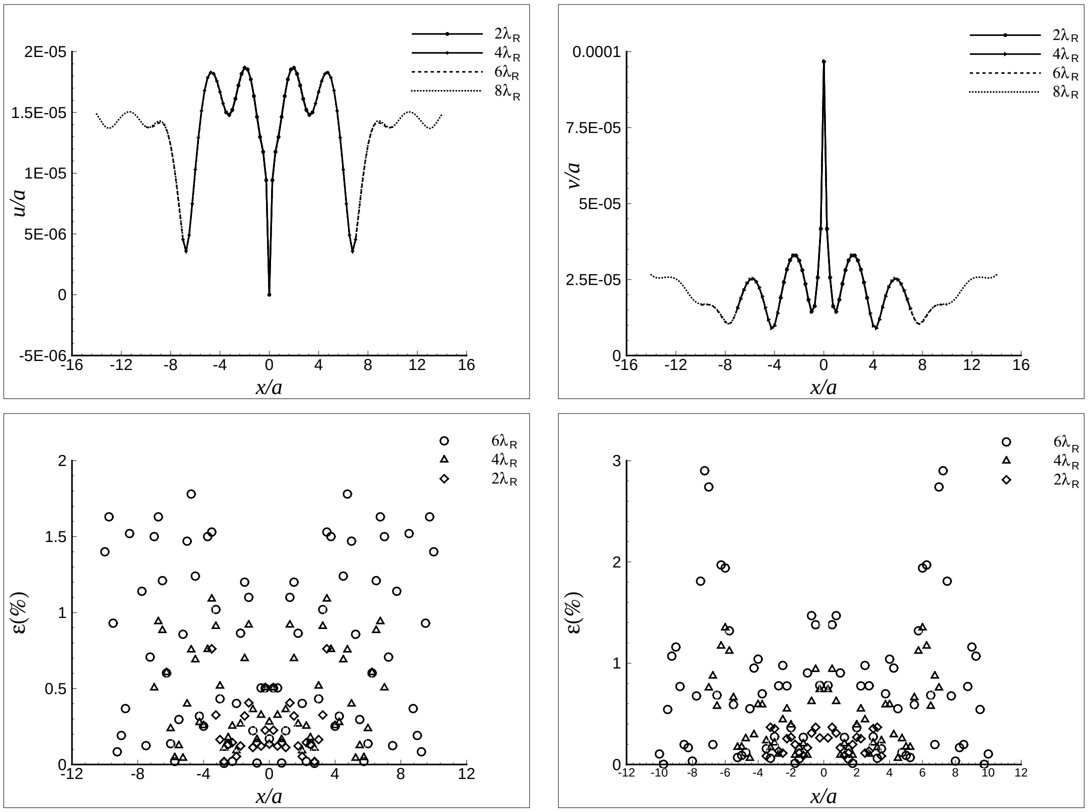

Figure 4.18: Horizontal (left) and vertical (right) surface displacements with their corresponding relative error of 2-layer soil profile.

Let us now analyse the dynamic behaviour of the two-layer soil medium in terms of critical frequencies, as was done for the homogenous single layer. If we consider a wave hitting the interface of the layered system, part of that incident wave will reflect back and the other part will travel into the bottom layer. The transmitted wave through the bottom layer will reflect at the bedrock and refract again at the two layer interface. Hadjian [102] estimated the fundamental period of a layered soil profile by an approximated relationship involving the thickness and the fundamental period of each soil layer and two other parameters which represent the ratio between the thicknesses of soil layers. Hadjian obtained a formula estimating the fundamental period of a layered soil profile which may be used in computer software. The equivalent fundamental frequencies have the following expressions

$$f = \frac{f_1}{\sqrt{\frac{\pi^2}{8}\left[0.75 + \left(\frac{f_1}{f_2}\right)^2 \left(1 + 2\frac{\rho_1 H_1}{\rho_2 H_2}\right)\right]}} \quad \text{for} \quad \frac{H_1}{H_2} > 1. \tag{4.8a}$$

$$f = \frac{f_1}{\left[1 + \beta \left(\frac{f_1}{f_2}\right)^n \left(1 + \frac{\rho_1 H_1}{\rho_2 H_2}\right)^n\right]^{1/n}} \quad \text{for} \quad \frac{H_1}{H_2} \leq 1, \tag{4.8b}$$

where $\beta = 1 - 0.2\left(\frac{\rho_1 H_1}{\rho_2 H_2}\right)^2$ and $n = 4 - 1.8\frac{\rho_1 H_1}{\rho_2 H_2}$. The fundamental frequencies f_1 and f_2 are related to the upper and the bottom layers, respectively. The fundamental frequency of the soil profile considered in our analysis is estimated from equation (4.8b) to be 5.32Hz. It should be indicated that the analytical solution derived in reference [102] has the ability to predict the fundamental frequency of a two-layer soil with a marginal error. This could be generalised to a layered soil profile and the fundamental period or frequency of the profile could be estimated by using the Successive Use of Two$-$Layer solutions. It is worth mentioning that the induced error is due to the fact of taking the first two terms in the cosine series expression.

Generally speaking, the fundamental period or frequency is the most important dynamic characteristic as the response will be at the first maxima. Moreover, undamped response was considered in the preceding formula, which is very practical. However, sometimes the second natural frequency could be also of practical importance but the aforementioned solution cannot predict this frequency.

Next, the developed numerical model will be checked against the above approximate solution. So, if we consider a soil domain of 30m length and 10m depth with the same material properties given at the beginning of the current section. A 1kN load is applied at the surface with different frequencies. Vertical and horizontal surface displacements are shown in Figure 4.19 for the considered frequencies. The same behaviour as in the case of homogenous soil layer over rigid bedrock of section 4.4.1 is observed; waves propagate when approaching the fundamental frequency of the soil medium and amplification occurs. Waves do not propagate when the frequency is lower than the fundamental frequency. The numerical model predicts the fundamental frequency to be around 5Hz which coincides well with the approximated solution of expression (4.8b).

A comparison between the homogenous layer response and the 2-layer soil profile response is presented in Figure 4.20 in terms of amplification by estimating the normalised area under the vertical displacement curve at the surface. The homogenous soil layer has the material properties of the upper layer of the 2-layer system. The fundamental frequency of the homogeneous layer is estimated to be around 3.3Hz and the numerical code predicts it to be around 3.4Hz. Resonance occurs when the applied frequency coincides with this fundamental frequency as it is shown in Figure 4.20.

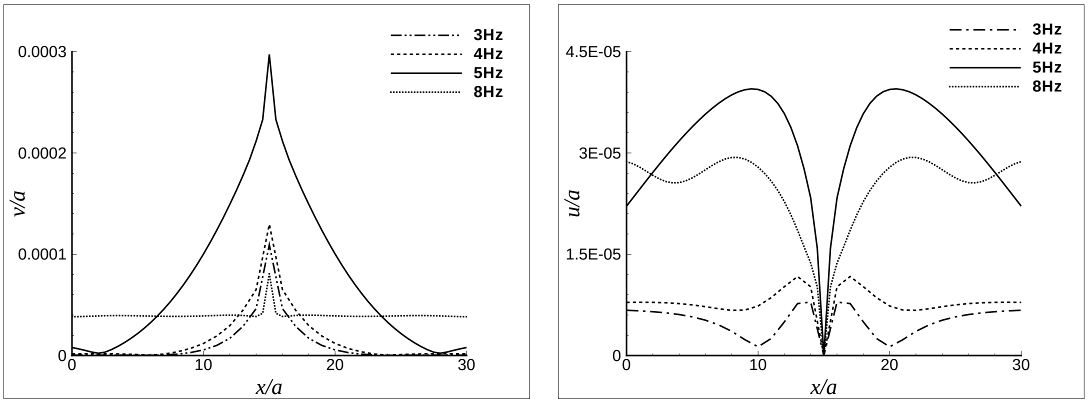

Figure 4.19: Vertical (left) and horizontal (right) surface displacements of a 2-layer soil profile over bedrock.

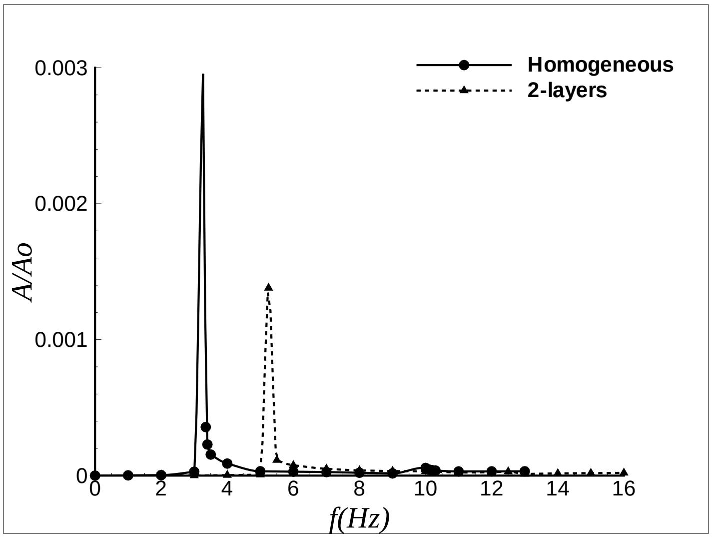

Figure 4.20: Resonance phenomena of homogeneous and 2-layer soil profiles.

In the 2-layer soil profile, the fundamental frequency has shifted to the right, or increased, due to the impedance effect of the two layers. As the bottom layer is stiffer than the upper layer, its fundamental frequency should be higher than the frequency of the overlain layer. In equation (4.8b), given that the fundamental frequency of the bottom layer is higher than of that of the upper layer and so the denominator decreases, which leads the fundamental frequency of the soil system to increase. This explains the shift in the fundamental frequency when comparing the homogenous case and the 2-layer soil profile, as it is shown in Figure 4.20.

4.6.2 Dynamic behaviour of a multi-layered soil profile with linear variation of stiffness

Using the Successive Use of Two−Layer solutions, the fundamental frequency of a multi-layered soil profile could be evaluated. The ability of the developed numerical model to simulate wave propagation in a multi-layered soil deposit with different material properties is examined next. As the 2-layer soil profile is validated against the approximated solution, a linear stiffness relation will be adopted in the numerical model to simulate wave propagation in the soil. However, the stiffness of the soil should not vary within each element. Nevertheless, the length of each element is very small and therefore the effect of considering constant stiffness over a small length may not have much effect. It is common practice to consider a homogeneous half-space with an average shear modulus but it is more practical to vary the shear modulus of the soil with depth as the homogeneous case underestimates the damping characteristics of the medium.

Here, a linear stiffness of the soil profile resting over horizontal rigid bedrock is assumed. A linear variation of the shear modulus with depth is chosen such that

$$\mu = \mu_0(1+\alpha z_i), \tag{4.9}$$

where α is the rate of linearity, μ is the shear modulus at a given depth, μ_0 is a reference shear modulus at the soil surface and z$_i$ is the depth below the soil surface. The rate of linearity is chosen to be 1 and the reference shear modulus equals to 5.77MPa. Soil density and Poisson's ratio are assumed to be constant for simplicity. Hence, the soil deposit is assumed to be soft at the surface and the stiffness is increased gradually to represent hard soil at the bottom. Having obtained the shear modulus for each layer we assume the soil density and Poisson's ratio to be 1550kg/m^3 and 0.3, respectively. No damping is considered. A 1kN vertical load with 10Hz frequency is applied at the soil surface. The length of the computational domain is changed from $2\lambda_R$ to $8\lambda_R$ with a fixed depth of $2\lambda_R$. The domain is divided into 20 layers with respect to depth, each layer has its own constant stiffness derived from the previous equation. As it is shown in Figure 4.21, vertical and horizontal surface displacements are plotted when increasing the length of the domain. Once again, the continuity of displacements for various lengths of the domain and low relative error show the good performance of the consistent transmitting boundary conditions to radiate the waves away to infinity. If we assume that the soil layer is homogeneous and has the reference elasticity modulus of 20MPa for the previous computational domain, the results of Figure 4.22 show a completely different response for the vertical and horizontal displacements at the soil surface in the case of homogeneous and linear variation of the soil stiffness.

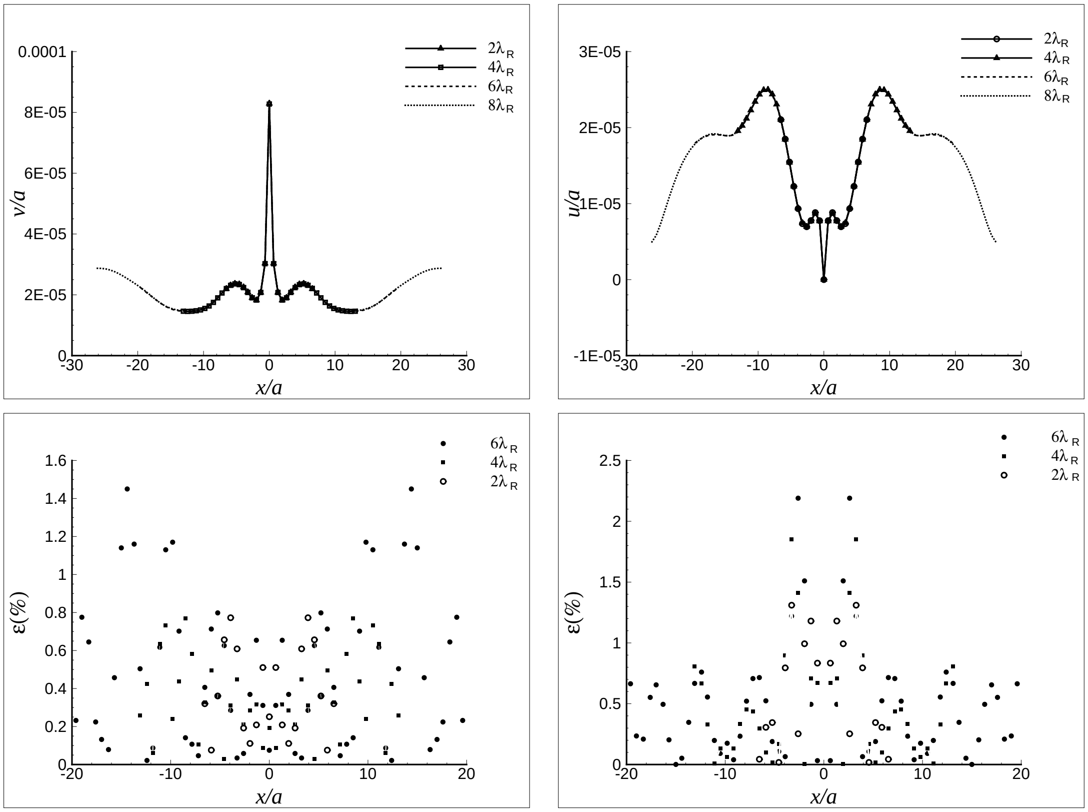

Figure 4.21: Vertical (left) and horizontal (right) surface displacements and their corresponding errors for domain length associated with linear variation of the stiffness.

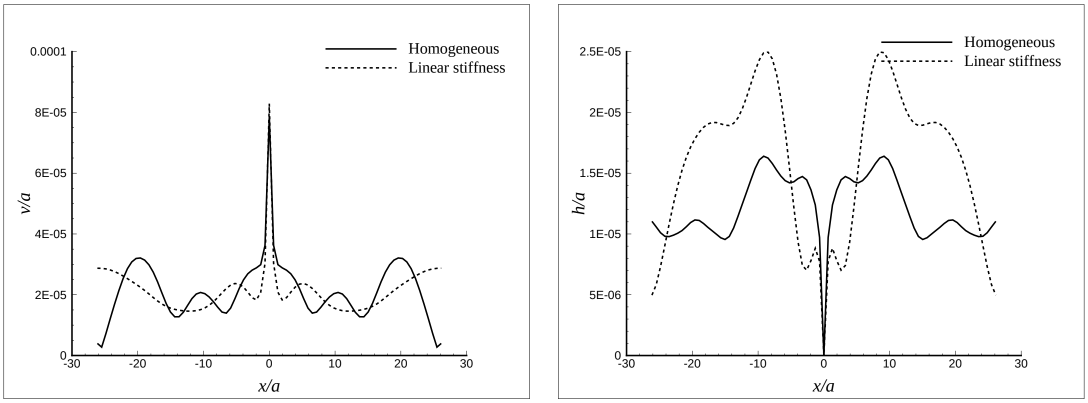

Figure 4.22: Vertical (left) and horizontal (right) displacements at the surface for homogeneous and linear variation of stiffness for the case of $8\lambda_R$.

A parametric study is performed to investigate the effect of the rate α has on the fundamental frequency of a multi-layered soil profile. Three different values of α have been assigned; 0, 0.5, and 1. A soil domain of 30m length and 10m depth is considered with 10 layers. The area underneath the vertical displacement curve at the soil surface is plotted for several frequencies and the three chosen values of α. From Figure 4.23, it is observed that the fundamental frequency of the soil profile has shifted to the right. It is increased with increasing the soil stiffness. Increasing α will increase the shear modulus of the soil and consequently the fundamental frequency of the soil deposit. In summary, the fundamental frequency increases with increasing the linearity coefficient α.

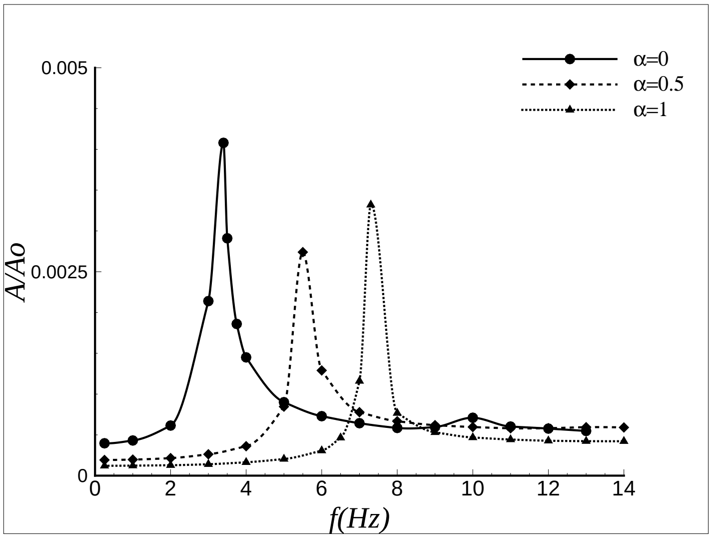

Figure 4.23: Effect of soil stiffness on the fundamental frequency.

4.7 Models with structured and unstructured mesh grids

So far only uniform structured mesh grids consisting of 4-node quadrilateral elements were used. Although such mesh grids are very simple to use but they are not practical especially when encountering complex geometries as it is the case of most engineering problems. The purpose of choosing such meshes is for simplicity and thus it is very common to use in problems with simple geometry. For problems of practical interest, the soil domain may contain some discontinuities or structures such as foundations, tunnels or wave barriers of complex shapes. Dealing with problems with a uniform structured mesh grid is difficult if not impossible in some cases. Therefore, using unstructured mesh grid is very important when solving such problems.

4.7.1 Structured triangular element mesh grids

A structured triangular grid is used first to mesh the domain and simulate wave propagation in a soil medium before adopting an unstructured mesh. Herein, each quadrilateral element is divided into two triangular elements. Hence, a structured triangular element mesh grids is obtained as shown in Figure 4.24. Triangular elements are either right or left-angle. Quadrilateral elements are replaced by triangular elements and consequently the stiffness and mass matrices routines are changed in addition to the post processing routines. Nodal forces simulating the effect of the two semi-infinite lateral media on the central domain remain unchanged. In order to satisfy the condition on the model size, the length of the element should be around one-fifteenth of the Rayleigh wavelength in order to obtain the length of the hypotenuse about $\lambda_R/10$ or less. It is found that a dimension of one-twentieth of the Rayleigh wavelength of the triangular elements gives reasonable results as the horizontal and vertical displacements converge towards the quadrilateral element mesh solution. Here, a soil domain of $4\lambda_R$ in length and $2\lambda_R$ in depth is considered. The soil has the following properties; density of 2000kg/m^3, elasticity modulus of 100MPa, Poisson's ratio of 0.25 and a damping ratio of 2.5%. It is subjected to a vertical surface harmonic load with a frequency of 20Hz. A higher number of nodes and consequently much higher number of degrees of freedom in the computational domain are used by the above mentioned discretisation. The number of elements in the central domain has increased by a factor of 8. The run time in the case of quadrilateral elements was 3s whereas in the case of triangular elements with one-twentieth of Rayleigh wavelength has increased to 15s, 5 times higher, as more degrees of freedom and elements are involved in the solution. Fortunately these run times are so small that the increase is not of importance.

One drawback of the right and the left-angle triangular elements is that the shape is not uniform; in other words, the length of the hypotenuse is greater than the other lengths. It was found that including triangular elements as in the top right (mesh type 1) or bottom left (mesh type 2) of Figure 4.24 has produced non-symmetrical results and it is more pronounced in the surface horizontal displacements, Figure 4.25. The loss of symmetry is less pronounced when decreasing the dimension of the finite element from one-tenth of the Rayleigh wavelength to one-twentieth. This obviously leads to more finite elements, degrees of freedom and eventually a higher computational cost.

As depicted in Figure 4.25, mesh type 3, half of the triangle elements inclined to the left and the other half to the right, is a symmetrical mesh and produces symmetrical displacements. In the case of mesh grids 1 and 2, the displacements were found to be non-symmetrical, however both meshes have shown that the results are close to the quadrilateral and to the mesh type 3 results.

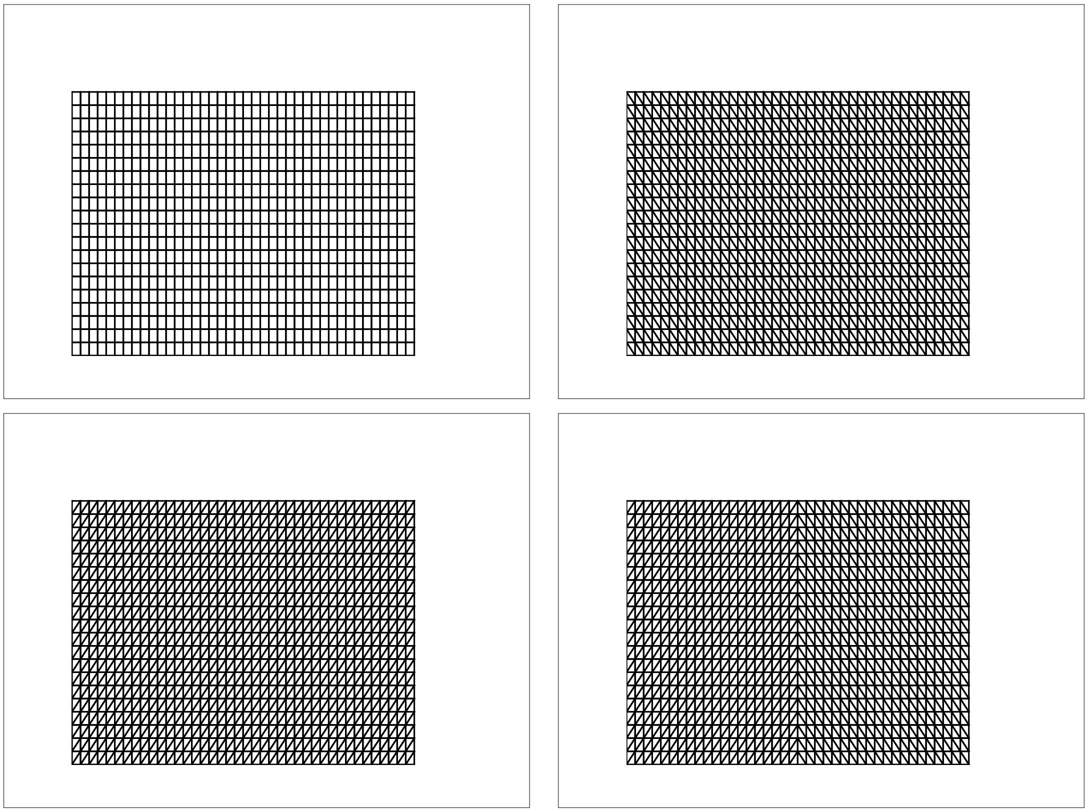

Figure 4.24: Mesh grids used in the analysis.

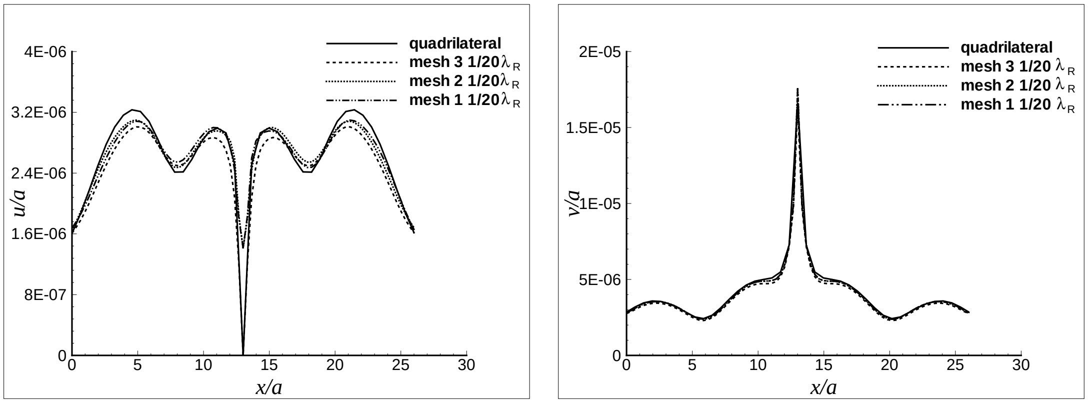

Figure 4.25: Effect of triangular element type on surface horizontal (left) and vertical (right) displacements.

To investigate the effect of mesh size on the accuracy of the solution, the mesh grid 3 is further refined. The number of nodes is increased from 10 to 20 and 30 per Rayleigh wavelength. As it is illustrated in Figure 4.26, for the case of one-twentieth of the Rayleigh wavelength the results are almost matching the quadrilateral element solution in the vertical direction but there is still some discrepancy in the horizontal direction. Better agreement is obtained by adopting even smaller elements with mesh size equal to one-thirtieth of the Rayleigh wavelength.

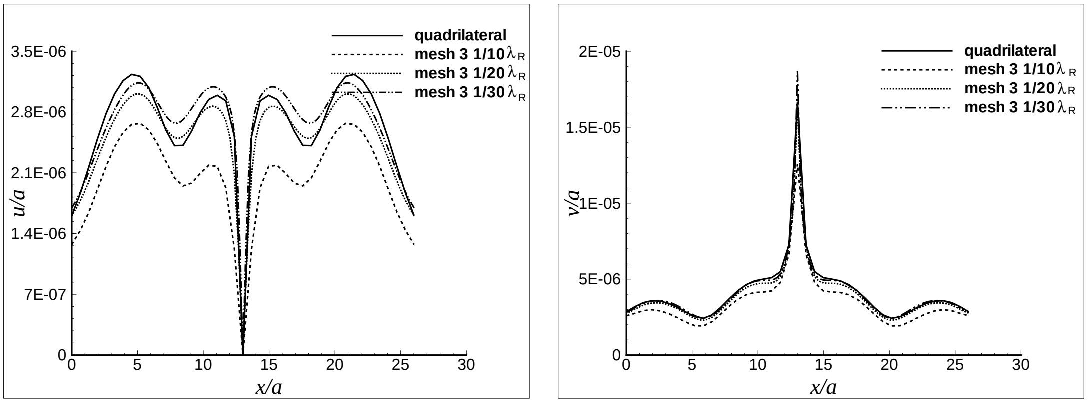

Figure 4.26: Effect of triangular element size on surface horizontal (left) and vertical (right) displacements.

4.7.2 Unstructured triangular element mesh grids

An automatic mesh generator such as the one introduced by Geuzaine and Remacle [103] is used in the current section to generate an unstructured triangular element mesh grid. The mesh generator produces a random grid for the computational domain with a specified element size at the surface by the user, by setting the element size factor, and with element length within the mesh grid less or equal to the specified size. Basically, the smaller the element size factor the smaller is the length of the element. The benefit of the mesh generator consists in its practicality to introduce many layers in the domain, include discontinuities with complex geometry and even consider an inclined rigid bedrock or inclined soil layers.

If we consider a soil medium of length 30m and depth of 15m which has the same characteristics presented in section 4.7.1. A 1kN oscillating load of 20Hz frequency is applied at the left boundary of the domain. An unstructured mesh grid with triangular elements is generated. The horizontal and vertical directions are divided into 67 and 34 nodes, respectively. If a unstructured mesh grid is adopted, 2599 nodes are required to construct 5064 elements. This mesh is much denser in comparison to 1091 nodes and 1800 element for the structured quadrilateral element mesh. Figure 4.27 shows the two types of meshing. Horizontal and vertical surface displacements are plotted in Figure 4.28. For the considered problem very good agreement is achieved when comparing the results from both grids. However, the computational cost of the analysis increased due to the increase in the number of degrees of freedom in the model, for the unstructured mesh.

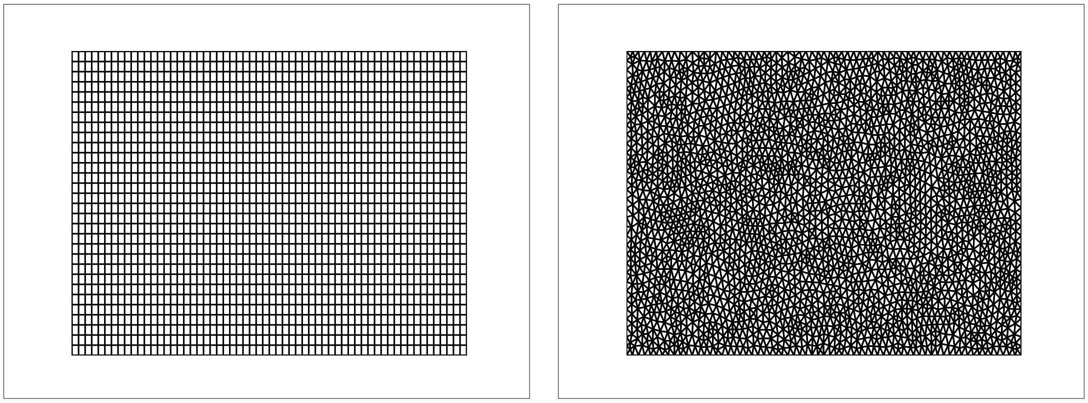

Figure 4.27: Structured quadrilateral versus unstructured triangular mesh grids.

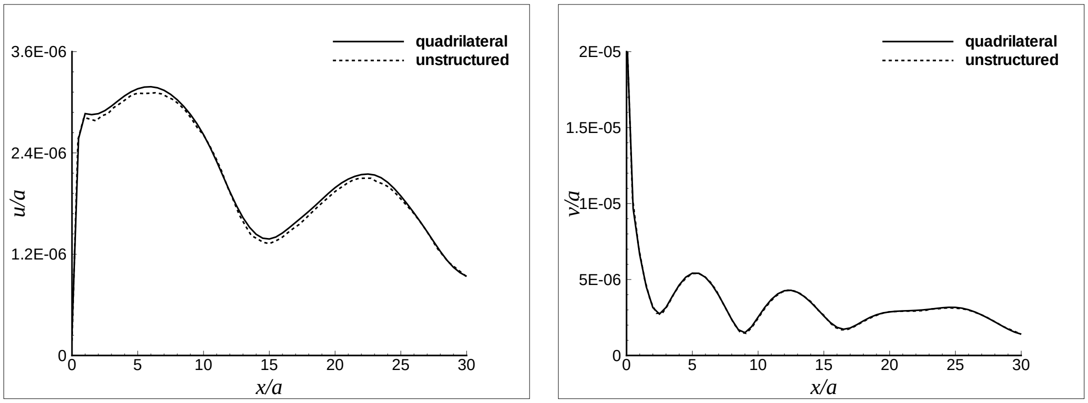

Figure 4.28: Horizontal (left) and vertical (right) surface displacements associated with structured and unstructured mesh grids.

The length of the computational domain is increased from 15m to 30m. The horizontal and vertical surface displacements are plotted in Figure 4.29. The continuity of the displacement field is clearly observed and hence the developed model is also effective with unstructured mesh grids.

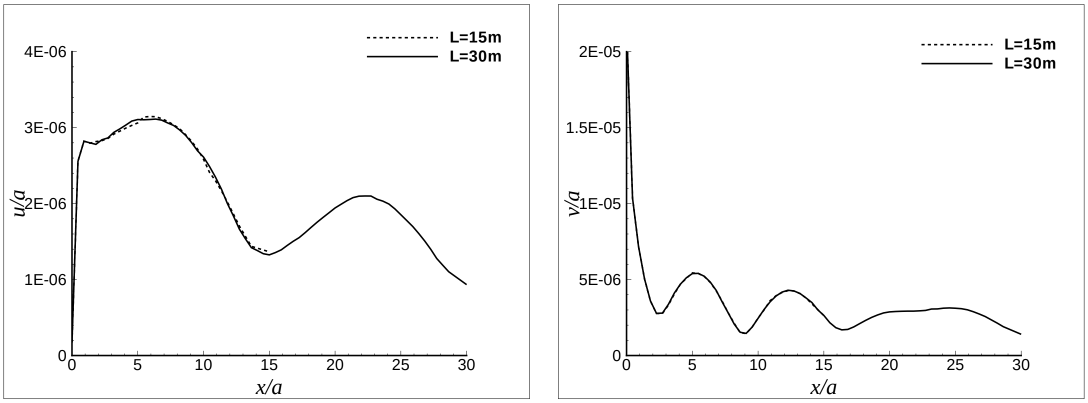

Figure 4.29: Horizontal (left) and vertical (right) surface displacements associated with unstructured mesh when extending the domain.

4.7.3 An application with unstructured mesh grids

The merits of using unstructured mesh grids is exploited extensively in Chapter 7 for various applications. A test example is introduced in the current section to show the flexibility of the numerical model, by incorporating unstructured triangular mesh grids, to deal with problems where a traditional uniform structured mesh could be troublesome.

Several assumptions have been made in section 4.4 to simplify the problem such as presuming that the soil layer is resting on horizontal rigid bedrock. Usually, neither soil layers nor the bedrock are horizontal. Therefore, it is worth investigating the effect of inclined rigid bedrock on the dynamic behaviour of the soil layer. A parametric study was performed by Jones [104] and Jones and Hunt [105] to investigate the effect of soil layer inclination overlaying half-space on surface wave propagation due to an interior dynamic load. In what follows, a series of numerical examples are used to investigate the effect of the base inclination of the soil domain on wave propagation. A soil layer of 30m in length and 15m depth resting on rigid bedrock is considered. Young's modulus, density, Poisson's ratio and damping ratio of the soil are assumed to be respectively; 100MPa, 1700kg/m^3, 0.30 and 2.5%. The dynamic load is 1kN and applied at the soil surface with a frequency of 20Hz. An unstructured 3-node triangular element mesh grid is employed where the base is considered first to be horizontal in order to obtain a reference solution which should match the solution when using 4-node quadrilateral elements. The rigid bedrock is then inclined with an angle θ varied from 0° to 9°. The main difference in the case of inclined soil base model, in comparison to the case of horizontal base, is that we have to solve two separate eigenvalue problems, as the two lateral boundaries of the computational domain are different in terms of depths and node numbers. Figure 4.30 shows an example of unstructured mesh grid for a soil layer over an inclined rigid bedrock, the semi-infinite lateral regions on the right and the left are assumed to have horizontal layers extending into infinity. Figure 4.31 depicts the effect of the angle of inclination on the vertical surface displacement.

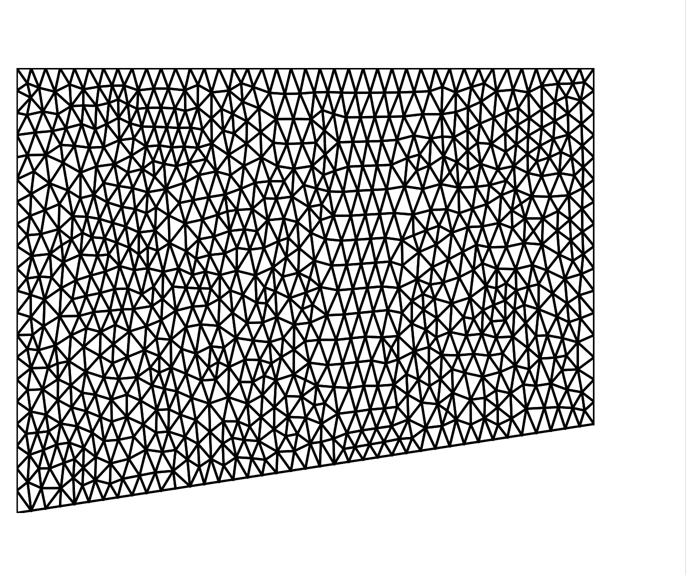

Figure 4.30: Unstructured mesh grids for soil layer over inclined base.

The right hand side depth of the soil layer is multiplied by the Rayleigh wavelength for better interpretation of the results. For low angles of inclination, there is no dramatic change in the surface vibration. With increasing the angle of inclination in such way that the shorter depth of the soil domain approaches $1.6\lambda_R$, the region of the shorter depth is first affected more than the region corresponding to the larger depth. However, the latter region becomes more affected as the angle of inclination is increased.

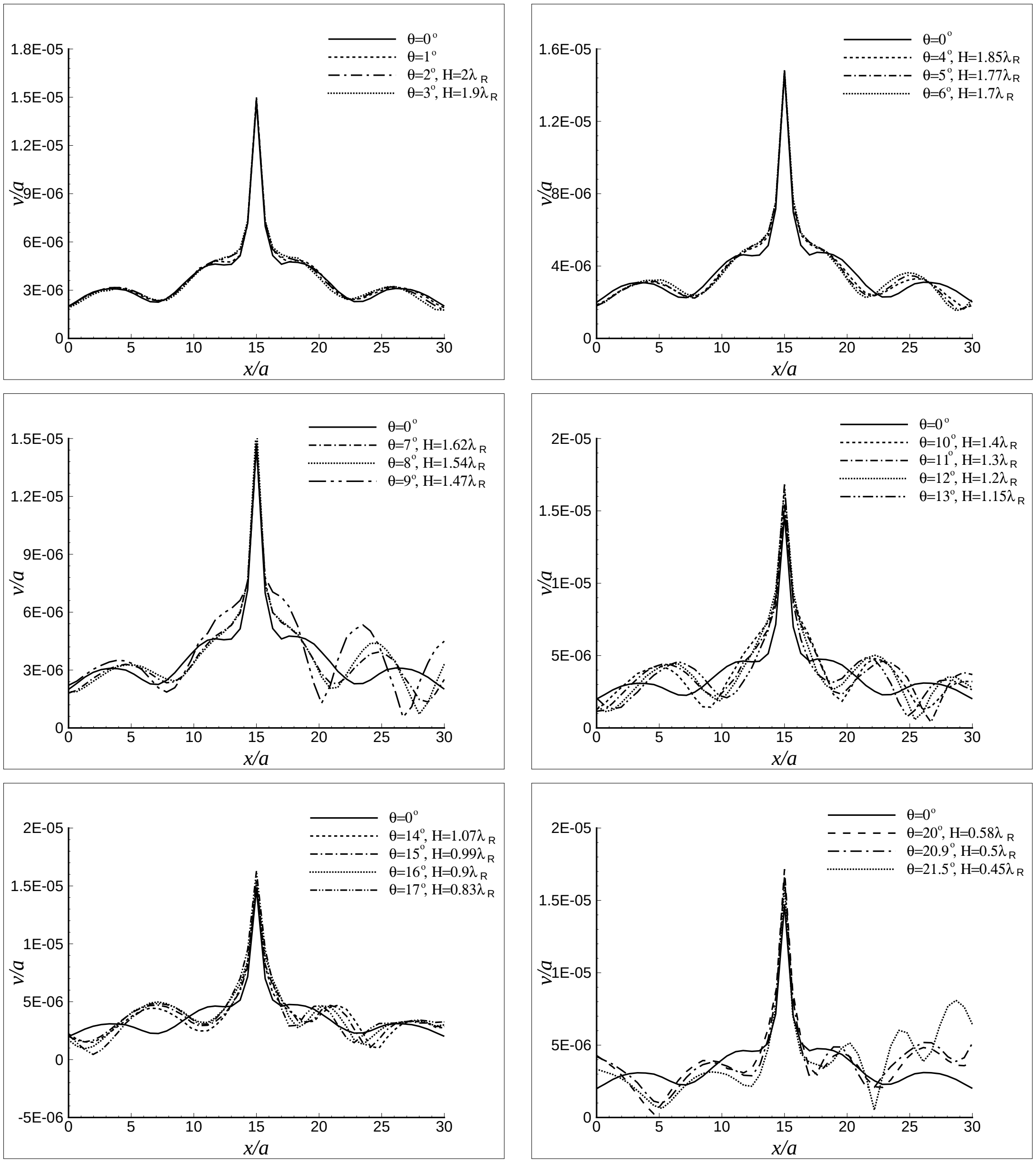

Figure 4.31: Effect of base inclination on surface vertical displacements.

4.8 Concluding remarks

In this chapter a parametric study is carried out primarily to validate the numerical model developed in Chapter 3. The soil medium is assumed to rest over rigid bedrock and the consistent transmitting boundaries simulate the unbounded character of the computational domain in the horizontal direction. The main conclusions are as follows:

- It is clear that untreated lateral boundaries of a computational domain, representing a soil medium, lead to erroneous dynamic response of the medium.

- The effectiveness of the consistent transmitting boundaries to radiate the incoming waves away to infinity at the lateral boundaries of a given computational domain is checked by considering different lengths. Indeed, both vertical and horizontal surface displacements remain unchanged irrespective of the domain length, with relative errors remaining very low, showing that the model simulates the infinite extent of the soil medium.

- The developed model is further validated by considering the dynamic behaviour of a soil layer overlaying rigid bedrock, in terms of the natural frequencies or critical depths. The model successfully captures the resonance effect due to the natural frequencies of the medium, for cases of fixed depth. Conversely, for a fixed frequency of the external load, the model captures resonance due to the critical depths of the rigid bedrock.

- The latter validation is extended to the case of multi-layered soil profiles, particularly to 2-layer soil media for which an approximate expression of the natural frequencies is available. The developed model predicted frequencies provided by the approximate theoretical approach.

- It is also shown that the developed model can incorporate the use of structured or unstructured mesh grids. In fact the ability to use unstructured mesh grids offers more flexibility in considering problems of engineering interest such as dealing with complex geometries. In summary, all numerical analyses carried out in this chapter lead us to trust the developed model and further extend it to deal with soil media over half-space.

Chapter 5

Wave propagation modelling in half-space soil media

5.1 Introduction

In Chapters 3 and 4, the soil medium is assumed to overlay rigid bedrock. As a consequence, the nodes at the base of the computational domain are fixed. This model may represent real engineering situations, in which the bedrock is at shallow or intermediate depths. However, when this is not the case and the soil medium is either very deep or extends to infinity in both lateral and vertical directions, the alternative model should be the half-space model. According to Andrade [106] there is no exact representation of the half-space within the framework of the FEM. An approach representing part of the half-space, below a domain of interest, as an absorbing or paraxial boundary would be of practical use.

In this chapter, the Paraxial Boundary Condition (PBC) is combined to the TLM approach to produce a model for half-space soil media.

5.2 Literature review

A first idea consisted to extend the TLM approach to the base of the computational domain and formulate the appropriate matrices which represent the contribution of the half-space. Treating the base of the domain with the same procedure used for the left and right lateral semi-infinite regions will lead to a costly computational model because of the eigenvalue problem. Moreover, following the TLM would require fixing certain nodes, for example at the two bottom corners of the computational domain, to avoid rigid modes. As this approach seemed unpractical for the considered applications, an alternative method is adopted. As mentioned above, it consists to couple the TLM with the PBC. Figure 5.1 shows a schematic diagram representating this coupled model.

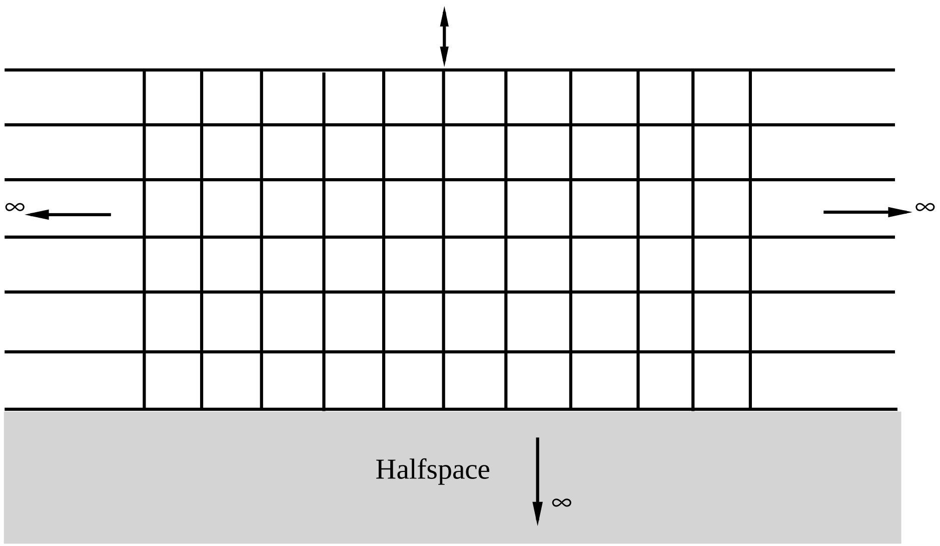

Figure 5.1: Two dimensional half-space representation.

In the following, a survey is conducted to review different approaches combined with the TLM to represent half-space media. Kausel and Roësset [107] used the stiffness matrix approach, by employing the Haskell-Thompson transfer matrix technique, to derive the dynamic stiffness matrix for layered media. This approach is based on isolating a specific layer and maintaining equilibrium by applying external loads at the upper and lower interface of the layer with different signs. As it was shown in Chapter 3, an algebraic eigenvalue problem was derived by applying the principle of virtual work on the wave equations to first compute the horizontal layers' matrices. Therefore, if one is seeking to model the unbounded domain by means of the TLM with another approach, the computed global stiffness matrix should also be of a polynomial form in the wavenumber. This could be achieved by using some polynomial approximation of the impedance matrix.

An explicit closed-form of the Green's function for a dynamic load acting on, or within, a layered soil system is derived by Kausel and Peek [108]. It is achieved by first inverting the stiffness matrix in the wavenumber domain, which is carried out by performing a spectral decomposition, and applying an integral transform to obtain the displacement vector. This has led to obtain algebraic expressions for the dynamic stiffness matrix for layered media over rigid base. A paraxial approximation for rigid base was derived by employing the Green's function which relate stresses and displacements at any location in an elastic medium caused by a dynamic source at any other location. Hull and Kausel [109] extended this procedure to obtain the Green's function of layered media over half-space and thereafter derived paraxial approximations for the impedance of the half-space by using Taylor series to approximate its stiffness matrix in a polynomial form. The impedance matrix of the half-space is then added to the stiffness matrix of the irregular region to obtain a model for the soil layer over half-space. In fact, PBC was first derived by Engquist and Majda [53].

Special formulations of the PBC for the half-space impedance matrix, derived by Kausel and Roësset [107], were further developed in reference [106] as follows. A layered half-space is truncated at the interface between the last layer and the underlain half-space. The tractions at the interface contribute to the external virtual work part of the principle of virtual work expression. Considering that the bottom layer is divided into elements and applying the virtual work equation on the tractions at the bottom of the last layer, the dynamic stiffness matrices of those elements, half-space elements, are deduced and hence are assembled with the stiffness of the finite elements of the irregular domain. The edge nodes of the last layer have also some contribution. For the lateral boundaries, the contribution of the half-space is accounted for and implemented in the algebraic eigenvalue problem. Nodal forces and the dynamic stiffness matrices of the regular regions are then computed and substituted back into the global dynamic equation.

The half-space impedance matrix of Kausel and Roësset [107] was also used by Kaynia *et al.* [110] to represent the soil media under the soil embankment. The authors used the disk loads Green's function to obtain the soil stiffness at the embankment-half-space interface which was assembled with the dynamic stiffness matrix of the embankment. This was implemented in a finite element code in the frequency domain to predict ground vibration induced by high speed trains in a layered viscoelastic half-space.

The stability and the accuracy of the PBC and the doubly asymptotic approximation are discussed by Maeda and Kausel [111] for the anti-plane shear case. Improvement of the paraxial boundary approximations is achieved by incorporating a *buffer layer* with the same material properties of the half-space at the interface between the soil medium of interest and the remaining of the half-space. It is reported that it is not accurate to use only the paraxial approximation for modelling half-space, adding a buffer layer is then necessary to improve its performance. Further details are supplied next, in section 6.5. Moreover, Kausel [112] investigated the physical interpretation of the PBC and its stability considerations which should be taken into account. For example, setting the determinant of the exact stiffness matrix to zero leads to finding pairs of wavenumbers which are all real. While, two pairs of roots, real or complex depending on the value of the Poisson's ratio, are obtained from the approximated matrix. Park [66] employed the same technique for anti-plane shear case and in-plane waves and proposed some improvements to the approximated stiffness matrix, depending on the value of the Poisson's ratio. An extensive study was performed and a comparison between the exact and the approximated matrix was carried out.

The concept of the second-order paraxial boundary conditions is extended by Lee *et al.* [113] to deal with water-saturated layered soil media over half-space. They first obtained the exact dynamic stiffness matrix of the water-saturated half-space and then a second-order approximation of the exact stiffness matrix is computed. Both anti-plane shear problems and plane strain problems are considered. The remaining steps of the procedure are identical to those presented by Andrade [106]. As an application, the dynamic stiffness of rigid impermeable or permeable strip foundations resting on water-saturated half-space is determined. This procedure is also adopted in reference [114] where a second-order paraxial approximation for three-dimensional wave motion in the Cartesian coordinates is determined by employing their previous derivations presented in reference [113] for plane and anti-plane cases. It is transferred then into cylindrical coordinates. The same steps in solving the problem are maintained leading to an eigenvalue problem of dimension $(6n+6)$ where n is the number of layers in the model.

Another technique for modelling wave propagation in arbitrary unbounded domains is to combine the TLM with high-order local absorbing boundary conditions which are expressed as polynomial functions of the horizontal wavenumber to be implemented within the framework of the TLM. The Continued Fraction Absorbing Boundary Conditions (CFABC), a high-order local absorbing boundary condition developed by Zahid [115], Savadatti and Gudatti [116], Savadatti and Gudatti [117] and other researchers, satisfies the latter condition as a quadratic function of the horizontal wavenumber. Lee and Tassoulas [118] combined the CFABC with the consistent transmitting boundary conditions where the stiffness of CFABC is determined by the mid-point rule. For layered half-space media, the half-space may be represented by a successive number of single layers of the CFABC where the accuracy is improved by increasing the number of layers. Lee and Tassoulas [118] stated that in order to obtain perfect absorbers for in-plane waves with a horizontal wavenumber, the CFABC layers could be used in pairs where one layer is used to absorb compression waves and the other for absorbing shear waves. Recently, Barbosa *et al.* [119] constructed an efficient model by combining the PML with TLM to simulate wave propagation in layered half-space.

5.3 Treatment of the half-space

In this work, the treatment of the irregular and regular regions are presented in sections 5.3.1 and 5.3.2, respectively. First, elements of the half-space interface within the irregular region are dealt with to form the elementary stiffness matrices. Then, the corner elements of the half-space are considered in the eigenvalue problem of the TLM. Figure 5.2 shows the representation of the mentioned regions.

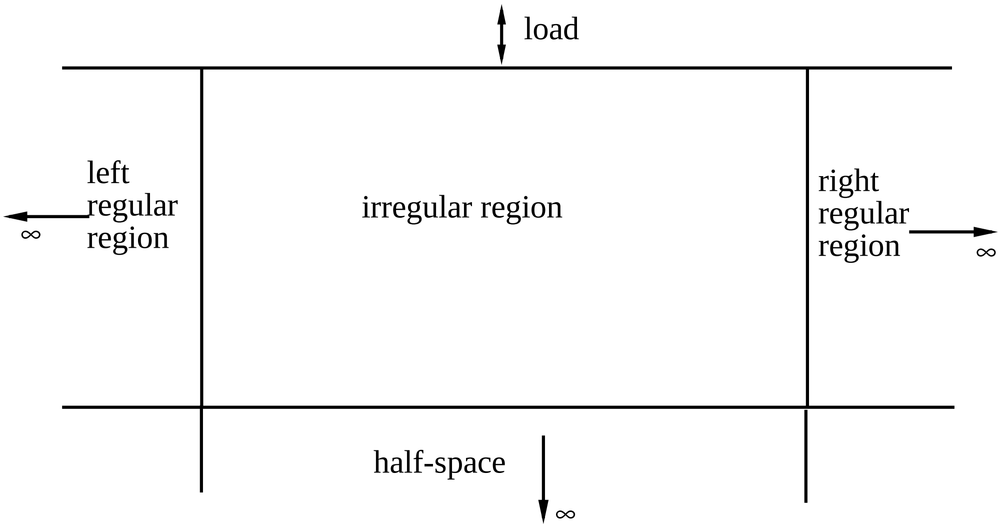

Figure 5.2: Treatment of the half-space model.

5.3.1 Treatment of the irregular region

The FEM is adopted in the irregular region, which is assumed to be resting over rigid bedrock. Now, half-space elements will replace the bedrock. Therefore it is needed to formulate these elements in order to account for their contribution.

The impedance stiffness matrix for SV-P waves in a half-space opens downward (one may reverse off-diagonal terms in the impedance matrix to represent half-space opens upward) is developed in reference [107] and expressed as

$$\mathbf{K} = 2k\mu \left[\frac{1-s^2}{2\,(1-rs)} \begin{bmatrix} r & -1 \\ -1 & s \end{bmatrix} - \begin{bmatrix} 0 & -1 \\ -1 & 0 \end{bmatrix} \right], \tag{5.1}$$

where parameters r and s are given by

$$r = \sqrt{1-\left(\frac{\omega}{kc_p}\right)^2} \qquad \text{and} \qquad s = \sqrt{1-\left(\frac{\omega}{kc_s}\right)^2}, \tag{5.2}$$

ω is the circular frequency of the dynamic load, μ is the shear modulus of the half-space, c_p and c_s are respectively the compression and shear wave velocities in the half-space, and k is the horizontal wavenumber. The impedance stiffness, an exact stiffness, is not a polynomial function of the wavenumber. Hence, expanding it and retaining the first three terms of the Taylor series about $k = 0$ yields a second order approximation with respect to the horizontal wavenumber of the form

$$\mathbf{K}(k) \approx \mathbf{K}(0) + k\mathbf{K}^{'}(0) + \frac{1}{2}k^2\mathbf{K}^{''}(0), \tag{5.3}$$

and subsequently

$$\mathbf{K} = \mathrm{i}\omega\rho c_s \begin{bmatrix} 1 & 0 \\ 0 & 1/\alpha \end{bmatrix} + \mu\frac{1-2\alpha}{\alpha}k \begin{bmatrix} 0 & 1 \\ 1 & 0 \end{bmatrix} + \mathrm{i}\mu\frac{c_s}{2\omega}k^2 \begin{bmatrix} -(2-\alpha)/\alpha & 0 \\ 0 & (1-2\alpha)/\alpha^3 \end{bmatrix}, \tag{5.4}$$

where ρ is the density of the half-space soil and α represents the ratio of the shear wave to dilational wave velocities. Expression (5.4) is an algebraic expression in k and a second order paraxial approximation of the half-space stiffness. It should be noted that reference [105] provides what appears to be an erroneous version of expression (5.4) inasmuch as the two diagonal terms in the matrix that multiplies k^2 are at variance of expression (5.4). However the correct terms might have been implemented in the authors numerical work leading to the same results obtained in this dissertation.

By expanding the impedance matrix about $k = 0$, the wavefronts of the incoming waves towards the half-space are assumed to be parallel to the horizontal surface of the half-space. Thus, a sufficient depth should be provided in order to allow the wavefronts to become horizontal when hitting the surface of the half-space. This has been investigated in section 6.2.2. Tractions and displacements at the surface of the half-space are related in the following form

$$\begin{bmatrix} \hat{F}_x \\ \mathrm{i}\hat{F}_y \end{bmatrix} = \mathbf{K} \begin{bmatrix} \hat{u} \\ \mathrm{i}\hat{v} \end{bmatrix}, \tag{5.5}$$

where the vertical traction and displacement are scaled by the imaginary number i to work with a symmetrical matrix. Combining the previous equation and the second order formulation of the impedance matrix of expression (5.4) and thereafter applying the Inverse Fourier Transformation (IFT) with respect to k yields

$$\begin{aligned} \frac{1}{2\pi}\int_{-\infty}^{\infty} \hat{F}_x e^{-\mathrm{i}kx} dk &= \mathrm{i}\omega\rho c_s \left[\int_{-\infty}^{\infty} \hat{u} e^{-\mathrm{i}kx} dk\right] \\ &+ \frac{\mathrm{i}\mu c_s (\alpha - 2)}{2\omega\alpha} \left[\frac{1}{2\pi}\int_{-\infty}^{\infty} k^2 \hat{u} e^{-\mathrm{i}kx} dk\right] \\ &- \frac{\mu(1-2\alpha)}{\alpha} \left[\frac{1}{2\pi}\int_{-\infty}^{\infty} \mathrm{i}k\hat{v} e^{-\mathrm{i}kx} dk\right], \end{aligned} \tag{5.6}$$

and

$$\begin{aligned}\frac{1}{2\pi}\int_{-\infty}^{\infty}\hat{F}_y e^{-\mathrm{i}kx}dk &= \mathrm{i}\omega\rho c_p\left[\int_{-\infty}^{\infty}\hat{v}e^{-\mathrm{i}kx}dk\right] \\ &+ \frac{\mathrm{i}\mu c_s(1-2\alpha)}{2\omega\alpha^3}\left[\frac{1}{2\pi}\int_{-\infty}^{\infty}k^2\hat{v}e^{-\mathrm{i}kx}dk\right] \\ &+ \frac{\mu(1-2\alpha)}{\alpha}\left[\frac{1}{2\pi}\int_{-\infty}^{\infty}\mathrm{i}k\hat{u}e^{-\mathrm{i}kx}dk\right].\end{aligned} \tag{5.7}$$

Taking into account Fourier transform properties on the previous two equations we obtain the following relationships between tractions and displacements at the surface of the half-space

$$F_x = \mathrm{i}\omega\rho c_s u - \frac{\mathrm{i}\mu c_s(\alpha-2)}{2\omega\alpha}u_{,xx} + \frac{\mu(1-2\alpha)}{\alpha}v_{,x}\,, \tag{5.8}$$

$$F_y = \mathrm{i}\omega\rho c_p v - \frac{\mathrm{i}\mu c_s(1-2\alpha)}{2\omega\alpha^3}v_{,xx} - \frac{\mu(1-2\alpha)}{\alpha}u_{,x}\,, \tag{5.9}$$

where u, $u_{,x}$ and $u_{,xx}$ represent the horizontal displacement and their first and second derivatives with respect to x. The same applies to the vertical displacement v and its derivatives with respect to x. Expressions (5.8) and (5.9) show the relationship between displacements, displacements derivatives and the tractions at the surface of the half-space. In order to apply these tractions at the interface boundary between the half-space and the irregular region, their signs must be reversed. Thereafter, the principle of virtual work is applied by considering the external virtual work by these traction forces

$$W = \int_0^l \delta u F_x^{nf}dx + \int_0^l \delta v F_y^{nf}dx, \tag{5.10}$$

where nf refers to the interface between the irregular region and half-space. Substituting the tractions from equations (5.8) and (5.9), after reversing the signs of all terms, into the previous equation and integrating by parts leads to

$$
\begin{aligned}
W &= -\mathrm{i}\omega\rho c_s u\int_0^l \delta u\, u\, dx - \frac{\mu\,(1-2\alpha)}{2\alpha}\int_0^l \delta u\, v_{,x}\, dx \\
&+ \frac{\mu\,(1-2\alpha)}{2\alpha}\int_0^l \delta u_{,x}\, v\, dx - \frac{\mathrm{i}\mu c_s\,(\alpha-2)}{2\omega\alpha}\int_0^l \delta u_{,x}\, u_{,x}\, dx \\
&- \mathrm{i}\omega\rho c_p v\int_0^l \delta v\, v\, dx + \frac{\mu\,(1-2\alpha)}{2\alpha}\int_0^l \delta v\, u_{,x}\, dx \\
&- \frac{\mu\,(1-2\alpha)}{2\alpha}\int_0^l \delta v_{,x}\, u\, dx - \frac{\mathrm{i}\mu c_s\,(\alpha-2)}{2\omega\alpha^3}\int_0^l \delta v_{,x}\, v_{,x}\, dx \\
&- \frac{\mu\,(1-2\alpha)}{2\alpha}\delta u v|_0^l + \frac{\mu\,(1-2\alpha)}{2\alpha}\delta v u|_0^l \\
&+ \frac{\mathrm{i}\mu c_s\,(\alpha-2)}{2\omega\alpha}\delta u u_{,x}|_0^l + \frac{\mathrm{i}\mu c_s\,(\alpha-2)}{2\omega\alpha^3}\delta v v_{,x}|_0^l .
\end{aligned}
\tag{5.11}
$$

The integration boundaries 0 and l represent the surface of the half-space over the entire domain, which could be subdivided into half-space elements and the integration will be performed on these 2-node elements (see Figure 5.3). If we introduce a linear interpolation function N for the displacement field in the x-direction, the displacements at any point p, located between nodes A and B (Figure 5.3), will be written as

$$
U_p = \begin{bmatrix} N(x) & 0 \\ 0 & N(x) \end{bmatrix} \begin{Bmatrix} u_j \\ u_{j+1} \\ v_j \\ v_{j+1} \end{Bmatrix} \qquad \text{where} \qquad N(x) = \begin{bmatrix} 1-\frac{x}{\Delta x} & \frac{x}{\Delta x} \end{bmatrix}, \tag{5.12}
$$

where $\Delta x = x_{j+1} - x_j$ represents the length of an individual half-space element and U_p is the displacement vector for the half-space element. It is given by its components

$$
U = \begin{Bmatrix} u_j \\ u_{j+1} \end{Bmatrix} \qquad \text{and} \qquad V = \begin{Bmatrix} v_j \\ v_{j+1} \end{Bmatrix}, \tag{5.13}
$$

with

$$
u = NU \qquad \text{and} \qquad v = NV. \tag{5.14}
$$

Variations of the nodal displacements within each element are given by

$$
\delta u = N\delta U \qquad \text{and} \qquad \delta v = N\delta V. \tag{5.15}
$$

The first derivative of the nodal displacements with respect to x are given by

$$
u_{,x} = N_{,x}U \qquad \text{and} \qquad v_{,x} = N_{,x}V. \tag{5.16}
$$

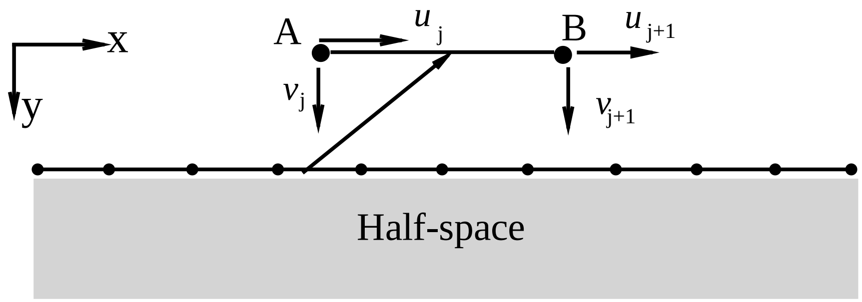

Figure 5.3: Half-space element.

Considering the relationship between the displacements and the shape functions, and then summing for all half-space elements will lead to

$$
\begin{aligned}
W \;=\; & \sum_{j=1}^{n}(-\mathrm{i}\omega\rho c_s \delta U^T \left[\int_{x_1}^{x_2} N^T N\, dx\right] U \\
& - \mathrm{i}\omega\rho c_p \delta V^T \left[\int_{x_1}^{x_2} N^T N\, dx\right] V \\
& - \frac{\mathrm{i}\mu c_s\,(1-2\alpha)}{2\omega\alpha^3}\delta V^T \left[\int_{x_1}^{x_2} N_{,x}^T N_{,x}\, dx\right] V \\
& - \frac{\mu\,(1-2\alpha)}{2\alpha}\delta U^T \left[\int_{x_1}^{x_2} N^T N_{,x}\, dx\right] V \\
& - \frac{\mu\,(1-2\alpha)}{2\alpha}\delta V^T \left[\int_{x_1}^{x_2} N_{,x}^T N\, dx\right] U \\
& + \frac{\mu\,(1-2\alpha)}{2\alpha}\delta V^T \left[\int_{x_1}^{x_2} N_x^T N_{,x}\, dx\right] V \qquad (5.17)\\
& + \frac{\mu\,(1-2\alpha)}{2\alpha}\delta V^T \left[\int_{x_1}^{x_2} N^T N_{,x}\, dx\right] U \\
& - \frac{\mathrm{i}\mu c_s\,(\alpha-2)}{2\omega\alpha}\delta U^T \left(\int_{x_1}^{x_2} N_{,x}^T N_{,x}\, dx\right) U) \\
& - \frac{\mu\,(1-2\alpha)}{2\alpha}\delta U\, V|_{x_1}^{x_2} + \frac{\mu\,(1-2\alpha)}{2\alpha}\delta V\, U|_{x_1}^{x_2} \\
& + \frac{\mathrm{i}\mu c_s\,(\alpha-2)}{2\omega\alpha}\delta U\, U_{,x}|_{x_1}^{x_2} + \frac{\mathrm{i}\mu c_s\,(1-2\alpha)}{2\omega\alpha^3}\delta V V_{,x}|_{x_1}^{x_2},
\end{aligned}
$$

where n is the number of the half-space elements. Integral terms in the virtual work equation are understood to define finite elements and their stiffness matrix can be calculated and assembled into the global dynamic stiffness matrix of the irregular region by means of standard direct stiffness techniques. The stiffness matrix of a 2-node half-space element has the form

$$\mathbf{K}=\begin{bmatrix}\mathbf{K}_{11} & \mathbf{K}_{12}\\ \mathbf{K}_{12}^{T} & \mathbf{K}_{22}\end{bmatrix}, \tag{5.18}$$

with

$$\mathbf{K}_{11}=\mathrm{i}\omega\rho c_s\int_{x_1}^{x_2}N^TN dx+\frac{\mathrm{i}\mu c_s\left(\alpha-2\right)}{2\omega\alpha}\int_{x_1}^{x_2}N_{,x}^TN_{,x}\,dx, \tag{5.19a}$$

$$\mathbf{K}_{12}=\frac{\mu\left(1-2\alpha\right)}{2\alpha}\int_{x_1}^{x_2}N^TN_{,x}dx-\frac{\mu\left(1-2\alpha\right)}{2\alpha}\int_{x_1}^{x_2}N_{,x}^TN\,dx, \tag{5.19b}$$

$$\mathbf{K}_{22}=\mathrm{i}\omega\rho c_p\int_{x_1}^{x_2}N^TN dx+\frac{\mathrm{i}\mu c_s\left(\alpha-2\right)}{2\omega\alpha^3}\int_{x_1}^{x_2}N_{,x}^TN_{,x}\,dx. \tag{5.19c}$$

The entries of equation (5.18) are determined by integrating the terms over the length of the half-space element in equations (5.19). The first entry in the stiffness matrix for a half-space element is computed and given by

$$\mathbf{K}_{11}=\frac{\mathrm{i}\omega\rho c_s\Delta x}{6}\begin{bmatrix}2 & 1\\ 1 & 2\end{bmatrix}+\frac{\mathrm{i}\mu c_s\left(\alpha-2\right)}{2\omega\alpha\Delta x}\begin{bmatrix}1 & -1\\ -1 & 1\end{bmatrix}. \tag{5.20}$$

Other terms have been obtained in the same way and are assigned additional notations to substitute back into the impedance matrix.

$$\begin{aligned}C_1&=\frac{\mathrm{i}\omega\rho c_s\Delta x}{6}, C_2=\frac{\mathrm{i}\omega\rho c_p\Delta x}{6}, C_3=\frac{\mathrm{i}\mu c_s\left(\alpha-2\right)}{2\omega\alpha\Delta x},\\ C_4&=\frac{\mu\left(1-2\alpha\right)}{2\alpha}, C_5=\frac{\mathrm{i}\mu c_s\left(1-2\alpha\right)}{2\omega\alpha^3\Delta x}.\end{aligned} \tag{5.21}$$

Substituting back into the stiffness matrix leads to

$$\mathbf{K}^{hs}=\begin{bmatrix}2C_1+C_3 & 0 & C_1-C_3 & C_4\\ 0 & 2C_2+C_5 & -C_4 & C_2-C_5\\ C_1-C_3 & -C_4 & 2C_1+C_3 & 0\\ C_4 & C_2-C_5 & 0 & 2C_2+C_5\end{bmatrix}. \tag{5.22}$$

The half-space 2-node element matrix $\mathbf{K}^{hs}$, of dimension 4×4, represents a typical half-space element stiffness matrix. It is a function of the properties of the half-space material, the length of the element and the frequency of the applied load. So far, the semi-infinite extent, far field, of the domain with respect to depth is represented by the impedance matrix of the half-space. Hence, in order to model the unbounded domain, the stiffness matrix of the half-space should be assembled with the irregular region global matrix as they share nodes at the interface between the half-space and the bottom boundary of the irregular region.

5.3.2 Treatment of the regular region

Half-space elements, located beneath the irregular region, are dealt with in section 5.3.1. The bottom node at each lateral boundary has also contribution into both the irregular and the regular regions. Figure 5.4 illustrates the treatment of the regular region over half-space.

If we derive the displacements in equation (5.14) and back substitute them in expressions (5.8) and (5.9) the horizontal and vertical tractions at the half-space and regular region interface are obtained

$$F_x = \mathrm{i}\omega\rho c_s U(y)e^{-\mathrm{i}kx} - \mathrm{i}k\frac{\mu\,(1-2\alpha)}{\alpha}V(y)e^{-\mathrm{i}kx} + k^2\frac{\mathrm{i}\mu c_s\,(\alpha-2)}{2\omega\alpha}U(y)e^{-\mathrm{i}kx}, \tag{5.23}$$

$$F_y = \mathrm{i}\omega\rho c_p V(y)e^{-\mathrm{i}kx} + \mathrm{i}k\frac{\mu\,(1-2\alpha)}{\alpha}U(y)e^{-\mathrm{i}kx} + k^2\frac{\mathrm{i}\mu c_s\,(1-2\alpha)}{2\omega\alpha^3}V(y)e^{-\mathrm{i}kx}, \tag{5.24}$$

where $U(y)$ and $V(y)$ are the mode shapes assuming that the horizontal and vertical displacement fields are described by;

$$u(x,y) = U(y)e^{-\mathrm{i}kx} \qquad \text{and} \qquad v(x,y) = V(y)e^{-\mathrm{i}kx}. \tag{5.25}$$

Let us consider the regular region on the right, at the half-space-last layer interface; ($x = 0$, $y = H$). Expressions (5.23) and (5.24) could be re-arranged in the following form

$$\begin{bmatrix} F_x \\ F_y \end{bmatrix} = \{k^2\frac{\mathrm{i}\mu c_s}{2\omega\alpha^3}\begin{bmatrix} (\alpha-2)\,\alpha^2 & 0 \\ 0 & (1-2\alpha) \end{bmatrix} + \mathrm{i}k\frac{\mu\,(1-2\alpha)}{\alpha}\begin{bmatrix} 0 & -1 \\ 1 & 0 \end{bmatrix} + \begin{bmatrix} \mathrm{i}\omega\rho c_s & 0 \\ 0 & \mathrm{i}\omega\rho c_p \end{bmatrix}\}\begin{bmatrix} U(H) \\ V(H) \end{bmatrix}. \tag{5.26}$$

Expression (5.26) is an algebraic equation in k and it is used to solve the modes of wave propagation of the regular region over half-space to express the contribution of the half-space into the regular region. It is similar to the algebraic equation of the regular region over rigid base derived in section 3.3.3 in Chapter 3.

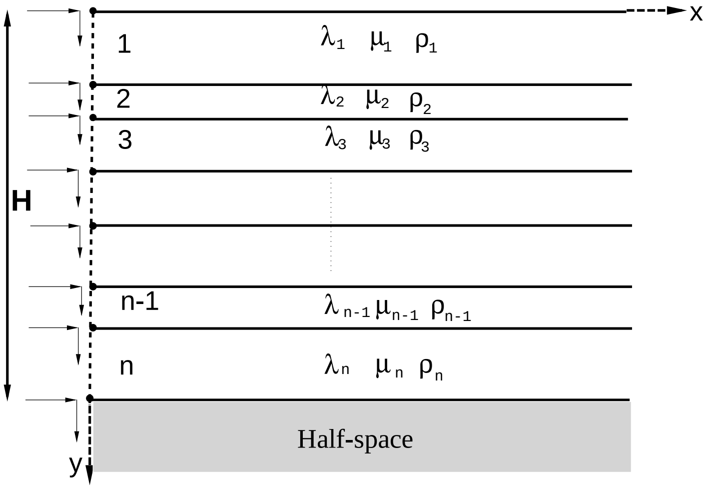

Figure 5.4: Layered region over half-space.

The matrix factors in equation (3.30), which are 4×4, are similar to 2×2 matrices of expression (5.26). A relationship between the tractions and the displacements at the top of the half-space is extracted in equation (5.26). Comparing this equation with an equivalent equation from the regular region over rigid bedrock leads us to deduce the following half-space matrices

$$\mathbf{A}_2^{hs} = \frac{\mathrm{i}\mu c_s}{2\omega\alpha^3}\begin{bmatrix} (\alpha-2)\,\alpha^2 & 0 \\ 0 & (1-2\alpha) \end{bmatrix}, \tag{5.27a}$$

$$\mathbf{A}_1^{hs} = \frac{\mu\,(1-2\alpha)}{\alpha}\begin{bmatrix} 0 & -1 \\ 1 & 0 \end{bmatrix}, \tag{5.27b}$$

$$\mathbf{C}^{hs} = \begin{bmatrix} \mathrm{i}\omega\rho c_s & 0 \\ 0 & \mathrm{i}\omega\rho c_p \end{bmatrix}. \tag{5.27c}$$

These 2×2 matrices reflect the contribution of the corner nodes at the interface of the half-space and the overlain regular regions, into the regular region. Basically, they are associated with the last two degrees of freedom of that node. Assembling previous matrices with the matrices derived in Chapter 3, section 3.3.3 and which represent the contribution of the horizontal layers over rigid bedrock, we obtain the regular region system matrices over half-space. Here, the dimension of the global matrices is $2(n+1)\times 2(n+1)$. In the case of rigid bedrock, the last two rows and columns of the global matrices are omitted due to the base fixity. In the half-space case, we must consider the whole matrix and add the contribution of the half-space into the last two rows and columns. The eigenvalue problem of equation (3.30) is replaced by the following eigenvalue problem

$$\left[k^2\mathbf{A}_2 + \mathrm{i}k\mathbf{A}_1 + \mathbf{C}\right] u_0 = 0, \tag{5.28}$$

where

$$\mathbf{A}_2 = \mathbf{A}_2^* + \mathbf{A}_2^{hs} \quad , \quad \mathbf{A}_1 = \mathbf{A}_1^* + \mathbf{A}_1^{hs} \quad \text{and} \quad \mathbf{C} = \mathbf{A}_\mathbf{0}^* - \omega^2\mathbf{M}_\mathbf{0}^* + \mathbf{C}^{hs}. \tag{5.29}$$

Global matrices $\mathbf{A}_2$, $\mathbf{A}_1$ and $\mathbf{C}$ are $2(n+1)\times 2(n+1)$ matrices. The matrices with the superscript * symbol represent the contribution of the regular region without the contribution of the half-space. The eigenvalue problem of expression (5.28) is of second order. It is reduced to a first order problem with the dimension being doubled to $4(n+1)\times 4(n+1)$. The eigenvalues of interest k_s, $s = 1,..,2n+2$, are stored in the diagonal matrix $\mathbf{H}$ as

$$\mathbf{H} = \begin{bmatrix} k_1 & & \\ & \ddots & \\ & & k_{2n+2} \end{bmatrix}. \tag{5.30}$$

The corresponding eigenmodes u_s^0 are stored in the modal matrix $\mathbf{V}$ columnwise. The displacement vector at the lateral vertical boundary is a linear combination of the $2(n+1)$ eigenvectors corresponding to the $2(n+1)$ eigenvalues

$$\left\{u^G\right\} = \sum_{s=1}^{2n+2} a_s \left\{u_s^0\right\} e^{\left(\mathrm{i}\omega t - k_s x\right)}, \tag{5.31}$$

where $\left\{u_s^0\right\}$ is the eigenvectors and a_s is a vector of dimension $2(n+1)$ which represents the mode shape participation factors. Thus, the displacement field at the right side lateral boundary is expressed as

$$\mathbf{U_R} = \sum_{s=1}^{2n+2} a_s \left\{u_s^0\right\} = a\mathbf{U}. \tag{5.32}$$

Next, the consistent nodal forces of the transmitting boundary conditions of the half-space model are derived as follows. If we consider the last four terms in equation (5.17)

$$\begin{aligned} &- \frac{\mu\,(1-2\alpha)}{2\alpha}\delta U\,V + \frac{\mu\,(1-2\alpha)}{2\alpha}\delta V\,U \\ &+ \frac{\mathrm{i}\mu c_s\,(\alpha-2)}{2\omega\alpha}\delta U\,U_{,x} + \frac{\mathrm{i}\mu c_s\,(1-2\alpha)}{2\omega\alpha^3}\delta V\,V_{,x}, \end{aligned} \tag{5.33}$$

the displacements corresponding to the last node are

$$U_{n+1} = u\,(0,H) = \sum_{s=1}^{2n+2} u_{2n+1}^s\, a_s \quad \text{and} \quad V_{n+1} = v\,(0,H) = \sum_{s=1}^{2n+2} v_{2n+2}^s\, a_s, \tag{5.34}$$

and hence

$$U_{,x}(0,H) = -\mathrm{i}ka_{2n+1}\,e^{\mathrm{i}(\omega t - k_{2n+1}x)} \quad \text{and} \quad V_{,x}(0,H) = -\mathrm{i}ka_{2n+2}\,e^{\mathrm{i}(\omega t - k_{2n+2}x)}. \tag{5.35}$$

Substituting back into the equations (5.33) yields into

$$\begin{aligned} W &= -\delta U_{n+1}\frac{\mu(1-2\alpha)}{2\alpha}V_{n+1} + \delta V_{n+1}\frac{\mu(1-2\alpha)}{2\alpha}U_{n+1} \\ &- \delta U_{n+1}\left(\mathrm{ik}\frac{\mathrm{i}\mu c_s(\alpha-2)}{2\omega\alpha}\right)U_{n+1} - \delta V_{n+1}\left(\mathrm{i}k\frac{\mathrm{i}\mu c_s(1-2\alpha)}{2\omega\alpha^3}\right)V_{n+1}. \end{aligned} \tag{5.36}$$

The nodal forces acting at the lateral vertical boundary of the right side of the domain are expressed as

$$\mathbf{F}_R^{hs} = \left[\mathrm{i}k\mathbf{A}_2^{hs} + \mathbf{A}_3^{hs}\right]\{u\}_{x=0}^{y=H}, \tag{5.37}$$

where $\mathbf{A}_2^{hs}$ being the matrix which was given in expression (5.27a) and $\mathbf{A}_3^{hs}$ is a 2×2 matrix given by

$$\mathbf{A}_3^{hs} = \frac{\mu(1-2\alpha)}{2\alpha}\begin{bmatrix} 0 & 1 \\ -1 & 0 \end{bmatrix}. \tag{5.38}$$

Matrix $\mathbf{A}_1^{hs}$ ia a skew symmetric matrix and obeys the relationship $\mathbf{A}_1^{hs}=\left[\mathbf{A}_3^{hs}\right]^T$-$\left[\mathbf{A}_3^{hs}\right]$. The forces and displacements associated with the regular region-half-space interface are therefore expressed as

$$\mathbf{F}_R^{hs} = \left\{\begin{array}{c} \mathbf{F}_{x(n+1)} \\ \mathbf{F}_{y(n+1)} \end{array}\right\} \qquad \text{and} \qquad \mathbf{u}_R^{hs} = \left\{\begin{array}{c} \mathbf{U}_{n+1} \\ \mathbf{V}_{n+1} \end{array}\right\}. \tag{5.39}$$

Half-space matrices $\mathbf{A}_1^{hs}$, $\mathbf{A}_2^{hs}$, $\mathbf{A}_3^{hs}$ and $\mathbf{C}^{hs}$ should be assembled into the matrices of the regular region $\mathbf{A}_1^*$, $\mathbf{A}_2^*$, $\mathbf{A}_3^*$ and $\mathbf{C}^*$ to form the global matrices. The assembling of these matrices is depicted in Figure 5.5. Equation (5.37) has the same form of equation (3.37) for the regular region over rigid bedrock. Assembling the matrices of these two equations produces the nodal forces vector at the right lateral boundary of the form

$$\mathbf{F_R} = \left[\mathrm{i}k\mathbf{A}_2\mathbf{VHV}^{-1} + \mathbf{A}_3\right]\{u\}_{x=0}^{y=H}, \tag{5.40}$$

where $\mathbf{F_R}$ represents the global forces at the right lateral boundary, $\mathbf{A}_2$ and $\mathbf{A}_3$ represent the global matrices of the regular region over half-space. The dimensions of these matrices are also $2(n+1)\times 2(n+1)$.

The modal matrix, columnwise matrix of dimension of $2(n+1)\times 2(n+1)$, is given by

$$\mathbf{V} = \begin{bmatrix} \mathbf{U}_1 & \dots & \mathbf{U}_{2n+2} \end{bmatrix}. \tag{5.41}$$

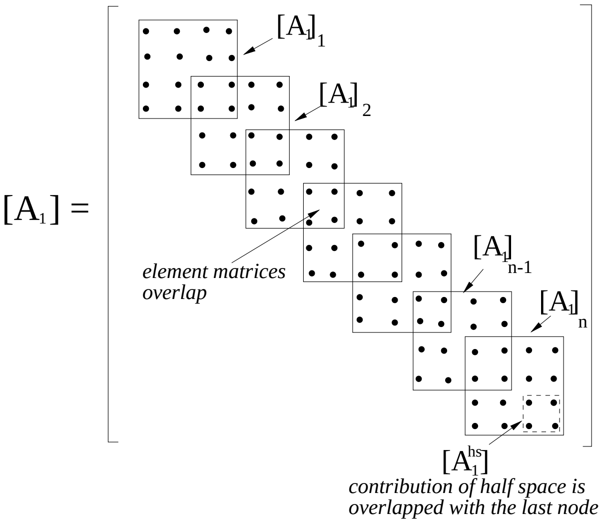

Figure 5.5: Global matrices structure for half-space model.

The dynamic stiffness matrix **R**, which is obtained from expression (5.40), relates the nodal forces to the nodal displacements at the specified boundary. Hence, the nodal forces applied at the right side regular region has the following form

$$\mathbf{F_R} = -\mathbf{R}\mathbf{U_R} \qquad \text{where} \qquad \mathbf{R} = \mathrm{i}\mathbf{A_2}\mathbf{V}\mathbf{H}\mathbf{V}^{-\mathbf{1}} + \mathbf{A_3}, \tag{5.42}$$

where $\mathbf{U_R}$ is the nodal displacement vector of the regular region on the right side boundary. The left side boundary is treated in the same manner as for the right side lateral boundary. The nodal forces of the left lateral boundary is expressed as

$$\mathbf{F_L} = -\mathbf{L}\mathbf{U_L} \quad \text{where} \quad \mathbf{L} = -\mathrm{i}\mathbf{A}_2\mathbf{V}^{'}\mathbf{H}^{'}\mathbf{V}^{'-1} - \mathbf{A}_3, \tag{5.43}$$

where **L** is the dynamic stiffness matrix of the left regular region and it relates the nodal forces to the nodal displacements. In such a way, the dynamic stiffness matrices of the regular regions are obtained and the unboundedness of the domain is modelled.

5.3.3 The half-space finite-element model

Figure 5.6 shows a schematic diagram of a soil medium overlaying half-space. For this model, the impedance matrix of the half space elements, expressed in equation (5.22), is assembled to the global dynamic stiffness matrix of the irregular region. The effect of the two regular regions is modelled by the consistent transmitting boundaries, obtained from expressions (5.42) and (5.43), in terms of nodal forces applied on the lateral boundaries of the irregular region. As these forces are functions of the nodal displacements of the lateral boundaries, which are unknown, the matrices **R** and **L** are also assembled to the global dynamic stiffness matrix of the irregular region. The finite element final system to solve is the expressed by

$$\left[\mathbf{K}-\omega^2\mathbf{M}+\mathbf{R}+\mathbf{L}\right]\mathbf{u}_0=\mathbf{F_0}. \tag{5.44}$$

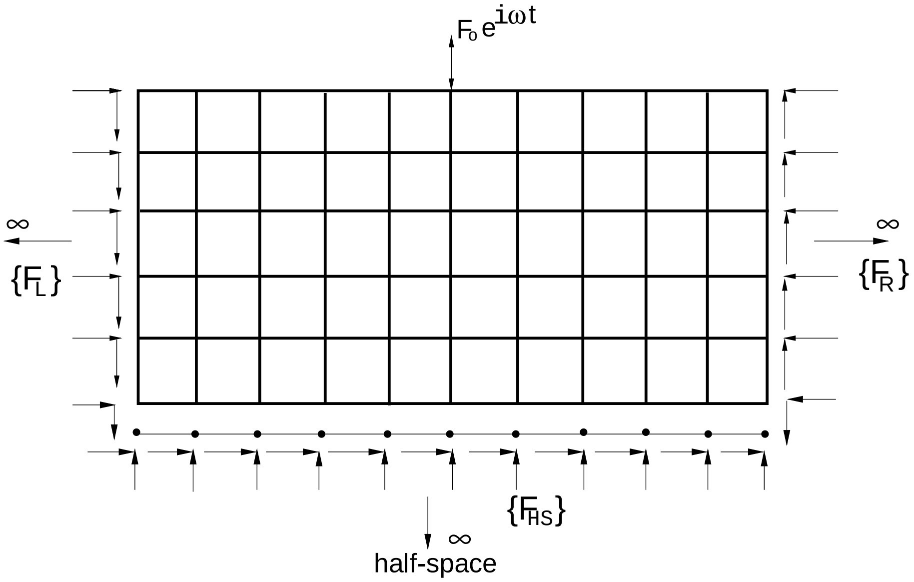

Figure 5.6: The finite element half-space model.

This system is linear and a direct solver is used to compute the nodal displacements, in the same way followed for the system (3.42) corresponding to a soil medium overlaying bedrock. The same methodology is also followed for the post-processing of the results.

5.4 Concluding remarks

In this chapter, the PBC is presented for modelling the semi-infinite extent of a soil domain with respect to depth. This is based on the expansion of the half-space stiffness matrix into Taylor's series, for which only three terms are retained. As a result, a second order matrix with respect to the wavenumber is obtained leading to the stiffness matrices of the half space elements, which are assembled into the global matrix of the irregular region, while the contribution of the corner elements of the half-space are involved in the eigenvalue problem for the consistent transmitting boundaries.

The ability of this TLM-PBC coupled model to simulate wave propagation in half-space soil media is investigated in the next chapter, where the use of a buffer layer in introduced and its effect on the performance of the model also analysed.

Chapter 6

Wave propagation in half-space soil media: validation & applications

6.1 Introduction

This chapter is dedicated to the validation of the numerical model developed in Chapter 5, for simulating wave propagation in half-space soil media. In this model, the TLM is coupled with the PBC to allow the waves to propagate away to infinity laterally and with respect to depth. The concept of the buffer layer is introduced in the model and its performance is investigated through numerical analysis. Applications dealt with including harmonic vibration of rigid surface foundation overlaying homogenous or layered half-space media and ground vibration reduction using wave barriers.

6.2 Wave propagation in homogenous half-space

Simulation of wave propagation in a homogenous half-space is performed in the following sections where the coupled model is first validated. The same rational approach, adopted in Chapter 4 by extending the length of the domain, is used here for extending the depth and the length of the domain, for which the relative error is computed.

6.2.1 Validation test example

The combined TLM-PBC half-space model is validated against the analytical solution, through a specific test example obtained by personal communication with Jones [104]. The analytical solution is based on coupling the Green's function of a homogenous layer and a homogenous half-space. The author has investigated in his PhD thesis the effect of an inclined soil layer over half-space from interior loads after validation of the method against surface loading. Hyperelements were used in his analysis.

In this numerical test, a homogenous half-space domain has the following properties; density of 1700kg/m^3, elasticity modulus of 100MPa, Poisson's ratio of 0.3 and a damping coefficient of 5% is used. A harmonic load of 1N is applied at the soil surface with a frequency of 25Hz. The soil domain is truncated at $3\lambda_R$ in depth and $10\lambda_R$ in length with the assumption that the soil domain extends to infinity in both depth and lateral directions with the same properties. The horizontal and vertical displacements at the surface of the domain are computed and plotted in Figure 6.1. The results obtained from the presented TLM-PBC are in very good agreement with the analytical and numerical results provided by reference [104]. Minor differences appear between the curves but overall the results are very similar.

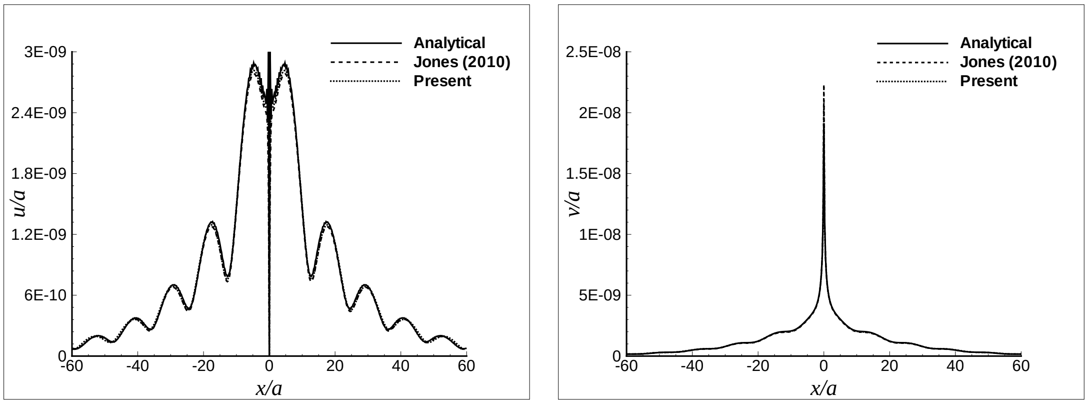

Figure 6.1: Validation of wave propagation in homogenous half-space.

Next, the effect of the depth of the soil model is studied and the efficiency of the coupled TLM-PBC is investigated. A minimum practical depth of the half-space model will be proposed based on the numerical results.

6.2.2 Effect of the half-space model depth

Jones [104] indicated that the minimum depth of the soil layer over the half-space should be $5\lambda_S$ in order to get convergent results towards the analytical solution. As the analytical solution is not available to us, the depth of the soil layer is increased from $1\lambda_R$ to $5\lambda_R$ and the relative error of the surface displacements related to two successive depths is estimated. A homogeneous half-space is taken in this case by considering the same material properties used in section 6.2.1. A harmonic load of 1kN in magnitude is applied at the surface of the domain with a frequency of 20Hz. Figures 6.2 and 6.3 show, respectively, the surface vertical and horizontal displacements with their corresponding errors for the homogeneous soil domain when varying its depth.

The results show that the error percentage is around $3-3.5\%$ in the case of $1\lambda_R$ and $2\lambda_R$ depths. Increasing the depth to $3\lambda_R$ reduces the error with the maximum difference, when compared to

$2\lambda_R$, is about 0.5% for the horizontal displacement. However, the relative error percentage is decreased dramatically to less than 0.15% and 0.1% for $4\lambda_R$ and $5\lambda_R$ depths. It is obvious that a depth of $2\lambda_R$ for the soil domain to represent a half-space is already satisfactory. If one seeks very accurate results for simulating wave propagation in homogenous half-space, the soil layer depth may be taken higher, > $4\lambda_R$. However, as the depth of $2\lambda_R$ produced acceptable differences, from an engineering point of view, it is retained here to represent the half-space model. It is worth indicating that the depth of $2\lambda_R$ of the half-space is around $1\lambda_P$ for the assumed material properties but this may not be always the case when changing the material properties. This is due to the dependance of wavelengths on Poisson's ratio. In the following, λ_P will be used as a measure of the depth as it was used in other references such as [66], for the sake of comparison.

The justification of high error percentage associated with shallow depths, $1\lambda_R$, of the homogenous half-space is as follows. It is known that the Rayleigh wave carries out most of the energy compared to shear and pressure waves. Therefore, if the half-space is not deep enough in such a way that Rayleigh waves hit the paraxial boundaries, spurious waves will reflect back. Now, if the depth of the domain is large enough to prevent Rayleigh waves from approaching the PB, body waves will travel deeper and might hit the boundary. Again, reflections of body waves may lead to spurious reflections in the domain. Therefore, the location of the paraxial boundaries should be deep enough to prevent body waves from reflecting. As the pressure wave has the longest wavelength, the depth of the homogenous half-space will be expressed in terms of its wavelength rather than Rayleigh wavelength. These two wavelengths and their ratio are largely affected by Poisson's ratio. For example, if we consider the two extreme values of Poisson's ratio; 0.01 and 0.49, for any material properties the ratio of the pressure and the Rayleigh wavelengths varies from 1.6 to 7.9, respectively, while this ratio is around 2 for the case of Poisson's ratio of 0.3. This indicates that expressing the depth in terms of the Rayleigh wavelength might not be appropriate as it will underestimate the depth associated with values of Poisson's ratio more than 0.35. In other words, if the depth is expressed in terms of the Rayleigh wavelength, $2\lambda_R$ is sufficient for Poisson's ratios less than 0.3. For Poisson's ratios greater than 0.3, the ratio $\frac{\lambda_P}{2\lambda_R} > 1$ and therefore $2\lambda_R$ will not be enough. A thickness of $5\lambda_S$ is recommended in reference [104] to be considered beneath the load, which was applied within the half-space and not at the surface. If we consider the depth to be around $5\lambda_S$, as proposed in reference [104], the ratio of $\frac{\lambda_P}{5\lambda_S} > 1$ for Poisson's ratios greater than 0.48 and again it is not deep enough to absorb the propagating waves towards the paraxial boundaries. It is worth noting that the thickness of $5\lambda_S$ provided in the previous reference is equivalent to $5\lambda_S$ for the used Poisson's ratio of 0.44. In summary, the depth is next expressed in terms of the pressure wavelength to avoid the likely effect associated with Poisson's ratio.

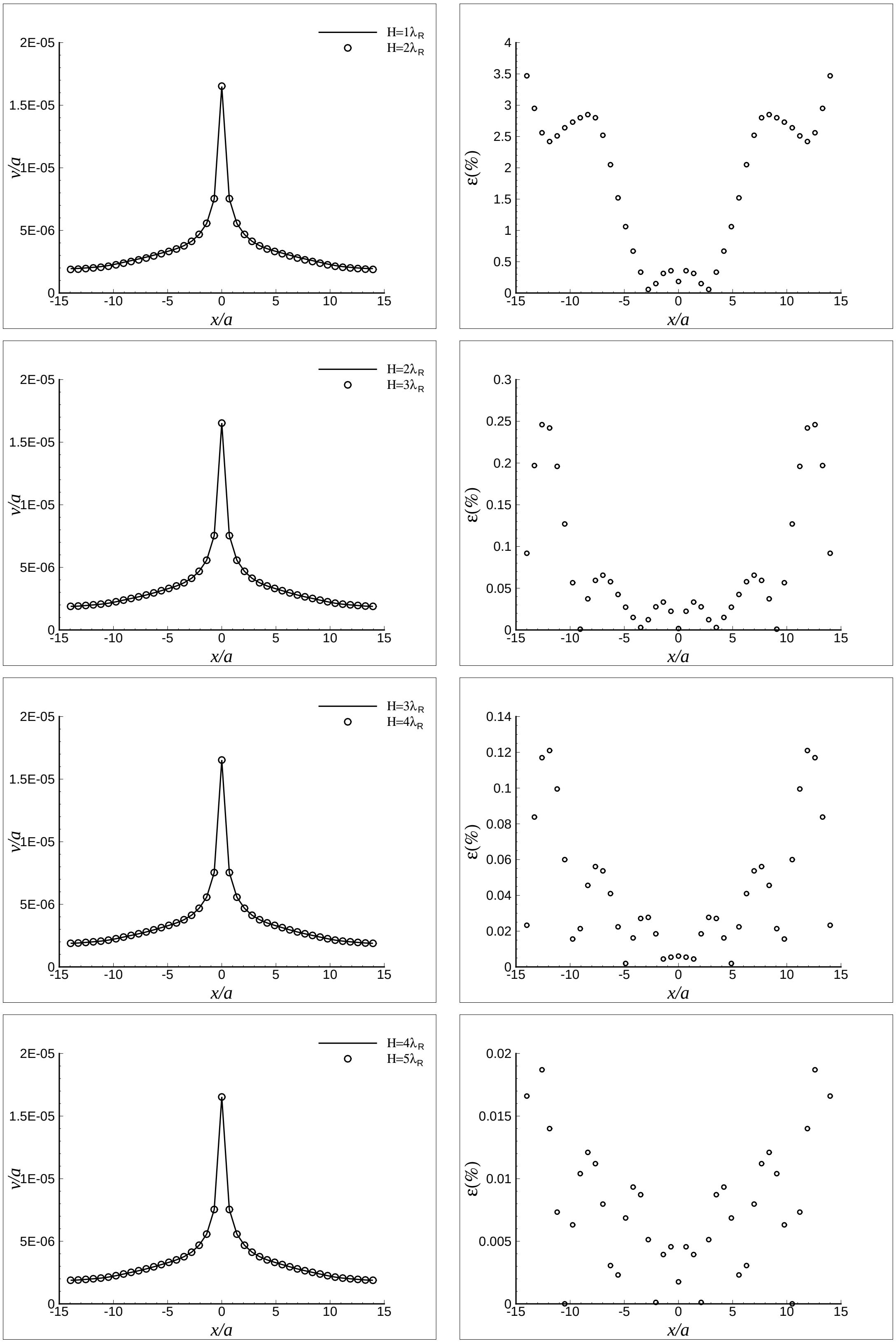

Figure 6.2: Effect of half-space depth: vertical surface displacements and associated relative errors.

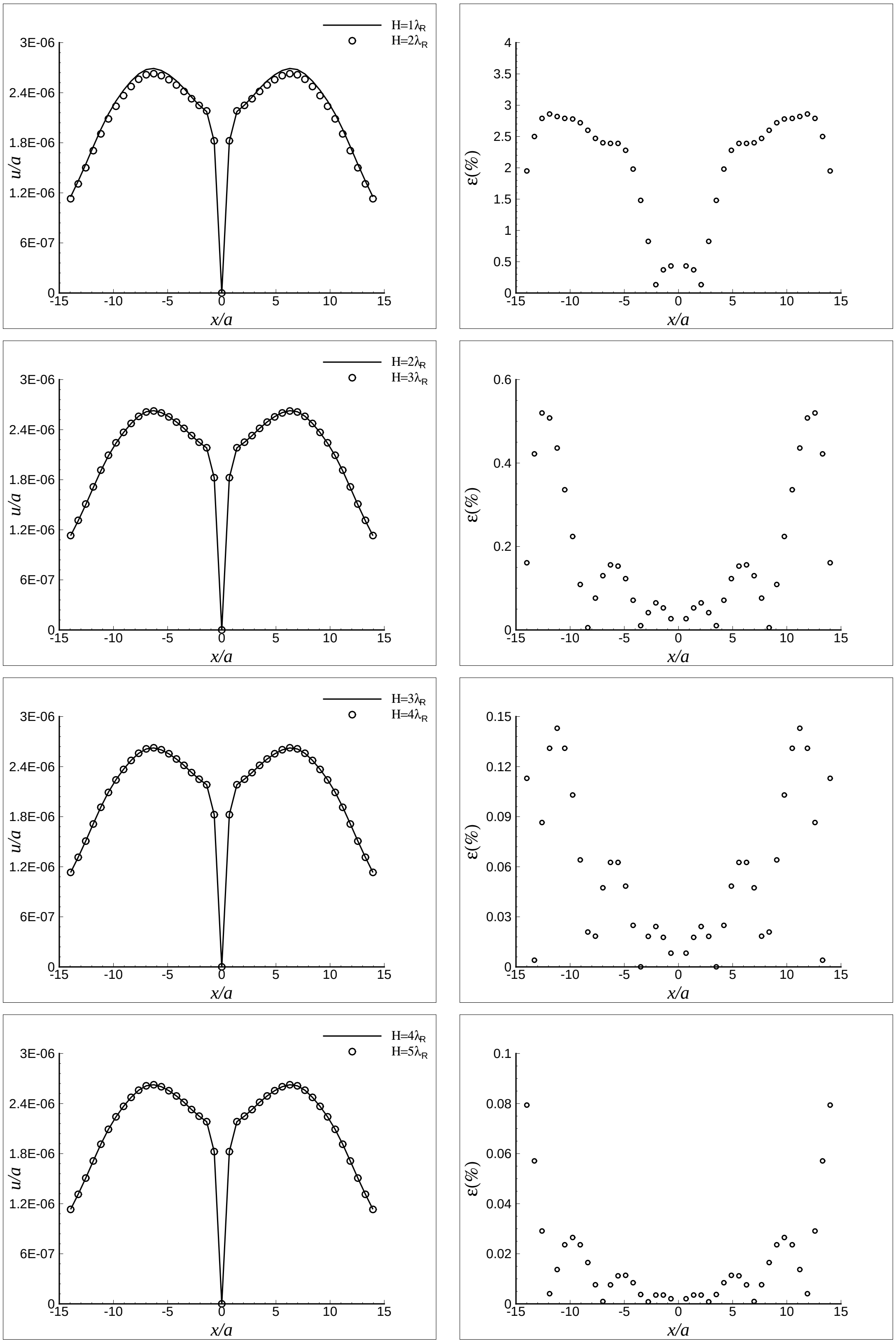

Figure 6.3: Effect of half-space depth: horizontal surface displacements and associated relative errors.

6.2.3 Effect of the model lateral extent

The performance of the half-space finite element model is examined when extending the lateral boundaries of the computational domain, in the same way followed for the soil layer over rigid bedrock in section 4.2. The half-space material properties are the same used in the previous section. The depth of the domain is maintained at $2\lambda_R$, which is equivalent to $1\lambda_P$ for this specific example, and the length is extended from $2\lambda_R$ to $10\lambda_R$. A 1kN harmonic load with 20Hz frequency is applied at the surface of the domain. Surface displacements are plotted and compared for each two successive domain lengths. Figures 6.4 and 6.5 show the vertical and horizontal displacements at the surface with their relative errors when increasing the domain length. The relative error does not exceed 0.5% and 1% for the vertical and horizontal displacements, respectively. This confirms again the good performance of the combined TLM-PBC model to simulate wave propagation in half-space soil media.

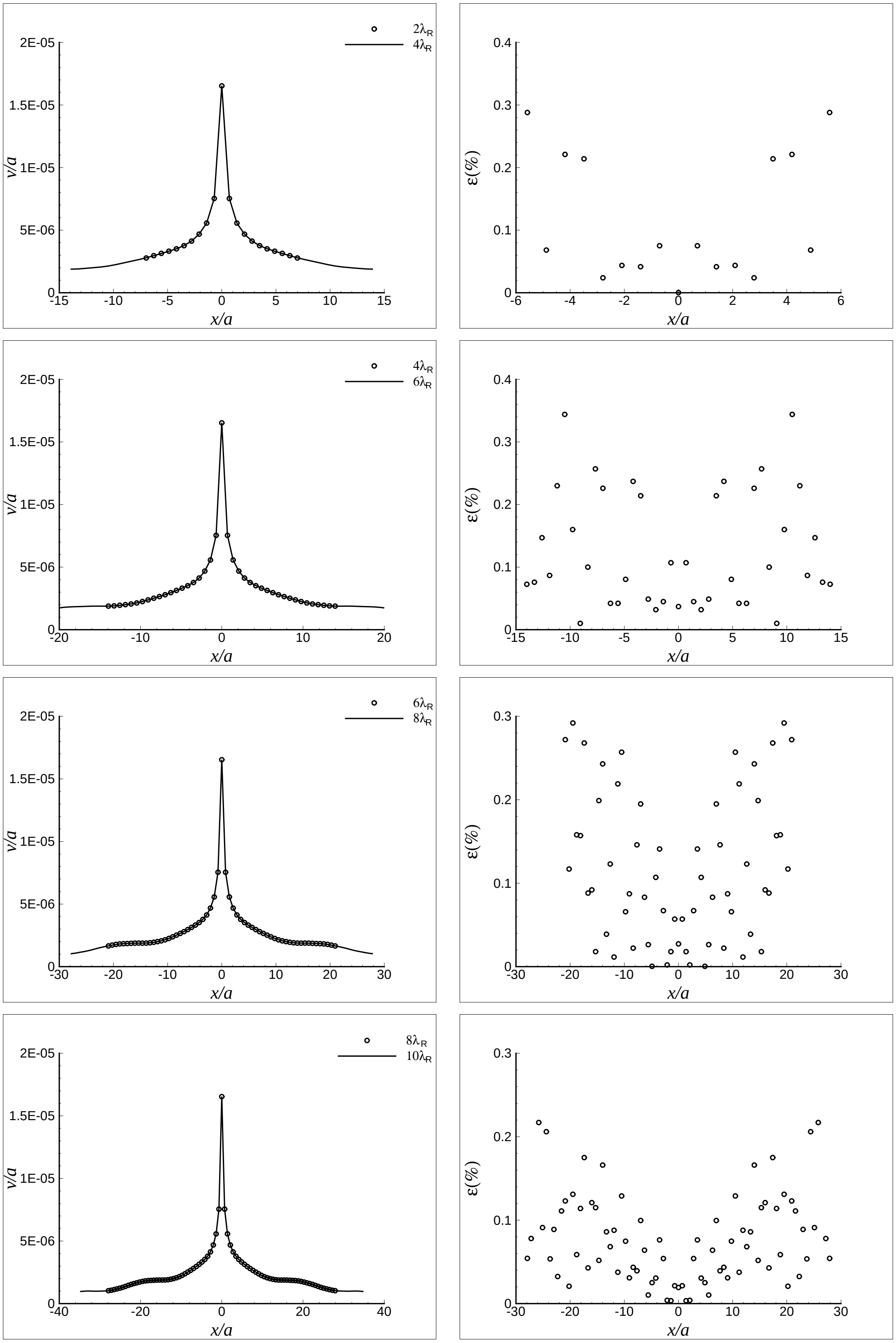

Figure 6.4: Vertical surface displacements and associated relative errors.

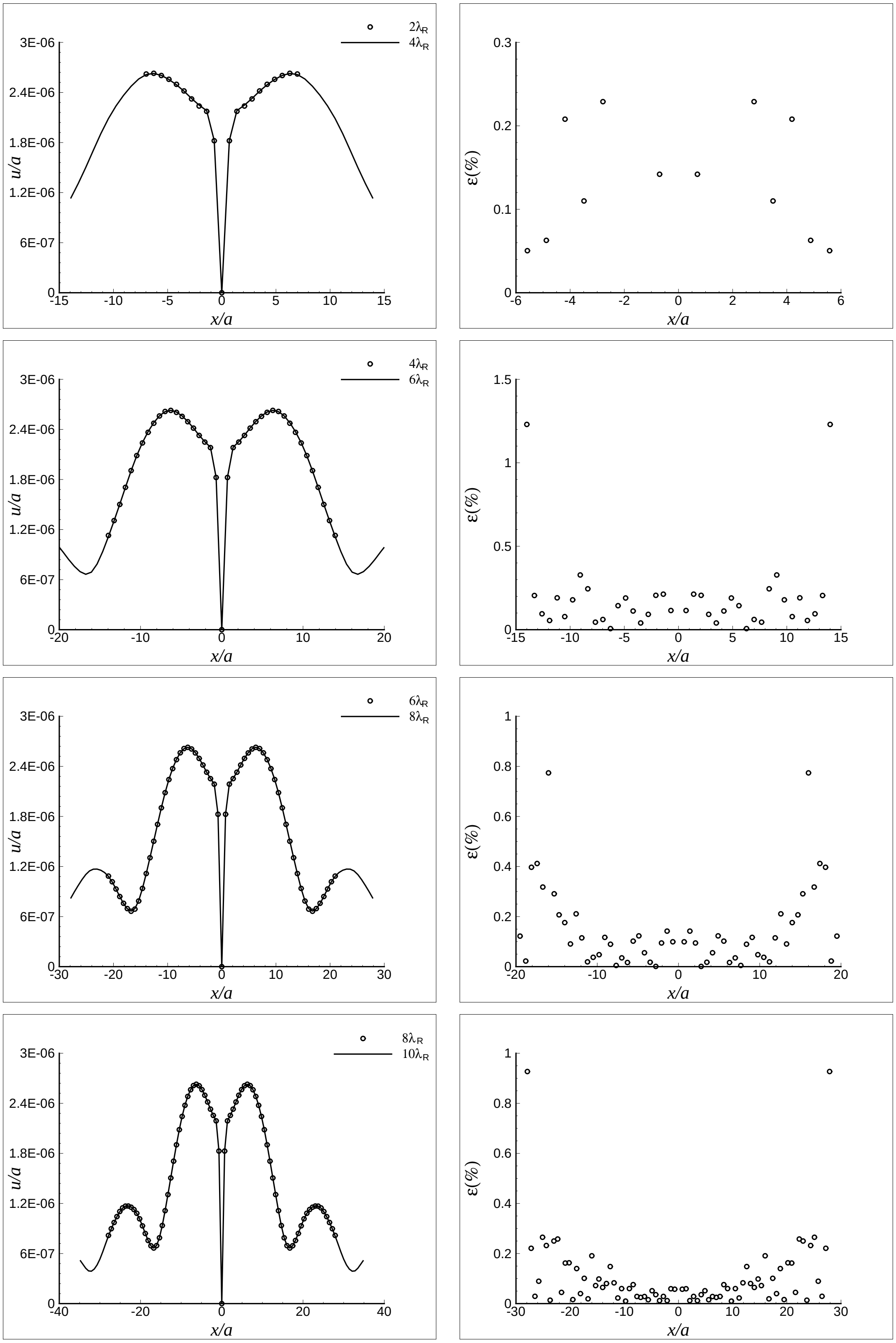

Figure 6.5: Horizontal surface displacements and associated relative errors.

6.3 Wave propagation in layered half-space

The homogenous half-space model, considered in section 6.2, could be of engineering interest. But, in general, layered half-space media are even more interesting. Next, the coupled TLM-PBC finite element model is numerically assessed to check its validity in simulating wave propagation in half-space layered media. Moreover, the concept of "buffer layer" will be introduced and used to improve the performance of the coupled model.

For wave propagation modelling in layered half-space media, Cohen [64] proposed introducing an interface element between the interior region and the paraxial boundary, within a FDM approach. Maeda and Kausel [111] investigated the accuracy of the paraxial boundaries in the case of anti-plane shear. They recommended the introduction of a buffer layer between the irregular region and the half-space with a minimum thickness of $0.5\lambda_S$ to obtain accurate results. The concept of adding a buffer layer was first introduced by Seale [65]. Its influence on the approximated impedance matrix was investigated by Park [66], where the thickness of the buffer layer was considered as a function of the pressure wavelength. A comparison between the approximated and the exact impedance matrix was also carried out. Next the dynamic behaviour of a soil layer overlaying half-space will be investigated by looking at the displacements at the surface as well as the soil-half-space interface, when a buffer layer is introduced.

The previously mentioned authors of references [65, 66] used the exact stiffness matrix to model the buffer layer, while in this work it is modelled by the FEM in which it is treated as part of the irregular region. For the sake of this study, a parameter γ is introduced. It represents the buffer layer thickness with respect to the pressure wavelength λ_P in the half-space.

6.3.1 Soil layer over half-space: $H_{lay} = 0.5\lambda_R$

A soil layer with a unit shear modulus and Poisson's ratio of 0.25 is considered to overlay a half-space with Poisson's ratio of 0.3 such that $c_{s_{hs}} = \sqrt{3}c_s$. Both the soil layer and half-space have 5% damping ratio. Let us consider an external excitation of 1Hz is applied at the surface. The length of the domain is taken to be $10\lambda_R$ and the depth of the soil layer is $0.5\lambda_R$. For generalisation, the depth of the model is increased also to $1\lambda_R$ in section 6.3.2. It is worth mentioning here that, in the first case, the depth of the model is very close to the first critical depth, if the soil layer was over rigid bedrock, but it is higher in the second model. In the following analysis, the PBC are implemented at the base of the model and the consistent transmitting boundaries are used on the lateral boundaries of the model.

To achieve a good discretisation level, each Rayleigh wavelength is meshed into 10 elements. Figures 6.6 to 6.9 show the displacements, with their relative errors, at the surface and at the soil-half-space interface, respectively, with $\gamma = 0$ and $\gamma \neq 0$. It is obvious from the results that the presence of the buffer layer affects the displacements even at low values of γ. Indeed as γ increases, the displacements converge towards those of what is believed corresponding to the half-space model. Introducing a buffer layer, even if it is of low thickness such as $0.11\lambda_P$, makes the solution follow those of greater thicknesses. High discrepancy is found between the displacements when comparing the case of $\gamma = 0$ and $\gamma = 0.11$, this case is not included in the following figures. However, the difference is reduced dramatically when comparing the displacements in the case of $\gamma = 0.11$ and $\gamma = 0.25$. Very similar results results are obtained when increasing the thickness of the buffer layer and the error is significantly reduced. All discussions are made for both surface and soil-half-space interface displacements. Good results are found for buffer layer thickness of $0.5\lambda_P$ where the error percentage is less than 5%. More precise results could be obtained if we increase the thickness, for example the error percentage is less than 0.5% for the case of thickness $1\lambda_P$. It is also noticed that the error percentage is slightly higher near the lateral boundaries of the model.

As it is clearly shown, the use of PBC does not allow to model layered half-space media and that a buffer layer must be used between the soil layer and the half-space. To conclude, a buffer layer of $0.5\lambda_P$ thickness leads to good results and if better accuracy is sought it could be increased to $1\lambda_P$.

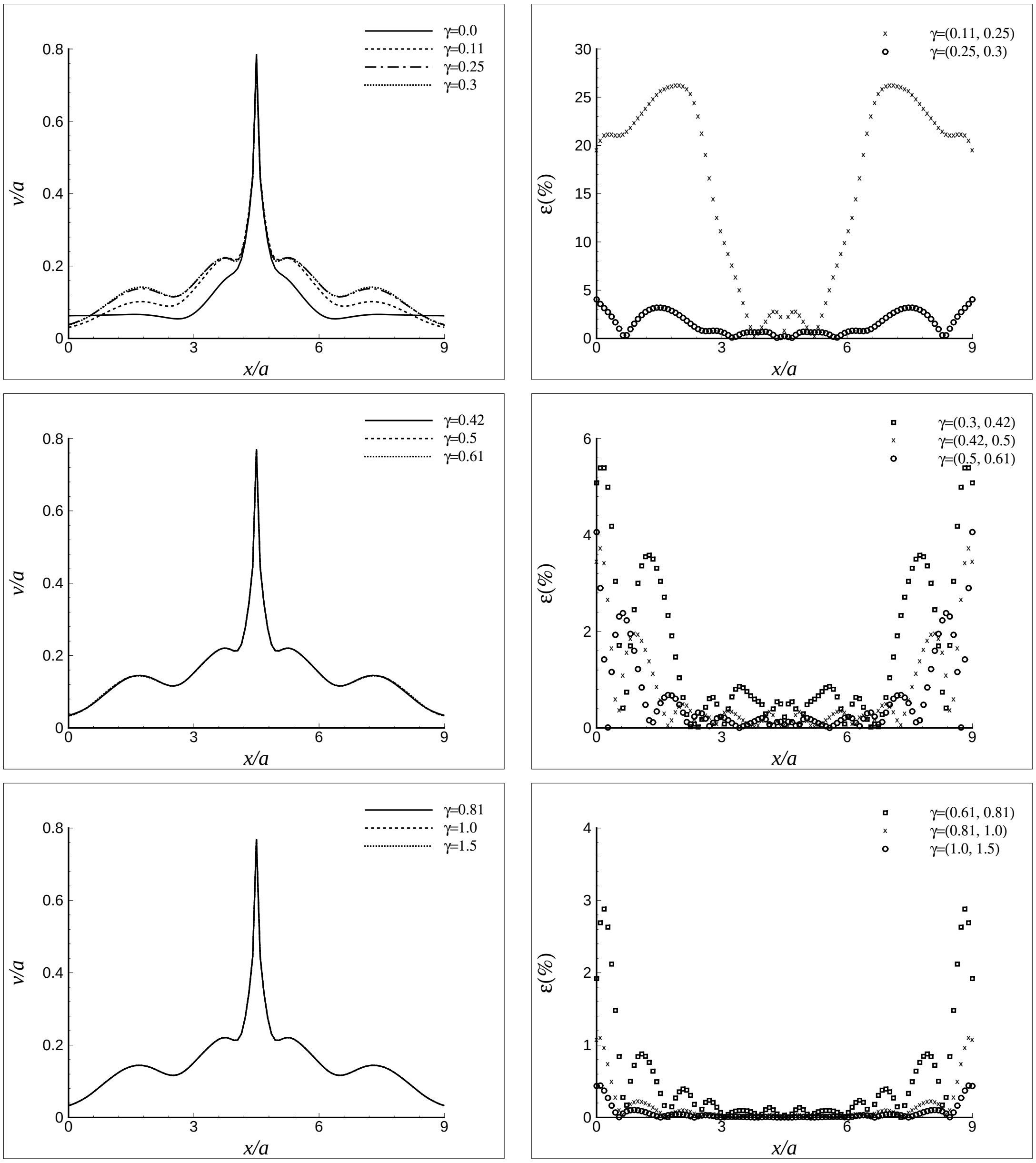

Figure 6.6: Effect of buffer layer thickness on vertical surface displacements: $H_{lay} = 0.5\lambda_R$.

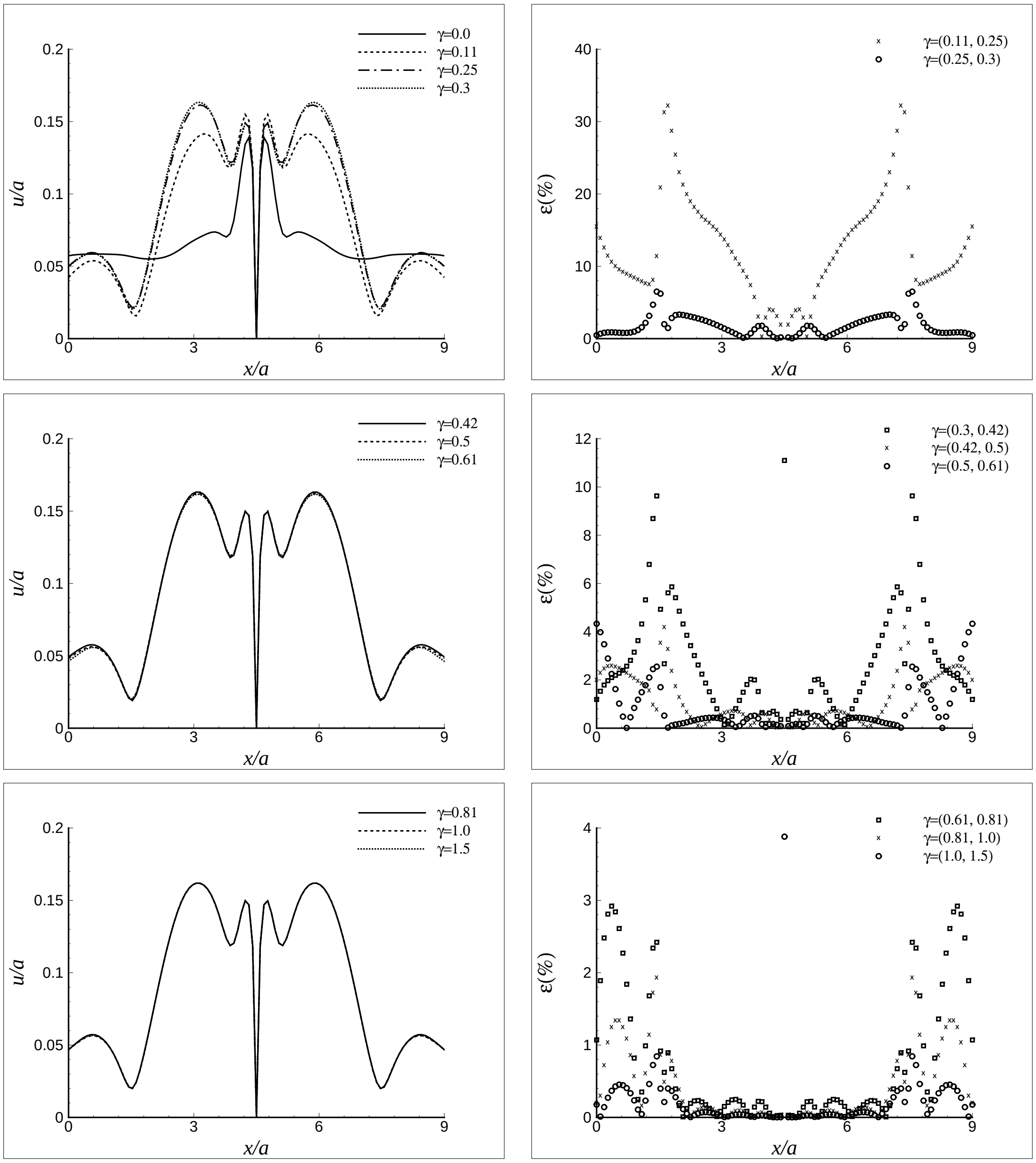

Figure 6.7: Effect of buffer layer thickness on horizontal surface displacements: $H_{lay} = 0.5\lambda_R$.

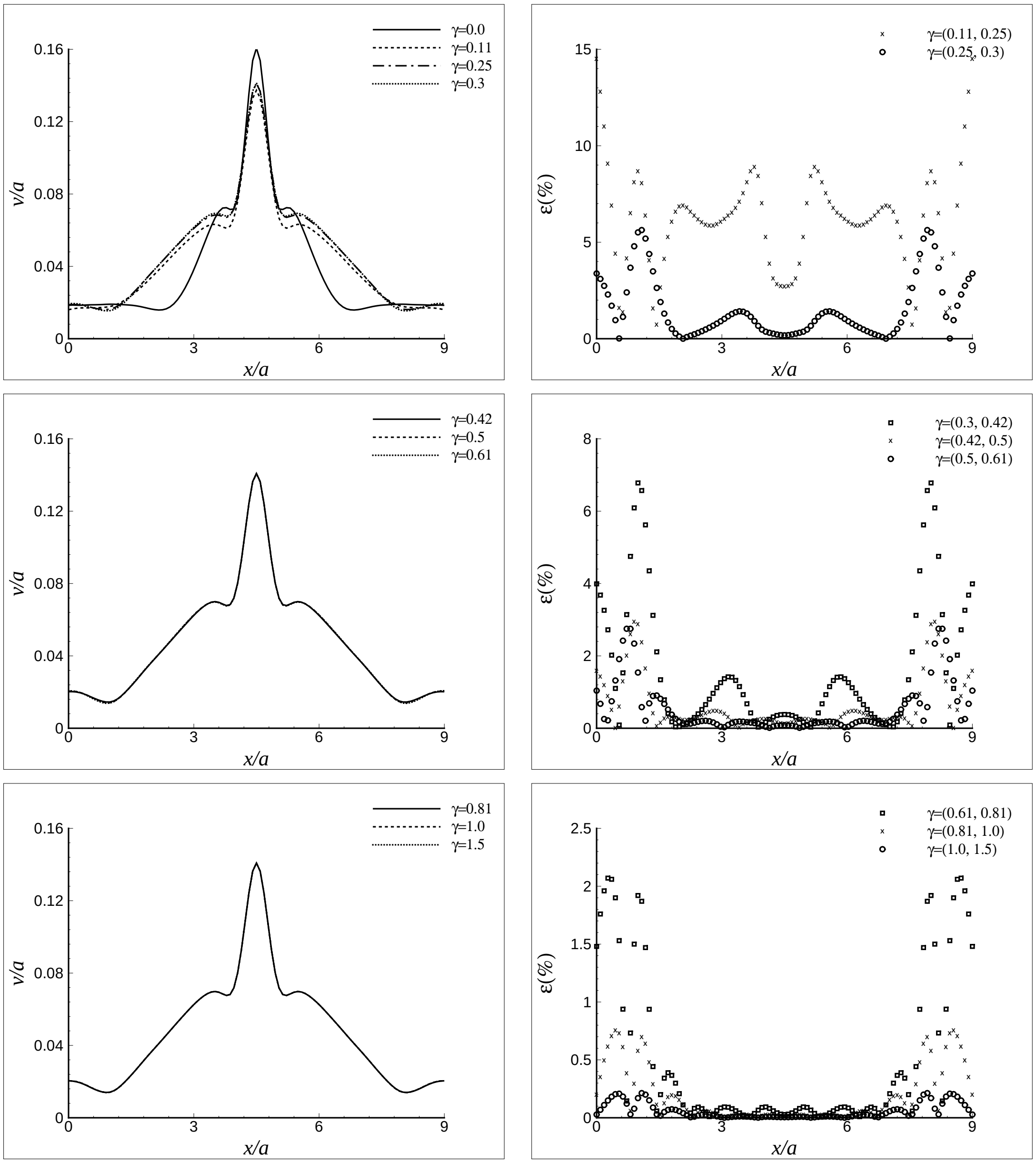

Figure 6.8: Effect of buffer layer thickness on vertical displacements at the soil-half-space interface: $H_{lay} = 0.5\lambda_R$.

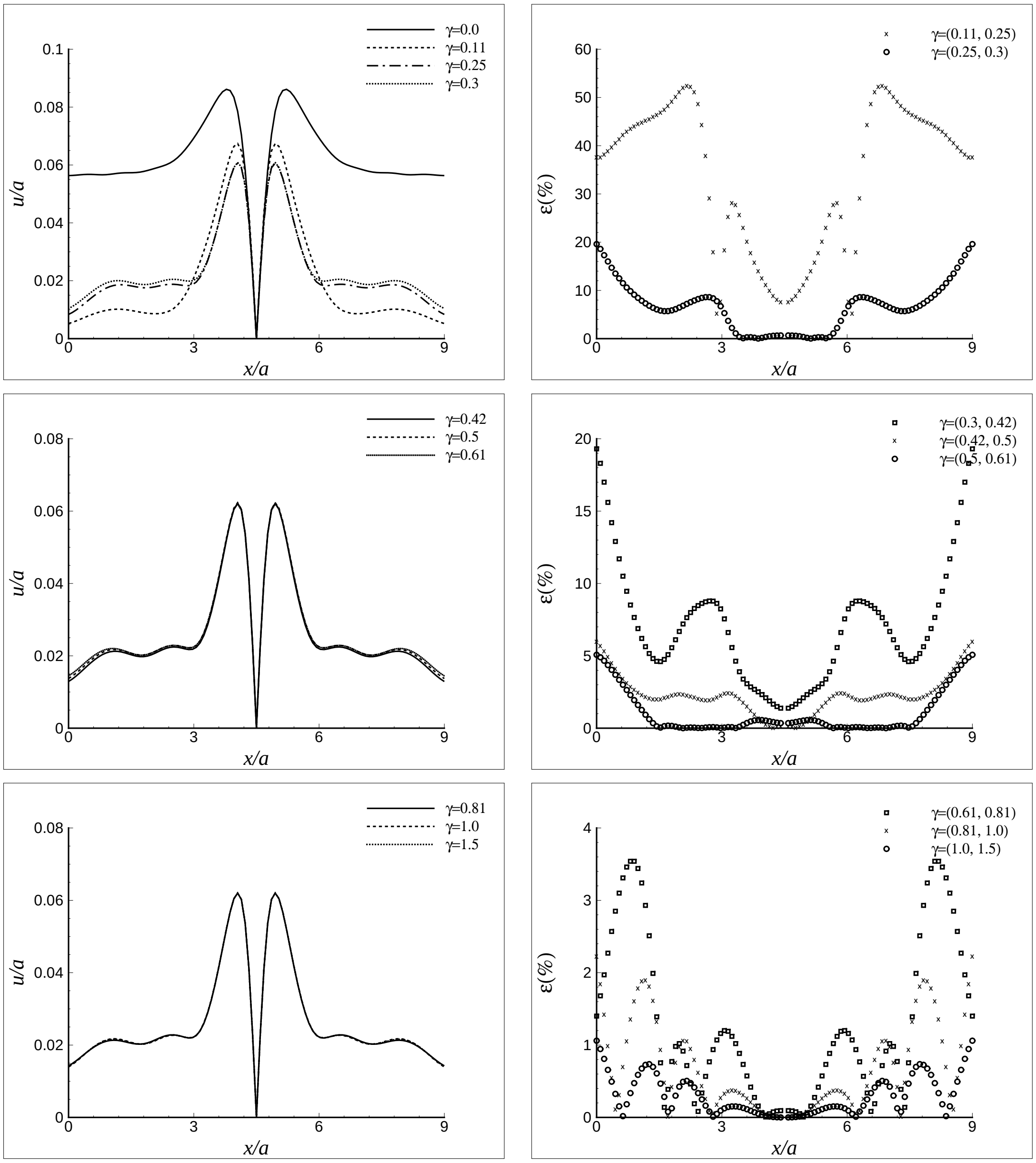

Figure 6.9: Effect of buffer layer thickness on horizontal displacements at the soil-half-space interface: $H_{lay} = 0.5\lambda_R$.

6.3.2 Soil layer over half-space: $H_{lay} = \lambda_R$

In this case, the soil layer depth is increased to $1\lambda_R$ with same material properties as in the previous analysis. This depth exceeds the critical depth, when comparing with soil layer over rigid bedrock.

Figures 6.10 to 6.13 summarise the numerical results for the current analysis, as was previously done. They show very similar trend to the case of $H_{lay} = 0.5\lambda_R$. The vertical and horizontal displacements at the surface and at the soil-half-space interface are in good agreement in the case of truncating the half-space at $0.5\lambda_P$ with the maximum relative error being around 5%. Again, more accurate results are obtained when increasing the buffer layer thickness to $1\lambda_P$. These two cases show that no matter what is the depth of the soil layer, a buffer layer is required to reduce the reflections associated to the paraxial boundaries. The results confirm that a minimum thickness of the buffer layer of $0.5\lambda_P$ is sufficient to obtain good results. The performance of the coupled model significantly improved by adding a buffer layer. In fact, this comes to an additional computational cost of the analysis due to the increase in the number of elements, in the irregular region, and the number of sub-layers, in the regular lateral regions, in the model. The effectiveness of the buffer layer will be further examined in the next section by considering applications related to rigid surface foundations subjected to harmonic vibration and surface vibration reduction by wave barriers.

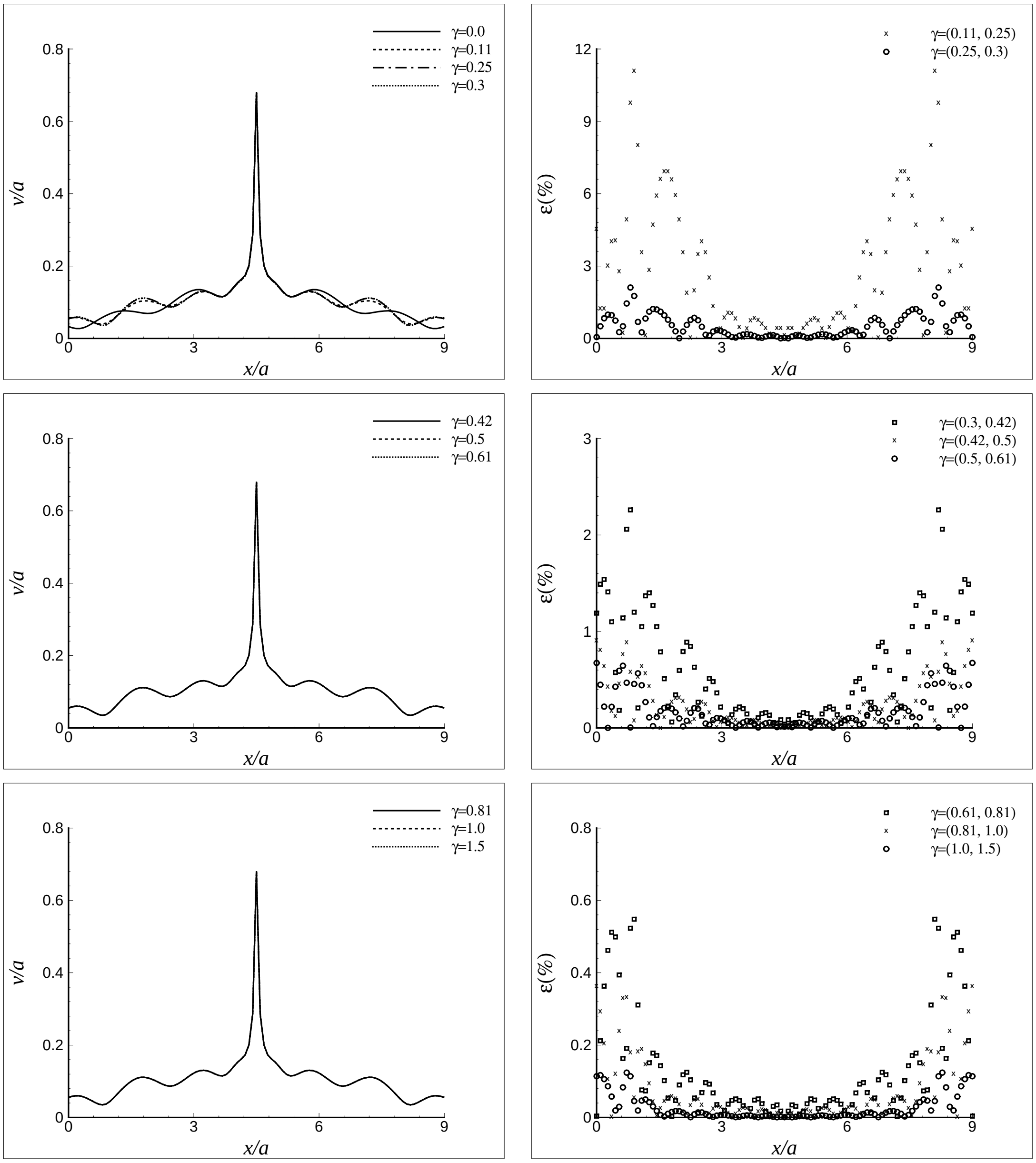

Figure 6.10: Effect of buffer layer thickness on vertical surface displacements: $H_{lay} = \lambda_R$.

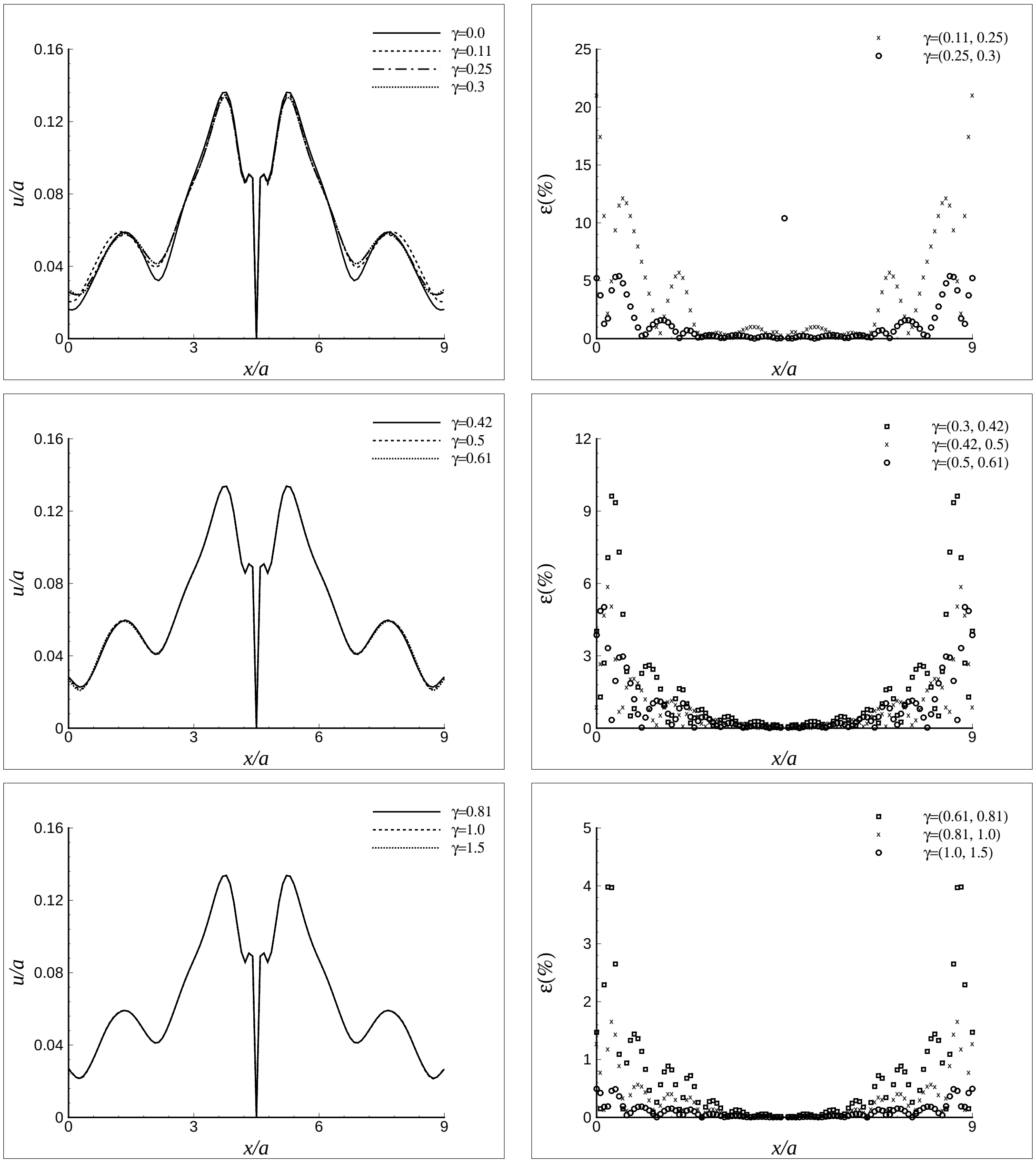

Figure 6.11: Effect of buffer layer thickness on horizontal surface displacements: $H_{lay} = \lambda_R$.

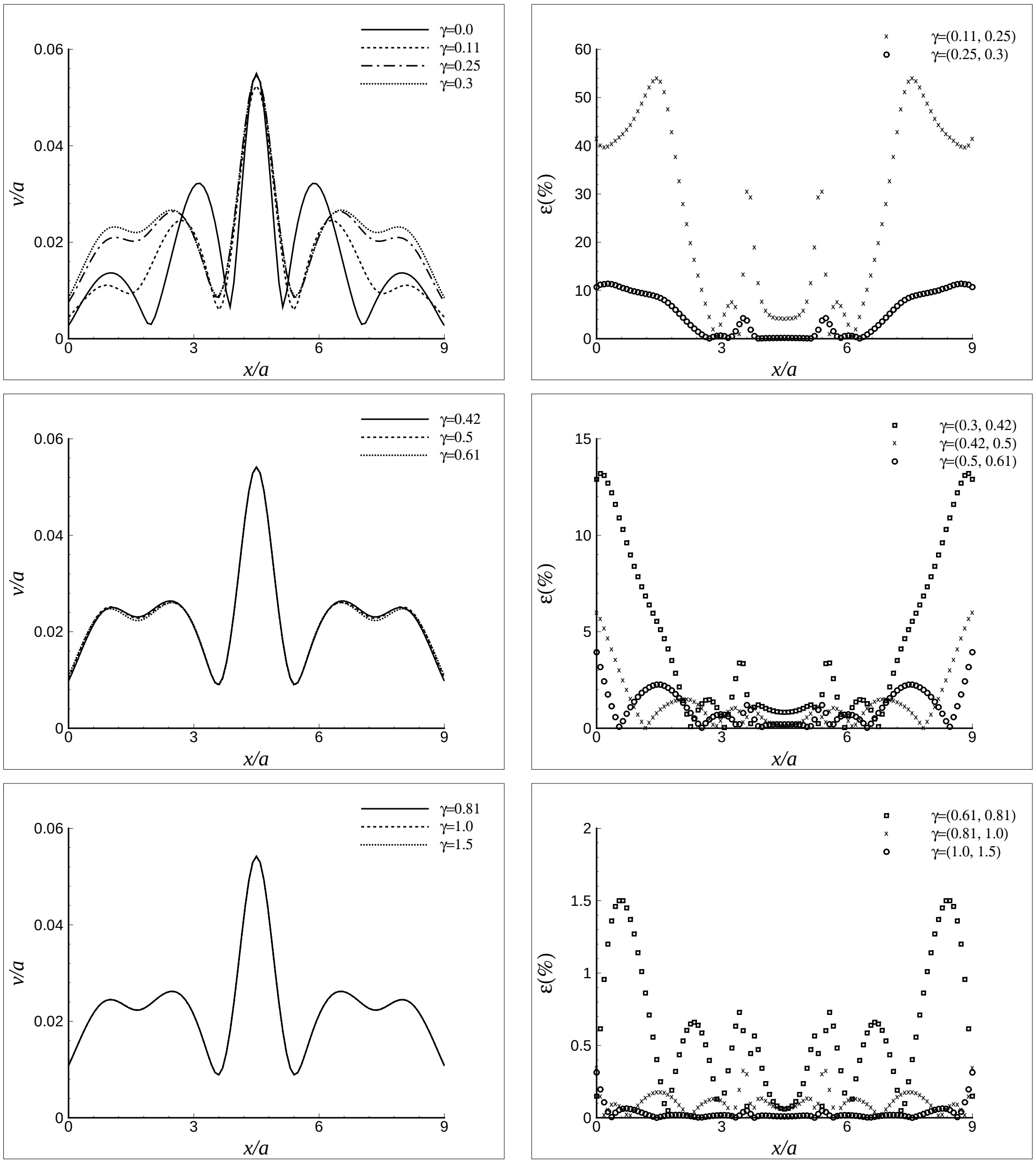

Figure 6.12: Effect of buffer layer thickness on vertical displacements at the soil-half-space interface: $H_{lay} = \lambda_R$.

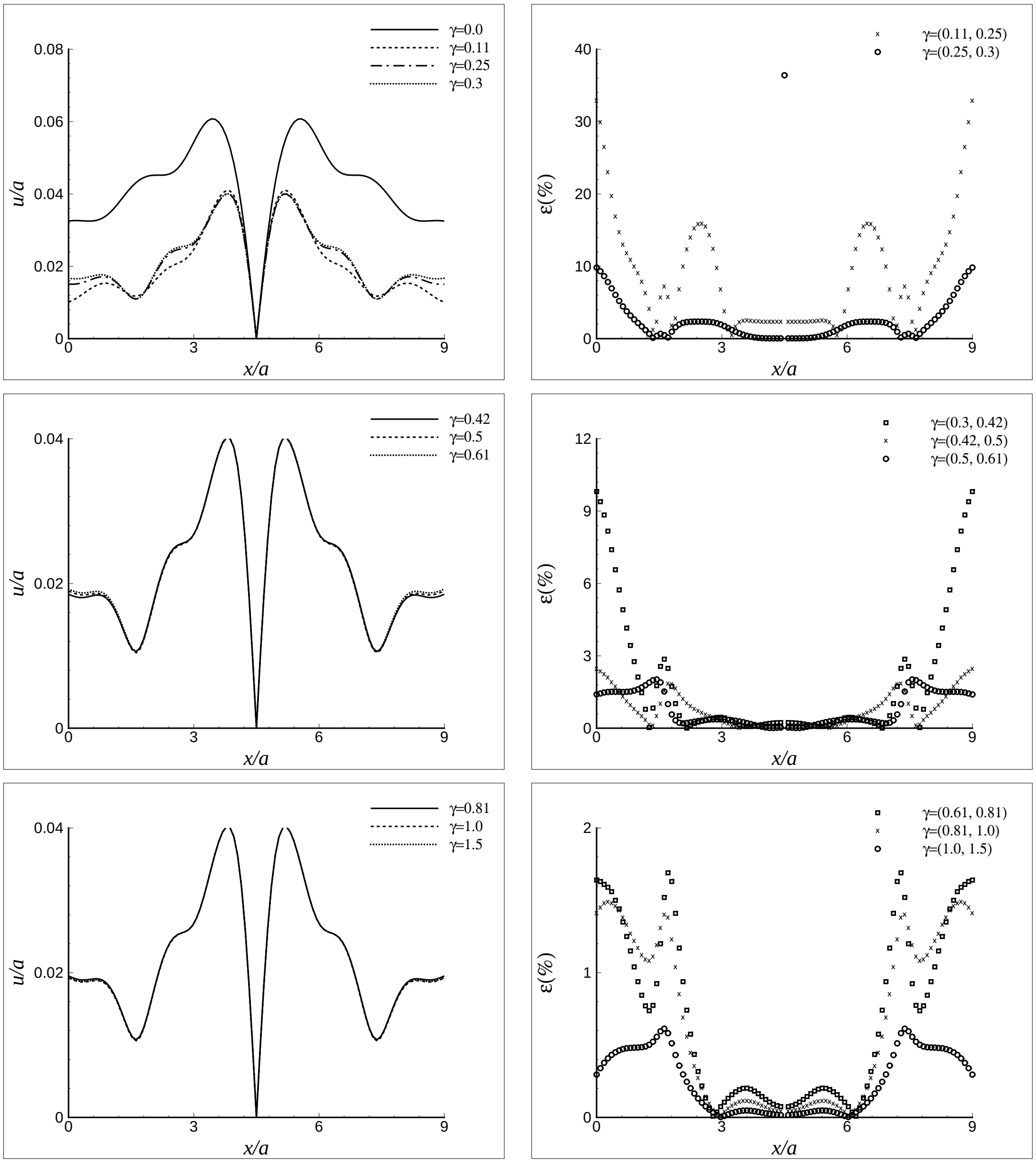

Figure 6.13: Effect of buffer layer thickness on horizontal displacements at the soil-half-space interface: $H_{lay} = \lambda_R$.

6.4 Applications

An interesting application when studying soil-structure interaction is the harmonic vibration of surface or embedded foundations. Next, the dynamic behaviour of surface rigid foundations overlaying either homogenous or layered half-space is investigated by using the coupled TLM-PBC model. It is worth mentioning that Andrade [106] investigated the dynamic behaviour of surface and embedded foundations resting only on homogenous half-space media. Here both homogenous and layered half-space media are considered.

6.4.1 Rigid surface foundation over homogenous half-space

It is shown in section 6.2.2 that the soil domain should be taken deep enough in the case of homogenous half-space to obtain good quality results. A more practical case is considered here and compared to published results in terms of dynamic compliances of rigid foundations when the forcing frequencies are very low. This is given special importance as the poor behaviour of PBC is associated with this range of frequencies.

Luco and Westmann [120] dealt with the foundation dynamics by the theory of singular integral equations where they reduced the problem into dealing with the numerical solution of two Fredholm integral equations. More recently, Lee and Tassoulas [118] coupled the continued fraction absorbing boundaries with the consistent transmitting boundaries and compared their results with those of references [106] and [120]. In this section, the results obtained by the coupled TLM-PBC are compared with the results of references [118, 120].

Figures 6.14a and 6.14b depict the problem configuration of a rigid massless surface foundation overlaying homogenous half-space and the corresponding finite element model. The consistent transmitting boundaries are applied at the lateral boundaries of the domain and the impedance stiffness matrix is used at the base of the soil to represent the paraxial boundaries. The width of the foundation is taken equal to $2B$ and the depth of the soil is $4.667B$, as taken in reference [118]. A value of 0.25 is assigned to Poisson's ratio and a unit value is assigned to the soil density and shear modulus. The damping ratio is considered to be 0.5%. It should be mentioned that a Poisson's ratio of 0.5 is valid for the results of reference [120] and also no damping was considered in their test examples. The low value of the damping is introduced to stabilize the solution.

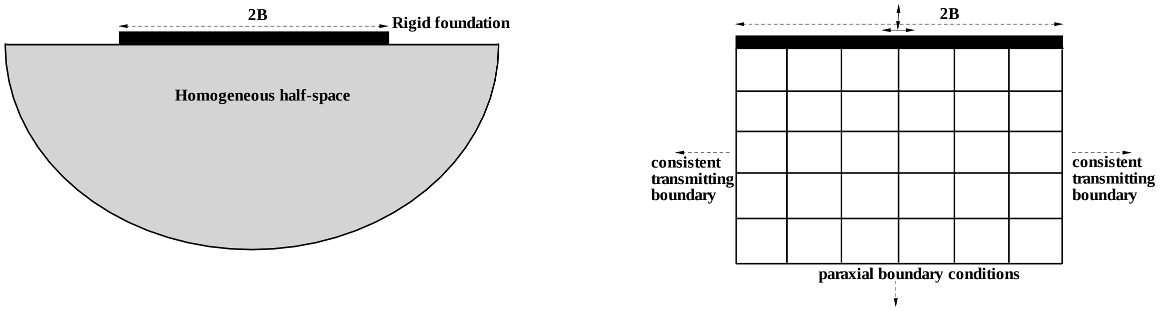

(a) Rigid foundation over half-space

(b) Finite element representation

Figure 6.14: Problem representation and idealization.

The dynamic compliances of foundations are explained in detail in many publications. Here, a brief description is given. The dynamic compliances of the foundation relate the external loads to their associated displacements. The relation between the external loads and the displacements is expressed as

$$\begin{bmatrix} U_v \\ U_h \\ B\phi_r \end{bmatrix} = \frac{1}{\pi\mu} \begin{bmatrix} C_{vv} & & \\ & C_{hh} & C_{hr} \\ & C_{hr} & C_{rr} \end{bmatrix} \begin{Bmatrix} F_v \\ F_h \\ M_r/B \end{Bmatrix}, \tag{6.1}$$

where F_v and F_h are the vertical and horizontal forces with their corresponding displacements, respectively, U_v and U_h, M_r is the rocking moment with the corresponding rocking angle of rotation ϕ_r, and μ is the shear modulus of the soil. The results are expressed in terms of the vertical and horizontal compliances of the foundation C_{vv} and C_{hh} as functions of the normalised frequency $a_0 = \omega B/c_s$.

Andrade [106] investigated the effect of the soil depth when it varied between $1B$ and $8B$. It is reported that for normailsed frequencies ≥ 0.4, the results converge rapidly leading to similar responses in the cases of $3B$ and $8B$. For the sake of validation and consistency, the half-space in this section is truncated at a depth of $4.667B$. It is common practice to express the size of the model in terms of the wavelength and here it is first expressed in terms of the half width of the foundation B and then it is expressed in terms of the pressure wavelength λ_P. To obtain an acceptable discretisation level, the irregular domain of depth $4.667B$ is meshed with 4-node square elements of size less than one-tenth of the Rayleigh wavelength while the remaining domain, up to $0.25\lambda_P$ is meshed into elongated elements (narrow element width and large vertical size) because of the long wavelength λ_P at low frequencies. It is worth noting that the maximum element size is always less than one-tenth of the Rayleigh wavelength. Moreover, the size of the elongated elements is maintained within acceptable limits.

Figure 6.15 depicts the vertical and horizontal compliances of the rigid foundation when taking the depth of the half-space equal to $4.667B$ and when increasing this depth gradually to $1\lambda_P$. As it is shown in the previous figure, good agreement is found between the current approach for values of normalised frequencies greater than 0.2. Discrepancy occurs for lower values of frequencies and poor performance is noticed. This was justified in reference [106] to be due to the approximation of the exact stiffness matrix of the half-space and more specifically due to the fact of including only the first three terms of the approximated stiffness. The performance is improved when increasing the depth of the model to $0.1\lambda_P$ and it is much better for the cases of $0.5\lambda_P$ and $1\lambda_P$. The error is less than 2.5% for these cases. Therefore, the depth of $0.5\lambda_P$ of the homogeneous half-space is used for the comparison with published results, which are presented in Figure 6.16.

Overall, the results of the current model compare well to those of references [118, 120]. It should be indicated here that some differences in the results might be due to the discretisation level and the properties of the rigid foundation. Previous authors considered 8 elements by shear wavelength and in the current analysis at least 10 elements are considered by Rayleigh wavelength at each considered frequency.

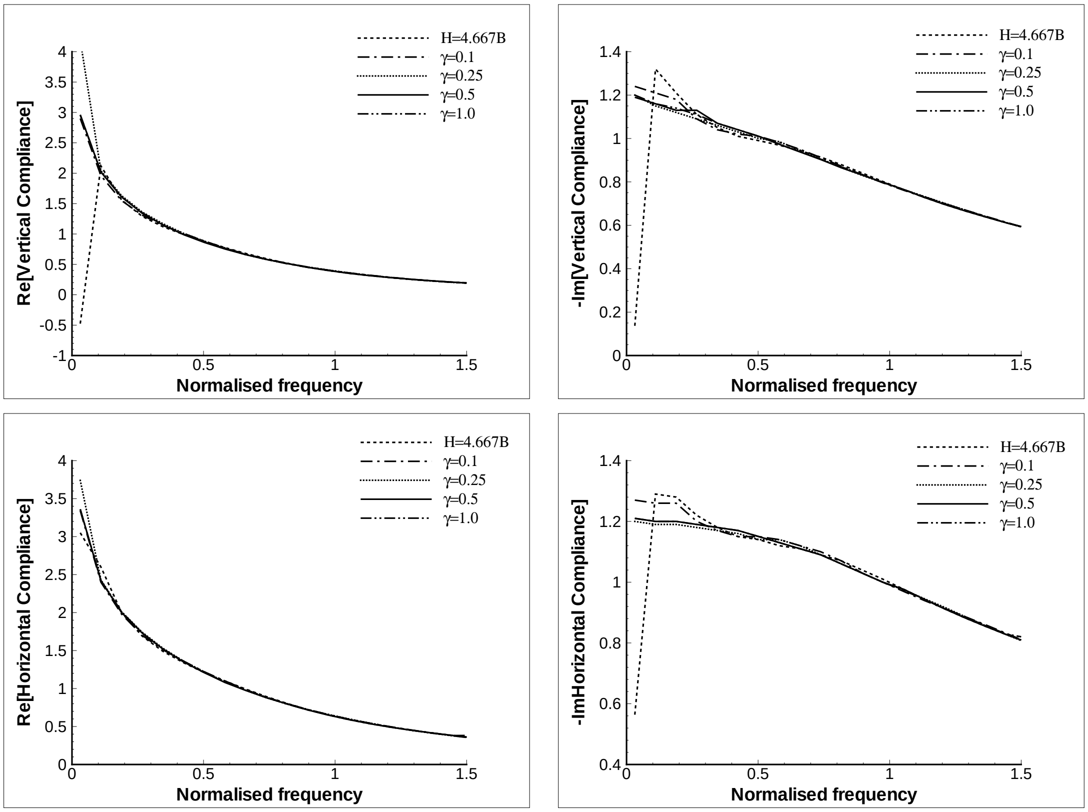

Figure 6.15: Effect of half-space depth on compliances of rigid foundation over homogenous half-space.

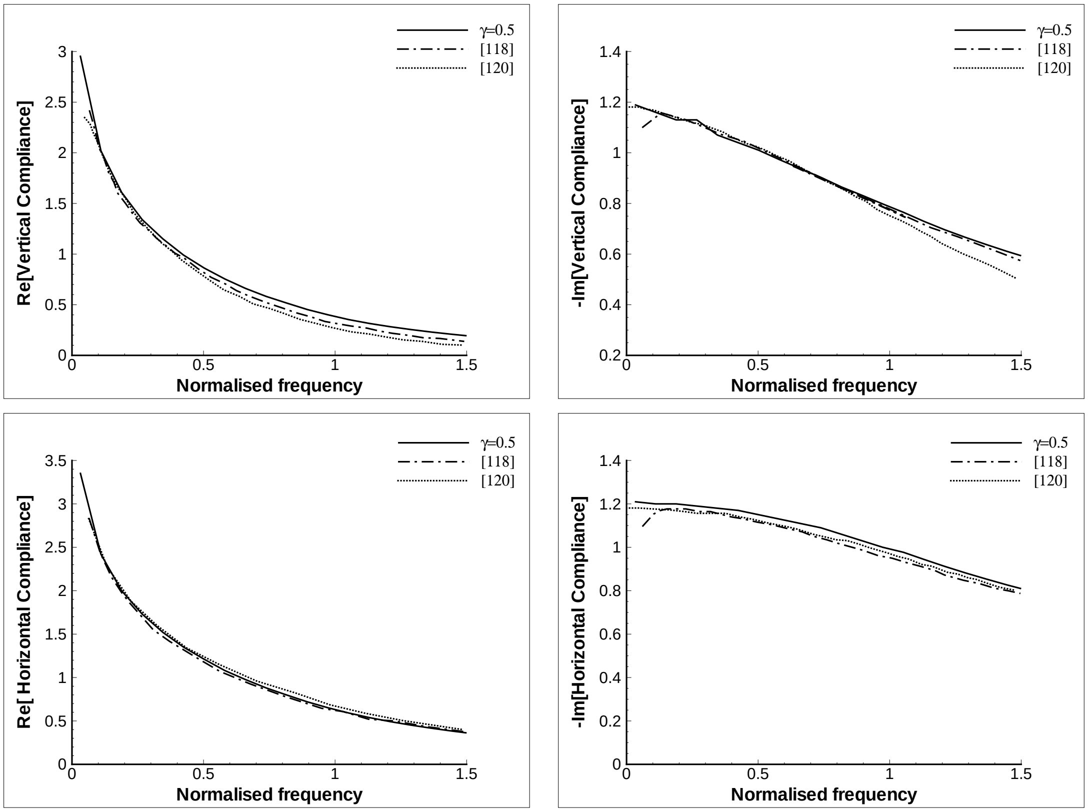

Figure 6.16: Comparison of compliances of surface rigid foundation over homogenous half-space of depth of $0.5\lambda_P$.

6.4.2 Rigid surface foundation over layered half-space

In this section, a soil layer over half-space is considered, in which the material properties of the soil layer are different from those of the underlain half-space. In order to assess the validity of the paraxial boundaries, two different depths of the soil layer are considered for which published solutions are available in the literature. Tzong and Penzien [121] computed the impedance matrix of the half-space and analysed a soil layer overlaying half-space. Thus, we will consider in the following a soil layer of two different depths, B and $2B$.

6.4.2.1 Soil layer over half-space: $\mathbf{H}_{lay} = B$

Figure 6.17 shows a rigid strip foundation overlaying a soil layer over half-space as well as the model configuration by the finite element method. Poisson's ratio and the damping ratio of the soil layer and of the half-space are taken 0.333 and 0.05, respectively. The characteristics of the soil layer and of the half-space are determined by taking $c_{s_{hs}} = \sqrt{3}c_{s_{soil}}$ with the assumption of unit value for the soil density in both media. The surface foundation is subjected to a harmonic load and the dynamic compliances of the foundation are computed for various normalised frequencies. First, the half-space is truncated at a depth $H = B$, where the PBC are implemented.

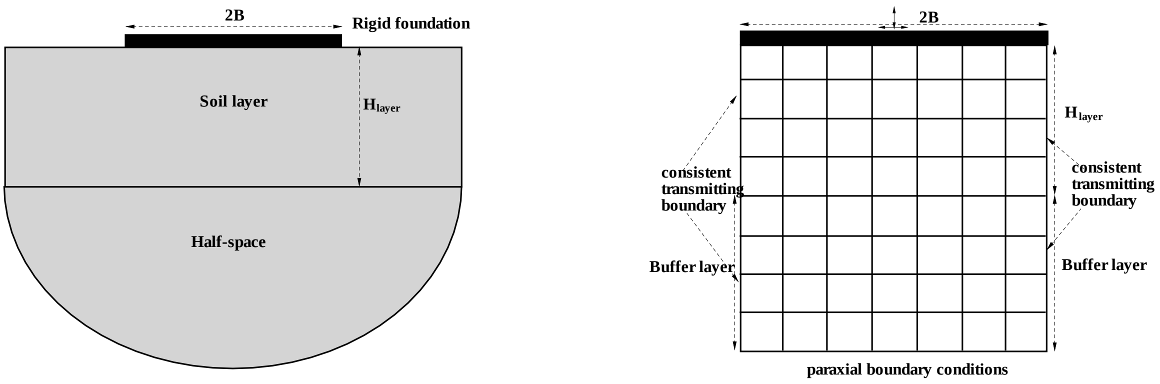

(a) Rigid foundation over layered half-space

(b) Finite element representation

Figure 6.17: Rigid foundation over layered-half-space.

The vertical and horizontal dynamic compliances of the foundation are shown in Figure 6.18. It is obvious from the results that the performance of the PBC is very poor not only at low frequency range, as reported in the literature, but all over the frequency range. Let us recall that the response in the case of homogeneous half-space was much better and discrepancy only occurred at low frequency range. In fact this shows that using only the PBC is not sufficient to represent a layered half-space, as stated in reference [111]. It is believed that the half-space model adopted here is not deep enough. To overcome this, the half-space is truncated at an appropriate depth by incorporating a buffer layer with an adequate thickness.

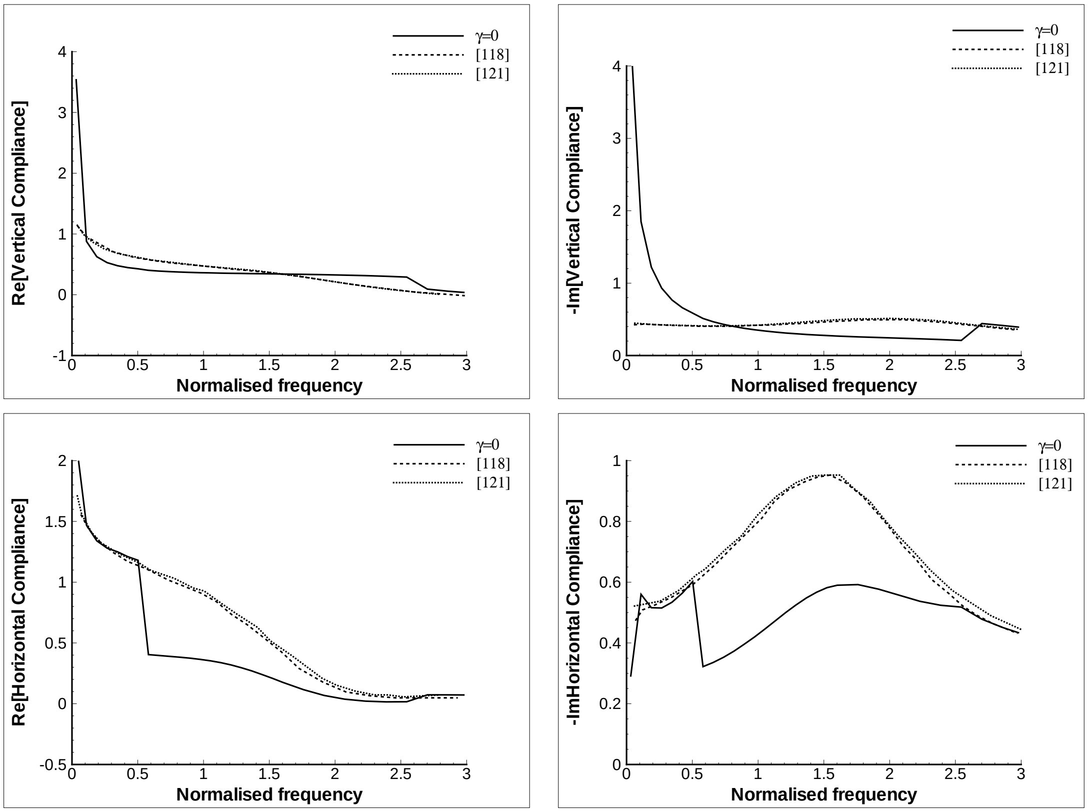

Figure 6.18: Compliances of surface rigid foundation over layered half-space, $H_{lay} = B$.

In the first instance, the dynamic compliances are computed when implementing the approximate impedance matrix directly at the soil layer-half-space interface, $\gamma = 0$. From Figure 6.18, it is clear the results are not of good quality if no buffer layer is used. There is a large discrepancy not only in the low frequency range but also across the whole computed normalised frequency range. Previous work [66] and [111], in addition to the numerical results presented in subsections 6.3.1 and 6.3.2, prompted this work to investigate the effect of adding a buffer layer with this application of rigid foundation over layered half-space.

Next, a buffer layer of different thicknesses is considered between the soil layer and the truncated half-space. It has the same material properties as the half-space and is modelled by meshing it into finite elements by considering at least 10 elements by Rayleigh wavelength of the half-space. The thickness of the buffer layer is considered to be proportional to the pressure wavelength of the half-space. It is worth noting here that it is very difficult to avoid the use of elongated elements in the mesh of the buffer layer. Hence, the aspect ratio, which represents the ratio of the longest to the smallest element is maintained as low as possible. For large depths, corresponding to the lowest frequency, the aspect ratio is taken between 5 and 10 and it is kept around 1 for higher frequencies. A maximum value of 10 for the aspect ratio is suggested by Liu and Quek [122] for displacement analysis. It is noticed from Figure 6.19 that significant improvement in the results is already observed when adding a buffer layer with a small thickness of $0.1\lambda_P$. The thickness of the buffer layer is able to absorb a considerable amount of energy and damp out the transmitted waves, hence reducing the magnitude of the reflected waves. The thickness of the buffer layer was subsequently increased from $0.1\lambda_P$ to $1\lambda_P$ and found to give improved quality results. The numerical results of Figure 6.19 indicate that very slight improvement is achieved by further increasing the thickness of the buffer layer beyond $0.5\lambda_P$. Indeed the results for $0.5\lambda_P$ are almost identical to those of $1\lambda_P$. Hence, the case of $0.5\lambda_P$ is considered when comparing to the results of references [118] and [121] as depicted in Figure 6.20. It is clear that great improvement is achieved when using a buffer layer of thickness $0.5\lambda_P$. Very similar results to those of references [118] and [121] are obtained over all the provided normalised frequency range, including the low frequency range.

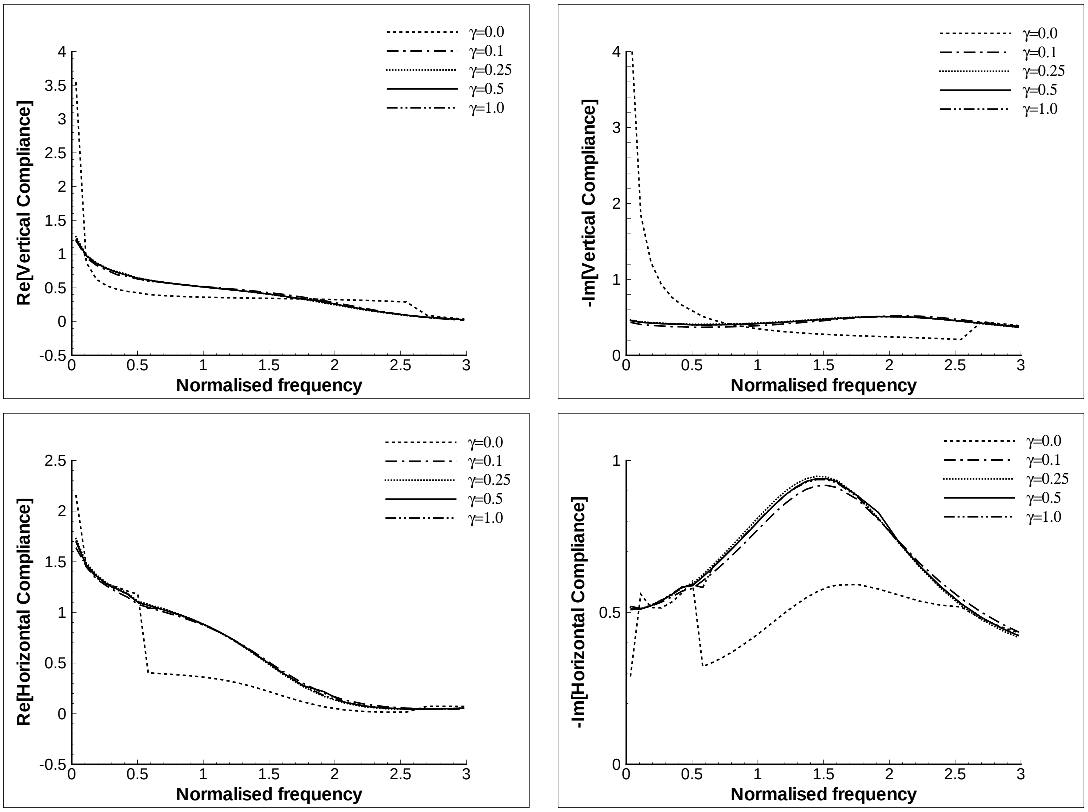

Figure 6.19: Effect of the buffer layer thickness on compliances of surface rigid foundation on layered half-space, H_{lay}=B.

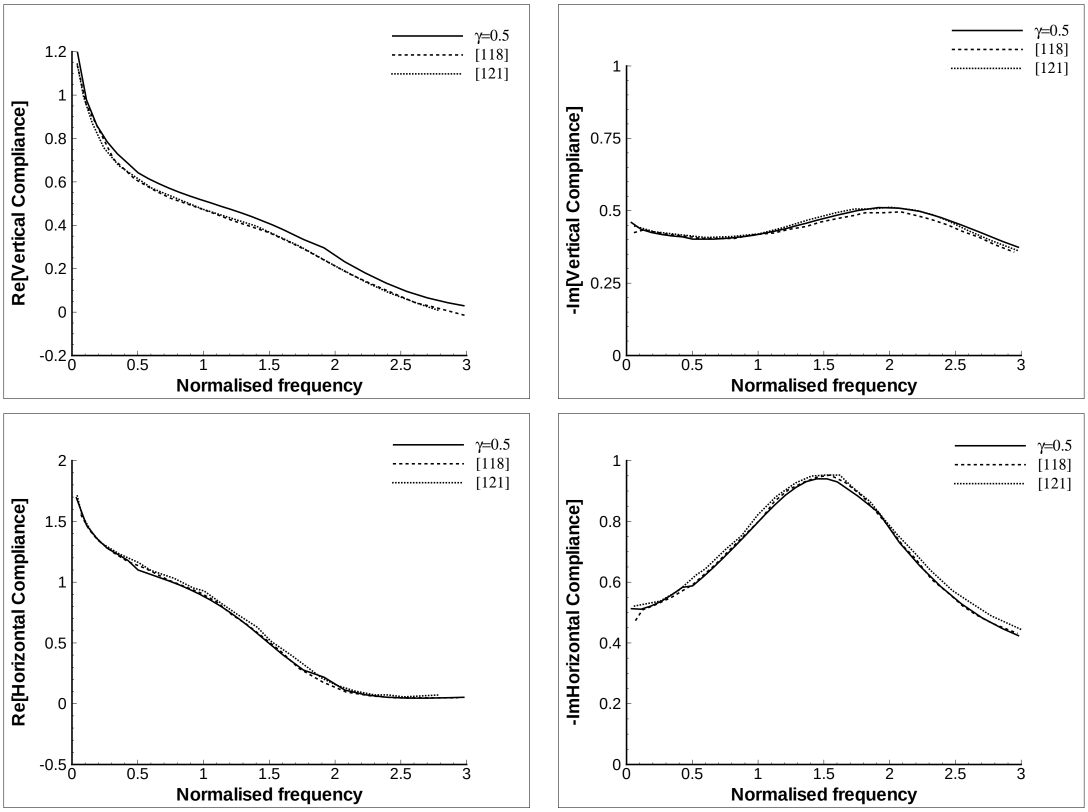

Figure 6.20: Vertical and horizontal compliances of surface rigid foundation over layered half-space, $H_{lay} = B$.

6.4.2.2 Soil layer over half-space, $\mathbf{H}_{lay} = 2B$

In this section, the soil layer depth is increased to $2B$. The performance of the paraxial boundaries is again examined. The problem is treated in the same manner as in section 6.4.2.1. Figure 6.21 displays the vertical and horizontal compliances of the foundation in the case of implementing the PBC immediately under the soil layer. There is large discrepancy in the results for normalised frequencies up to 1.5 when comparing to the results of references [118] and [121]. As was discussed in the previous section, using only the paraxial boundaries is not enough to model the problem correctly and in order to improve the performance of the model, a buffer layer of thickness of 0.1, 0.25, 0.5 and $1\lambda_P$ is attached at the bottom of the soil layer and the associated results are plotted in Figure 6.22. As the thickness of the buffer layer increases the response converges towards the solution of the problem. Including a buffer layer of thickness of $0.5\lambda_P$ leads to good quality results for the whole range of normalised frequencies. Figure 6.23 shows a comparison of the results of the coupled model when attaching a buffer layer of thickness $0.5\lambda_P$ with the results of reference [118] and [121]. Indeed, they are in very good agreement.

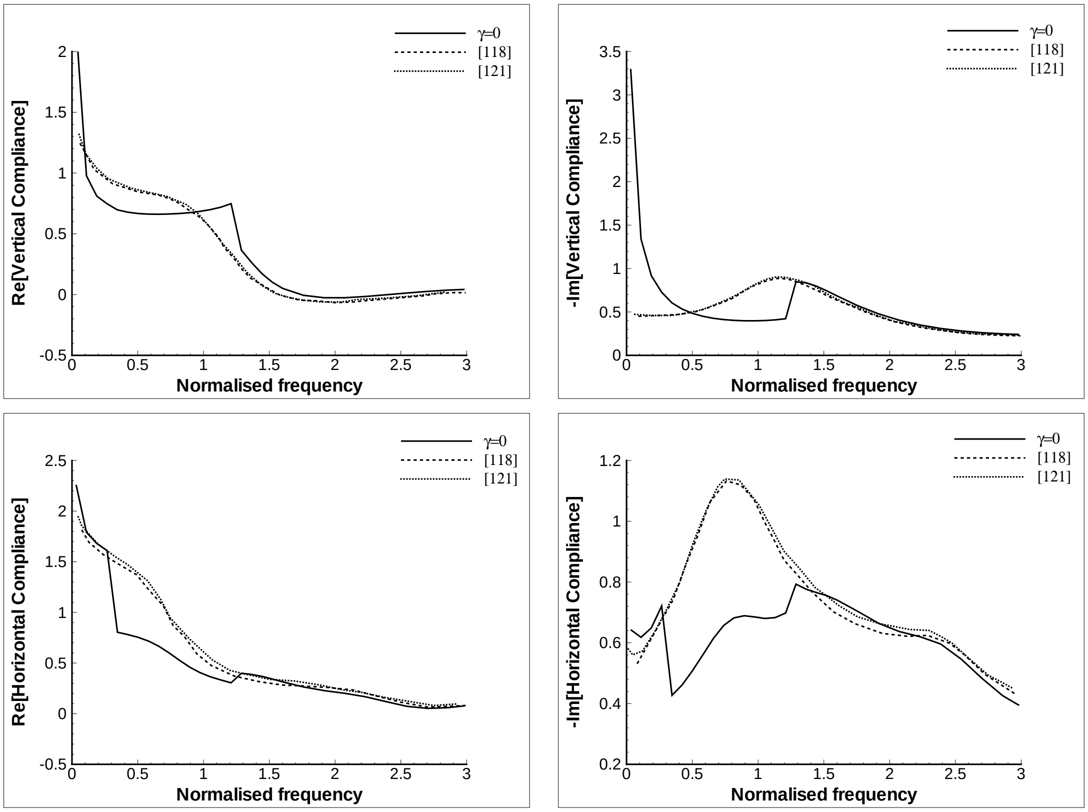

Figure 6.21: Compliances of surface rigid foundation over layered half-space, $H_{lay} = 2B$.

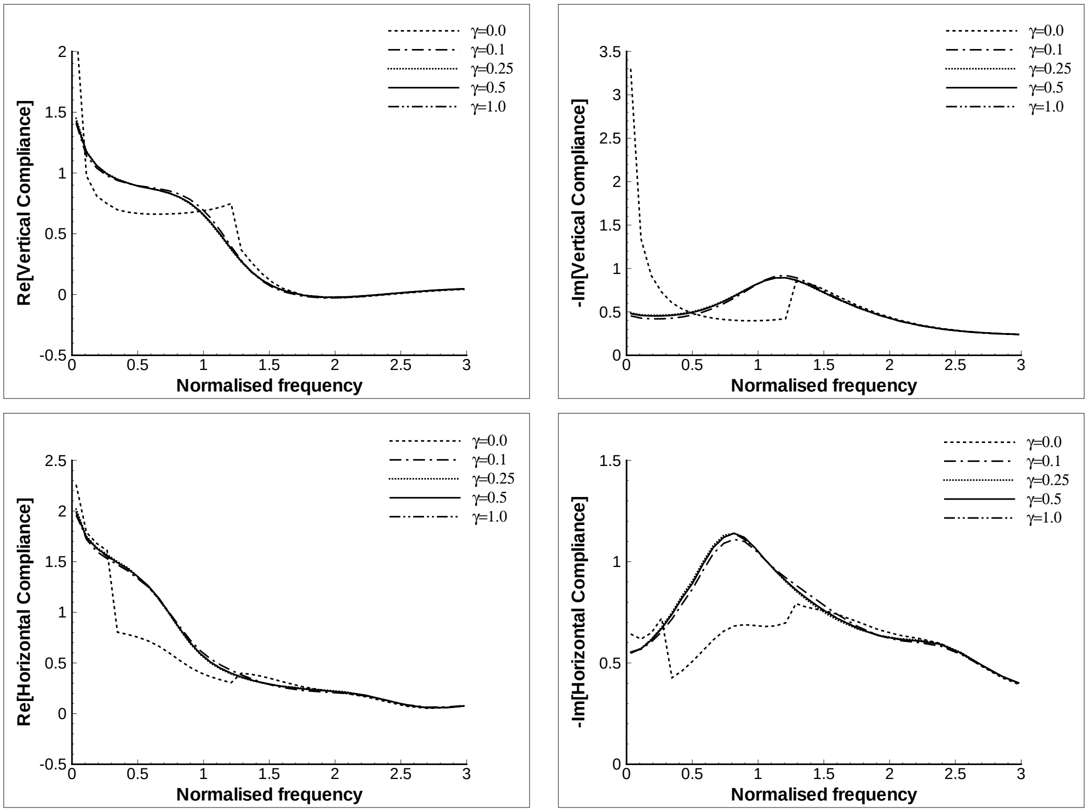

Figure 6.22: Effect of the buffer layer thickness on dynamic compliances of surface rigid foundation on layered half-space, H_{lay}=2B.

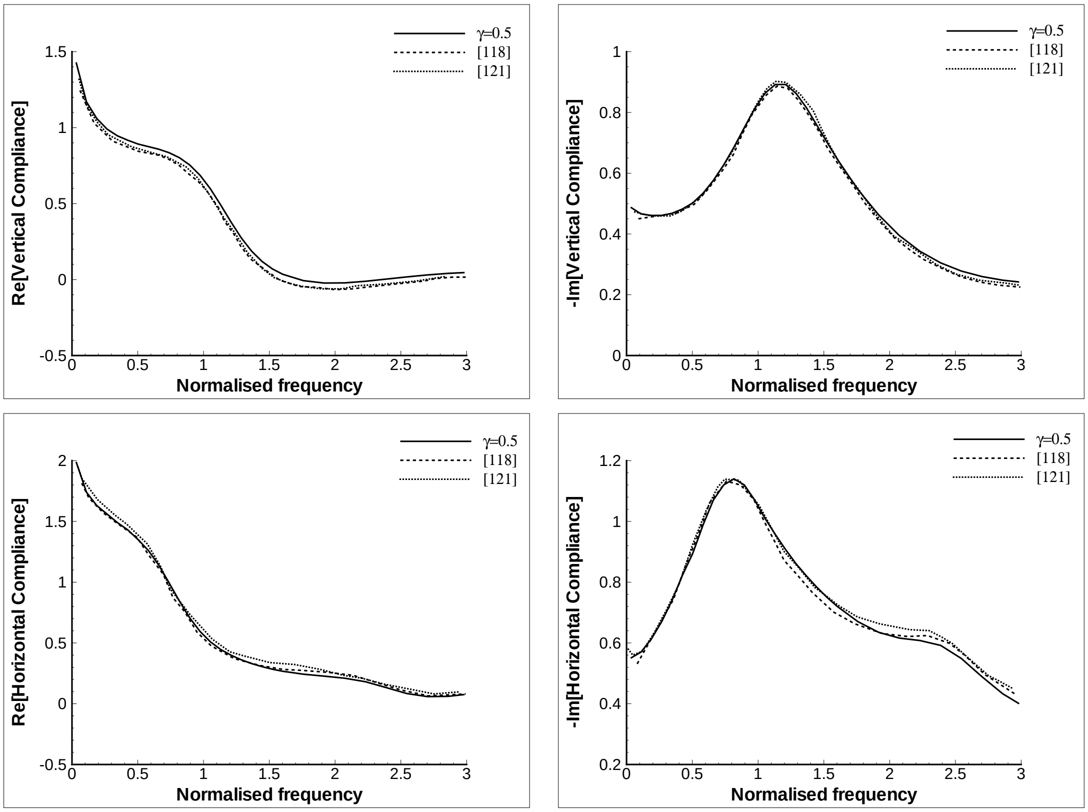

Figure 6.23: Compliances of surface rigid foundation over layered half-space, $H_{lay} = 2B$.

6.4.3 Application to ground vibration reduction

The developed coupled model is used here for the case of ground vibration reduction by an empty trench. It is presented due to the fact that the presence of discontinuities within the model produces multiple reflections and refractions. Thus, the waves' amplitudes will vary within the homogenous half-space. Let us consider a soil domain of $20\lambda_R$ length and $4\lambda_R$ depth subjected to a surface vertical harmonic load on the middle of the domain and with a frequency of 31Hz. It should be noted that the $4\lambda_R$ depth of the model is very close to $0.5\lambda_P$. Soil properties, in this example, are adopted from Yang and Hung [123]. An empty trench is installed at a distance of $5\lambda_R$ from the harmonic load. The vertical displacements at the surface of the domain are computed, respectively, with and without the presence of the trench. The amplitude reduction factor which relates the ratio between the displacements after installing the trench to the ratio of the displacements without the trench is computed for a distance of $5\lambda_R$ after the trench. The results are compared with several results presented in the literature as in references [124, 125, 126], and presented in Figure 6.24. The same trend is observed when comparing the coupled model results with the mentioned results from the literature. It is worth indicating that different numerical approaches are used in these references. A constant element-base boundary is used in reference [124], an advanced direct boundary element method is used in reference [125] and the commercial software ABAQUS with infinite elements is used in reference [126].

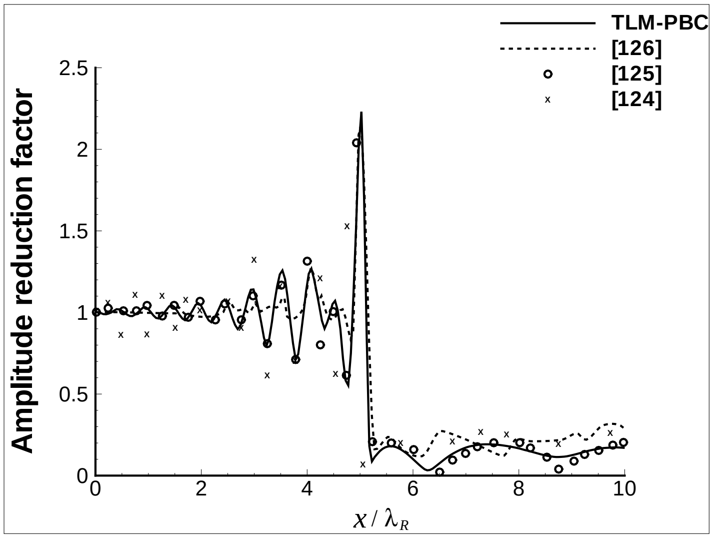

Figure 6.24: Amplitude reduction factor for vibration reduction by an empty trench.

6.5 Stability issues of the PBC

It is demonstrated in the previous sections that the buffer layer eliminates wave reflection and improves the performance of the paraxial boundaries. It is also reported that there is negative energy associated with certain Poisson's ratio values. This in turn will produce a supply of energy rather than dissipation of energy as reported by Maeda and Kausel [111]. Therefore, modelling half-space only with the approximated stiffness matrix is not sufficient as part of the energy will reflect back into the domain. It is worth noting that in the case of homogenous half-space many authors adopted large soil depths to allow the response to converge towards the exact solution.

Cohen [64] and Cohen and Jennings [127] presented an alternative approach different from the one employed in reference [58] to derive the paraxial boundary conditions for scalar and linear wave equations. They started from the one dimensional wave equation seeking a solution of the differential equation in such a manner to allow the waves to travel only in one direction, to represent the boundary where waves only impinge through it. This was extended to 2D scalar wave equation deriving what they call silent boundary conditions. In their silent boundaries, a term of $(c_s to \frac{c_p}{2})$ which is similar to $(1-2\alpha)$ in equation (5.4) is also found. A negative stiffness term is encountered in the case of Poisson's ratios $\nu \geq 1/3$, which leads to conclude that the PBC are unstable for this range of Poisson's ratios. The authors proposed to eliminate that term to avoid the negative energy. Seale [65] and Kausel [112] also explored the stability of the paraxial boundaries by examining the characteristic equation of the PBC by setting the determinant of equation (5.4) to zero. They concluded that for Poisson's ratio $\nu \geq 1/3$ the half-space is too stiff leading to instability issues. Also, for Poisson's ratio $\nu < 0.110394$ poor performance is exhibited.

Meade [128] obtained three approximations for the artificial boundaries in time and harmonic analyses for the scattering of elastic waves by inhomogenous obstacles under plane strain conditions. Their third approximation depends on six coefficient matrices where two of them are positive semi-definite, dissipative boundary, for any point at the boundary if and only if $c_s/c_p \geq 0.5$ which implies $\nu \leq 1/3$.

As it is shown, Poisson's ratio has a key role in the performance of the paraxial boundaries. It is also reported that the PBC exhibit poor performance at low frequencies which is shown in section 6.4.2. Also, it was shown in section 6.2.2 that the convergence was achieved by increasing the depth of the homogenous half-space. In the following, we will address the effect of the buffer layer thickness and Poisson's ratio on the performance of the PBC. As the second term in equation (5.4) brings a negative energy, and hence leads to reflected waves into the irregular domain, this term is omitted. The modified matrix is expressed as

$$\begin{aligned}
\mathbf{K} &= \mathrm{i}\omega\rho c_s \begin{bmatrix} 1 & 0 \\ 0 & 1/\alpha \end{bmatrix} + \mu \frac{1-2\alpha}{\alpha} k \begin{bmatrix} 0 & 1 \\ 1 & 0 \end{bmatrix} \\
&+ \mathrm{i}\mu \frac{c_s}{2\omega} k^2 \begin{bmatrix} -(2-\alpha)/\alpha & 0 \\ 0 & (1-2\alpha)/\alpha^3 \end{bmatrix}, \qquad \text{for} \qquad \nu < 1/3. \qquad (6.2a)
\end{aligned}$$

$$\begin{aligned}
\mathbf{K} &= \mathrm{i}\omega\rho c_s \begin{bmatrix} 1 & 0 \\ 0 & 1/\alpha \end{bmatrix} + \mu \frac{1-2\alpha}{\alpha} k \begin{bmatrix} 0 & 1 \\ 1 & 0 \end{bmatrix} \\
&+ \mathrm{i}\mu \frac{c_s}{2\omega} k^2 \begin{bmatrix} -(2-\alpha)/\alpha & 0 \\ 0 & 0 \end{bmatrix}, \qquad \text{for} \qquad \nu \geq 1/3. \qquad (6.2b)
\end{aligned}$$

Now, the stiffness matrix of the 2-node half-space element of expression (5.22) is modified according to the new approximated impedance matrix of expression (6.2b). Moreover, the regular region matrices should also be modified. Thus, following the procedure of deriving the half-space elementary stiffness matrix we obtain

$$\mathbf{K}^{hs}_{modified} = \begin{bmatrix} 2C_1+C_3 & 0 & C_1-C_3 & C_4 \\ 0 & 2C_2 & -C_4 & C_2 \\ C_1-C_3 & -C_4 & 2C_1+C_3 & 0 \\ C_4 & C_2 & 0 & 2C_2 \end{bmatrix}. \qquad (6.3)$$

Let us proceed now to deal with the regular regions. Modification of the impedance matrix yields to only modifying the matrix $\mathbf{A}_2^{hs}$ given in equation (5.27a) and will be replaced by (6.4)

$$\mathbf{A}_{2_{modified}}^{hs} = \frac{\mathrm{i}\mu c_s}{2\omega\alpha^3} \begin{bmatrix} (\alpha-2)\,\alpha^2 & 0 \\ 0 & 0 \end{bmatrix}. \tag{6.4}$$

Now, the modified PBC combined with the TLM is used. A sensitivity analysis is carried out in the following section to examine the above mentioned modifications for the stability of the PBC. Improvement brought to the performance of the method in homogenous and layered half-spaces is outlined below.

6.5.1 Performance of the modified PBC in homogenous half-space media

To assess the modifications introduced in section 6.5, let us recall the example illustrated in section 6.4.1. Figure 6.25 shows the effect of Poisson's ratios of 0.35 and 0.4 on the dynamic compliances of the foundation. It is clear that there is some inconsistency in the response, for example, for thicknesses of the buffer layer less than $0.5\lambda_P$. However, the cases of $0.5\lambda_P$ and $1\lambda_P$ seem to produce similar results. The inconsistency in the results is reduced, as it is shown in Figure 6.26, when applying the modifications presented in section 6.5.

6.5.2 Performance of the modified PBC in layered half-space media

The example presented in section 6.4.2.2 is revisited again by applying the modification presented in section 6.5. The results are plotted in Figures 6.27 and 6.28. Again, a similar trend to the homogenous half-space response is noticed. The difference is significantly reduced by applying the presented modifications. Although, the difference is reduced, it seems sufficient to apply a thickness of a buffer layer of $0.5\lambda_P$ and without modifying the matrix.

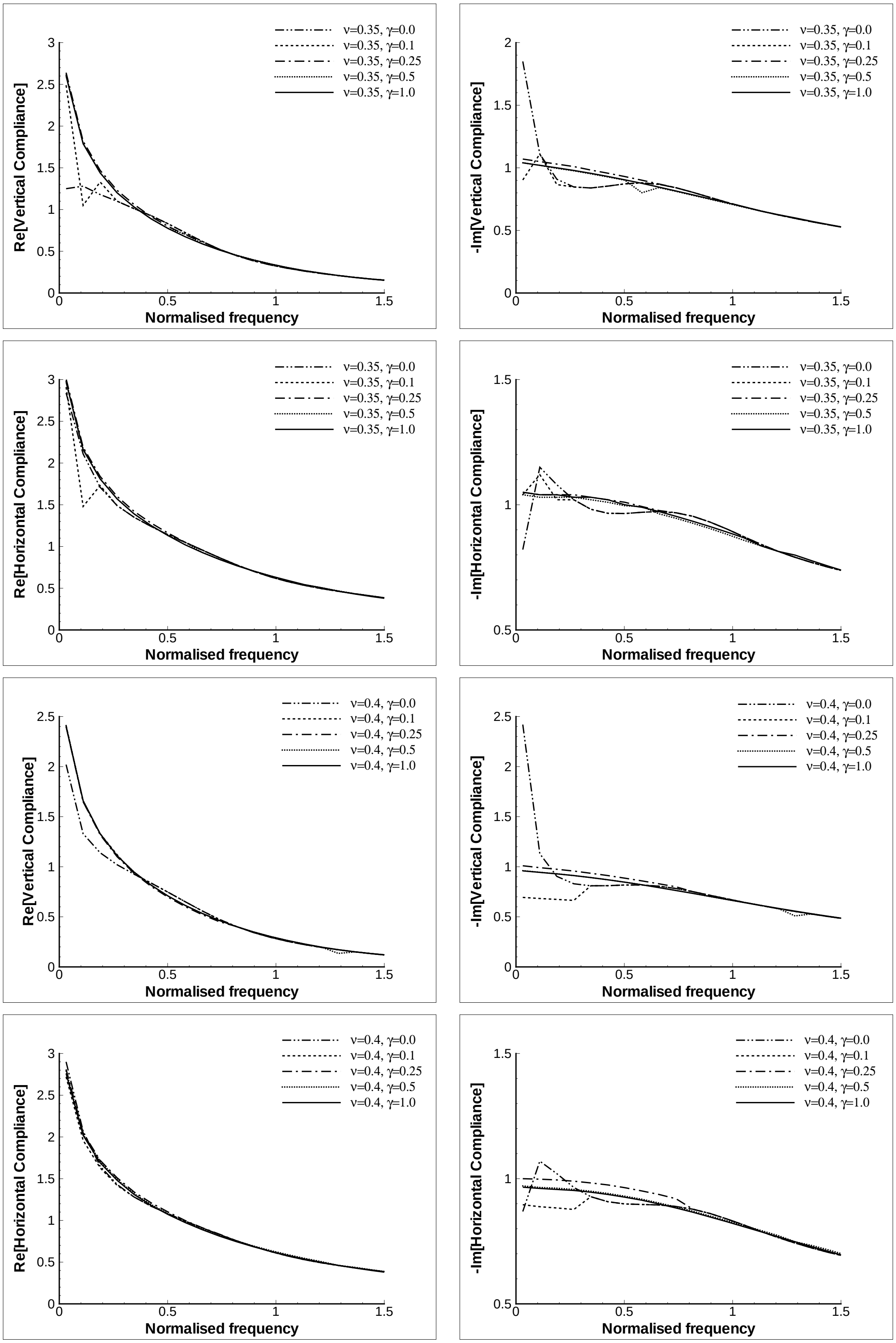

Figure 6.25: Effect of Poisson's ratio and the buffer layer thickness on the performance of homogenous half-space TLM-PBC model, $\nu = 0.35$ and $\nu = 0.4$.

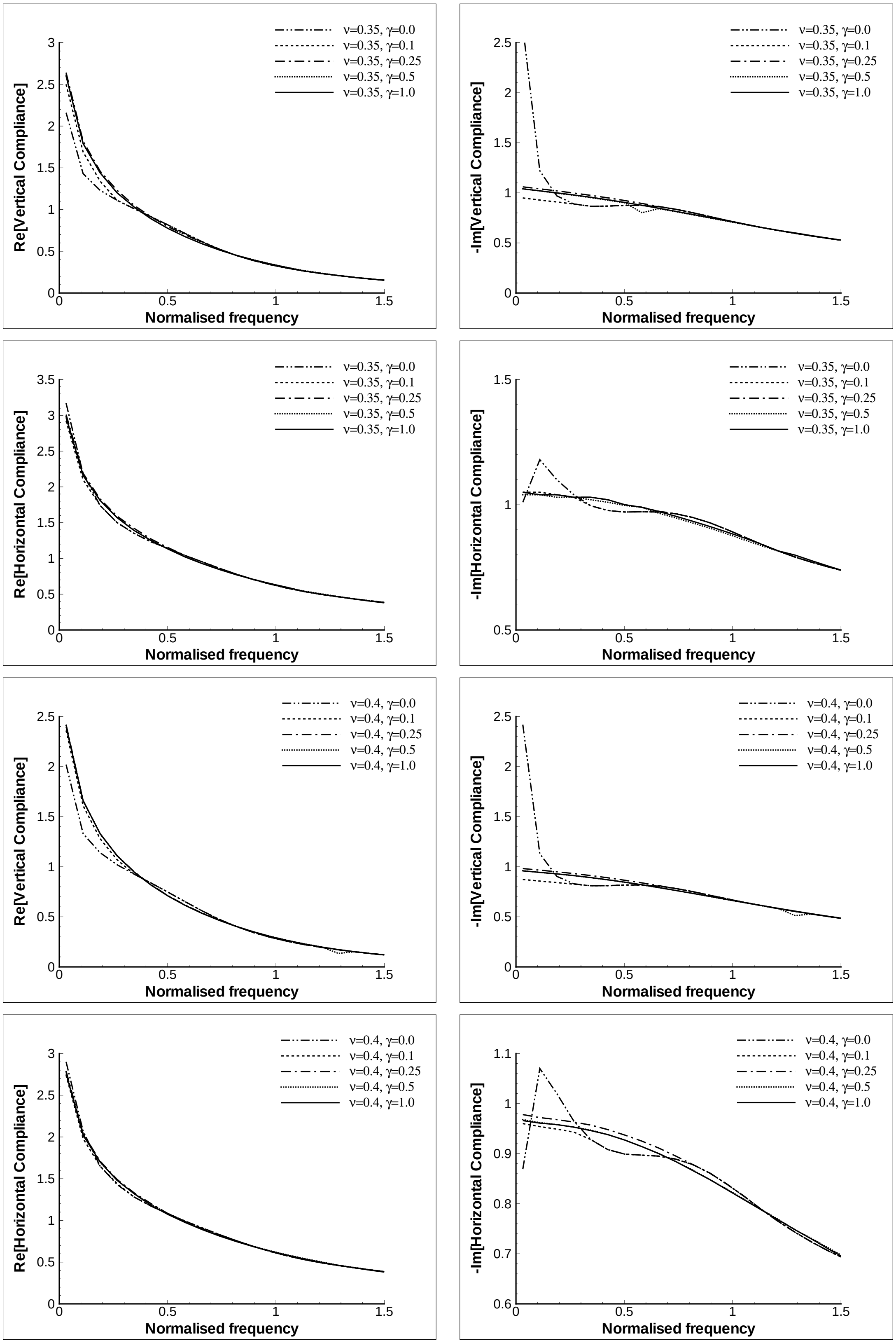

Figure 6.26: Effect of Poisson's ratio, modified matrix, and the buffer layer thickness on the performance of homogenous half-space TLM-PBC model, $\nu = 0.35$ and $\nu = 0.4$.

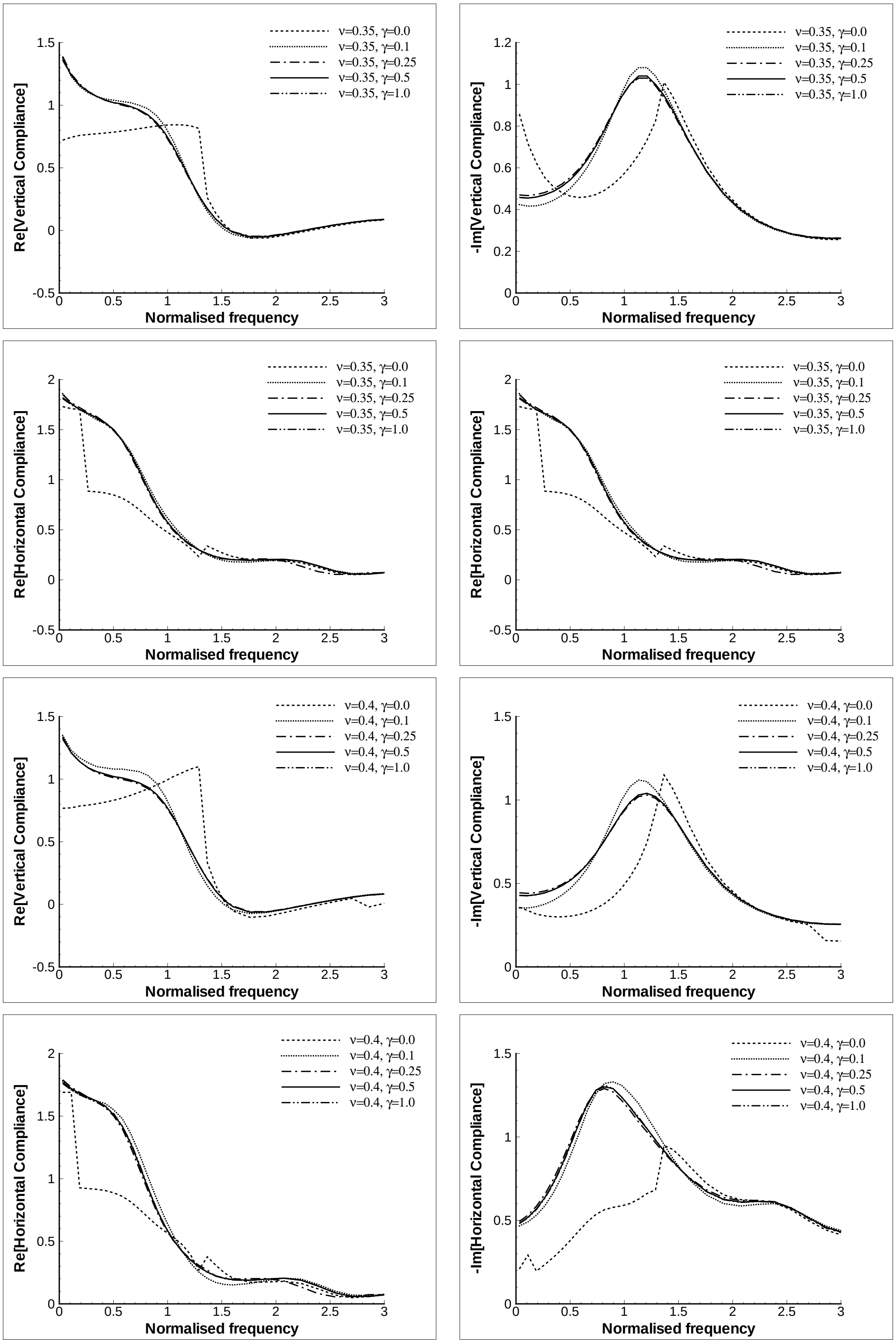

Figure 6.27: Effect of Poisson's ratio and the buffer layer thickness on the performance of layered half-space TLM-PBC model; $H_{lay} = 2B$, $\nu = 0.35$ and $\nu = 0.4$.

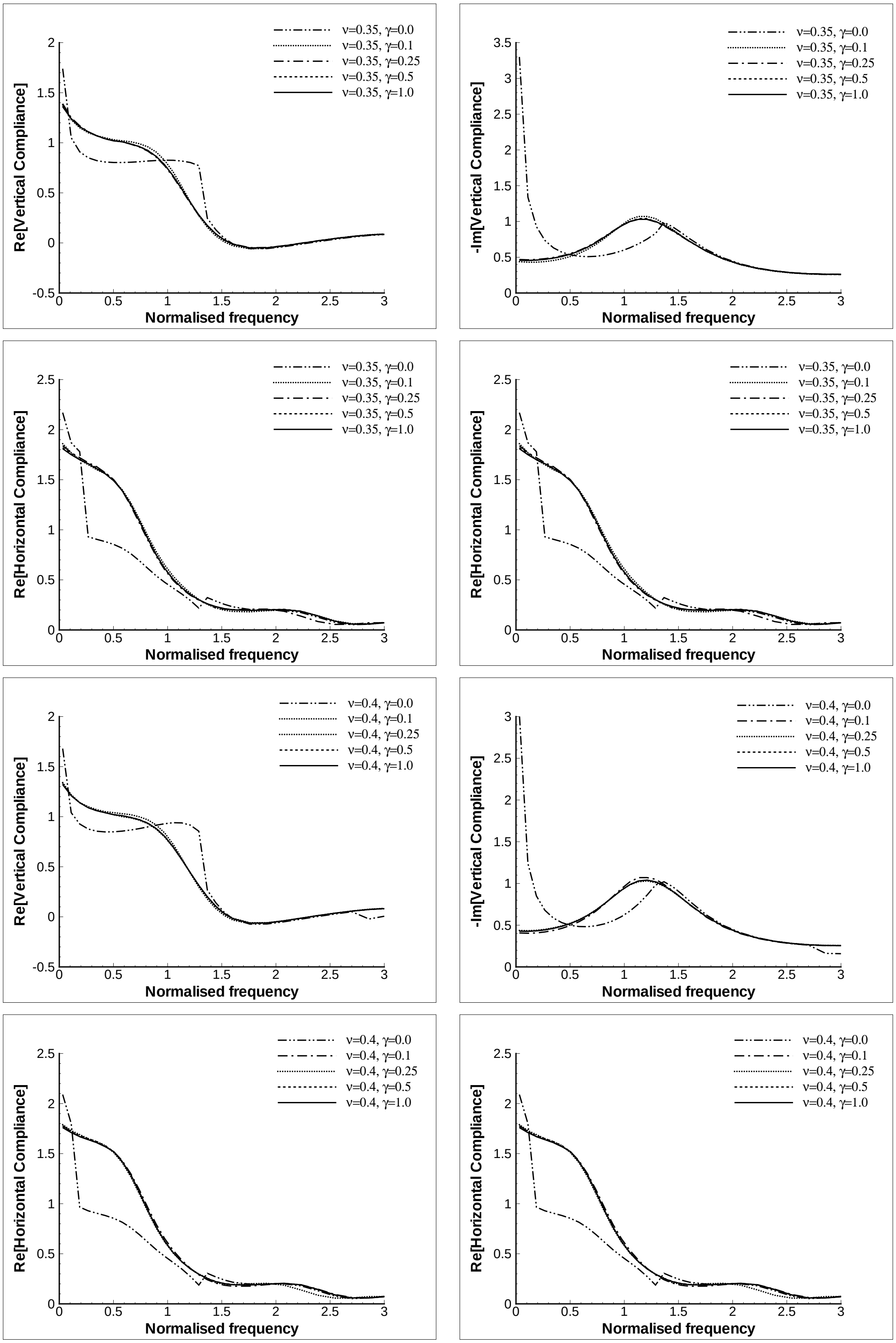

Figure 6.28: Effect of Poisson's ratio, modified matrix, and the buffer layer thickness on the performance of layered half-space TLM-PBC model; $H_{lay} = 2B$, $\nu = 0.35$ and $\nu = 0.4$.

6.6 Concluding remarks

The coupled TLM-PBC model developed in Chapter 5 for wave propagation in half-space soil media is numerically validated in the current chapter through various test examples. The main conclusions are as follow:

- To model wave propagation in homogenous half-space soil media, the model thickness of at least one pressure-wavelength should be considered to achieve good quality results. For thicknesses below the indicated one, the model would induce spurious reflections at the half-space base, where the PBC is used. This is due to the derivation of the PBC based on an approximation of the impedance of the half space.

- For wave propagation in layered half-space soil media, it is shown that the coupled TLM-PBC model is not capable to properly simulate such problems without introducing a buffer layer, at the irregular region-half-space interface. The latter layer is of the same properties of the half-space and of at least half of the pressure-wavelength thickness. For even better quality results, the thickness of the buffer layer may be further increased to one pressure-wavelength.

- Test examples related to the dynamics of rigid foundations overlaying half space showed that the discrepancy associated with low dimensionless frequencies, in the case of homogeneous half-space, was eliminated by taking a thickness of $0.5\lambda_P$ of the half-space. In the case of surface foundations over layered half-space, a buffer layer of at least $0.5\lambda_P$ thickness must be inserted.

- Instability of the PBC for Poisson's ratio greater than 1/3 is illustrated and an attempt to overcome it was presented. This is based on a deliberate omission of a term in the half-space impedance expansion.

The introduction of the buffer layer obviously leads to an increase of the computational cost related to the coupled TLM-PBC as it involves more nodal points in both the finite element model of the irregular region and in the eigenvalue problem associated with the regular regions. The computational burden becomes even more obvious when modelling large domains and covering wide ranges of frequencies.

Chapter 7

Consistent transmitting boundary conditions with a reduced number of eigenmodes

7.1 Introduction

In the formulation of the consistent transmitting boundaries presented in Chapter 3, within the TLM model, and in Chapter 5, within the coupled TLM-PBC, all eigenmodes deduced from the second order eigenvalue problem were included in the computation of the lateral nodal forces simulating the effect of the right and left regular regions. In this chapter, the effect of reducing the number of participating eigenmodes in the formulation of the lateral forces is investigated. First, the wave nature of the exponential terms involving the wavenumbers obtained from the eigenvalue problem is analysed. Then modified transmitting boundary conditions are formulated and assessed. Last, guidelines are provided on the use of dominant eigenmodes in the newly formulated transmitting boundary conditions.

7.2 Background and concept

Waas [3] indicated that in seismology scientists usually tackle expensive eigenvalue problems by calculating the dispersion curves for the Love waves, which describe the relationship between the frequency of the wave and its wavenumber. The fundamental mode and only one or two higher modes are usually considered. This latter idea is explored here in the context of the TLM and analogy with structural dynamics practice, where only a few lower modes are usually taken into account, is briefly reviewed.

With the development of advanced computers, analysts are able to compute the structural response for large computational models with many degrees of freedom. However, sometimes the capability of computers is not sufficient when considering very large soil problems. This is tackled by employing the modal reduction schemes, the mode superposition method, Ritz vector and the Quasistatic Ritz vector method, to reduce the size of the problem. These methods are different in essence but their objective is based on reducing the size of the global dynamic stiffness matrix to a smaller size and hence saving the time required for the global matrix inversion. More details about the modal reduction schemes could be found in reference [129]. The mode superposition method for dynamic analysis of structures is based on selecting a reduced number of vibrating modes depending on the frequency range of interest. Basically, the reduced number of modes is obtained by retaining only a few corresponding eigenfrequencies.

López and Cruz [130] investigated the effect of higher modes and determined the required number of modes to be included in the elastic design for dynamic analysis of buildings subjected to horizontal shaking. To quantify the validity of reducing the number of modes, the authors calculated the relative error when using all modes and when using a reduced number. Significant reduction in the error percentage is found when including two or three modes rather than only the first one. A simplified formula is provided in reference [130] to keep the relative error low.

Within the context of the TLM, it is obvious that the computational time needed for computing the eigenmodes is significant in comparison to the time needed for the whole analysis. In other words, if more sub-layers are included in the regular region model then many nodes should be used with respect to depth. Hence the size of the diagonal matrix (3.31) and the modal matrix (3.38) will be larger. As it was explained in Chapter 3, $4n$ eigenvalues and their corresponding eigenvectors are computed when considering a rigid base model. For example, for a square soil domain model of $4\lambda_R$ in both depth and length, with a discretisation level of ten elements per Rayleigh wavelength, would require 41 nodes on each lateral boundary. This leads therefore to computing 160 eigenvalues with their corresponding eigenvectors. The time needed for computing the eigenvalues is 3s and for computing the eigenvectors is 4s, whereas the time needed for the assembling process and the solution is only 2s. These times are estimated on 1.95GB and 1.99GHz computer. This is a small size problem but gives an idea on how cpu time is allocated to the different steps of the analysis.

Next, the eigenvalue problem related to the TLM is revisited and the eigenvalues are analysed for both damped and undamped soil models.

7.3 Eigenvalue problem and wave nature of the solution

The eigenvalue problem presented in expression (3.30) is of second order. It is reduced into a first order problem by introducing a change of variable. This leads to double the size of the problem. This is a convenient and straightforward procedure, but computationally expensive, for solving the second order eigenvalue problem. Briefly, the change of variable consists to introduce q such that

$$q = \mathrm{i}ku, \tag{7.1}$$

and construct vector Q defined by

$$\mathbf{Q}^t = \{q^t, u^t\}. \tag{7.2}$$

The eigenvalue problem becomes

$$[\mathbf{A} - \lambda \mathbf{I}]\mathbf{Q} = 0, \tag{7.3}$$

where $\mathbf{I}$ is the identity matrix and matrix $\mathbf{A}$ is given by

$$\mathbf{A} = \begin{bmatrix} \mathbf{A}_2^{*-1}\mathbf{A}^* & \mathbf{A}_2^{*-1}\left(\mathbf{A}_0^* - \omega^2\mathbf{M}^*\right) \\ \mathbf{I} & 0 \end{bmatrix}. \tag{7.4}$$

Matrices $\mathbf{A}_0^*$, $\mathbf{A}_1^*$, $\mathbf{A}_2^*$ and $\mathbf{M}^*$ are all defined in Chapter 3. It is obvious from the structure of matrix $\mathbf{A}$ that the size of the eigenvalue problem has doubled. The "new" eigenvalues are λ, rather than k, and the "new" eigenmodes are Q rather than u. For a soil medium overlaying rigid bedrock, the "new" eigenvalue problem is of dimension $4n$, n being the number of sub-layers in the regular regions.

The displacement field in the right regular region is written as a linear combination of all eigenmodes obtained from the solution of the "new" eigenvalue problem of expression (7.3) for $k_s = \kappa_1 + \mathrm{i}\kappa_2$, with $\kappa_2<0$. It is given by

$$\{u^*\} = \sum_{s=1}^{2n} a_s\{u_s^0\}e^{\mathrm{i}(\omega t - k_s x)}. \tag{7.5}$$

Expression (7.5) represents a combination of waves which are harmonic in time and propagating horizontally in the positive x-direction. The wave types included in the solution (7.3) depend basically on the wavenumbers k_s and several cases occur as reported by Waas [3]:

1. If the wavenumber is complex; $k = \kappa_1 + \mathrm{i}\kappa_2$, ($\kappa_1 \neq 0$ and $\kappa_2 \neq 0$), then the motion is expressed as

   $$\{u\} = a\{u^0\}e^{\mathrm{i}(\omega t - \kappa_1 x)}e^{\kappa_2 x}, \tag{7.6}$$

   which represents a propagating wave in the x-direction with increasing or decaying amplitude depending on the sign of the imaginary part κ_2.

2. If the wavenumber is real; $k = \kappa_1$, ($\kappa_1 \neq 0$ and κ_2=0), the motion is of the form

   $$\{u\} = a\{u^0\}e^{\mathrm{i}(\omega t - \kappa_1 x)}, \tag{7.7}$$

   which represents a wave travelling in the *x*-direction with a constant amplitude. This type of wave could not occur in the damped case as waves attenuate with distance from the source of vibration.

3. If the wavenumber is imaginary; $k = \mathrm{i}\kappa_2$, ($\kappa_1 = 0$ and $\kappa_2 \neq 0$), the motion is expressed by

   $$\{u\} = a\{u^0\}e^{\mathrm{i}\omega t}e^{\kappa_2 x}. \tag{7.8}$$

   This is a wave which varies exponentially in the *x*-direction but does not propagate.

4. Finally, if the wavenumber is zero; k=0, ($\kappa_1 = 0$ and $\kappa_2 = 0$), the motion is independent of *x* and is expressed by

   $$\{u\} = a\{u^0\}e^{\mathrm{i}\omega t}. \tag{7.9}$$

   This is a standing wave which could occur only in the undamped case and at certain frequencies. Wavenumbers of this type may not exist if damping is included.

As it is already mentioned, the 2*n* computed eigenvalues, or wavenumbers, with negative imaginary part, κ_2<0, describe waves propagating in the positive *x*-direction with decaying amplitude. On the other hand, the other 2*n* eigenvalues with positive imaginary part, κ_2>0, describe waves propagating in the negative *x*-direction with decaying amplitude. The nature of the motion is dependent on the type of the wavenumber which in turn depends on the presence of damping, while the number of eigenmodes is dictated by the number *n* of the sub-layers in the regular region. Next, numerical tests are carried out to present all possible types of wavenumbers under undamped and damped conditions.

7.3.1 Undamped case

In the absence of damping, matrices $\mathbf{A}_0^*$, $\mathbf{A}_1^*$ and $\mathbf{A}_2^*$ of equation (3.30) are real. However, complex eigenvalues with their corresponding complex eigenvectors are obtained. Wavenumbers in the undamped case could be complex, real or imaginary. To illustrate this, an example of a soil model of 30m in length and 10m in depth subjected to 1kN harmonic load of frequency 4Hz is considered. Half of the computed wavenumbers corresponding to the right regular region, which represent propagating waves in the positive *x*-direction, are tabulated in Table 7.1.

n	$-\kappa_2$	κ_1
1	5.87080419324460	9.917485262926976E-017
2	5.33650965620063	3.881378380881605E-016
3	4.49195670821783	3.949369079082468E-016
4	3.56305391411867	-2.301572451243074E-016
5	2.67829245388722	-3.162047183676384E-016
6	1.94832270565977	1.098055607470449E-015
7	1.86566456158340	4.302016737950528E-016
8	1.48721791823830	-5.434680040119120E-016
9	1.37395295938099	6.144048557706494E-016
10	1.88588115836173	0.179724211854971
11	0.214597481226497	0.136645469801204
12	0.214597481226497	-0.136645469801204
13	1.38096361328397	-0.165447605369872
14	1.38096361328398	0.165447605369872
15	0.585679087665297	0.218039747282778
16	1.88588115836173	-0.179724211854970
17	0.944222978139081	-0.239727753648631
18	0.944222978139080	0.239727753648632
19	0.585679087665298	-0.218039747282780
20	-2.857625564527434E-015	2.807184179997326E-002

Table 7.1: Imaginary and real parts of wavenumbers for the undamped case.

As it is shown in Table 7.1, three types of wavenumbers are present in the undamped case. In the case of complex wavenumbers, they appear in pairs; with positive and negative imaginary parts. This is obvious, for example for *n*=10 and 16, and *n*=11 and 12. However, for *n*=20 it is purely real.

7.3.2 Damped case

When damping is included, matrices $\mathbf{A}_0^*$, $\mathbf{A}_1^*$ and $\mathbf{A}_2^*$ are complex. The same soil domain considered in section 7.3.1 is used here with a damping ratio of 2.5%. All wavenumbers have nonzero imaginary parts as shown in Table 7.2. In the damped case, complex wavenumbers, do not appear in pairs unlike the undamped case.

7.3.3 A method for selecting eigenmodes

In expression (7.5) of the displacement field, all eigenmodes are taken into account, where each mode is weighted with the factor a_s. In the formulation of the dynamic stiffness matrices **R** and **L**, however, the factors a_s do not intervene and therefore all modes contribute equally. For selecting a few eigenmodes, the proposed approach in this work consists to rank the 4*n* eigen-

n	$-\kappa_2$	κ_1
1	5.87080985908597	1.132953268934870E-004
2	0.585807164510774	0.218799159581013
3	5.33651580200005	1.228893478633891E-004
4	0.585628316991176	-0.217271582172299
5	4.49196383961546	1.425887915195512E-004
6	8.601496723589494E-003	2.893149720468033E-002
7	3.56306263791666	1.744117008670624E-004
8	0.214541166835173	0.139164575546165
9	2.67830387627921	2.283166631093965E-004
10	0.214942166524979	-0.134160625328525
11	1.88593597347341	0.179940663880394
12	1.88584822782740	-0.179503429069688
13	1.94832770335401	9.976496579846834E-005
14	1.86566906375030	8.994782045994271E-005
15	1.38104948346212	0.165918179384498
16	1.38092482056506	-0.164970460501847
17	1.48721825497958	3.581384569191966E-006
18	1.37395549300977	4.451500541061514E-005
19	0.944318538411235	0.240198990875966
20	0.944175109977053	-0.239249458815423

Table 7.2: Imaginary and real parts of wavenumbers for the damped case.

values with increasing imaginary part κ_2 then display the magnitude of the exponential term $\exp(\mathrm{i}k_s x)$ of expression (7.5) with distance beyond the lateral boundary.

As a test case, a soil domain of $8\lambda_R$ in length and $4\lambda_R$ in depth is used. The shear modulus, density and Poisson's ratio are 40MPa, 1700kg/m^3 and 0.25, respectively. Damping is taken into account by considering β =5%. Time harmonic motions are considered for the frequency of 20Hz, which is much greater than the first cut-off frequency of the soil layer. The soil domain is discretized into 40 sub-layers, $n = 40$, by considering 10 linear elements per Rayleigh wavelength. The eigenvalue problem leads to the computation of 160 eigenvalues with their corresponding eigenmodes. Half of the modes, which are related to the right lateral boundary ($\kappa_2 < 0$), are ranked as stated above. The magnitude of the exponential terms $\exp(\mathrm{i}k_s x)$, with $s = 1,80$, is displayed as a function of the log-scale of the dimensionless distance x/a, where a is a unit distance.

Figure 7.1 displays the magnitude of the exponential terms corresponding to the ranked eigenvalues k_s, Hamdan *et al.* [131]. For clarity purpose some wavenumbers are skipped as their effect is either identical or very close to those already displayed.

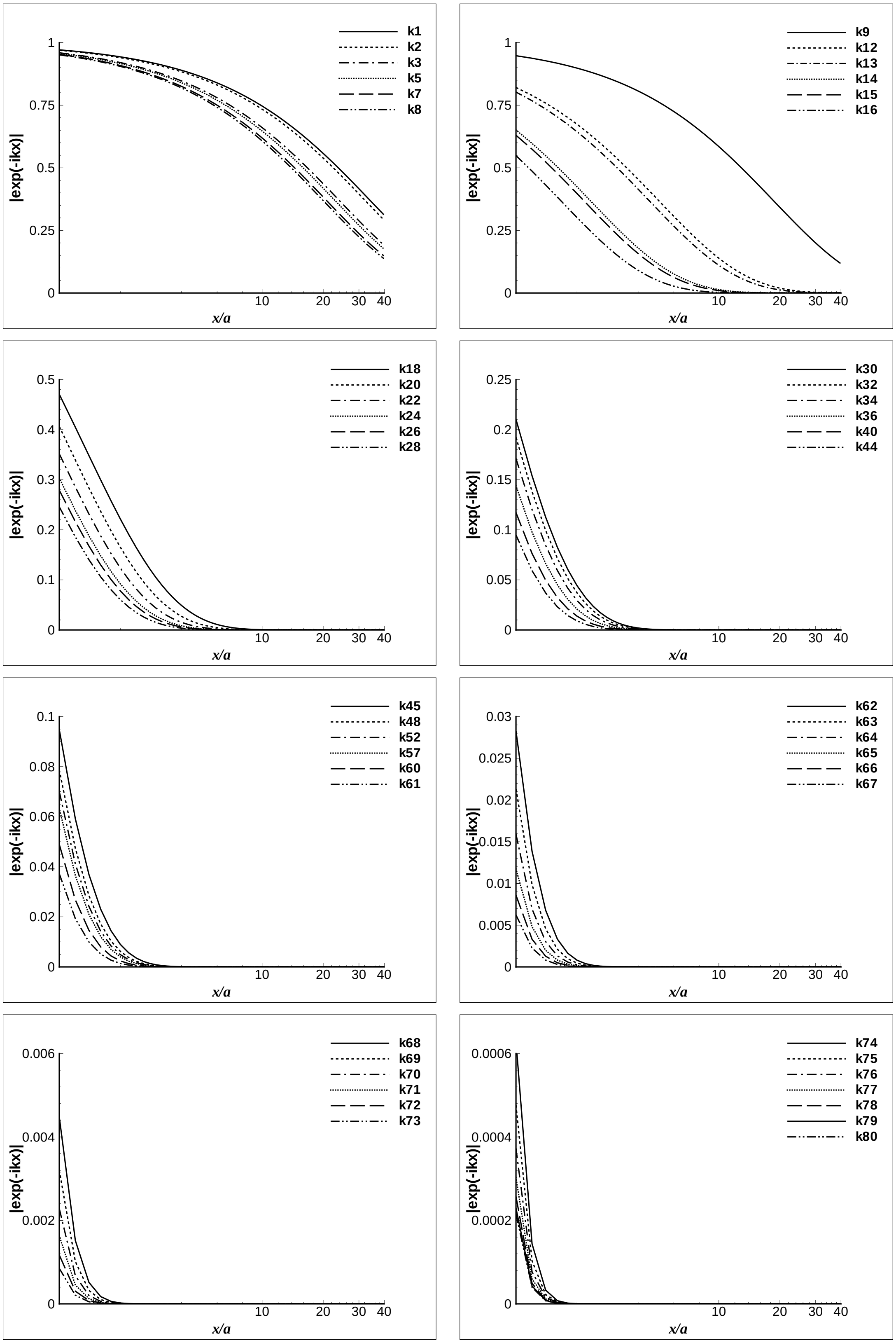

Figure 7.1: Variation of the exponential terms of the displacement beyond the lateral boundary, Hamdan *et al.* [131].

The first obvious remark is that all modes decay with the distance x. For the adopted ranking, the first modes present a less pronounced decay in comparison to the later modes. For example, the first eight modes, while decaying, the magnitude of $\exp(\mathrm{i}k_s x)$ is still greater than 0 by the distance x/a=40. The following modes, $9 \leq s \leq 16$, decay with a higher rate and some of which decay to 0 by $x/a \approx$10. For the last modes, the decay is very sharp and the magnitude reaches the zero value at very low distance. The other obvious remark is related to the magnitude of the exponential term which is around 1 for the first modes and then reduces with increasing ranking to become insignificant at the last modes, $|\exp(\mathrm{i}k_s x)| < 0.0006$. In other words, the modes with the smallest imaginary part present a significant response in terms of the magnitude of the exponential term and consequently a large distance beyond the lateral boundary is affected. With increasing the magnitude of the imaginary part of the wavenumbers the affected zone beyond the lateral boundary as well as the magnitude of the exponential terms are significantly reduced.

It is noticeable that the sharp decrease in the response of the exponential term and the very small affected zone beyond the lateral boundary are related to wavenumbers with minor influence. Those with major influence on the response, however, are to be investigated and will be called dominant modes. In what follows various numbers of these dominant modes are considered, n, $n/2$ and eventually 3. The solutions corresponding to these cases are compared to the solution of reference in which all $2n$ modes are included in the dynamic stiffness matrices.

The aim is to reduce the dimension of the modal matrix by reducing the number of modes and consequently reducing the related computational effort. More importantly, reducing the number of modes will lead to significant time saving in the analysis especially for soil domains with large number of sub-layers. This is a common practice in structural dynamics and seismology where analysts include only a few modes of vibration. However, the question of accuracy emerges such as what is the allowable percentage of error or to what extent is the solution is acceptable? Yoon [129] indicated that "*it is often advantageous and sometimes necessary to transform a set of the system equations of complex FE model into a set of reduced equations with a smaller number of degrees of freedom, the accuracy is inevitably affected, but the reduced accuracy is adequate from an engineering standpoint*". This will be dealt with in this work to validate the modified consistent transmitting boundaries formulated next.

7.4 Modified consistent transmitting boundary conditions

Selecting only some of the eigenmodes in the formulation of the consistent transmitting boundaries requires some mathematical alterations of expressions (3.37) and (3.39). Assume a number m of eigenmodes is selected, with $m < 2n$. In such case, the diagonal matrix $\mathbf{H}$ containing m eigenvalues remains square of dimension $m \times m$, the modal matrix $\mathbf{V}$ containing the eigenmodes becomes rectangular of dimension $2n \times m$. Seeking its inverse leads to an over-determined system and the inverse matrix is replaced by the pseudoinverse, or the Moore-Penrose inverse, which is denoted by $\mathbf{V}^{\dagger}$. Recalling equation (3.28)

$$\mathbf{F}^* = \left[\mathbf{A}_2^* \mathbf{u}^*_{,\mathbf{x}} + \mathbf{A}_3^* \mathbf{u}^*\right]_{x=0}, \tag{7.10}$$

and substituting the displacement vector derivatives with respect to x gives

$$\mathbf{F}^* = -\left[\mathrm{i}\mathbf{A}_2^* \mathbf{V}\mathbf{H}\mathbf{V}^{-\mathbf{1}} + \mathbf{A}_3^* \mathbf{V}\mathbf{V}^{-\mathbf{1}}\right] \mathbf{u}^*{}_{x=0}. \tag{7.11}$$

If the modal matrix is square then the product $\mathbf{V}\mathbf{V}^{-1}$ is the identity matrix. However, if the modal matrix is rectangular, the pervious product does not lead to the identity matrix, see Appendix **A**. Thus, the contribution of this product must be taken into account in the formulation of the matrix **R** corresponding to the dynamic stiffness of the right regular region. The dimension of the dynamic stiffness matrix **R** is still $2n \times 2n$. It is given by

$$\mathbf{R} = \mathrm{i}\mathbf{A}_2^* \mathbf{V}\mathbf{H}\mathbf{V}^{\dagger} + \mathbf{A}_3^* \mathbf{V}\mathbf{V}^{\dagger}, \tag{7.12}$$

where **H** contains the selected m wavenumbers, with $\kappa_2 < 0$, and **V** contains their corresponding eigenmodes columnwise. The dynamic stiffness matrix of the left regular region is formulated in the same manner leading to

$$\mathbf{L} = -\mathrm{i}\mathbf{A}_2^* \mathbf{V}^{'} \mathbf{H}^{'} \mathbf{V}^{'\dagger} - \mathbf{A}_3^* \mathbf{V}^{'} \mathbf{V}^{'\dagger}, \tag{7.13}$$

where $\mathbf{H}^{'}$ contains the selected m wavenumbers, with $\kappa_2 > 0$, and $\mathbf{V}^{'}$ contains their corresponding eigenmodes columnwise. The diagonal matrices **H** and $\mathbf{H}^{'}$ are of dimension $m \times m$.

Next, the computed wavenumbers are ranked in an ascended manner with respect to their imaginary part κ_2. The solutions corresponding to the cases $m = n$ and $m = n/2$ are computed and compared to the reference solution for which all eigenmodes are taken into account, $m = 2n$, in the formulation of the matrices **R** and **L**.

7.4.1 Test example: undamped soil model

Two depths of a soil domain, $1\lambda_R$ and $4\lambda_R$ are considered in order to show if there is any effect on the response when considering small and large sizes eigenvalue problems. The soil domain has the following characteristics: ρ =2000kg/m^3, E =100MPa and ν =0.25. Figures 7.2 and7.3 show a comparison of the surface displacements when using all eigenvalues and when selecting only half or quarter. In total, 40 and 160 eigenvalues with their corresponding eigenvectors are computed for the considered depths. For the lower depth, 10 and 5 eigenvalues are chosen in the current analysis for each lateral region when reducing the number of eigenmodes. As it is shown in Figure 7.2, the results are not in good agreement in terms of surface displacements. The relative error graphs show high values for both horizontal and vertical displacements exceeding 10%.

In the case of $4\lambda_R$ depth, where a total of 160 eigenmodes are calculated, 40 and 20 modes are used in the determination of the modified transmitting boundaries. A comparison of the surface vertical and horizontal displacements in Figure 7.3 shows that the results are relatively of better quality, in comparison to the case of $1\lambda_R$ depth, as the relative error is below 10% when half of the modes are used.

7.4.2 Test example: damped soil model

The previous example is used in this section with the introduction of damping and the same procedure is followed. Figures 7.4 and 7.5 show the vertical and horizontal displacements at the surface with their corresponding errors for $1\lambda_R$ and $4\lambda_R$ domain depths, respectively, when using all computed eigenmodes, half or only a quarter.

Similar conclusions are also drawn for the damped soil model. In the case of low depth model, using the modified transmitting boundaries lead to large discrepancies when comparing to the reference surface displacements, where all modes do contribute in the transmitting boundaries. In fact using half or a quarter of the modes for the case of $1\lambda_R$ depth lead to only use 10 or 5 modes, which are low numbers as the total number is 20 for each lateral boundary. For $4\lambda_R$ depth, however, the total number of modes is 80 and using half or a quarter, lead to use 40 and 20 respectively, and consequently provide better quality results.

From here, it is concluded that for small depth domains, it is not worth considering the modified transmitting boundaries as this leads to spurious reflections on the lateral boundaries and the number of sub-layers is not important anyway to make any savings in the computational time. For large depth domains, however, for which the number of sub-layers is important, it is shown that the modified transmitting boundaries lead to engineering quality results. Furthermore, using the modified version of the transmitting boundaries for such cases leads to significant computational savings

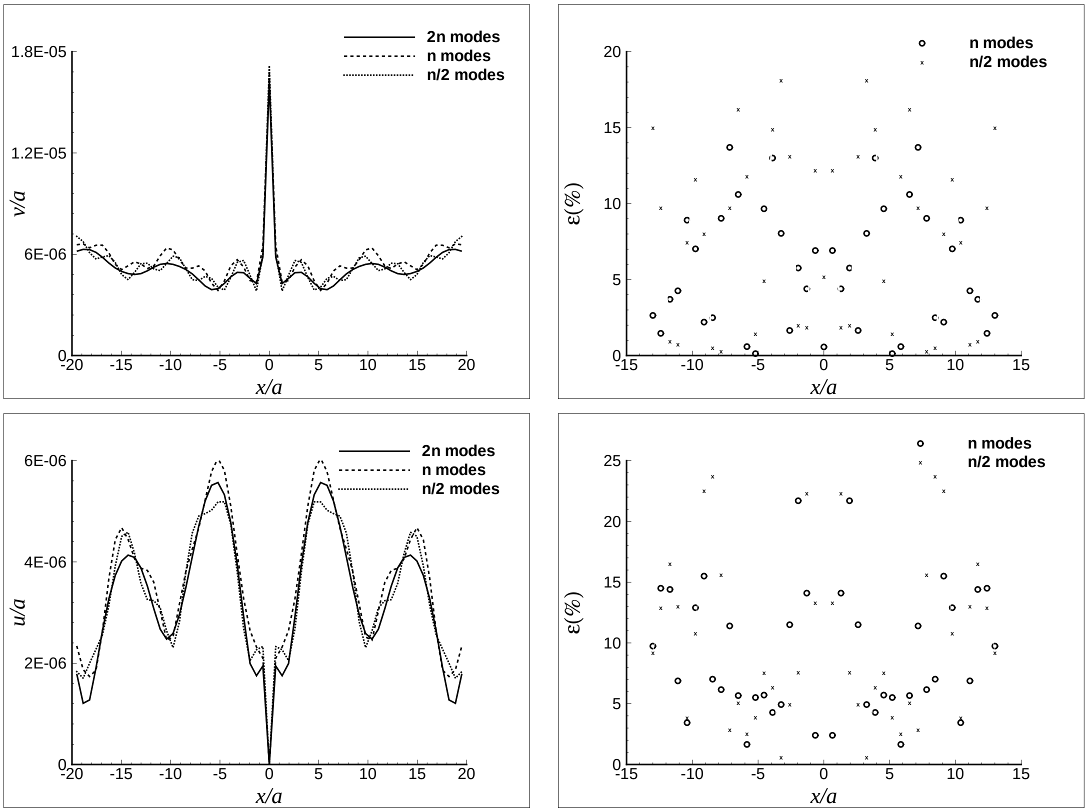

Figure 7.2: Surface displacements in the undamped case and their corresponding errors: $1\lambda_R$ depth.

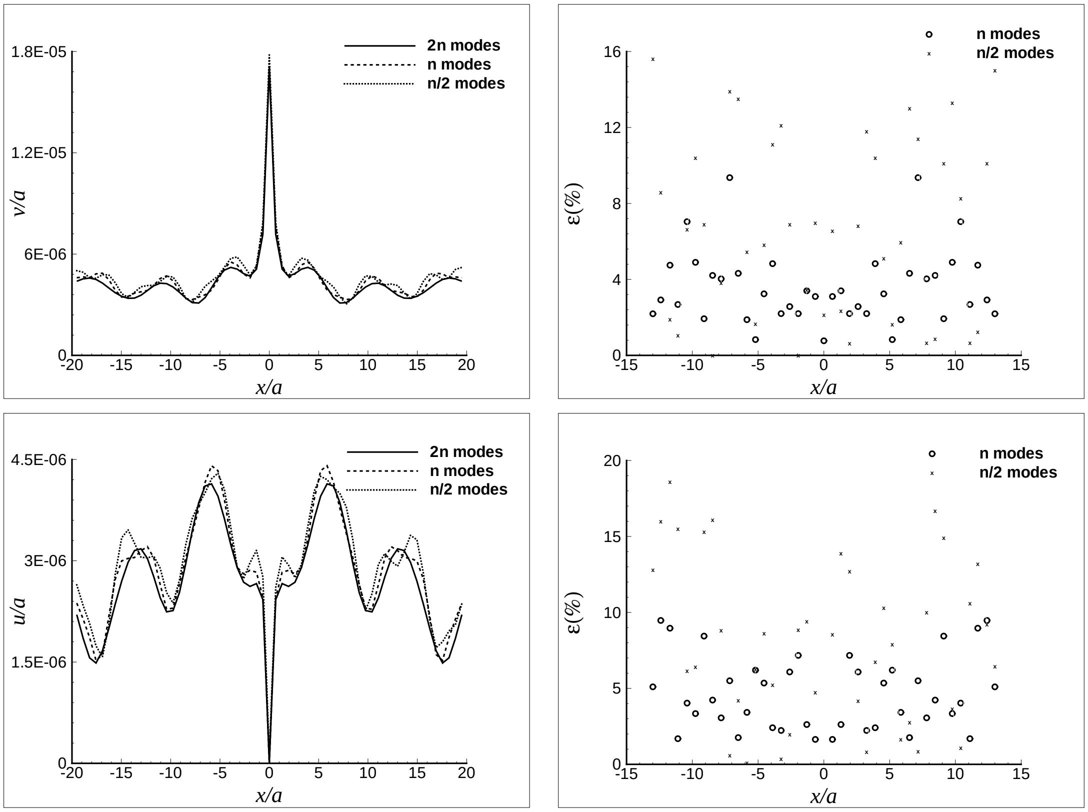

Figure 7.3: Surface displacements in the undamped case and their corresponding errors: $4\lambda_R$ depth.

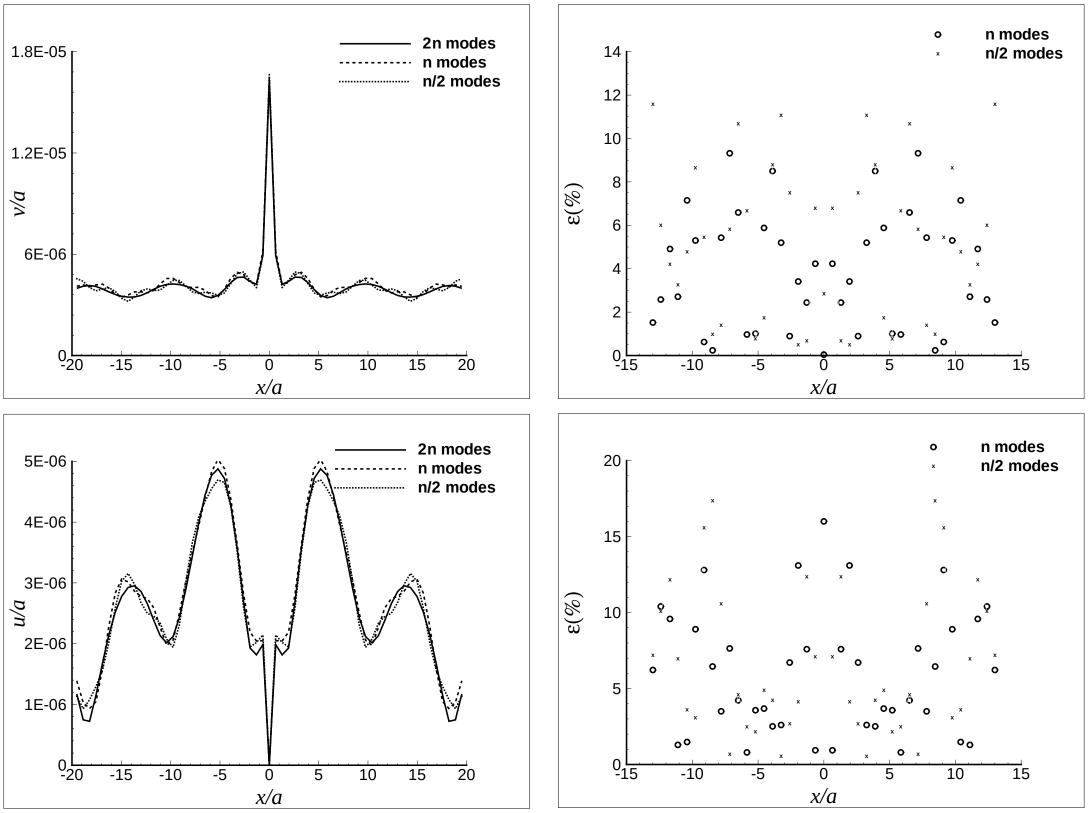

Figure 7.4: Surface displacements in the damped case and their corresponding errors: $1\lambda_R$ depth.

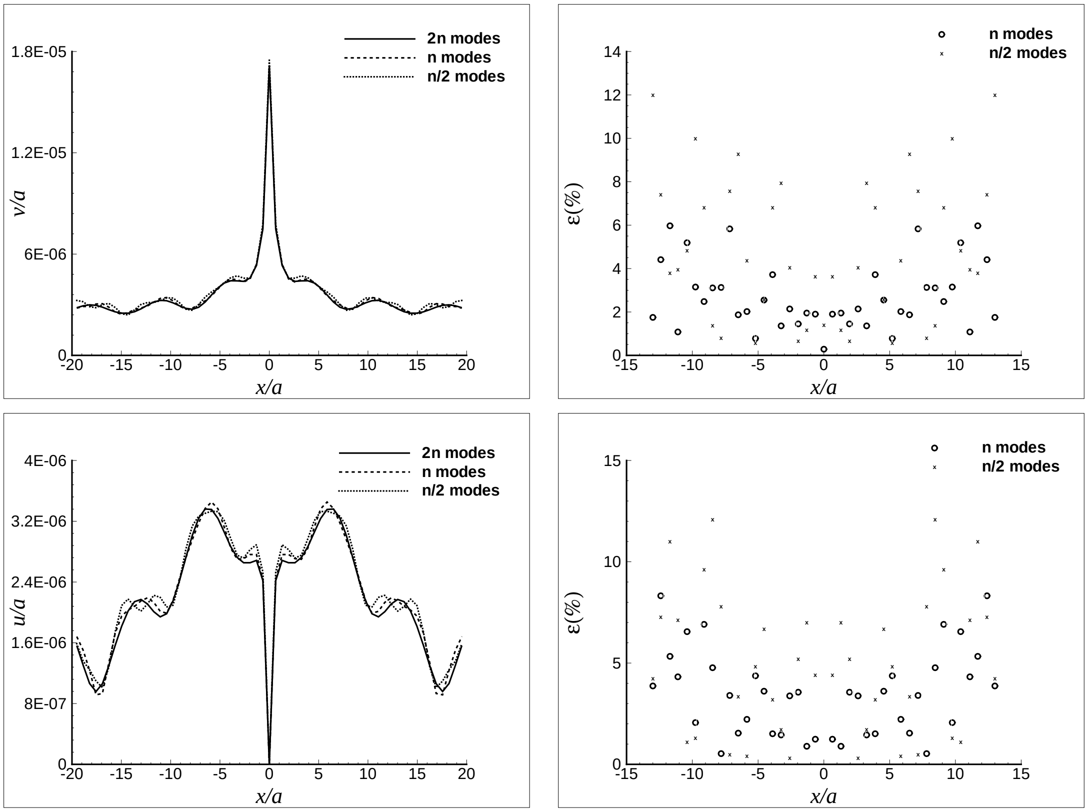

Figure 7.5: Surface displacements in the damped case and their corresponding errors: $4\lambda_R$ depth.

Figures 7.6a and 7.6b show the variations of the horizontal and vertical displacements with the normalised depth, z/λ_R, when different numbers of modes are used. Those are $2n$, n, $n/2$ and 3 modes. The results show that the responses for the cases using n and $n/2$ dominant modes is in good agreement with the case where all $2n$ modes are used, with the case of n modes giving better accuracy. The response corresponding to the use of only 3 modes with the lowest imaginary parts shows large discrepancies in comparison to the reference case. This shows that using very few modes does not allow enough energy radiation to infinity and hence causes waves to reflect at the lateral boundaries.

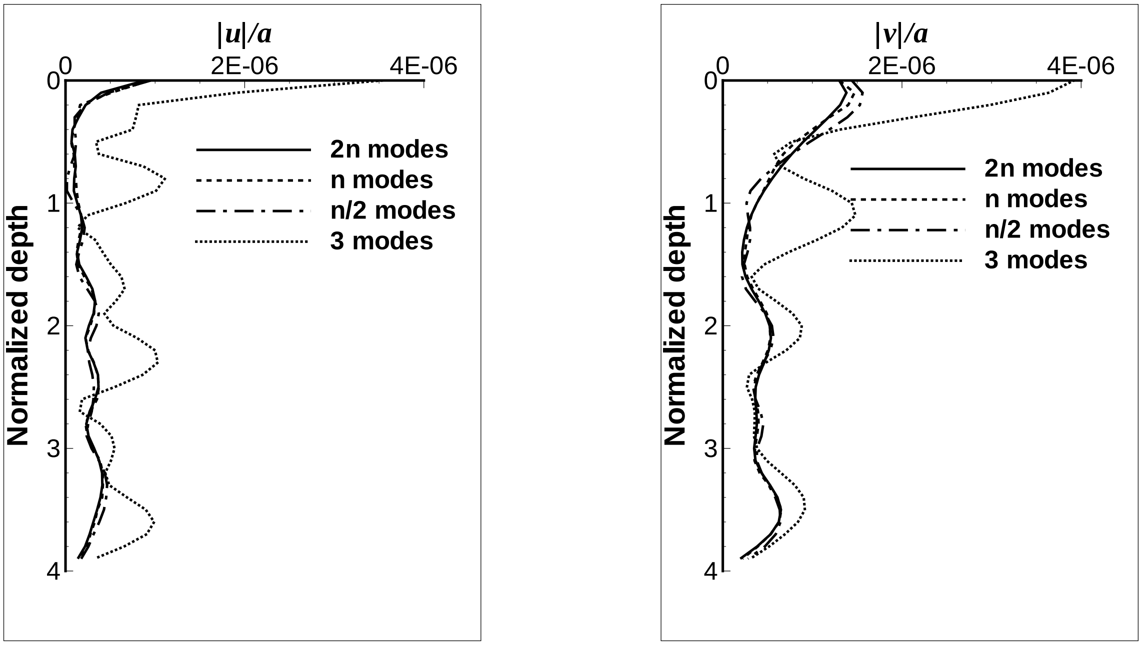

(a) Horizontal Displacement

(b) Vertical Displacement

Figure 7.6: Displacements variation with depth at the right lateral boundary, Hamdan *et al.* [131].

7.5 Effect on computational time

The effect of reducing the number of contributing eigenmodes on the computational effort is investigated. If a selected number of eigenmodes is used, it is therefore not necessary to compute all $4n$ eigenvectors of the eigenvalue problem (3.30). This obviously allows a significant reduction of the computational cost especially for large-depth computational domains. Figure 7.7a shows an example of cpu time used to compute the eigenmodes.

As the modifications introduced in section 7.4 affect the dynamic stiffness matrices of the lateral boundary, the determination of these matrices is also altered but in favour of saving some computational time as less columns are included in each matrix. Consequently, matrix inversion is also affected. The alteration in terms of run time depends, now, on the pseudoinverse.

Figure 7.7b shows the cpu time used to compute the dynamic stiffness matrix **R** corresponding to the right lateral boundary and eventually **L** corresponding to the left boundary, for different numbers of selected eigenmodes when the number of sub-layers is increased.

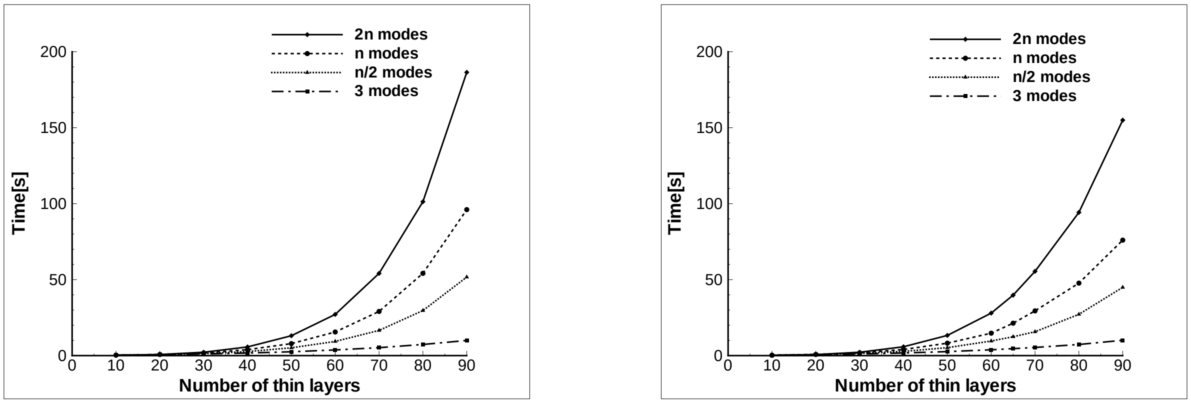

(a) Elapsed time for computing eigenvectors

(b) Elapsed time for computing the consistent dynamic stiffness matrices

Figure 7.7: Computational efficiency of the approach, Hamdan *et al.* [131].

It is clear from the results of Figure 7.7 that, when considering a high number of sub-layers and taking into account all eigenmodes, the computational cost corresponding to the computation of the eigenmodes and/or the computation of the dynamic stiffness matrices tends to increase exponentially. Reducing the number of contributing eigenmodes significantly reduces the computational time. For example, at high numbers of sub-layers, halving the number of contributing modes leads to around 50% saving in computational time. This is obvious from the previous figure where, for example, the run time required to compute either the eigenvalues or the dynamic stiffness matrices is reduced from 100s when using all eigenvectors in the solution to 50s when reducing this number by half. Better reduction is achieved for further reduction in the number of eigenmodes. The calculations were performed using a Fortran 77 code with double precision variables on an Intel(R) Xeon(R) 2.33 GHz processor with 1.95 GB of RAM under Microsoft Windows Server 2003.

7.6 Efficiency of the modified consistent transmitting boundary conditions

As demonstrated in the previous section, the computational cost is significantly reduced when using a reduced number of eigenmodes, when considering large depth soil media. To further assess the efficiency of the modified transmitting boundaries, examples of practical interest are dealt with next.

7.6.1 Wave propagation in multi-layered soil profile

Let us revisit the example presented in section 4.6.2 for simulating wave propagation in a soil profile with linear variation of stiffness, provided in expression (4.9) where α is the rate of linearity. In Chapter 4, the fundamental frequency of the soil medium was estimated by considering the area under the surface displacement curve and all computed modes were used in the formulation of the transmitting boundary conditions. The purpose of reconsidering this example is to investigate whether the finite element model with the modified transmitting boundaries would lead to similar results.

In an attempt to reproduce the results of Figure 4.23, the same numerical simulations are carried out again but this time with the modified transmitting boundaries. Figure 7.8 shows the results for the normalised area as a function of frequency, for various values of the linearity coefficient, when 2n, n, n/2 and only 3 eigenmodes are used. It is clear that using the modified transmitting boundaries with half or a quarter of the eigenmodes leads to similar results obtained with the unmodified transmitting boundaries, i.e. with 2n modes. However, using only 3 modes leads to discrepancies in the results at high frequencies. At the same time, if we are after the fundamental frequency of the soil medium, the results show that it is possible to predict it even with only 3 modes accounted for in the modified transmitting boundaries.

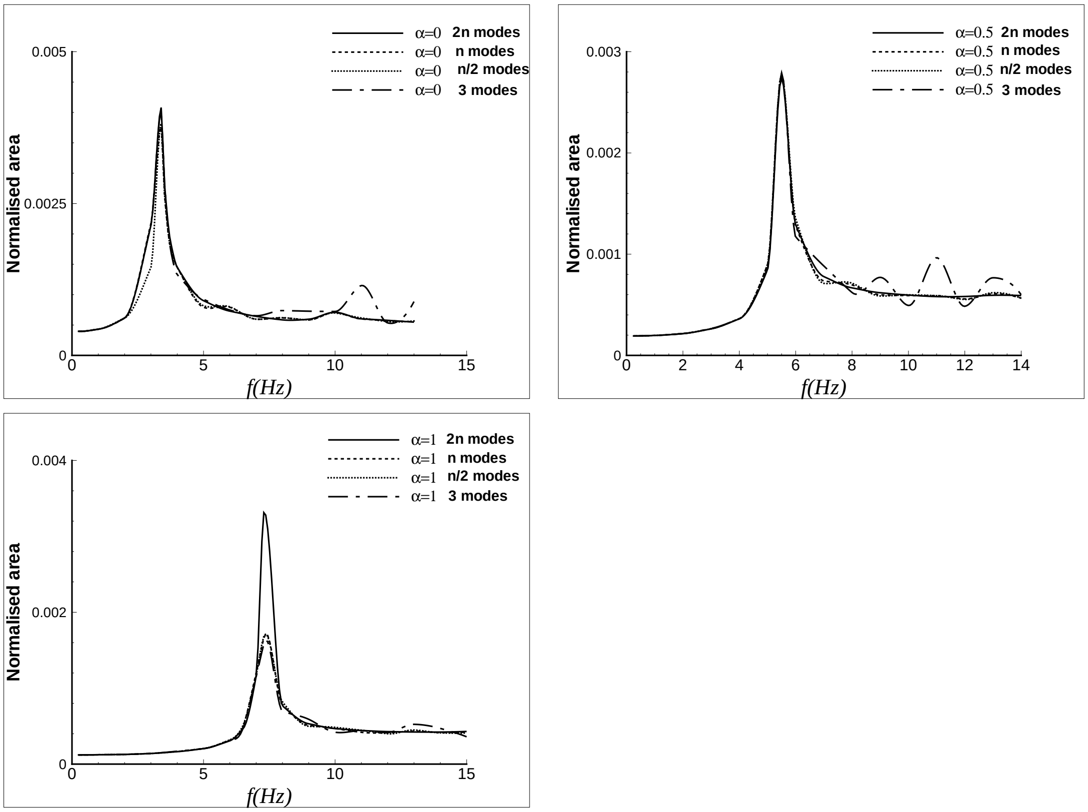

Figure 7.8: Effect of reduced number of eigenmodes on the fundamental frequency of layered soil profile.

Actually, great discrepancy for including only three modes is found especially in the high frequency region. The explanation of this is as follows. In the case of low frequencies, more precisely lower than the fundamental one, waves do not propagate and the response is similar to the static response. As the frequency increases and approaches the fundamental one, waves start to propagate all over the domain as it is demonstrated in sections 4.4.1 and 4.4.2. Including only the first three smallest wavenumbers produced significant difference in the surface displacements in sections 7.4.1 and 7.4.2. Accordingly, the surface area is affected by this discrepancy leading to the difference at frequencies higher than the fundamental frequency of the soil profile. Overall and based on the numerical results, reducing the number of eigenmodes to include only n and $n/2$ at each lateral boundary produced good agrement compared to including all modes. Including only the smallest 3 eigenmodes is not sufficient enough to generate very accurate results especially for frequencies higher than the fundamental frequency of the medium.

7.6.2 Surface rigid foundation on a stratum

A rigid surface strip foundation is assumed to be resting over a homogenous soil layer overlaying bedrock. The foundation has a width of $2B$, where $2B = H$ and H being the depth of the soil layer. The soil medium has shear modulus and density of unit value, a Poisson's ratio of 0.3 and a damping ratio of 0.05. For the sake of validation, the numerical example presented by Tassoulas [29] is used in this section. Figure 7.9 illustrates a schematic diagram of the finite element model.

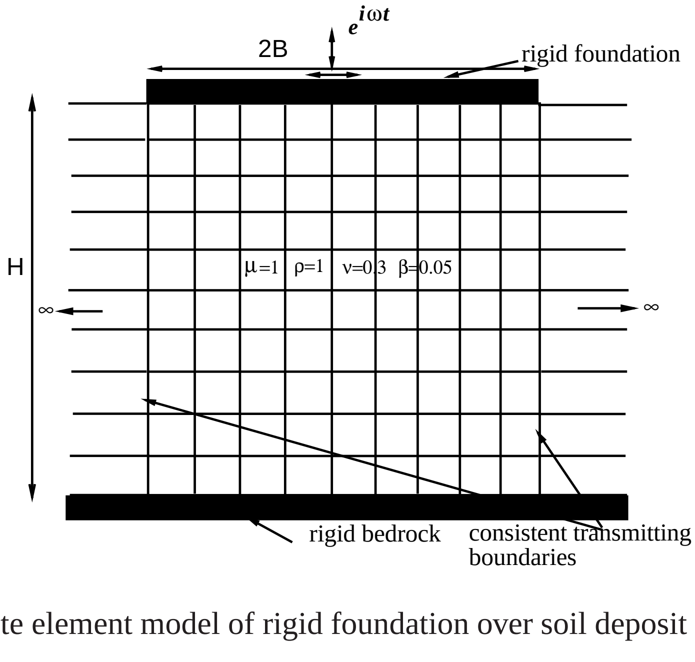

Figure 7.9: The finite element model of rigid foundation over soil deposit over rigid bedrock.

The centre of the foundation is subjected to a unit time-harmonic load with a wide range of frequencies ω. The vertical and horizontal displacements $\mu|v|$ and $\mu|u|$ are computed under the load and displayed for various dimensionless frequency values $\omega H/2\pi c_s$, where c_s is the shear wave velocity of the soil medium. The computational domain is divided into 10 sub-layers, $n = 10$, with equal thicknesses not exceeding a tenth of the Rayleigh wavelength corresponding to the highest applied frequency. The highest applied frequency was 0.1Hz which corresponds to a Shear wavelength of 10m, which is equivalent to the layer depth. A total of 20 wavenumbers are computed and used to compute the lateral boundaries nodal forces using the consistent transmitting boundaries.

Figure 7.10 shows the real and imaginary parts of the horizontal and vertical dynamic compliances against the dimensionless frequency when using the modified consistent transmitting boundaries with 10 and 5 modes, which correspond to n and $n/2$ respectively. The case with only 3 modes is also considered. In comparison to the results involving the consistent transmitting boundaries, with all $2n$ modes, the results show very similar variations and an overall acceptable agreement. Although the case with only 3 modes produces roughly similar results, it leads to the largest discrepancies, while the case with n modes leading to the closest results. Overall, the same trend is generated even when reducing the number of eigenmodes to only the first three ones. However, if accurate solutions are sought more eigenmodes must be included in the analysis.

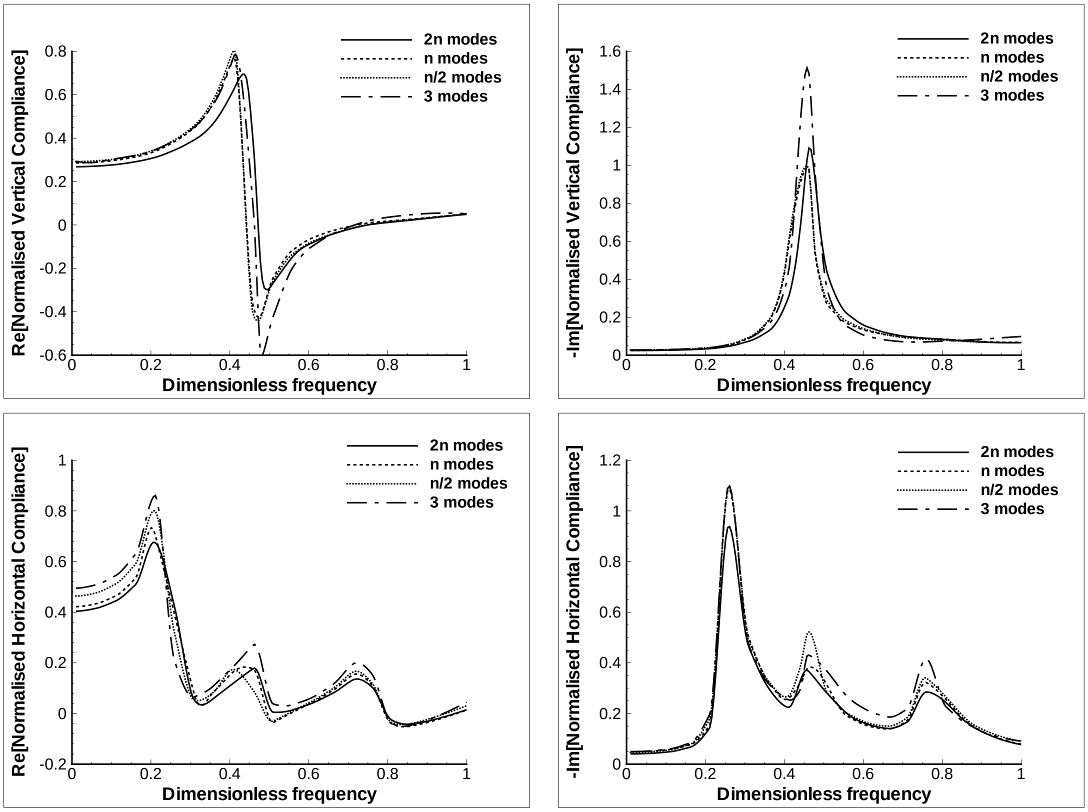

Figure 7.10: Dynamic compliances of rigid foundation over a soil layer overlaying bedrock, Hamdan *et al.* [131].

Increasing the number of wavenumbers in the analysis to n produces a closer response to the reference solution. In the vertical response, there is a slight shift in the response towards the left, which is a decrease in the fundamental frequency of the soil stratum. However, reducing the number of eigenmodes generated the same response with amplifying or de-amplifying the response. The horizontal compliances of the foundation results show that there is no change in the fundamental frequency but the curve for each case has shifted up indicating the stiffness of the soil has decreased. The variation of the normalised displacements under the centre of the foundation are also displayed in Figure 7.11. To sum up, the general trend is produced when reducing the number of wavenumbers in the analysis. Using only the first three lowest wavenumbers leads to the discrepancy but the trend is very acceptable.

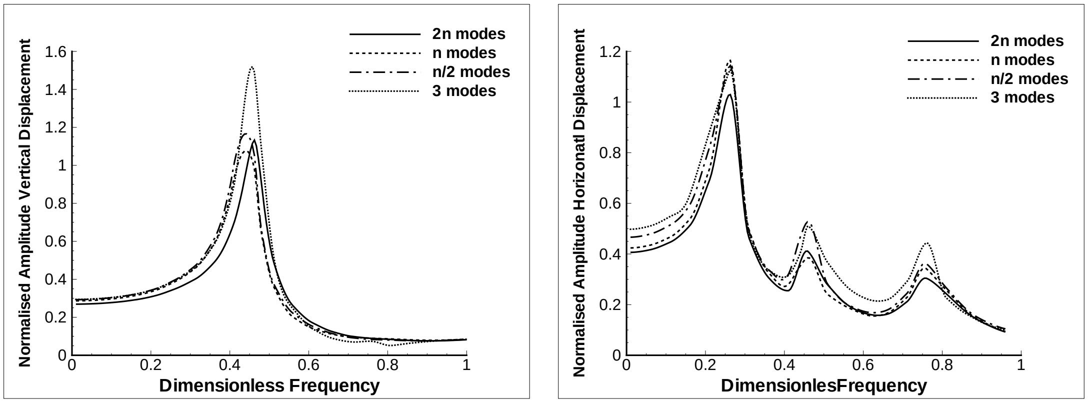

Figure 7.11: Variation of normalised displacements with frequency.

7.6.3 Wave reduction by empty trench

A soil domain of $30\lambda_R$ in length and $3\lambda_R$ in depth subjected to a time-harmonic load at the soil surface centre is considered here. The characteristics of the soil are 40MPa, 1700kg/m^3, 0.25 and 2.5% for the shear modulus, density, Poisons' ratio and damping ratio, respectively. The associated Rayleigh wavelength is around 7.1m. An empty trench is installed at $5\lambda_R$ from the dynamic load to reduce the effect of transmitted waves towards the right part of the domain. This kind of problem is typical and was dealt with by many authors, such as Segol *et.al* [132], Laghrouche and Le Houedec [99, 100], and Ahmad and Al-Hussaini [125]. To investigate the wave barrier effectiveness, the amplitude reduction factor and the average amplitude reduction factor could be used. The amplitude reduction factor, A_r, evaluates the effectiveness locally and is defined as the ratio between the amplitude of the displacement at the surface after installing the trench to the amplitude of the surface displacement at the same point before installing the trench. The average reduction factor, however, is a global measure as it considers the effect of the wave barrier over a certain distance X of the protected area beyond the wave barrier. It is given by

$$\bar{A_r} = \frac{1}{X}\int_0^X A_r dx. \tag{7.14}$$

This example is used to determine the effectiveness of the wave barrier when using the consistent transmitting boundaries and the modified version. The soil medium is subdivided into 30 sub-layers (n=30) and hence a total of 60 eigenmodes are obtained for each of the lateral boundaries. First, the amplitude reduction factor is computed from the point of application of the load for normalised depth d/λ_R and width b/λ_R of the trench taken as 1 and 0.1, respectively. A distance of $10\lambda_R$ is considered after the trench. It is computed for the cases corresponding to $m = 2n$, n and $n/2$. The case involving only 3 eigenmodes is also considered and the results are displayed in Figure 7.12a. The figure clearly shows that the results for n and $n/2$ eigenmodes are in very good agreement with those obtained when all $2n$ eigenmodes are included. This indicates that the corresponding modified consistent transmitting boundaries perform as well as the original version which uses all eigenmodes. However, the results associated with including only 3 modes deteriorates in the vicinity of the vertical lateral boundary of the domain. This indicates partial wave reflection at the boundary.

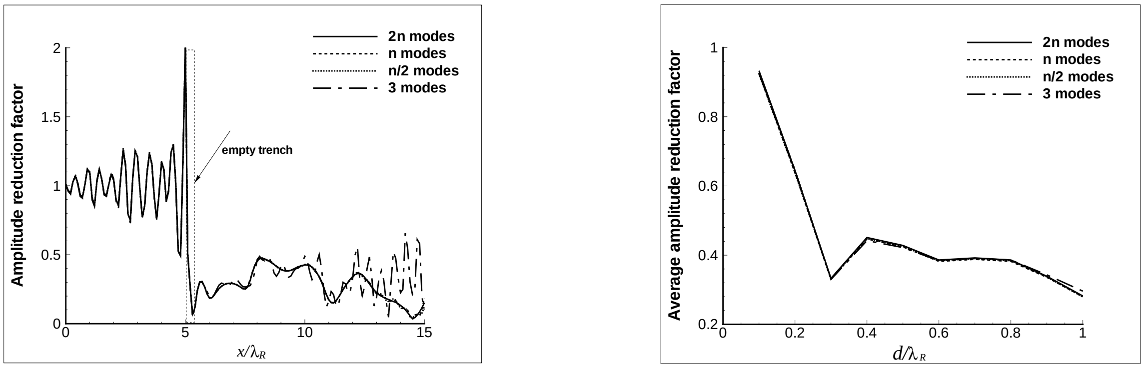

(a) Amplitude reduction factor at the surface

(b) Average amplitude reduction factor with normalised depth

Figure 7.12: Effect of the number of eigenmodes on the screening efficiency of an empty trench, Hamdan *et al.* [131].

The average amplitude reduction factor $\bar{A_r}$ given in expression (7.14) is computed for various normalised depths when its width is fixed, b/λ_R=0.1. The results shown in Figure 7.12b illustrate the variation of $\bar{A_r}$ with d/λ_R when considering both the consistent transmitting boundaries and the proposed modified version with n, $n/2$ and 3 eigenmodes in the formulation. The results are in very good agreement again with the reference solution. Nonetheless, there is some difference in the case of including only 3 wavenumbers, though the results follow the same trend. Overall, there is good agreement when considering the average amplitude reduction factor even when using only 3 modes unlike the case of computing the amplitude reduction factor. This may be due to the fact that the oscillation effect around the reference solution seen in Figure 7.12a cancels when using the integral in expression (7.14). In fact, the provided results compare very well to those provided in reference [126] obtained by the finite element package Abaqus.

7.7 Concluding remarks

The TLM is revisited in this chapter with the aim to reduce its computational cost. For a Cartesian computational domain with n sub-layers, a second-order eigenvalue problem of dimension $2n$ is reduced to the first order with the dimension doubled to $4n$, as a consequence. The obtained solution leads to the evaluation of the dynamic stiffness matrices with $2n$ eigenmodes included in each of the force vectors applied on the lateral boundaries to allow the radiation of waves away to infinity.

The proposed modified version of the consistent transmitting boundaries involves fewer eigenmodes with dominant effect. Those are defined as the modes whose eigenvalues have the smallest imaginary part. The modal matrices become rectangular and hence pseudoinverse matrices are used in the formulation of the modified consistent transmitting boundaries.

It is shown that computing a selected number of eigenmodes significantly reduces the computational cost of the model especially for problems with large depths, in terms of the wavelength, and when a wide range of frequencies is to be covered. For the test problems considered in this chapter, the modified consistent transmitting boundaries performed like the unmodified version when the most dominant eigenmodes are included in the dynamic stiffness matrices. Using only the first 3 modes, performs well except in the vicinity of the lateral boundaries of the computational domain where wave reflection occurs leading to erroneous solutions.

Chapter 8

Some applications with unstructured triangular mesh grids

8.1 Introduction

This chapter is devoted to some applications exploiting the benefits of the numerical tool, developed throughout this dissertation, with unstructured triangular mesh grids. The advantages of using unstructured mesh grids include the possibility of employing available mesh generator packages and the flexibility they offer to include complex geometries and discontinuities. This obviously makes the numerical tool more attractive for dealing with problems of practical interest as well as offering possibilities for further developments. The dynamic behaviour of non-horizontal soil profiles is first analysed. It is followed by applications of surface rigid foundations over non-horizontal profiles. Various shapes of wave barriers are then introduced to examine surface vibration reduction. This chapter closes by presenting stationary harmonic loading of several configurations of railway embankments where structured mesh grids can be difficult to obtain. The soil-foundation, the soil-slab and the soil-barrier interfaces are assumed to be in fully bonded contact.

8.2 Dynamic behaviour of soil media with non-horizontal profile

The fundamental frequency of a soil layer over horizontal rigid bedrock can be estimated from expressions (4.1) and (4.2). However, for cases where the bedrock is inclined the previous expressions are not valid anymore. Therefore, numerical solutions are the alternative for such cases and for many problems of practical engineering interest. In the case of 2-layer soil profile, approximated solutions are also available and presented in expressions (4.8a) and (4.8b). If the layers interface is inclined, the fundamental frequency of the system will be affected and again numerical solutions can be used. Therefore, the effect of inclined rigid bedrock and inclined soil layer interface over horizontal bedrock on the fundamental frequency of the soil deposit is investigated next. It is worth indicating that two separate eigenvalue problems are solved here, one for each lateral regular region, due to the difference of geometry for the two lateral boundaries.

8.2.1 Dynamic behaviour of a soil layer over inclined bedrock

A numerical example was presented in section 4.7.3 to demonstrate the ability of the numerical code to simulate wave propagation in the case of soil layer over inclined rigid bedrock. A more detailed parametric study is performed here by exploiting the benefits of the numerical model with unstructured triangular mesh grids.

A homogenous soil domain of length and depth of 30m and 12m, respectively, and with the same properties used in section 4.2 is revisited. A damped case is considered by taking a damping ratio of 5%. Two configurations of the model are illustrated in Figure 8.1. The bedrock is assumed to be horizontal for the reference solution where the fundamental frequencies of the vertical and horizontal loadings are respectively 5.9Hz and 3.1Hz. The bedrock is inclined by angles of 10°, 15° and 20° leading to a decrease in the volume of the soil layer, for the case of Figure 8.1a, due to the decrease of the depth of the right side lateral boundary by $\Delta H = X \tan\theta$, with X being the length of the domain.

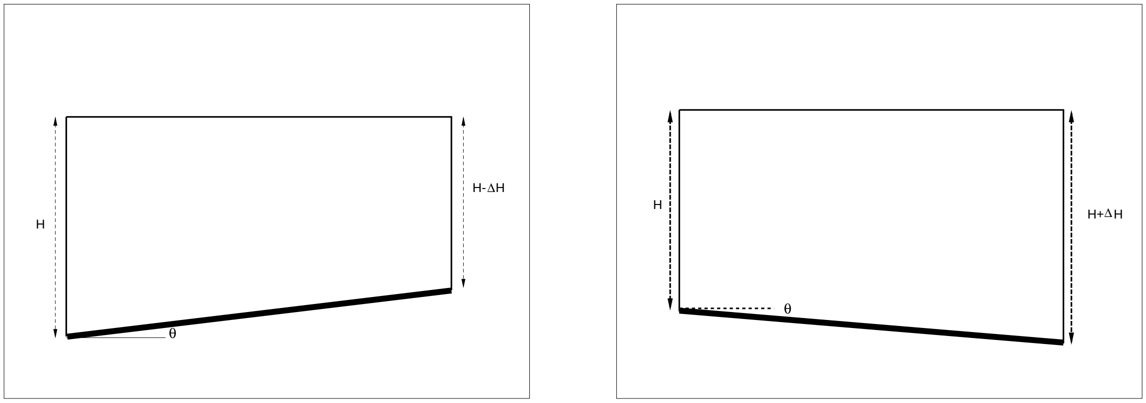

(a) Soil layer over inclined base (volume decrease) (b) Soil layer over inclined base (volume increase)

Figure 8.1: Schematic diagram of a soil layer over inclined bedrock.

Following the analysis of section 4.4, the frequency of the applied load is varied and the area under the surface displacement curves is computed for both vertical and horizontal loading cases. The top plots of Figure 8.2 show the normalised area corresponding to the vertical (left) and horizontal (right) responses of the inclined soil model for several angles of base inclination, which lead to a reduction in the volume of the soil domain. It is clear that there is a shift in the vertical and horizontal fundamental frequencies for each angle of inclination. The fundamental frequencies are increased. This was anticipated as the average depth of the soil layer is decreased, the fundamental frequency should increase due to the decrease in the denominators of expressions (4.1) and (4.2).

The bedrock is then inclined by the same angles but with increasing the volume of the soil layer due to increasing the right side depth of the layer by ΔH. The corresponding results are plotted in the bottom graphs of Figure 8.2. Again, as expected, the fundamental frequencies of the soil layer decrease as the average depth of the soil increases. It is clear that the fundamental frequency of the vertical response has increased from 5.9Hz, for $\theta = 0^\circ$, to around 12Hz, for $\theta = 20^\circ$, in the case of "volume decrease" where as it is decreased from 5.9Hz, for $\theta = 0^\circ$, to around 3.8Hz, for $\theta = 20^\circ$, in the case of "volume increase". The same observation is also noticed in the case of the of horizontal loading.

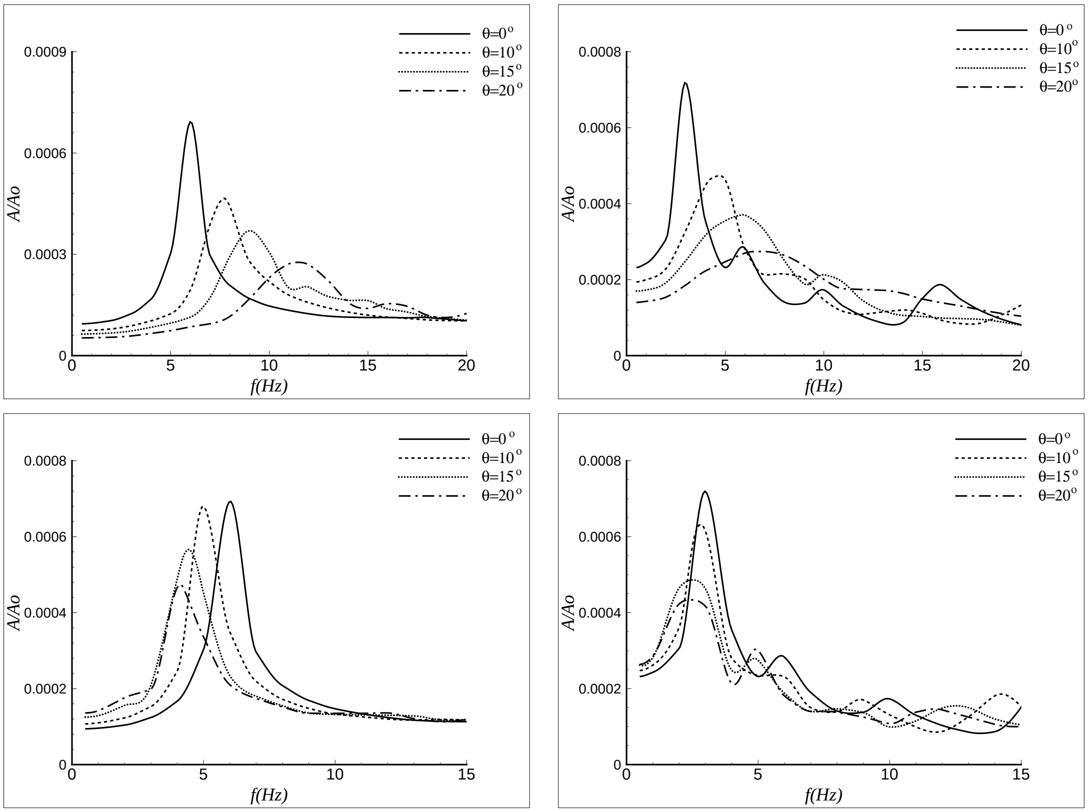

Figure 8.2: Dynamic response of a soil layer over inclined rock: vertical response of volume decrease (top left), horizontal response of volume decrease (top right), vertical response of volume increase (bottom left) and horizontal response of volume increase (bottom right).

8.2.2 Dynamic behaviour of a two-layer soil medium with inclined interface over horizontal bedrock

Up to now, horizontal layering of the soil medium is assumed. For example, Jones and Hunt [105] examined the effect of a soil layer inclination over half-space on the surface vibrations induced by an internal loading. A stepwise fashion method was employed in their simulation to mesh the interface between the inclined layer and the underlain half-space. There is no need for such meshing as unstructured mesh grids are employed here. An approximated solution for estimating the fundamental frequency of a 2-layer soil profile was presented in section 4.6.1 and is used here to obtain the reference solution for horizontal layers. In the current section, the same example is revisited but with considering an inclined interface between the layers. Hence, the dynamic behaviour of the 2-layer soil profile is re-examined. The configurations of the model are illustrated in Figure 8.3. The upper layer is first inclined with angles of 5° and 7.5°, respectively. This leads to a decrease of the right side thickness of the upper layer for the left figure and an increase in the case of the right side figure, respectively. The fundamental frequencies of the vertical and horizontal responses of the soil profile are displayed in the upper diagrams of Figure 8.4, left and right, respectively.

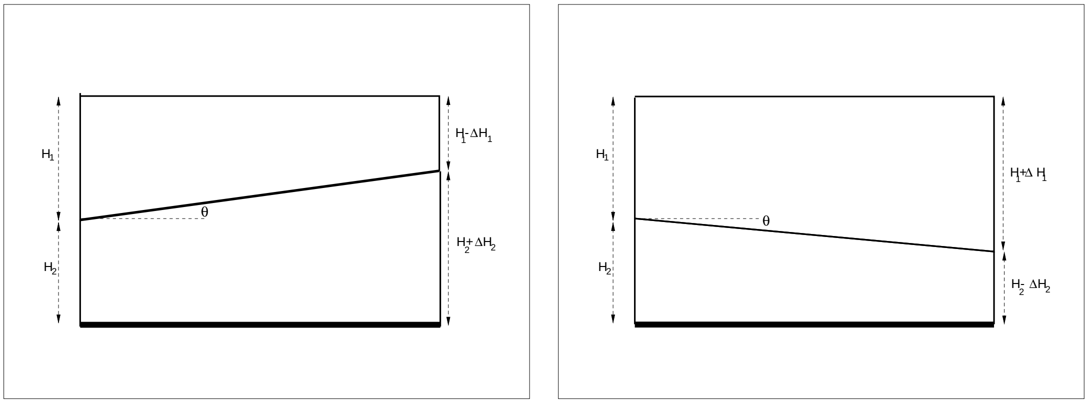

Figure 8.3: Schematic diagram of 2-layer soil profiles with inclined interface over horizontal bedrock.

It is obvious that the fundamental frequencies are affected by the inclination of the interface, in comparison to the horizontal interface case. Those are increased in the top graphs and decreased in the bottom graphs. However, there is no noticeable change related to the two angles of inclination, which are very close to each other. Further inclination with larger angles would probably affect the frequencies.

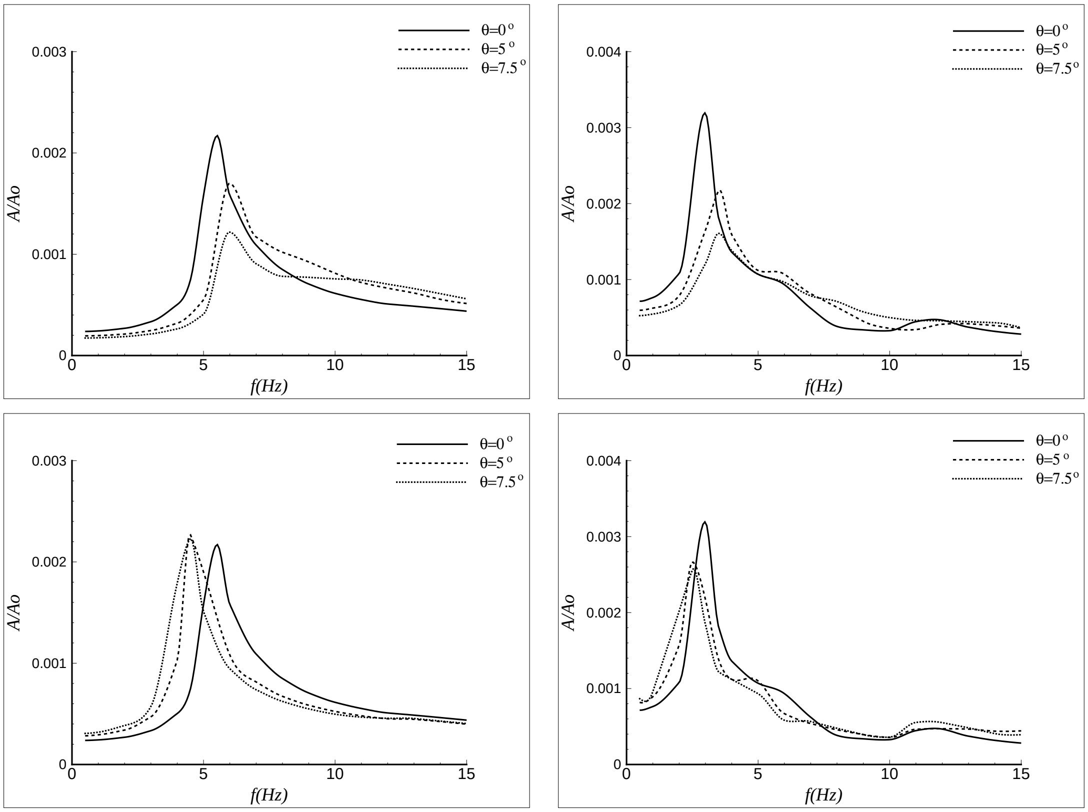

Figure 8.4: Dynamic response of an inclined interface 2-layer soil over horizontal bedrock: vertical response of volume decrease of upper layer (top left), horizontal response of volume decrease of upper layer (top right), vertical response of volume increase of upper layer (bottom left) and horizontal response of volume increase of upper layer (bottom right).

8.3 Harmonic vibration of a surface rigid foundation over soil media with non-horizontal profile

Similar soil profiles are considered in this section with a surface rigid foundation subjected to a harmonic loading. The effect of bedrock and soil layer interface inclination on the dynamic compliances are investigated for various inclination angles.

8.3.1 Rigid foundation over soil layer over inclined rigid bedrock

An application related to the harmonic vibration of rigid foundations resting over a soil layer overlaying horizontal rigid bedrock was presented in section 7.6.2. The same example is revisited again here but with considering an inclined bedrock. The dynamic response of the rigid foundation is examined by comparing its behaviour with the reference case, with the horizontal bedrock. The angle of inclination is increased leading to a decrease or an increase in the depth of the right lateral boundariy. The dynamic compliances of the foundation are computed and plotted against the dimensionless frequency; both terms are defined in section 7.6.2.

Figure 8.5 shows the horizontal and vertical compliances for the case where bedrock inclination leads to a volume decrease (Figure 8.1a). For the case where the bedrock inclination leads to an increase of volume (Figure 8.1b), the compliances results are reported in Figure 8.6. For the first case, the results of Figure 8.5 show the response of the foundation shifts to the right as the angle of inclination increases. This was expected as the real part of the compliance represents the stiffness and inertia of the soil, while the imaginary part represent the soil damping. As the soil volume decreases, the soil resonance frequency increases. For the second case, Figure 8.6, the main remark is that as the depth of the right lateral boundary increases, the resonance frequency of the soil decreases. The other remark is that the amplitude of the horizontal resonance for the inclined base cases are much higher than for the reference case. This is more obvious, as shown in Figure 8.7, when plotting the normalised amplitudes of the vertical and horizontal displacements.

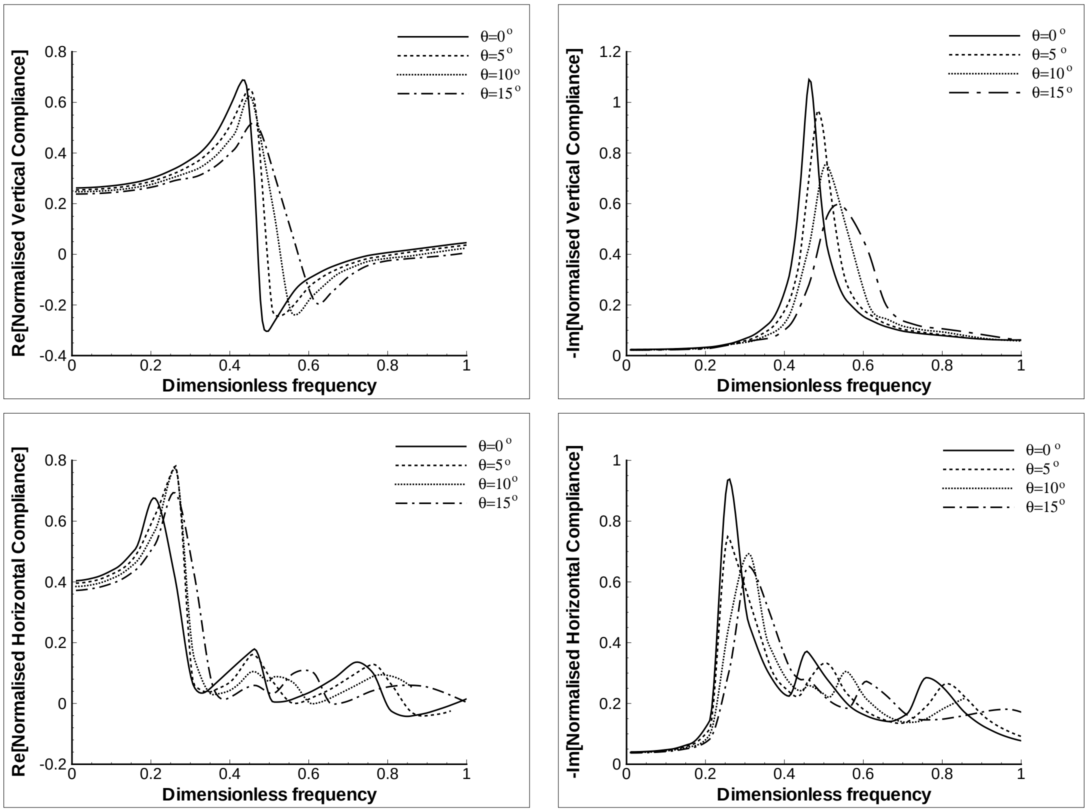

Figure 8.5: Compliances of surface rigid foundation over inclined rigid bedrock (volume decrease).

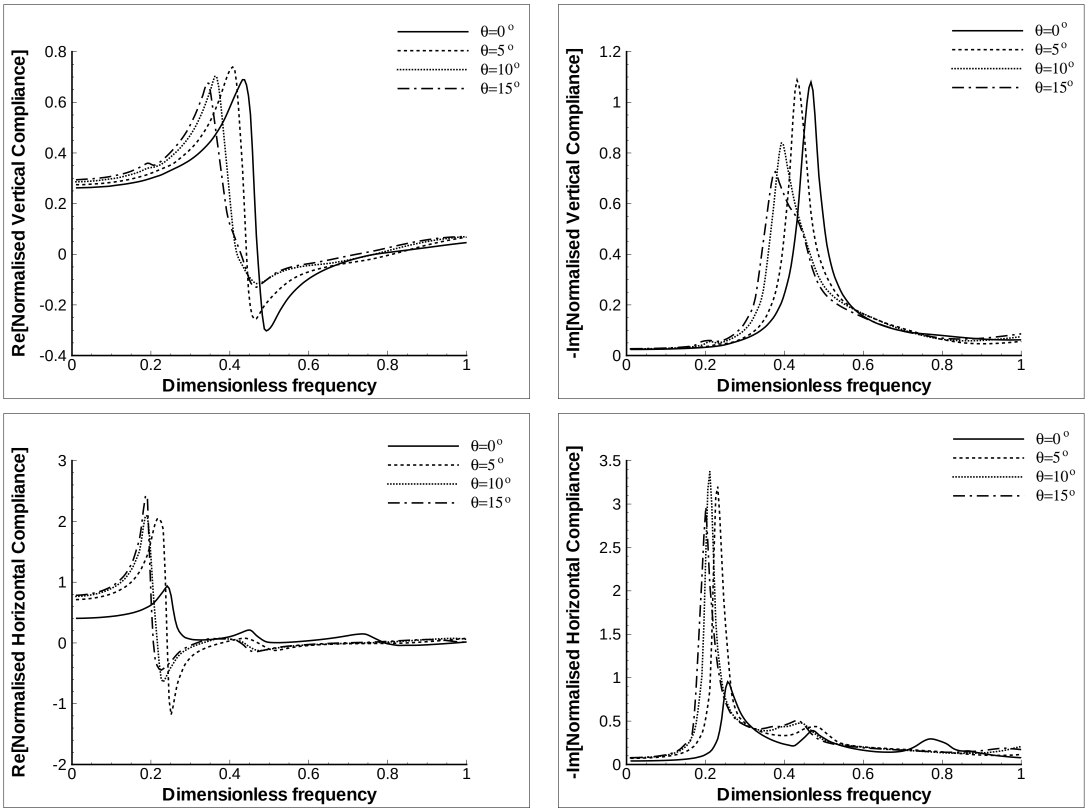

Figure 8.6: Compliances of surface rigid foundation over inclined rigid bedrock (volume increase).

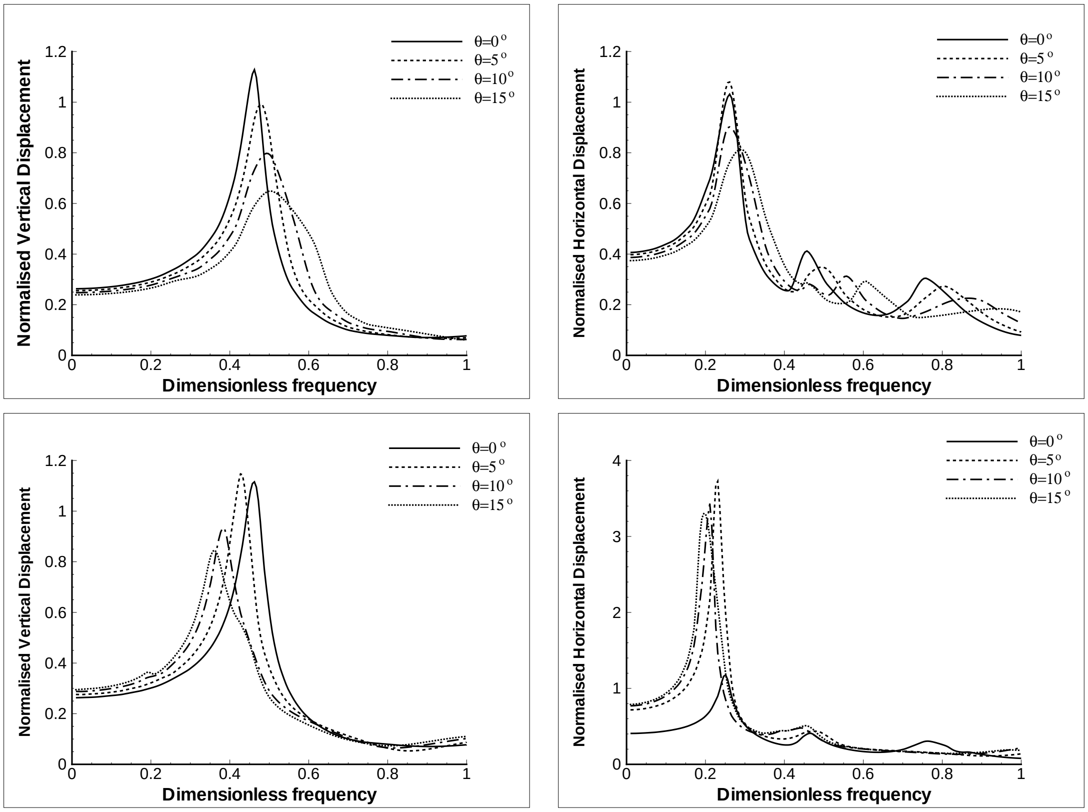

Figure 8.7: Variation of displacements amplitude with frequency: vertical response of volume decrease (top left), horizontal response of volume decrease (top right), vertical response of volume increase (bottom left) and horizontal response of volume increase (bottom right).

8.3.2 Rigid foundation over 2-layer soil medium with inclined interface over horizontal bedrock

In this section, the effect of a soil interface inclination between two layers over horizontal bedrock on surface foundation compliances is examined. The interface is inclined in the same manner as in section 8.2.1. The total depth of the soil profile satisfies (H/B=4), where B is the half width of the foundation. The shear modulus of the bottom layer is twice the shear modulus of the upper layer. The soil densities, Poisson's ratios and damping ratios are considered the same for both layers, (ρ_1/ρ_2=1), (ν_1/ν_2=1) and (β_1/β_2=1). The interface is thereafter inclined by 5°, 10° and 15° and the compliances of the foundation are plotted in Figure 8.8. It is obvious from Figure 8.9 that the interface inclination does not have significant effect on the natural frequency of the soil profile. The variations of the compliances with the dimensionless frequency remain practically unchanged for all inclinations considered.

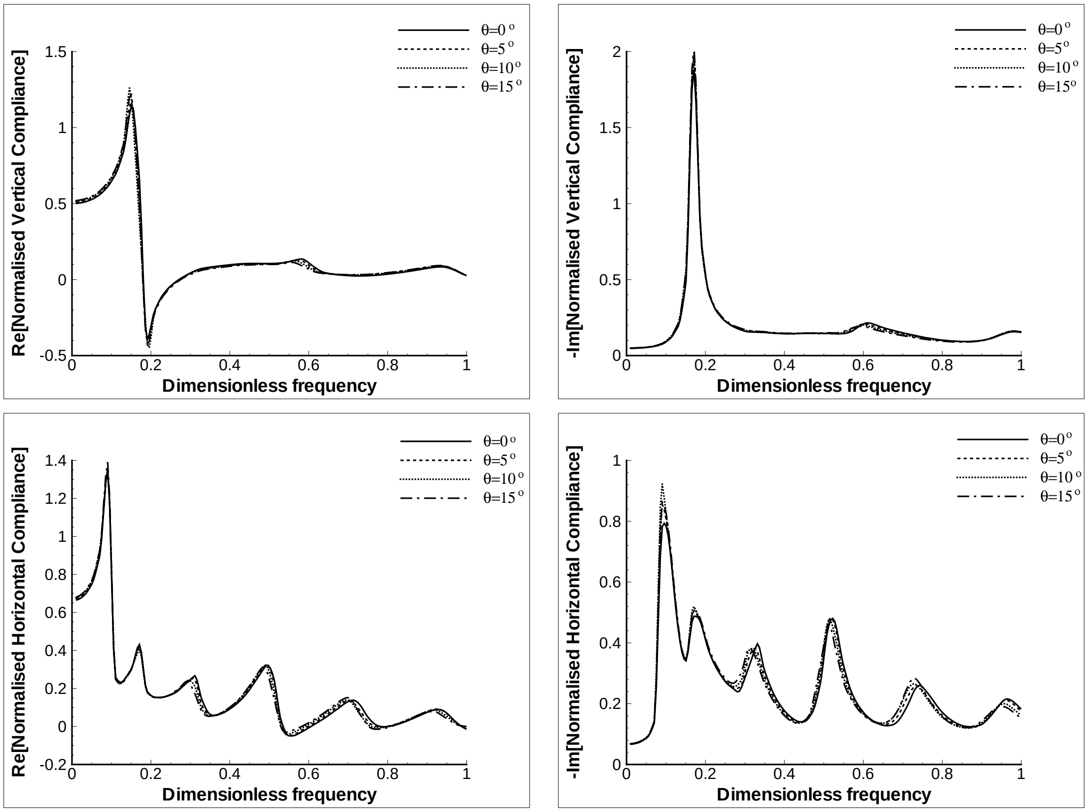

Figure 8.8: Effect of soil interface inclination on compliances of surface rigid foundation.

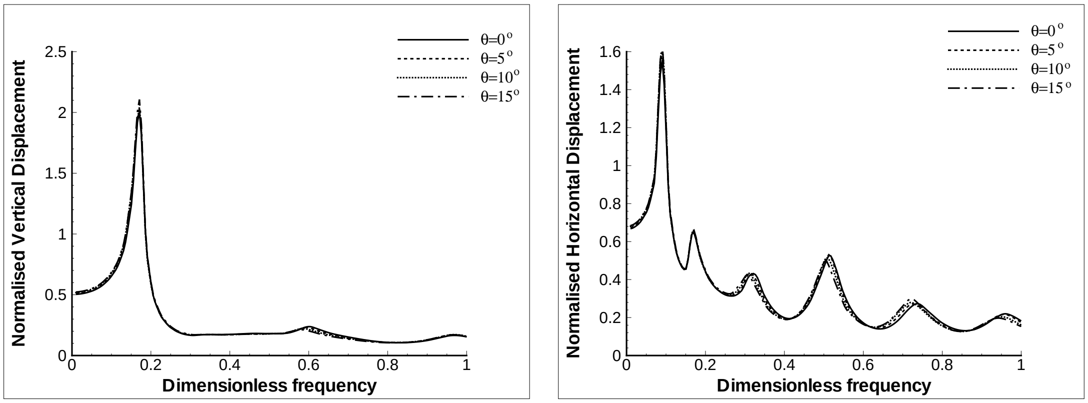

Figure 8.9: Variation of normalised displacements amplitude with frequency.

8.3.2.1 Effect of μ_1/μ_2

Israil and Ahmad [133] presented a parametric study, using BEM, for the dynamic behaviour of strip foundations overlaying a homogenous half-space, or a soil layer over half-space and a soil layer over bedrock. The authors examined the effect of the material damping, the relative stiffness between the soil layer and the half-space and the effect of stratum depth considering only vertical loading. A similar parametric study is carried out in the current work to investigate the dynamic response of surface strip footings over 2-layer soil media with inclined interface overlaying bedrock. Horizontal and vertical excitations are considered. In the current section the effect of the relative stiffness between the two layers is studied.

Both layers are assumed to have the same thickness in this section, H_1/H_2=1. The two layers have 0.3 Poisson's ratio and 0.05 damping coefficient. The ratio between their relative stiffnesses is taken 0.25, 0.5, 2 and 4. The dynamic compliances of the foundation are computed and plotted in Figures 8.10 to 8.13 for several angles of inclination of the interface between the two layers. The case of μ_1/μ_2=1 is excluded as it represents a homogenous layer over bedrock. From the graphs of Figures 8.10 to 8.13, it is clear that very minor changes occur in the dynamic compliances of the foundation, for all cases of relative stiffness, when the angle of inclination is changed from 0° to 15° in increments of 5°. As mentioned before, probably this is due to the fact that the angles of inclination of the interface are not large enough to induce significant changes in the dynamic compliances. The normalised displacements underneath the foundation also confirm these remarks (Figure 8.14).

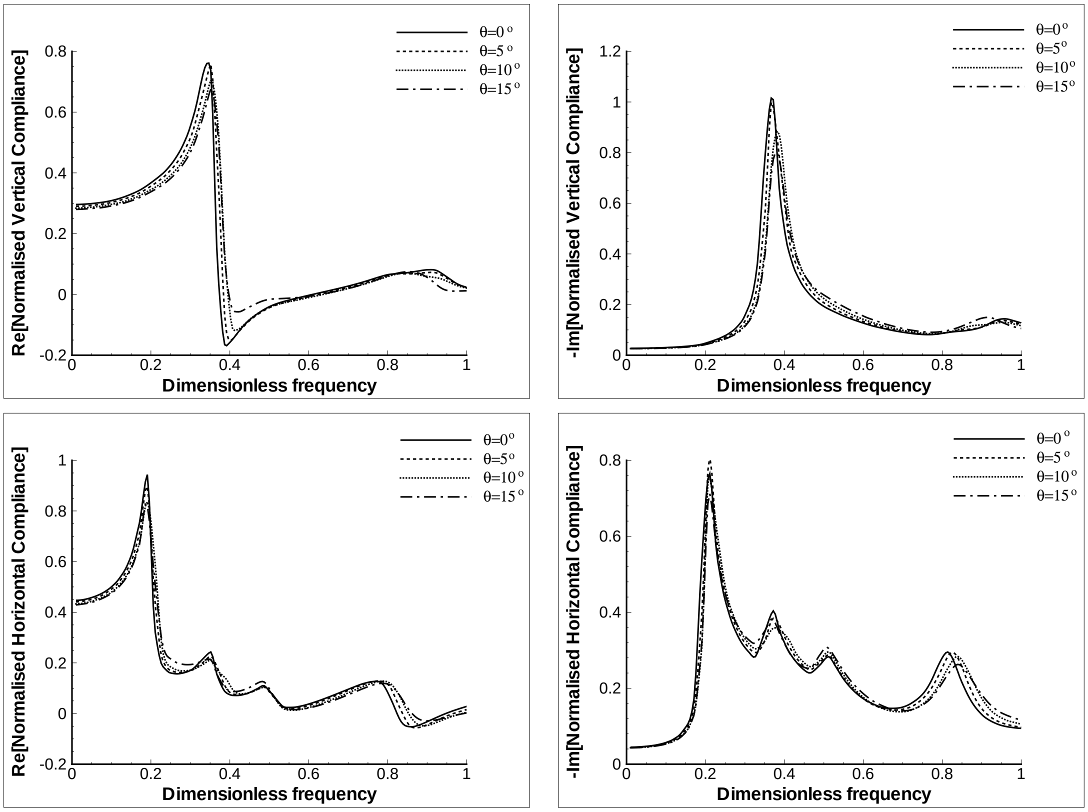

Figure 8.10: Normalised compliances of the surface rigid foundation for μ_1/μ_2=0.25.

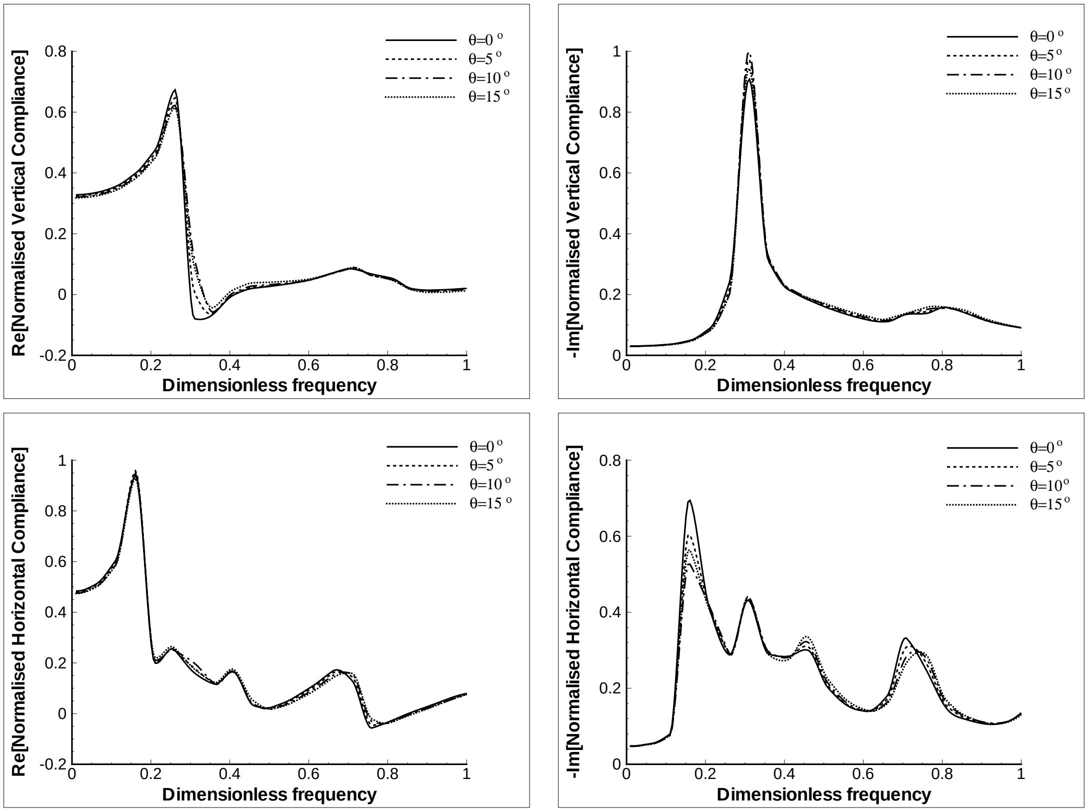

Figure 8.11: Normalised compliances of the surface rigid foundation for μ_1/μ_2=0.5.

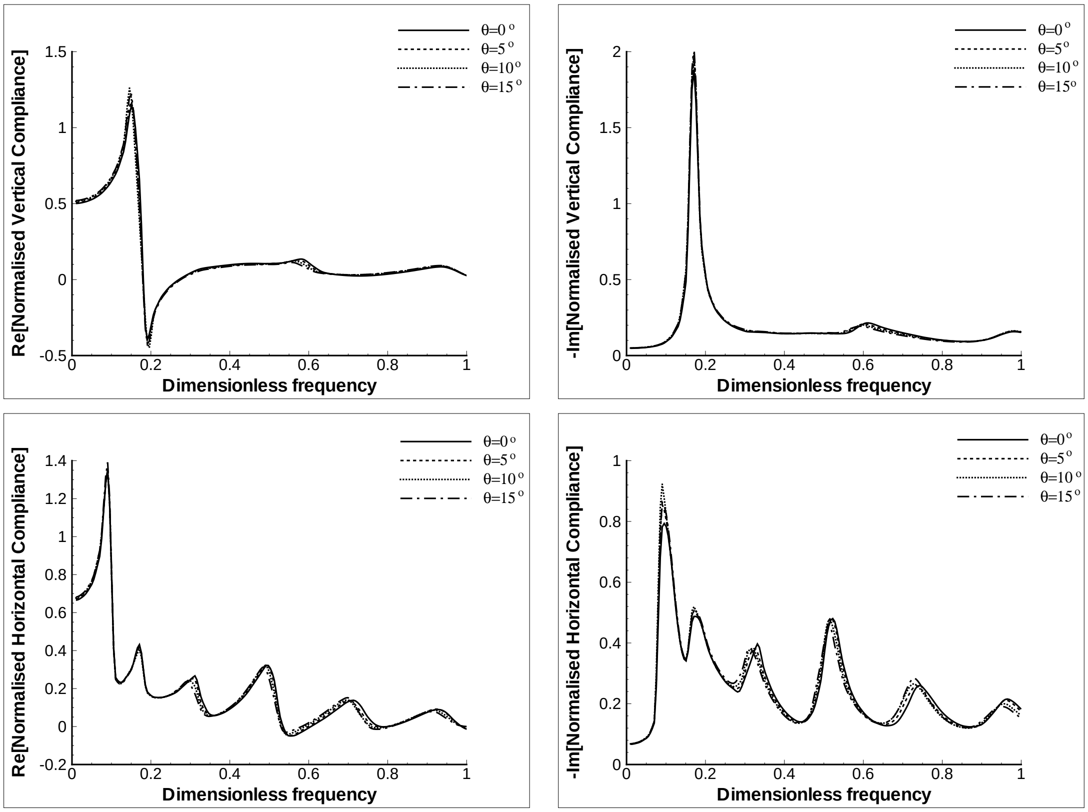

Figure 8.12: Normalised compliances of the surface rigid foundation for μ_1/μ_2=2.

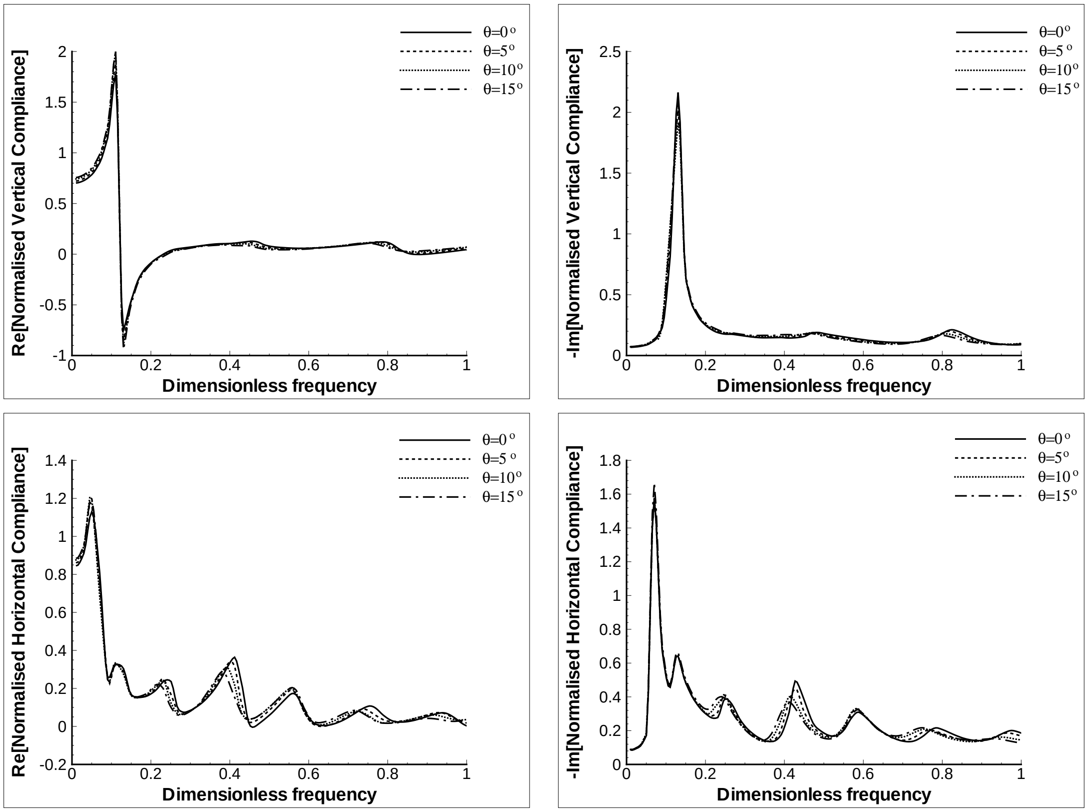

Figure 8.13: Normalised compliances of the surface rigid foundation for μ_1/μ_2=4.

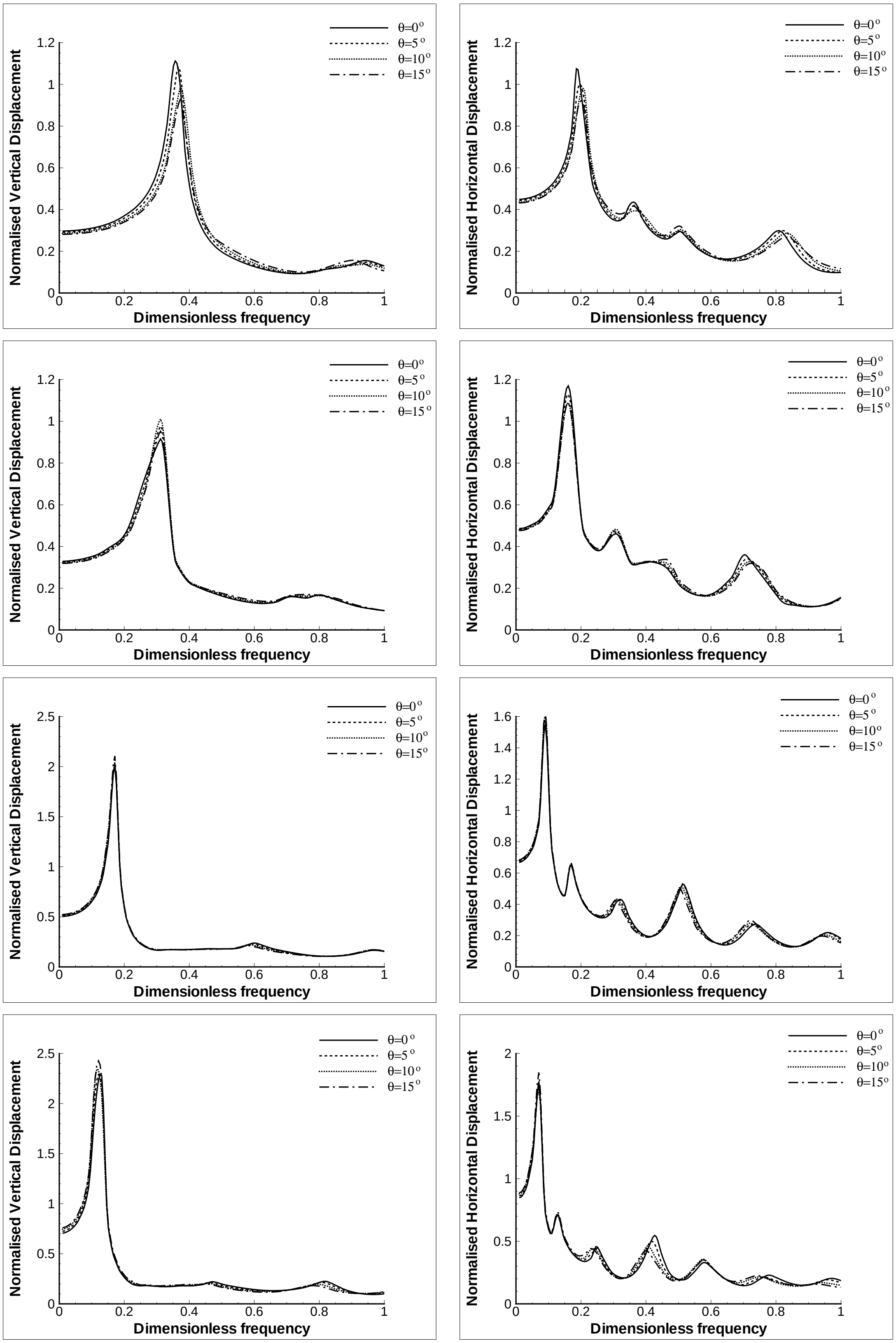

Figure 8.14: Variation of normalised displacements amplitudes underneath the foundation for μ_1/μ_2=0.25, 0.5, 2 and 4, from top to bottom.

8.3.2.2 Effect of H_1/H_2

The fundamental frequency of a layered soil strata is a function of the material properties and the thicknesses of the layers, as it was shown in expressions (4.8a) and (4.8b). In fact the thicknesses of the soil layers have a major effect in the fundamental frequency of the soil profile. They appear in the denominator in the form of $(\rho_1 H_1)/(\rho_2 H_2)$ and each layer thickness is included in the terms f_1 and f_1/f_2, implicitly. Therefore, the effect of the ratio of the relative thicknesses of the two layers on the dynamic compliances of the foundation overlaying a 2-layer soil profile with an inclined interface over bedrock is investigated here. Poisson's ratio, damping ratio and soil densities are considered the same for both layers. The only difference in material properties is the ratio of the relative stiffness, μ_1/μ_2, it is taken as 0.25. The total depth of the stratum is kept constant as $4B$. The ratio of the layer thicknesses H_1/H_2 is varied to take the values; 0.25, 0.333, 0.6, 1, 1.67, 3 and 4. For each ratio, the interface is inclined by the angles 5°, 10° and 15° in a way to decrease the volume of the upper layer. The dynamic compliances of the foundation are shown in Figures 8.15-8.21.

The results show that the interface inclination has an influence on the dynamic compliances, especially at low values of H_1/H_2. For example, for H_1/H_2=0.25, the real and imaginary parts of the dynamic compliance decrease when the angle of inclination θ increases. Moreover, the peak values show slight shifts with respect to the dimensionless frequency. The indicated changes are also obvious for H_1/H_2=0.333 and H_1/H_2=0.6. However, for H_1/H_2=1, 1.67, 3 and 4, the interface inclination leads to very little change in comparison to the previous cases. Once again, these conclusions are confirmed by the results of the normalised displacements underneath the foundation, shown in Figures 8.22 and 8.23, where the effect of the interface inclination is clearer for H_1/H_2<1.

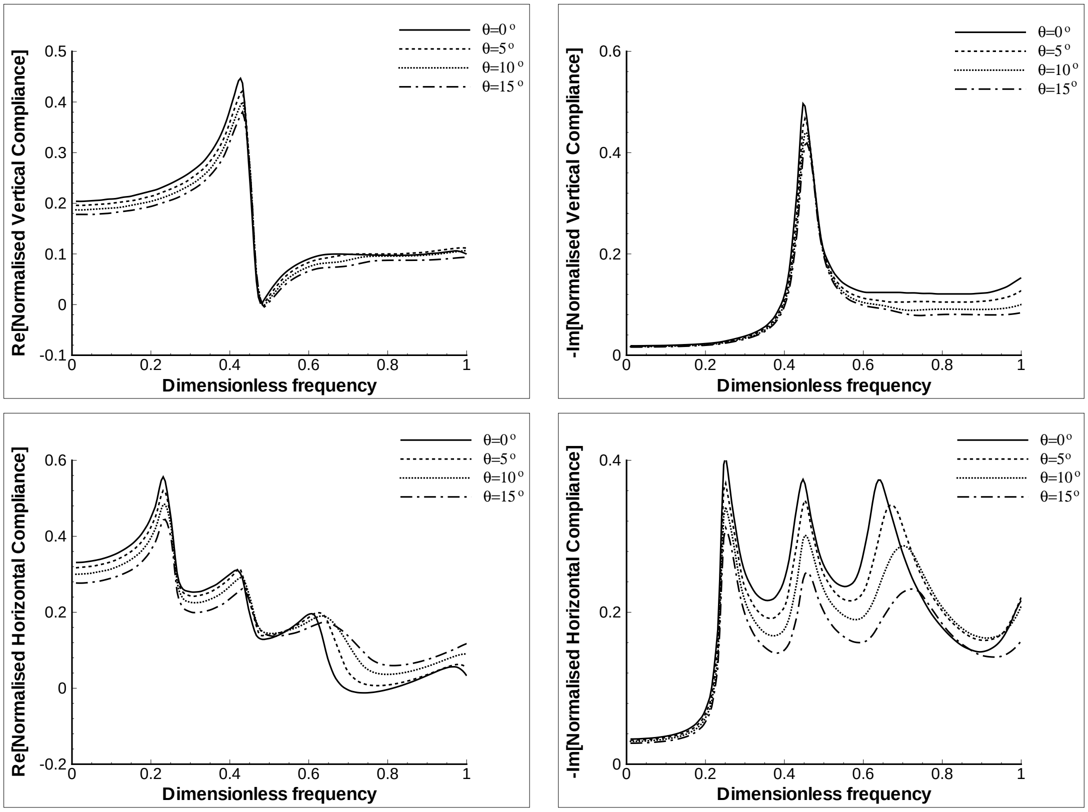

Figure 8.15: Normalised compliances of the surface rigid foundation for H_1/H_2=0.25.

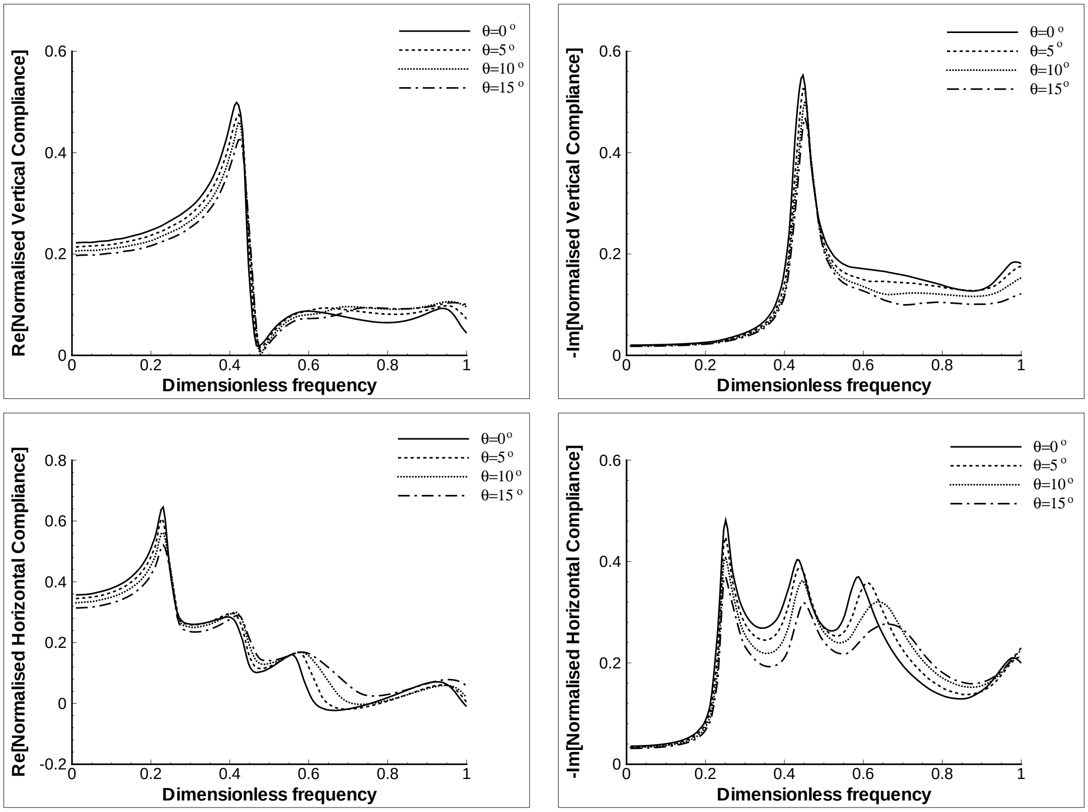

Figure 8.16: Normalised compliances of the surface rigid foundation for H_1/H_2=0.333.

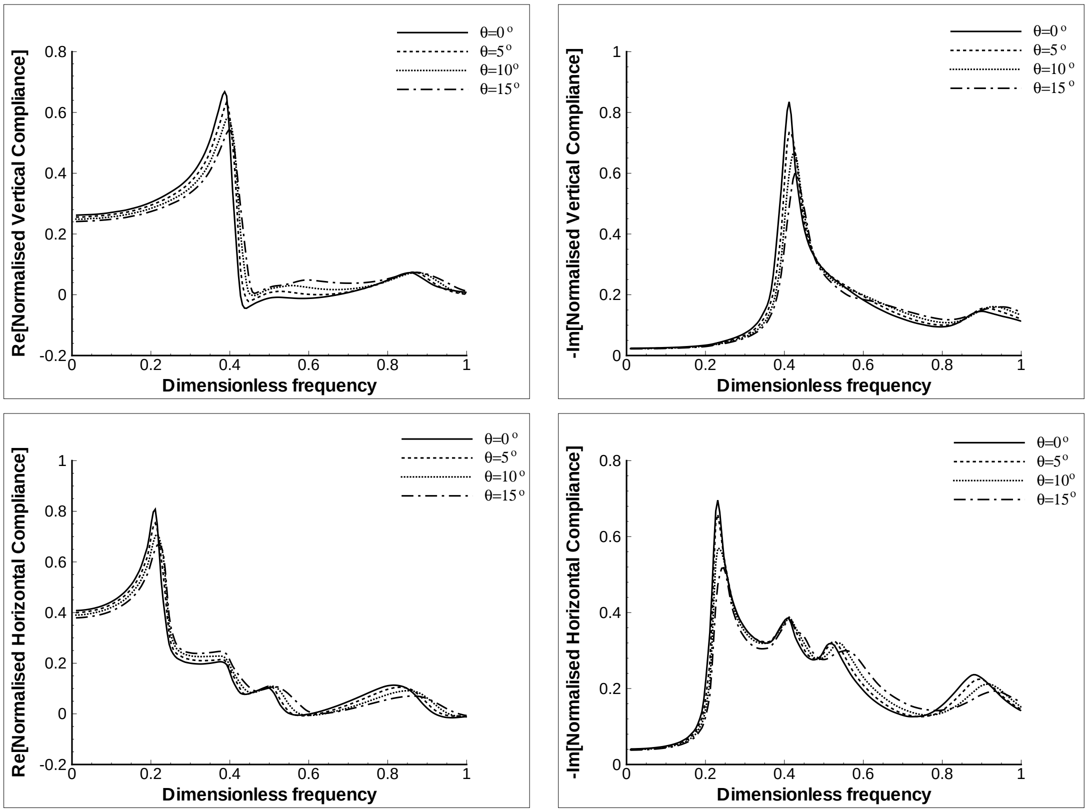

Figure 8.17: Normalised compliances of the surface rigid foundation for H_1/H_2=0.6.

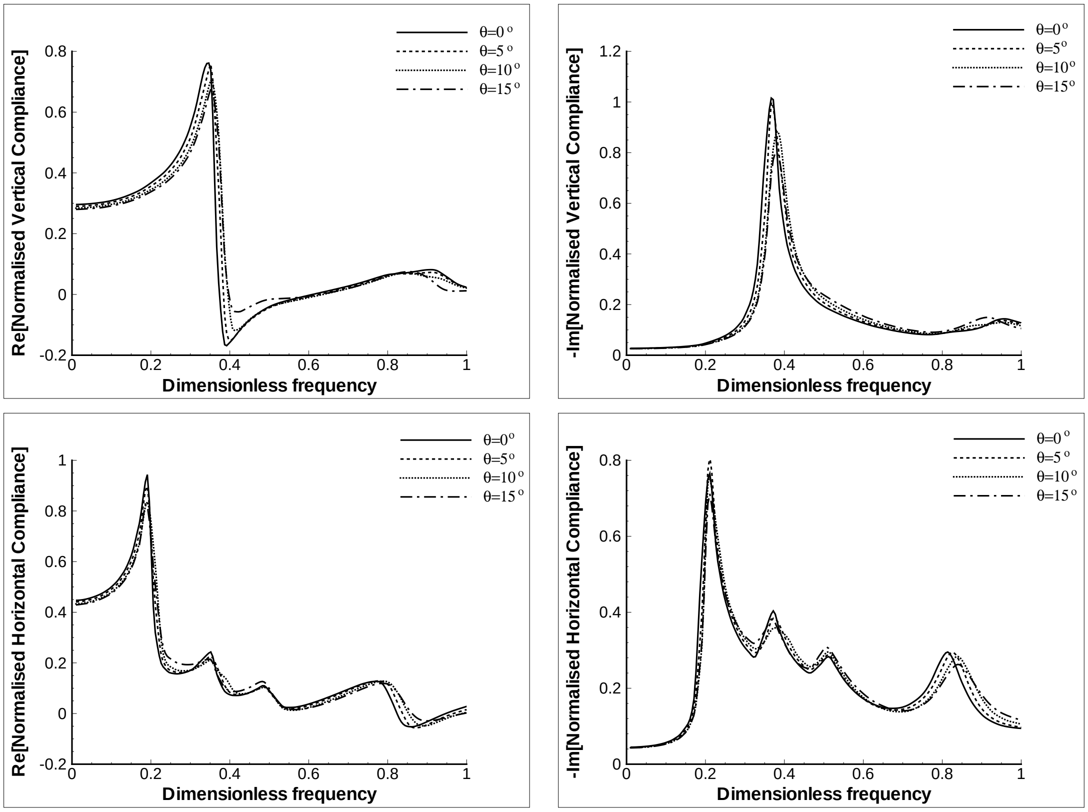

Figure 8.18: Normalised compliances of the surface rigid foundation for H_1/H_2=1.

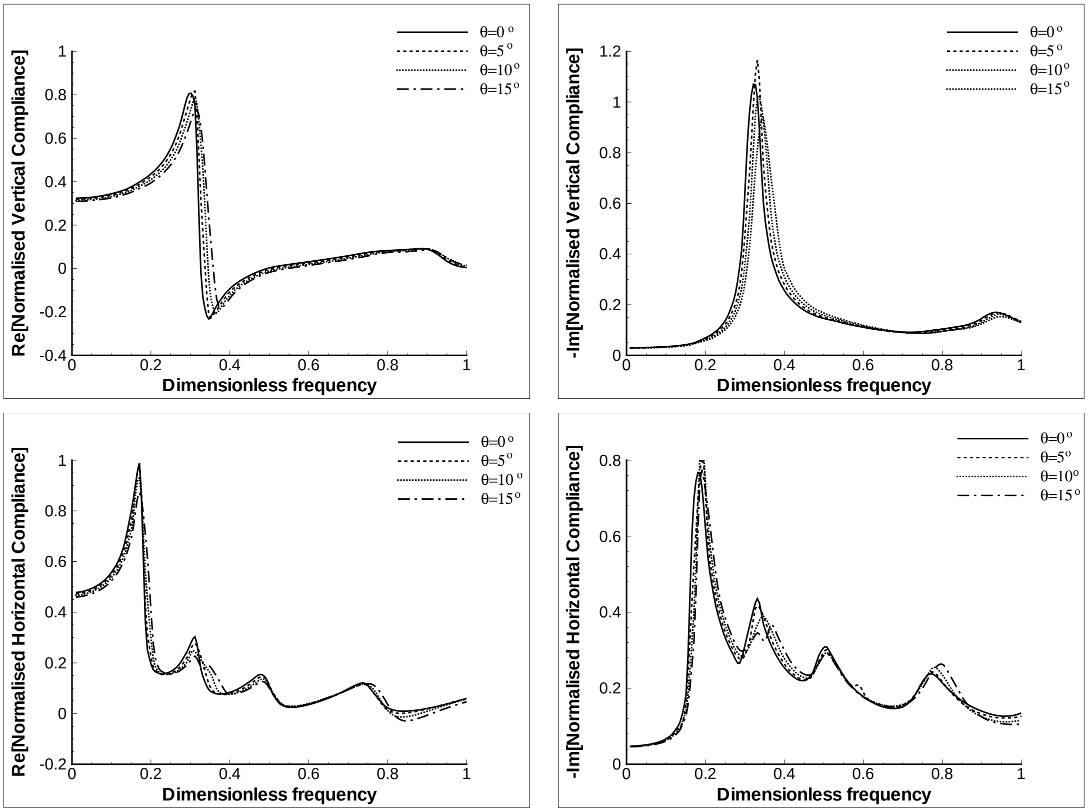

Figure 8.19: Normalised compliances of the surface rigid foundation for H_1/H_2=1.67.

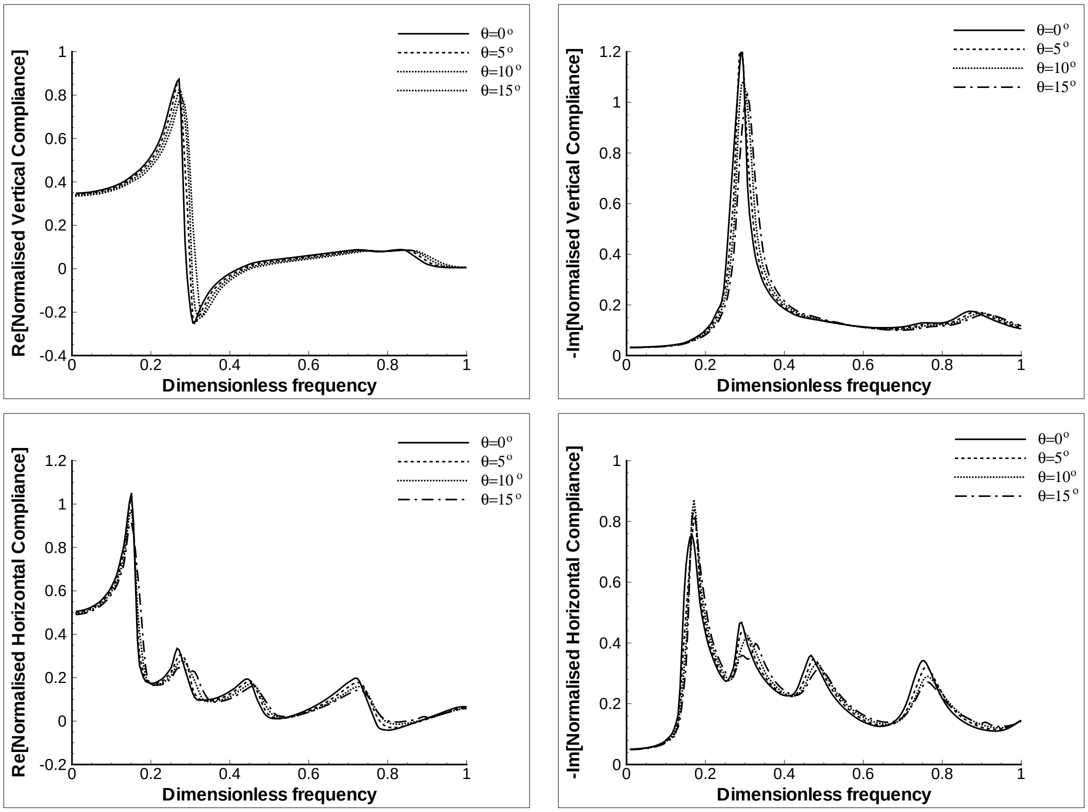

Figure 8.20: Normalised compliances of the foundation for H_1/H_2=3.

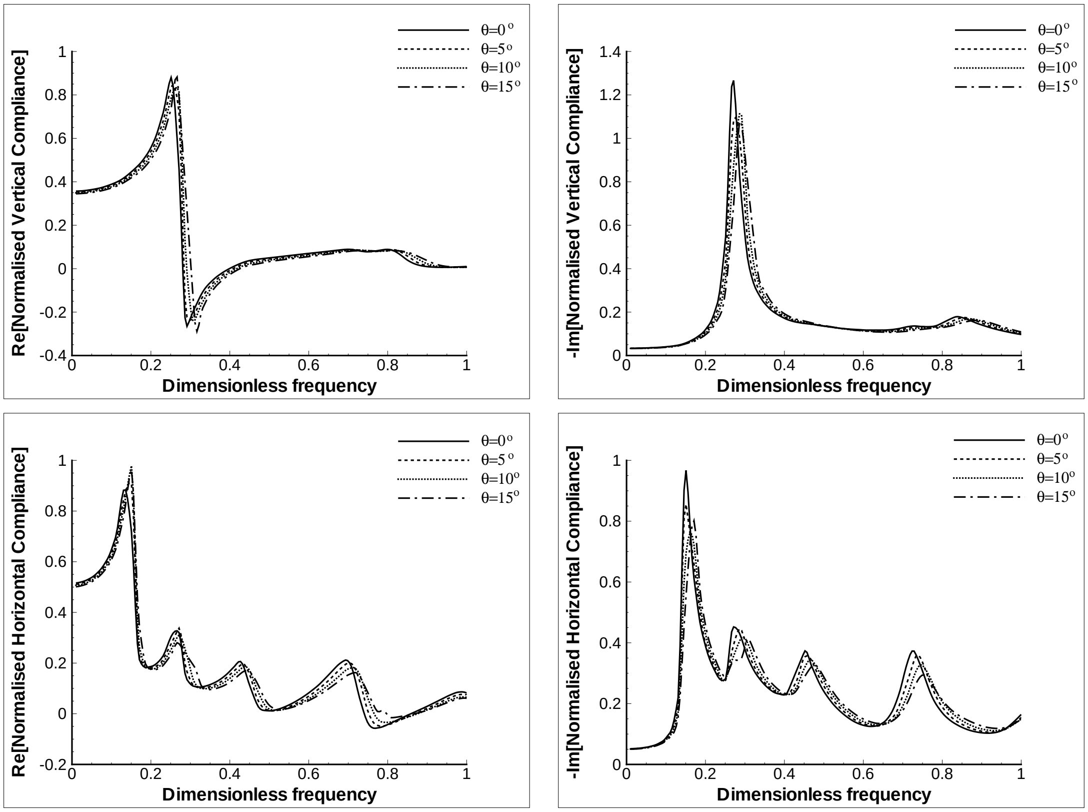

Figure 8.21: Normalised compliances of the surface rigid foundation for H_1/H_2=4.

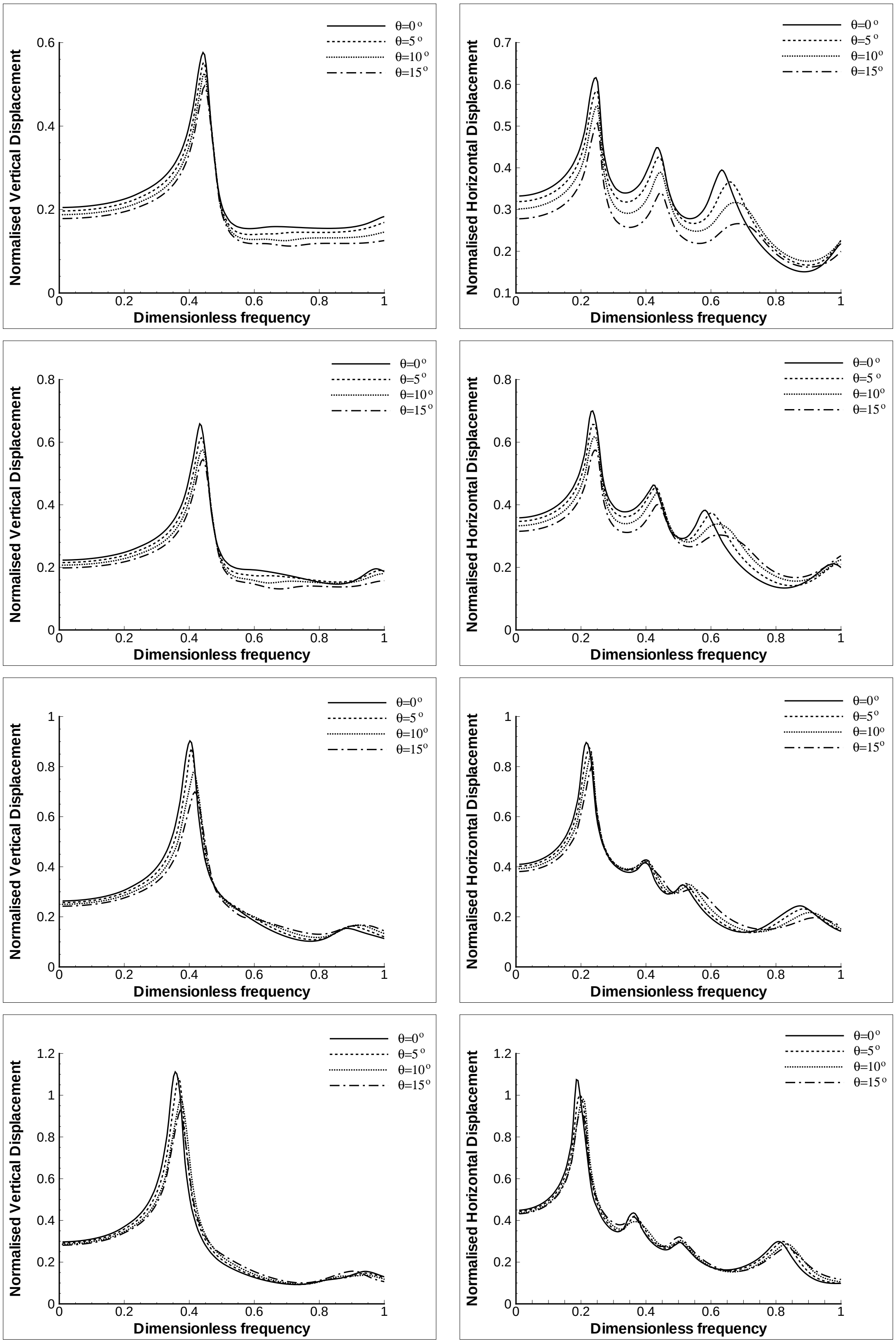

Figure 8.22: Variation of normalised displacements amplitudes underneath the foundation for H_1/H_2=0.25, 0.333, 0.6 and 1.

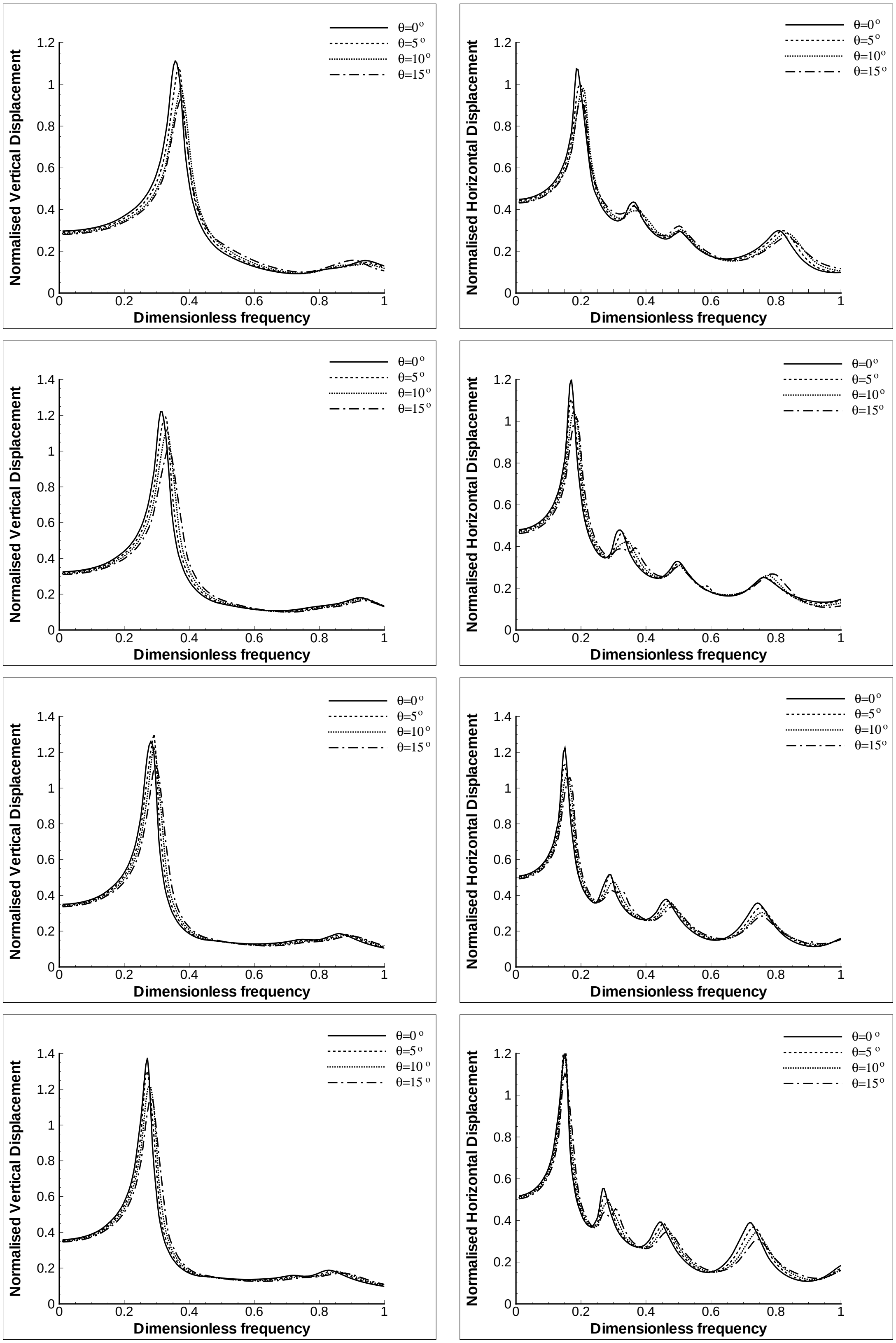

Figure 8.23: Variation of normalised displacements amplitudes underneath the foundation for H_1/H_2=1, 1.67, 3 and 4.

8.4 Surface ground vibration reduction by wave barriers

Various shapes of wave barriers are considered in the following section to show the flexibility of the numerical model in dealing with complex geometries. Then, the case of wave reduction by an inclusion, soft or rigid embedded mat, is considered.

8.4.1 Vibration reduction by wave barriers of various shapes

Wave reduction, either by empty or in-filled trenches, is almost dominated by the use of rectangular shape trenches, wave impedance blocks or by installing piles. They have proved successful in achieving the desired level of ground vibration reduction. However, other shapes have not been usually considered due to either installation difficulties or other practical considerations. This section aims to investigate the efficiency of rectangular inclined barriers, triangular barriers, L-shape barriers and trapeziums barriers as illustrated in Figure 8.24a.

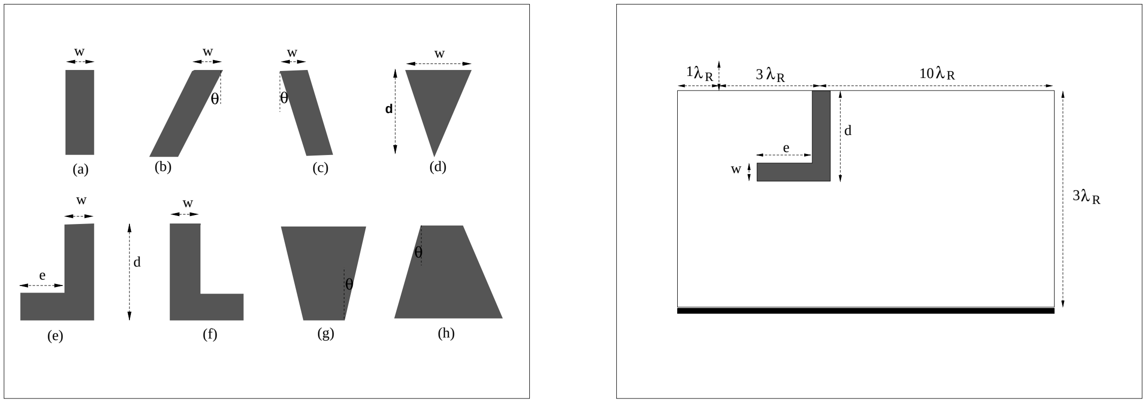

(a) Several types of used wave barriers

(b) Schematic diagram of the model

Figure 8.24: Schematic diagrams of wave barriers and the problem configuration.

First, a rectangular concrete in-filled trench is used to provide an idea about its effectiveness on wave reduction and to be used for comparison to various wave barriers. The length and the depth of the domain are taken $14\lambda_R$ and $3\lambda_R$, respectively, (Figure 8.24b). The load is applied at a distance of $3\lambda_R$ from the centre of the barrier and $1\lambda_R$ from the left lateral boundary of the domain with a frequency of 20Hz. A zone of $10\lambda_R$ is permitted after the barrier's centre, it is reported in reference in [125] that good screening effect is achieved for a zone of $10\lambda_R$ after the trench. The soil density, shear modulus and Poisson's ratio are 1700kg/m^3, 20MPa and 0.25, respectively, with a damping ratio of 2.5%. The vibration reduction at the surface of the model is assessed by computing the average amplitude reduction factor as a global measure. For in-filled concrete trenches, Ahmad and Al-Hussaini [125] proposed a normalised depth of the trench of 1.2; except for normalised width less than 0.3 as it achieves less than 40% reduction (see Figure 8.25a). The normalised dimensions, with respect to the Rayleigh wavelength, of the rectangular barrier are varied as in Figure 8.25a and their screening effects are assessed. Next, the barrier is inclined by an angle of 5°, 10° and 15° toward and outward the point of application of the load.

The reason for choosing such low angles is that this could happen during the installation process as it is not always guaranteed to maintain the vertical orientation when digging the trench in the field and thus it is worth investigating the influence of its inclination on its screening effects. The normalised depth of the barrier is then increased to 2 for a normailsed width of 0.4 and the results are shown in Figures 8.26a and 8.26b, respectively. In the diagrams, the case θ=0° refers to a vertical barrier. The results show that the performance of the barrier is not affected by the inclination and almost the same reduction level is achieved for all cases.

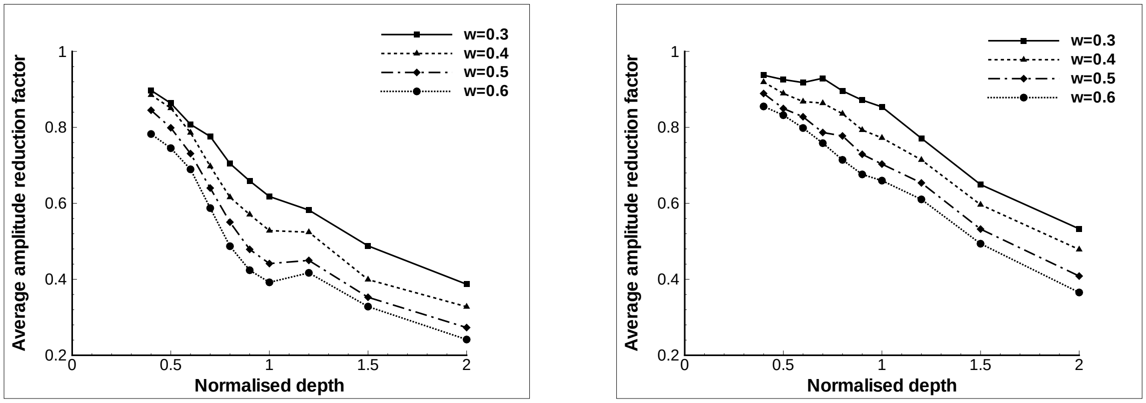

(a) Rectangle barrier

(b) Triangle barrier

Figure 8.25: Effect of barrier shape on screening efficiency.

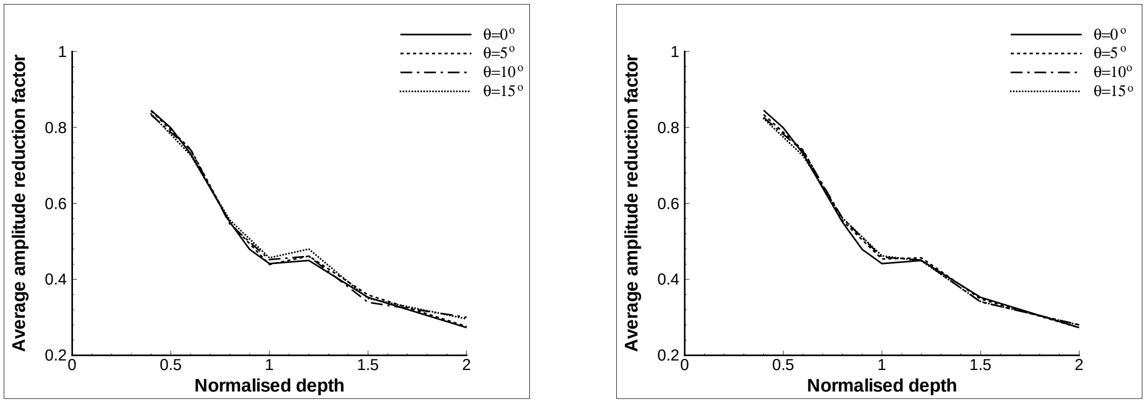

(a) Inclined barrier (b) in Figure 8.24a

(b) Inclined barrier (c) in Figure 8.24a

Figure 8.26: Effect of barrier inclination on reduction efficiency.

The triangular shape barrier is then used where the base and the depth of the triangle are varied. The results are plotted in Figure 8.25b where the same trend is obtained for all cases. This type of barriers reduces considerably the vibration level. However, the achieved reduction level is lower than for the rectangular barrier of the same width. If this type is used then the depth of the barrier could be increased to achieve better reduction level. For example, a level of around 60% is achieved for a triangular shape barrier with a normalised width of 0.5 and a depth of 2. The same level is achieved by rectangular barriers of 0.5 width and 1.2 depth. In spite of the larger depth of the triangular barrier, it requires less area compared to the rectangular barrier.

The L-shape in-filled trench, which could be considered as a retaining wall, is used here and it achieved between 40% to 60% reduction level in both cases of its shape as shown in Figure 8.27. The base of the barrier, the normalised embedded width e, does not have significant effect. Maintaining low normalised embedded width, $e \approx 0.4$, is enough to achieve a reduction level of around 50%.

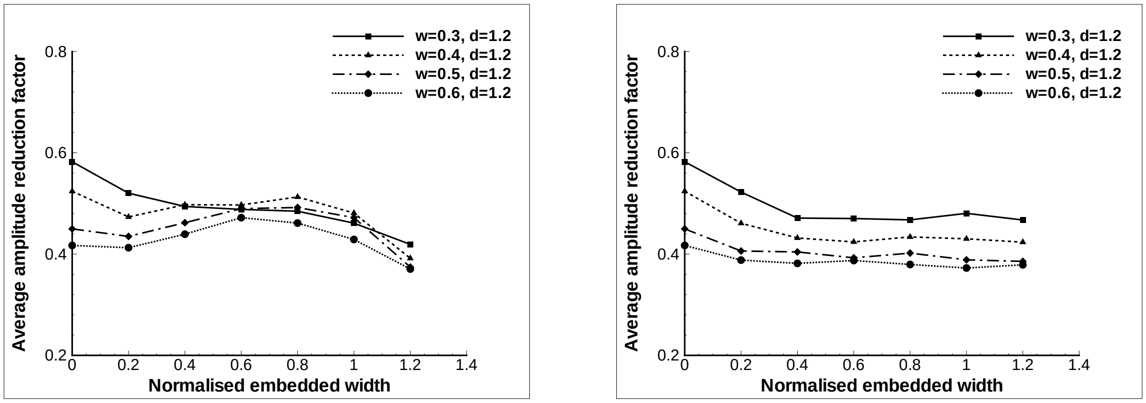

(a) L-shape barrier (e) in Figure 8.24a

(b) L-shape barrier (f) in Figure 8.24a

Figure 8.27: Effect of L-shape barriers on screening efficiency.

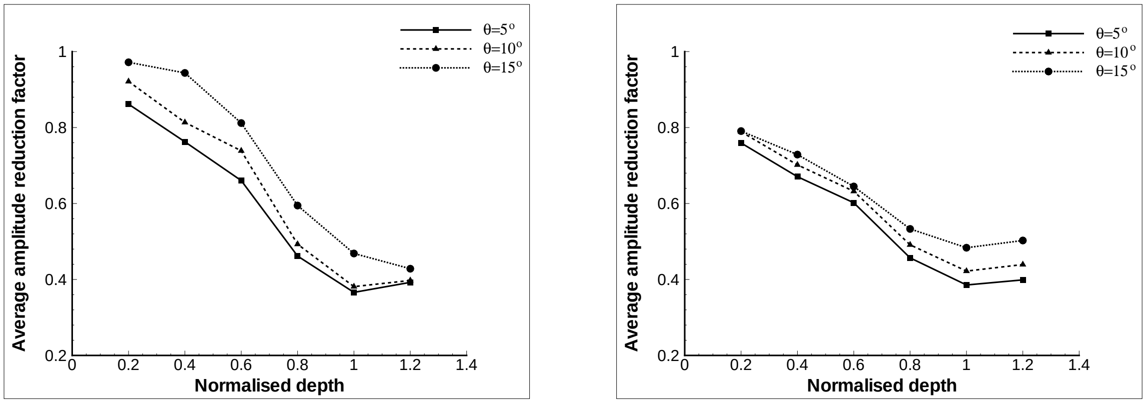

(a) Trapezium shape barrier (h) in Figure 8.24a

(b) Trapezium shape barrier (g) in Figure 8.24a

Figure 8.28: Effect of trapezium shape barriers on screening efficiency.

Trapezium blocks are used then by reversing their position. The narrow normalised base is taken as 0.2 and the large base is increased according to the angle θ. Good reduction level is obtained by using this type of trenches, see Figure 8.28, due to their large contact surface. However they are difficult to build on site and engineers may prefer in this case to increase the dimensions of the rectangular trench to obtain a similar level of reduction, as it is more practical.

For comparison purpose, the normalised area of the barriers, with respect to a unit area of the Rayleigh wavelength, is calculated and plotted in Figure 8.29 against the average amplitude reduction factor for all shapes, excluding the inclined ones. A level of 60% reduction is achieved in the case of rectangular barriers for normalised area of around 0.6. However, the triangular barriers reduced the vibration by 40% for normalised area of around 0.4. The level of reduction could be increased by maintaining a normalised width of 0.4 and increasing the normalised depth to more than 1.2. This is also obtained by the L-shape barriers but with higher normalised area, 0.8 to 1.2. The trapezium blocks reduced the vibration to the same level achieved by the rectangular barriers but with higher normalised area; between 0.6 and 0.8.

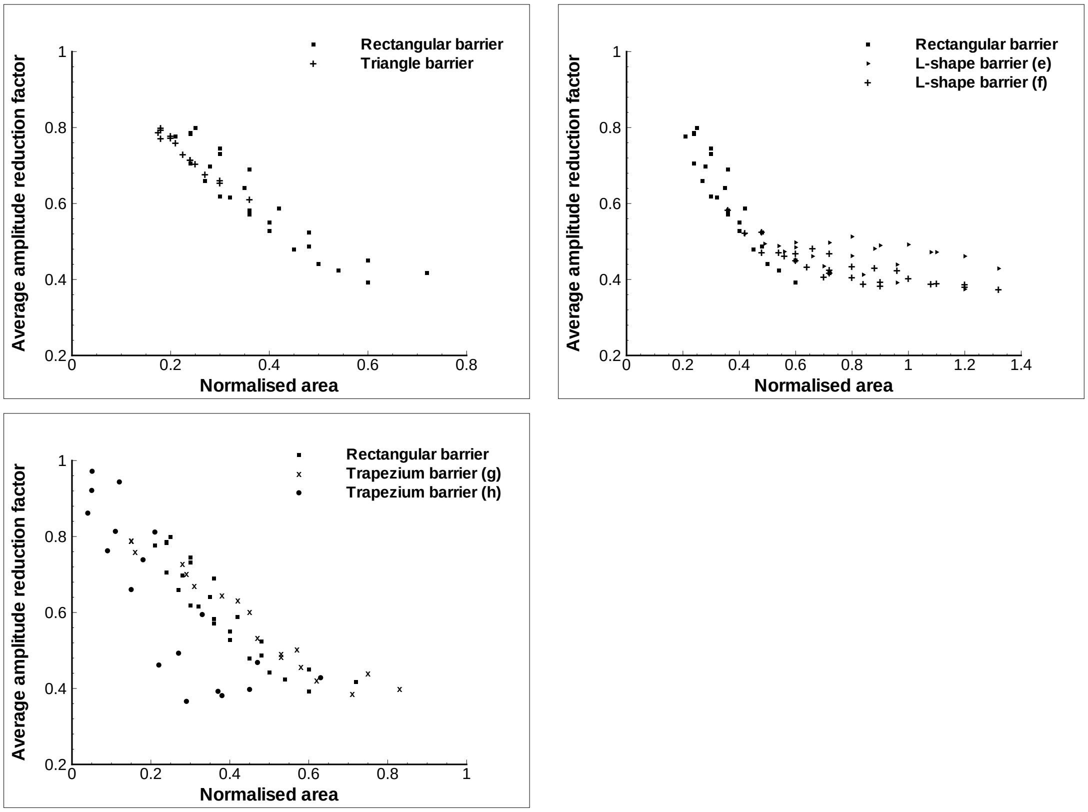

Figure 8.29: Effect of normalised area of the barrier on the screening efficiency.

The numerical results showed that good level of vibration reduction could be obtained by using for example triangular barriers. For a normalised width and depth of 0.5 and 1.2, respectively, reduction levels of around 50% and 36% are achieved for rectangular and triangular barriers. The corresponding normalised areas are 0.6 and 0.3, respectively. Nonetheless, the reduction level achieved by the triangular barrier could be increased to 50% by increasing its depth to 2. In spite of that, its normalised area, 0.5, is still less than the area of the rectangular barrier.

8.4.2 Vibration reduction by an inclusion

Elastic slab mats have been in use for vibration mitigation from railway systems. For example, Cui and Chew [134] investigated the effectiveness of a floating slab on reducing the transmitted forces to the ground due to a stationary harmonic load and a moving load. They indicated that the floating slab is very effective for frequencies larger than 1.5 of the designed resonance frequency. Hussein and Hunt [135] modelled floating-slab tracks on rigid foundations by accounting for moving loads. Xin and Gao [136] investigated the efficiency of an elastic layer inserted between slab track and bridge on the transmitted vibration to the bridge. They concluded that there is amplification in the vibration level associated with certain frequencies. The effect of the slab stiffness on the rail and the slab displacement is also studied in the previous reference. In fact, the application of an embedded mat gives similar results obtained for the floating slab where an increase in the vibration level is encountered below a certain frequency. In fact, this depends on the depth of the mat as it shown in the following analysis. The mat reduces the vibration level and an intersection frequency is identified depending on the depth of the mat.

To examine this, a soil domain of $8\lambda_R$ and $3\lambda_R$ in length and depth (as depicted in Figure 8.30), respectively, is used in the analysis with the same material properties as in the previous section. The domain is subjected to a surface harmonic load of 10Hz frequency. A mat, of soft or rigid material properties, of length of $1\lambda_R$ and thickness of 0.5m is installed at various normalised depths. The density, elasticity modulus and Poisson's ratio of the soft mat are 150kg/m^3, 1MPa and 0.25 while concrete properties are used for the rigid mat. The area under the displacement curves at the surface of the model is computed and normalised with a unit area as shown in Figure 8.31. It is clear from the left graph of Figure 8.31 that there is a reduction before a certain depth of the rigid mat then amplification takes place. In fact, amplification happened at a normalised depth of around 0.5 which is close to the critical depth of the domain. In the case of the soft mat, amplification happened before the critical depth and reduction occurred with depths around the critical depth of the model. In other words, reduction in the vibration level is achieved for normalised depths of the rigid mat of less than 0.45 while amplification happened in the case of soft mat. In addition, the rigid mat amplified the response between 0.5 and 1 of the normalised depth while reduction is achieved in the case of soft mat. Similar response is found after a normalised depth of 1 for both mats.

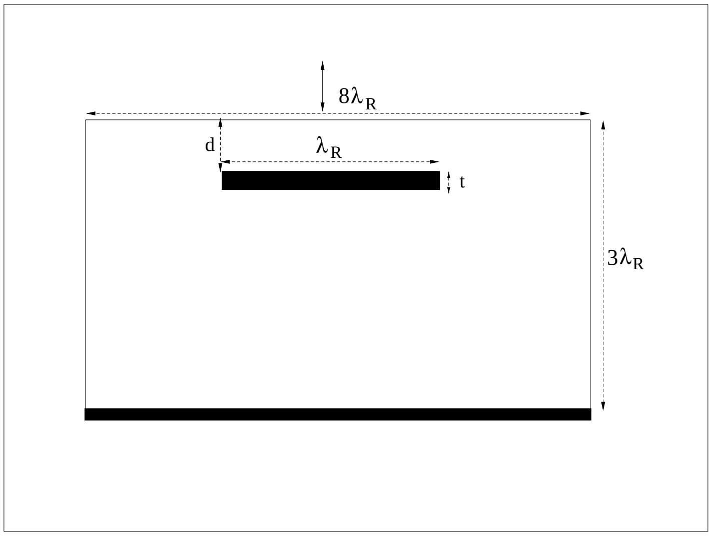

Figure 8.30: Schematic diagram of surface vibration reduction by an inclusion.

Next, normalised depths of 0.5 and 0.75 are considered and the frequency of the harmonic load is varied. The only difference from the previous case is the imposed frequency. As it is shown in right graph of Figure 8.31, for the case of 0.5 normalised depth, amplification occurs. For the soft mat case, a slight reduction level is achieved before a frequency of 5Hz after which the response is amplified. The case of 0.75 normalised depth showed that the response is amplified in the case of rigid mat and reduced, to achieve around 35% reduction level, in the case of soft mat.

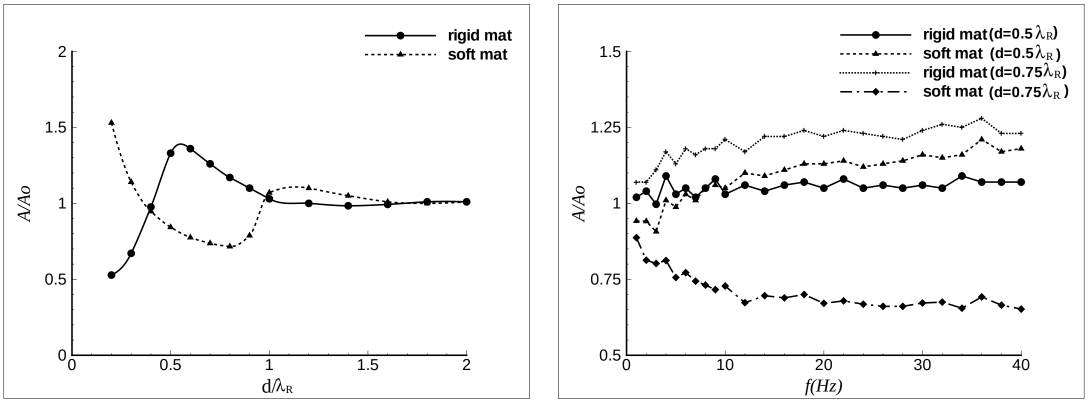

Figure 8.31: Comparison of the efficiency of soft and rigid mats on surface vibration reduction.

8.5 Harmonic loads on railway embankments

The high demand for railways as a major transport mode has given rise to various issues with ground induced vibration being one of them. Some challenges are usually encountered such as crossing soft soil deposits, passing through urban areas, and the level of induced vibrations.

High level of vibration and amplification could happen in case of coincidence of the passing frequency with the natural frequency of the soil deposit or if the depth of the strata is close to the critical depth. A very popular type of railway lines is the embankment structure. Typical railway embankments are of low and intermediate heights with slopes of 35°. This leads to an increase of the base of the low embankment by a factor of 1 from each side compared to the top width. This factor is increased to 2 in the case of intermediate height embankment, *i.e.* the width of the base of low height embankment is around 21m where it is around 35.6m in the case of intermediate height embankment. In other words, the surface of the occupied land is three times and five times the width of the top of the embankment in the case of low and intermediate height embankments, respectively. As a matter of fact, this is costly where, indeed, it becomes one of the important factors to consider when passing through urban areas. The purpose of the current section is to examine the level of vibration induced by surface harmonic loads in addition to present some alternatives where savings in both the amount of fill materials required for the embankment and the occupied space are significantly reduced. More specifically, the effect of the embankment geometry on surface vibrations. An introduction is first given about various configurations of possible railway embankments. Numerical results are then presented in sections 8.5.1 and 8.5.2.

The developed finite element model is used here to simulate vibrations induced by harmonic loads on several configurations of the railway embankments, 10 cases are studied. Figure 8.32 depicts the schematic diagrams of these cases. The first case represents a low embankment, and it is shown in Figure 8.32a. The soil layer underlain low embankment is improved by installing Constant Modulus Columns (CMC) as it is depicted in Figure 8.32d. An additional two cases correspond to intermediate height embankment. Highly Compacted Geomaterials with Retaining Walls (HCG-RW) are used in Figures 8.32b and 8.32e, instead of traditional embankments. Constant Modulus Columns are used to stiffen the underlain soil. The last two cases represent embedded HCG-RW as it is shown in Figures 8.32c and 8.32f. For each case, two lines of harmonic loads of magnitude 83kN are applied at the surface to simulate two passing trains, in this work only harmonic stationary loads are considered. Each line consists of two axis point loads. Examples of the geometries used in the low embankment and the low HCG-RW are shown in Figure 8.33.

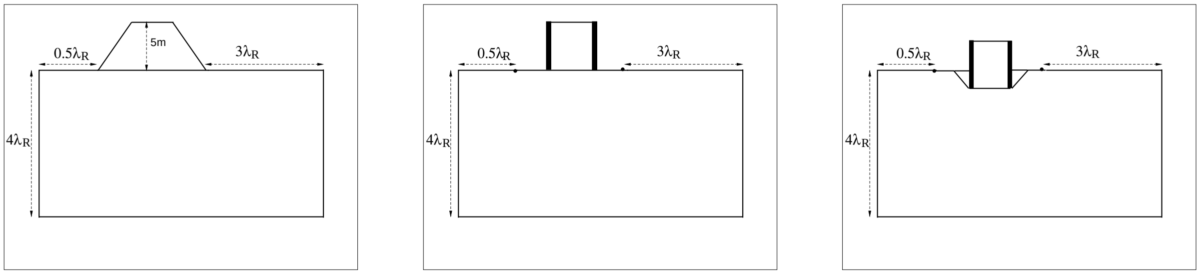

(a) Low height railway embankment

(b) Low height HCG-RW representation

(c) Embedded low height HCG-RW representation

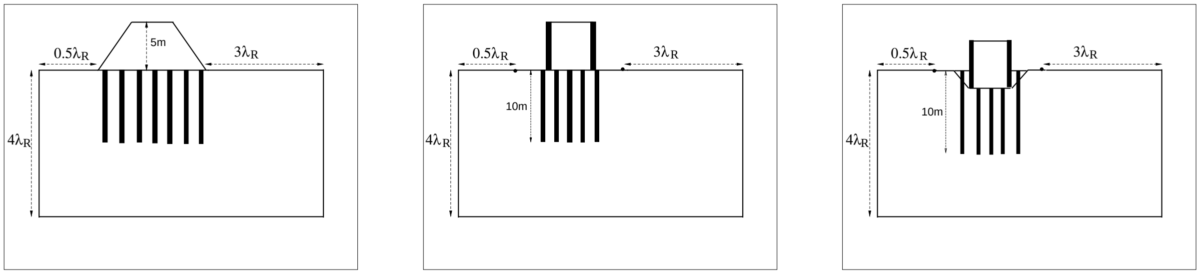

(d) Low height railway embankment over soil layer stiffened with CMC

(e) Low height HCG-RW over soil layer stiffened with CMC

(f) Embedded Low height HCG-RW over soil layer stiffened with CMC

Figure 8.32: 2D configuration of railway embankment over soil layer resting on bedrock.

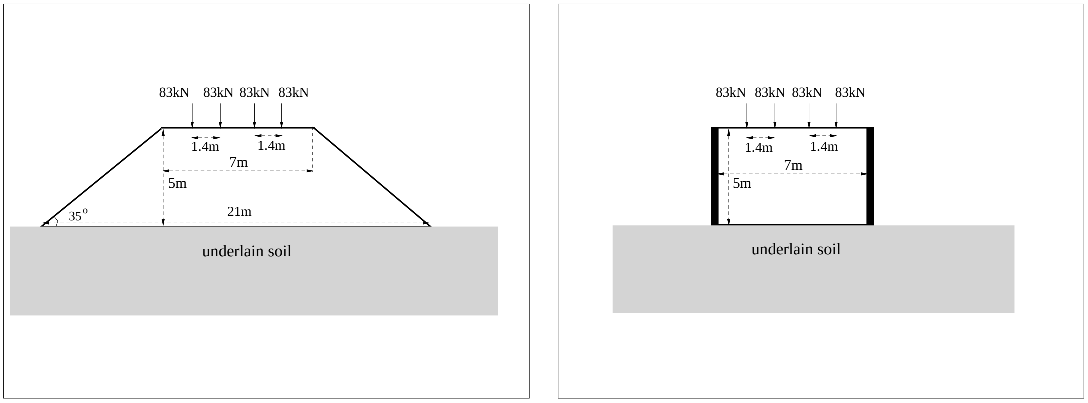

Figure 8.33: Schematic diagrams of loads on railway embankments.

8.5.1 Railway embankment

A medium-stiff low height embankment is first considered. The height of the embankment is taken as 5m where it is inclined with an angle of 35° leading to 7m width at the top and 21m at the embankment-underlain soil layer interface as it was depicted in Figure 8.33. It is a typical and common practical case. The numerical model is used to simulate the behaviour of the domain under stationary harmonic loading. The domain is meshed into 3-node triangular elements with element size less than one-tenth of the Rayleigh wavelength in each layer. Distances of $3\lambda_R$ and $0.5\lambda_R$ are taken beyond the lower edges of the embankment on the right and left sides, respectively. The embankment is assumed to be overlaying a soil layer of $4\lambda_R$ in depth which rests on rigid bedrock. Typical unstructured triangular mesh grids of the low embankment and the underlain soil, for a load frequency of 18Hz, is presented in Figure 8.34. Material characteristics are tabulated in Table 8.1.

	ρ (kg/m^3)	μ (MPa)	ν	β (%)
Embankment	1700	18.8	0.33	2.5
Soft soil	1500	7.4	0.35	2.5
HCG	2000	83.3	0.20	1.0
CMC/RW	2500	6521×10^6	0.15	1

Table 8.1: Material properties

The vertical displacements curves at the surface are computed for the $3\lambda_R$ distance beyond the right side edge of the embankment. Comparing, for example, two displacement curves does not give a general and obvious idea about the response. Hence, the area underneath each vertical displacement curve, for each applied frequency, is computed and used for comparison purpose as it gives better indication about the level of vibration. Figure 8.35a shows the results for a range of frequencies up to 26Hz. Next, the soil layer underneath the embankment is stiffened by installing CMC, of 10m depth, 0.5m of width and at intervals of 1.5m. As it is shown in Figure 8.35a, both cases exhibit high level of vibration for low frequencies, up to 3Hz, where it is dramatically reduced to very low levels with increasing the frequency.

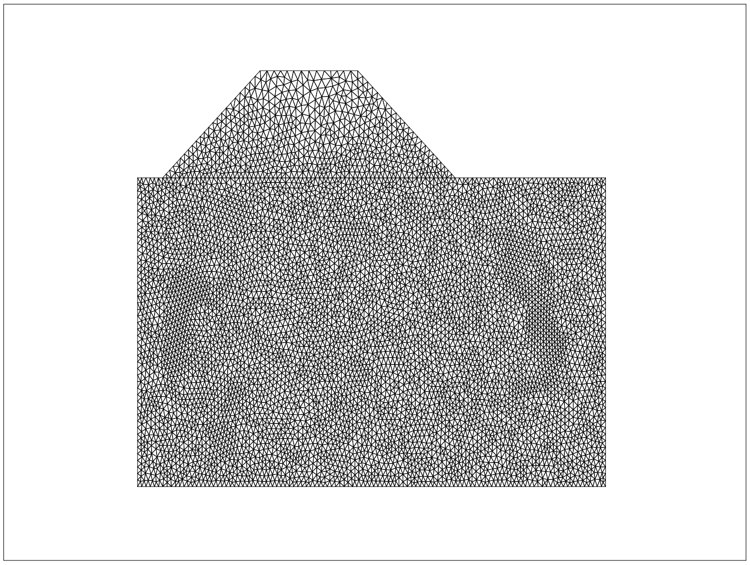

Figure 8.34: Example of unstructured triangular mesh for low embankment: F=18Hz.

To distinguish the difference in response for both cases, the area underneath the vertical displacements curves of the low embankment over stiffened soil is normalised by the area under the vertical displacement of low embankment. The results are shown in Figure 8.35b. It is clear that the level of vibration is reduced when considering the CMC. However, there is an amplification associated with some frequencies. In fact it is related to the fundamental frequency of the low embankment, which is around 10.4Hz, by considering the embankment as a soil layer over rigid base. An interesting example was presented by Adam and Schmid [137] where the BEM is used to describe the semi-infinite extent of the domain. It consisted of a railway embankment supported by a vertical retaining wall only from one side due to a restriction in the nearby property. They computed the response on the surface of the embankment and also for some distance beyond the vertical wall. Resonance occurred in both cases for frequencies close to the fundamental frequency of the embankment. Their model was based on a half-space one.

The height of the embankment is further increased to 10m to consider an intermediate height embankment. The length of the base of the embankment is also increased in this case to become 35.6m. This case does not represent only an increase in the volume of the fill materials required to construct the embankment but also significant increment in the area of the occupied land by the embankment. In addition to that, the distance needed after the embankment where regulatory design codes allow constructing residential buildings is as well affected. The soil under the intermediate height embankment is again stiffened by CMC. The area under the vertical displacement curves of the latter case is normalised by the area under the displacement curve of the intermediate height embankment. The results are shown in Figure 8.35. As for the low embankment height, there is amplification in the response associated with the fundamental frequency of the intermediate height embankment which is around 5.2Hz.

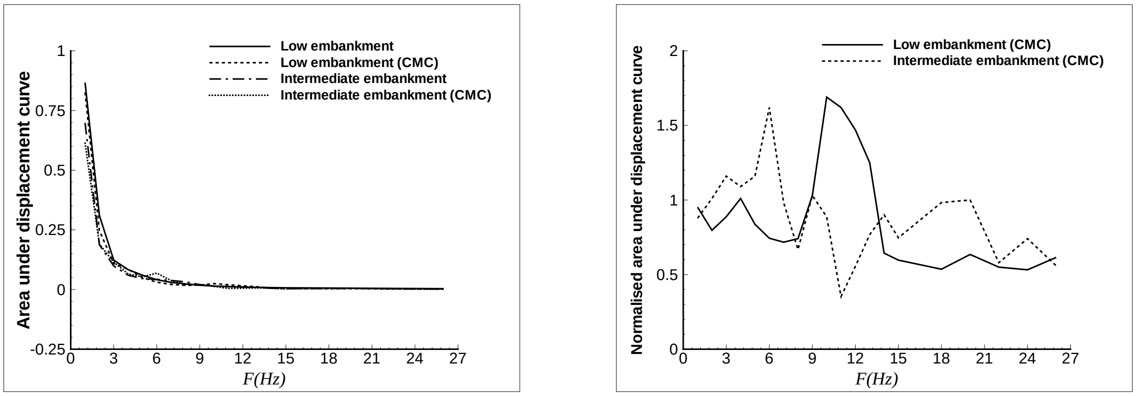

(a) Area under displacement curves for embankment case

(b) Normalised area under displacement curves

Figure 8.35: Vibration reduction by railway embankment over soil layer resting on bedrock.

As depicted in Figure 8.35, two main remarks are observed. The first one that the area under the vertical displacement curve is decreasing with increasing the frequency for the four cases. In other words, low frequencies generate significant level of vibrations in comparison to frequencies higher than 3Hz. The other remark is that when normalising the area under the displacement curve two peaks appear which are associated with the fundamental frequency of the embankment. De-amplification is more pronounced in the case of intermediate height embankment. This may be justified by the effect of the height of the embankment where waves are damped and reduced in magnitude.

8.5.2 Other alternatives

It is difficult sometimes to construct an embankment due to, for example, the presence of existing buildings and infrastructures where space is very limited and restrictions apply. The high price of the land is also another important factor even in the case of low heights. Other alternatives could be used instead of the embankment with an additional treatment. This treatment could be achieved by improving the soil with geosynthetic materials or as it is done here by applying HCG. For example, a method consisting to construct an embankment of HCG and supported by RW could be used. This will save two-thirds of the base size of the embankment required to construct a low embankment and 80% in the case of an intermediate height embankment. In terms of area, a saving of half of the area is obtained if the low embankment is replaced by HCG-RW while two-thirds are saved if an intermediate height HCG-RW replaces the intermediate height embankment. Here, the low embankment is replaced by HCG-RW, with the material properties assumed in Table 8.1. The soil under the HCG-RW structure is also stiffened by CMC and the results are presented in Figures 8.36a and 8.36b. Again, the level of vibration decreased by increasing the load frequency, for the studied range of frequencies. In the case of CMC, there is an amplification in the response and it is corresponding to the natural frequency of the HCG-RW structure, around 16.7Hz. The intermediate embankment is also replaced with HCG-RW with the same height. In addition, CMC are installed in the soil under the intermediate height HCG-RW with CMC. The results are depicted in Figures 8.36c and 8.36d.

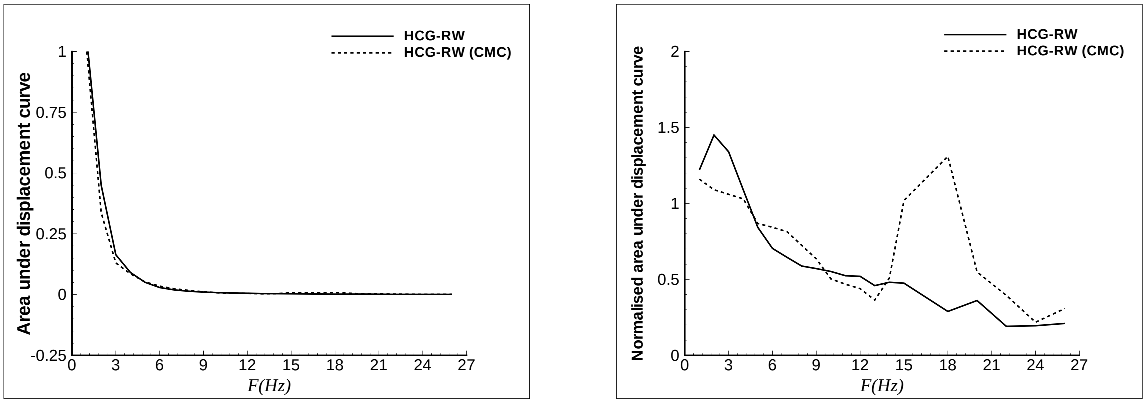

(a) Area under displacement of low height HCG-RW

(b) Normalised area under displacement of low height HCG-RW

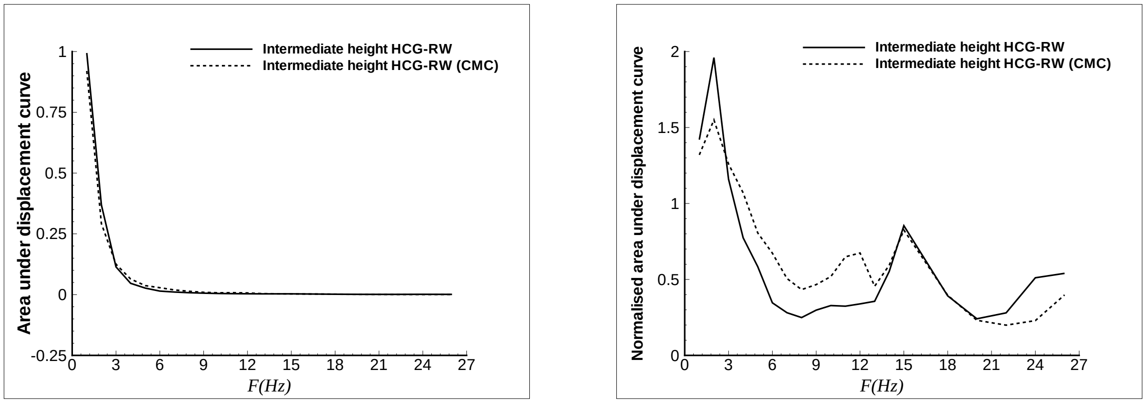

(c) Area under displacement of intermediate height HCG-RW

(d) Normalised area under displacement of intermediate height HCG-RW

Figure 8.36: HCG-RW cases.

Another common case is the embedded HCG-RW as the one depicted in Figure 8.32c. It is handled as in previous cases with and without CMC. The low height is only considered in this case. The results are presented in Figure 8.37. The purpose of such example is to give an indication about the response when considering such a structure with and without CMC. It is clear that the case of embedded HCG-RW with a strengthened soil medium by CMC gives better level of reduction of vibration as the normalised area is lower than for the case of only embedded HCG-RW. Amplification does also appear at the fundamental frequency of the HCG-RW structure.

Contour plots of the vertical displacements of several cases are shown in Figure 8.38. It is clear that the displacement level decreased in the strengthened soil case both underneath the embankment and beyond it. The contour plots show symmetrical profiles, with respect to the vertical axis of symmetry of the embankment, despite the fact the problems are not symmetrical, thanks to the good performance of the transmitting boundary conditions.

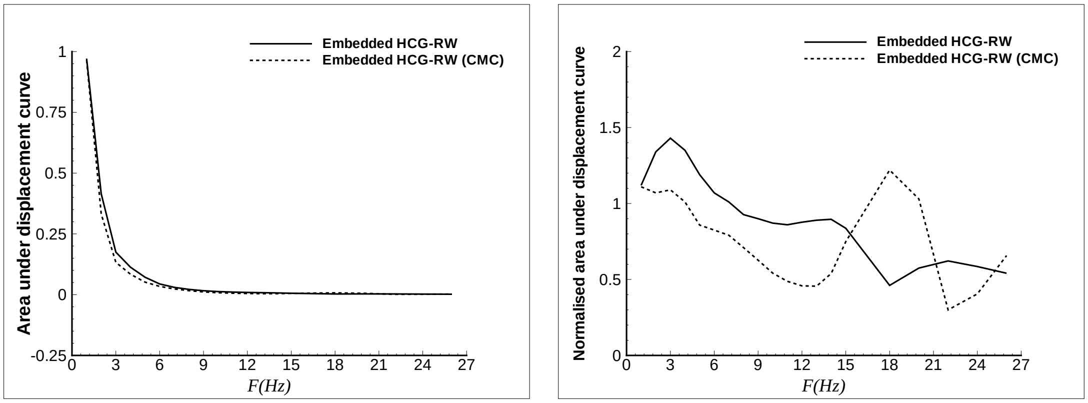

Figure 8.37: Embedded HCG-RW cases.

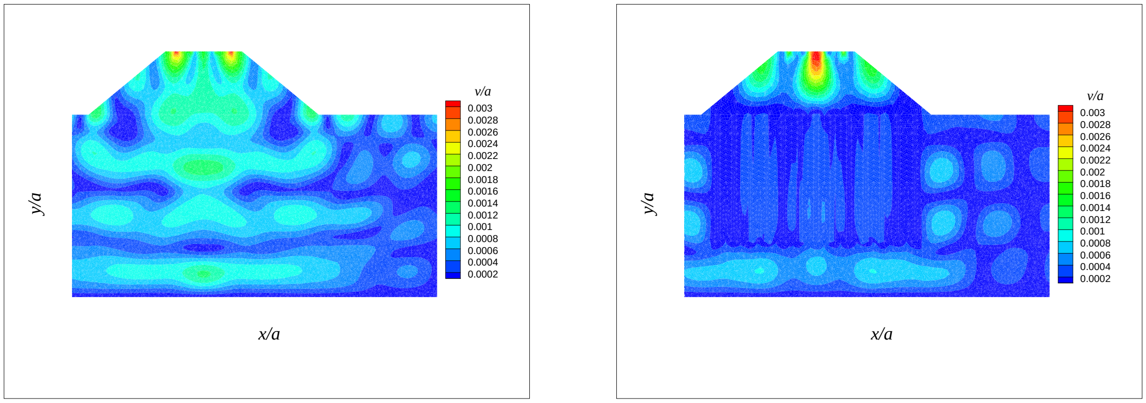

(a) Low embankment

(b) Low embankment with CMC

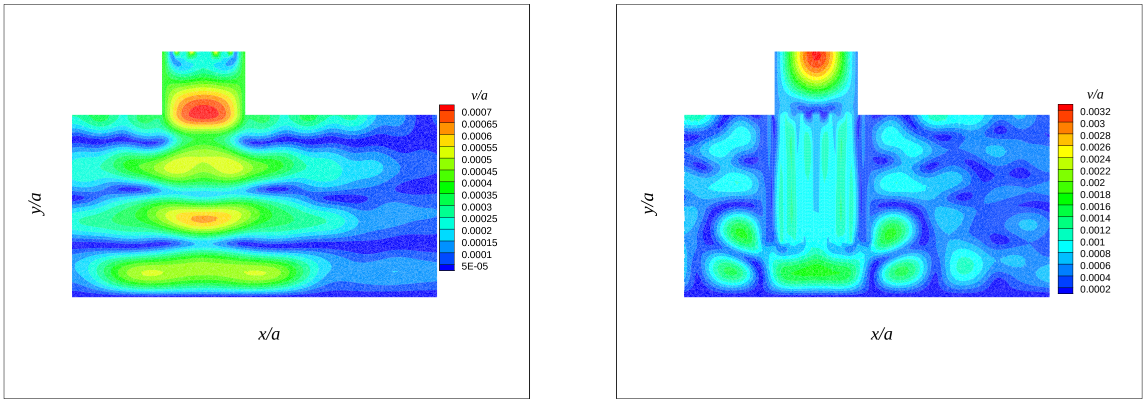

(c) Low height HCG-RW

(d) Low height HCG-RW with CMC

Figure 8.38: Contour plots of the vertical displacements, F=18Hz.

8.6 Concluding remarks

Various numerical examples are analysed in this chapter using the TLM model with unstructured mesh grids. The main remarks deduced from the results are listed below.

- The fundamental frequency of soil media with non-horizontal profile is determined numerically. It is shown that there is a significant change in the fundamental frequency of soil layer over inclined base. This is also confirmed by the application of rigid foundation over soil layer over inclined bedrock. The fundamental frequency of a 2-layer soil medium with inclined interface over horizontal bedrock is slightly affected by the angle of inclination. In the case of rigid foundation over 2-layer soil medium with inclined interface over horizontal base, the relative thicknesses of the soil layers has a noticeable effect, for ratios less than 1, on the dynamic behaviour of the foundation.

- Vibration reduction by various shapes of wave barriers is also studied. Triangular wave barriers could be used as they lead to similar reduction levels of the rectangular barriers. A reduction in the area of the barrier is also achieved. Other types of barriers also achieved good reduction level but with a significant increase in the area of the barriers in addition to installation difficulties.

- The vibration induced by stationary harmonic loads representing railway loads is also investigated. Various configurations of railway embankments are used showing the flexibility of the numerical model when using unstructured triangular mesh grids.

In summary, the developed model is capable to simulate wave problems in a two-dimensional configurations thanks to the flexibility offered by unstructured mesh grids and to the good performance of the implemented transmitting boundary conditions.

Chapter 9

Conclusions and Prospects

A numerical model for simulating wave propagation in soil media due to the effect of harmonic loads has been developed in the current work. The model is two-dimensional under the assumption of plane strain condition. The soil medium can be homogeneous or layered and it may overlay rigid bedrock or half-pace. A more attractive version of the finite element model is developed where unstructured mesh grids are employed to mesh the irregular region. This attracts practitioners as they are usually interested in dealing with models of complex geometries. Furthermore, the TLM is modified in this dissertation where a faster version is proposed by reducing the contributing number of eigenmodes in the solution. This has led to a more efficient model in terms of computational cost. Major conclusions are summarised below.

- For soil media overlaying rigid bedrock, a finite element model has been developed in which wave radiation to infinity through the vertical lateral boundaries, is ensured through nodal forces which are derived using the thin layer method (TLM).
- For soil media over half-space, the TLM has been coupled with the paraxial boundary condition to create a model capable of simulating wave radiation with respect to both lateral directions and depth.
- Both models, soil media over bedrock and soil media over half-space, have been validated through the consideration of various test examples investigating the dynamic behaviour, in terms of natural frequencies, critical depths, surface foundation compliances and other useful comparisons to past published work.
- Various parametric studies have allowed us to deduce guidelines such that the developed numerical tools lead to correctly model problems of practical interest, particularly in the case of soil media over half space. In fact, for this case a minimum depth for the homogeneous half space and a minimum thickness of a buffer layer in the case of layered half-space are required in the finite element model.
- Practical engineering problems usually include complex geometries. In order to make the developed numerical tool flexible, unstructured mesh grids based on linear triangular

finite elements are incorporated. As shown in this dissertation work, it allows considering discontinuities of various shapes as well as non horizontal layering of soil profiles or non horizontal rigid bedrock.

- For large-size soil domains, in terms of the Rayleigh wavelength, and for wide ranges of analysis frequencies, the developed models lead to high computational effort. In order to reduce this effort, a modified version of the transmitting boundary conditions has been proposed. It was shown to lead to good quality results if the included eigenmodes are carefully selected.

What is achieved in this dissertation shows that a lot of work remains to be done. Some obvious tasks are identified as follows:

- Enhancement of the PBC could be achieved by improving the approximate impedance matrix of the half-space. This could be done by taking more terms in the Taylor series approximating the impedance matrix to prevent the generation of negative energy in the model.
- The proposed model could be extended to develop a numerical tool based on anti-place shear and axisymmetric cases. Extending to three-dimensional cases would be even more attractive as it allows dealing with more practical problems. Modifying the corresponding transmitting boundaries could also be formulated for these cases to reduce the computational effort.
- Last, investigating more effective ways to absorb wave energy at the artificial boundaries of the computational domain would be another option, especially if it leads to better quality results and low computational cost.

Appendix: The Moore-Penrose Pseudoinverse

The solution of a linear system $Ax = b$ is straightforward if the matrix A is square. However, if A is rectangular, the Moore-Penrose pseudoinverse or the genralised inverse simplifies the problem by treating it in a least square manner. It was studied first by Moore in 1922. Years later, Penrose [138] rediscovered Moore's work, which was named: the Moore-Penrose pseudoinverse.

The Moore-Penrose pseudoinverse of a complex rectangular matrix A of dimension $(m \times n)$ is denoted by $A^{\dagger}(n \times m)$. It satisfies some of the characteristic properties of inverses. Penrose [138] summarised some of the characteristics of the pseudoinverse as in the following

$$AA^{\dagger}A = A. \tag{1}$$

$$A^{\dagger}AA^{\dagger} = A^{\dagger}. \tag{2}$$

$$(AA^{\dagger})^{*} = AA^{\dagger}. \tag{3}$$

$$(A^{\dagger}A)^{*} = A^{\dagger}A. \tag{4}$$

The $*$ refers to the conjugate transpose of the matrix.

$$A^{\dagger}A = (A^{*}A)^{\dagger}A^{*}A. \tag{5}$$

$$AA^{\dagger} = (AA^{*})^{\dagger}AA^{*}. \tag{6}$$

Penrose [138] showed that the unique matrix, $A^{\dagger}$, satisfies equations (1) and (3). The general solution of the linear system $Ax = b$ is

$$x = A^{\dagger}b + (I - A^{\dagger}A)y, \tag{7}$$

where y ia an arbitrary vector.

References

[1] J. Lysmer, U. Takekazu, and T. Chan-Feng. FLUSH: A computer program for approximate 3-D analysis of soil-structure interaction problems. Earthquake Engineering Research Center, University of California, Berkeley, 1975.

[2] M. Schevenels, S. François, and G. Degrande. EDT: An ElastoDynamics Toolbox for MATLAB. *Computers and Geoscience*, 35(8):1752–1754, 2009.

[3] G. Waas. *Linear two dimensional analysis of soil dynamics problems in semi infinite layered media*. PhD thesis, University of California, Berkeley, 1972.

[4] E. Kausel. Local transmitting boundaries. *J. Eng. Mech.*, 114(6):1011–1027, 1988.

[5] D. Givoli. Non-reflecting boundary conditions. *J. Comput. Phys.*, 94:1–29, 1991.

[6] S. V. Tsynkov. Numerical solution of problems on unbounded domains. *A review, Appl. Numer. Math.*, 27:465–532, 1998.

[7] D. Givoli. High-order local non-reflecting boundary conditions: a review. *Wave Motion*, 39:319–326, 2004.

[8] D. E. Beskos. Boundary element methods in dynamic analysis. *Appl. Mech. Rev., ASME*, 40:1–23, 1987.

[9] C. A. Brebbia, J. C. F. Telles, and L. C. Wrobel. *Boundary Element Techniques, Theory and Applications in Engineering*. Springer-Verlag, Berlin Heidelberg New York Tokyo, 1984.

[10] G. D. Manolis and T. G. Davies. *Boundary Element Techniques in Geomechanics*. Computational Mechanics Publications, Elsevier Applied Science, London New York, 1993.

[11] W. S. Hall and G. Oliveto. *Boundary Element Methods for Soil-Structure Interaction*. Kluwer Academic Publishers, New York Boston, Dordrecht, London, Moscow, 2003.

[12] D. E. Beskos. Boundary element methods in dynamic analysis: Part II (1986-1996). *Appl. Mech. Rev., ASME*, 50:149–197, 1997.

[13] Y. J. Liu, S. Mukherjee, N. Nishimura, M. Schanz, W. Ye, A.Sutradhar, E. Pan, N. A. Dumont, A. Frangi, and A. Saez. Recent advances and emerging applications of the boundary element method. *Appl. Mech. Rev.*, 64:1–38, 2011.

[14] G. D. Manolis and D. E. Beskos. *Boundary Element Methods in Elastodynamics*. Unwin-Hyman (Chapman & Hall), London, 1988.

[15] L. Y. Fu and M. Bouchon. Discrete wavenumber solutions to numerical wave propagation in piecewise heterogeneous media- I. theory of two-dimensional SH case. *Geophs. J. Int.*, 157:481–498, 2004.

[16] Z. Ge and X. Chen. Wave propagation in irregularly layered elastic models: a boundary element approach with a global reflection/transmission matrix propagator. *Bull. Seis. Soc. Am.*, 97:1025–1031, 2007.

[17] Z. Ge and X. Chen. An efficient approach for simulating wave propagation with the boundary element method in multilayered media with irregular interfaces. *Bull. Seis. Soc. Am.*, 98:3007–3016, 2008.

[18] M. Bouchon, C. A. Schultz, and M. N. Toksoz. A fast implementation of boundary integral equation methods to calculate the propagation of seismic waves in laterally varying layered media. *Bull. Seis. Soc. Am.*, 85:1679–1687, 1995.

[19] S. Chaillat, M. Bonnet, and J. F. Semblat. A multi-level fast multipole BEM for 3-D elastodynamics in the frequency domain. *Comput. Methods Appl. Mech. Engrg.*, 197:4233–4249, 2008.

[20] S. Chaillat, M. Bonnet, and J. F. Semblat. A new fast multi-domain BEM to model seismic wave propagation and amplification in 3-D geological structures. *Geophs. J. Int.*, 177:509–531, 2009.

[21] E. Grasso, S. Chaillat, M. Bonnet, and J. F. Semblat. Application of the multi-level time-harmonic fast multipole BEM to 3-D visco-elastodynamics. *Eng. Anal. Bound. Elem.*, 36:744–758, 2012.

[22] M. Messner and M. Schanz. An accelerated symmetric time-domain boundary element formulation for elasticity. *Eng. Anal. Bound. Elem.*, 34:944–955, 2010.

[23] Z. Y. Yan, J. Zhang, and W. Ye. Rapid solution of 3-D oscillatory elastodynamics using the pFFT accelerated BEM. *Eng. Anal. Bound. Elem.*, 34:956–962, 2010.

[24] I. Benedetti and M. H. Aliabadi. A fast hierarchical dual boundary element method for three-dimensional elastodynamic crack problems. *Int. J. Numer. Meth. Engng.*, 84:1038–1067, 2010.

[25] T. Takahashi, N. Nishimura, and S. Kobayashi. A fast BIEM for three-dimensional elastodynamics in time domain. *Eng. Anal. Bound. Elem.*, 27:491–506, 2003.

[26] E. Kausel. Forced vibrations of circular foundations on layered media. MIT Research report R74-11, Department of Civil Engineering, MIT, Cambridge, MA 02139, 1974.

[27] E. Kausel, J. M. Roësset, and G. Waas. Dynamic analysis of footings on layered media. *J Eng. Mech. Div., ASCE*, 101:679–693, 1975.

[28] E. Kausel and J. M. Roësset. Semianalytical hyperelement for layered strata. *J Eng. Mech. Div., ASCE*, 103:569–588, 1977.

[29] J. L. Tassoulas. Elements for the numerical analysis of wave motion in layered media. Research report R81-2, Department of Civil Engineering, Massachusetts Institute of Technology, Cambridge, MA, 1981.

[30] H-T. Lin and J. L. Tassoulas. A hybrid method for three-dimensional problems of dynamics of foundations. *Earthquake Engrg. Struc. Dyn.*, 14:61–74, 1986.

[31] J. K. Kim, M. H. Koh, K. J. Kwon, and J. S. Yi. A three dimensional transmitting boundary formulated in cartesian coordinate system for the dynamics of non-axisymmetric foundations. *Earthquake Engrg. Struc. Dyn.*, 19:1527–1546, 2000.

[32] T. Hanazato, K. Ugai, and M. Mori. Three-dimensional analysis of traffic induced ground vibration. *J. Geotech. Engrg.*, 117(8):1133–1151, 1991.

[33] S.-H. Park and J. L. Tassoulas. Time-harmonic analysis of wave propagation in unbounded layered strata with zigzag boundaries. *J. Eng. Mech.*, 128:359–368, 2002.

[34] I. Jr. Ikeda and J. L. Tassoulas. Wave computations in irregular layered media using a semidiscrete finite element perturbation method. *Int. J. Numer. Meth. Engng.*, 76:376–399, 2008.

[35] J. M. O. Barbosa and E. Kausel. The thin-layer method in a cross-anisotropic 3d space. *Int. J. Numer. Meth. Engng.*, 9:537–560, 2011.

[36] C. Song and J. P. Wolf. Consistent infinitesimal finite-element-cell method: out-of-plane. *J. Eng. Mech.*, 121:613–619, 1995.

[37] J. P. Wolf and C. Song. Consistent infinitesimal finite-element cell method: in-plane motion. *Comput. Methods Appl. Mech. Engrg.*, 123:355–370, 1995.

[38] C. Song and J. P. Wolf. The scaled boundary finite-element method-alias consistent infinitesimal finite-element cell method-for elastodynamics. *Comput. Methods Appl. Mech. Engrg.*, 147:329–355, 1997.

[39] J. P. Wolf and C. Song. The scaled boundary finite-element method - a primer: derivations. *Comput. Struct.*, 78:191–210, 2000.

[40] J. P. Wolf and C. Song. The scaled boundary fnite-element method - a primer: solution procedures. *Comput. Struct.*, 78:211–225, 2000.

[41] C. Song and J. P. Wolf. The scaled boundary finite-element method: analytical solution in frequency domain. *Comput. Methods Appl. Mech. Engrg.*, 164:249–264, 1998.

[42] C. Song. Dynamic analysis of unbounded domains by a reduced set of base functions. *Comput. Methods Appl. Mech. Engrg.*, 195:4075–4094, 2006.

[43] C. Song and M. H. Bazyar. A boundary condition in Padé series for frequency-domain solution of wave propagation in unbounded domains. *Int. J. Numer. Meth. Engng.*, 69:2330–2358, 2007.

[44] C. Song and M. H. Bazyar. Development of a fundamental-solution-less boundary element method for exterior wave problems. *Commun. Numer. Meth. En.*, 24:257–279, 2008.

[45] D. Givoli and J. B. Keller. Non-reflecting boundary conditions for elastic waves. *Wave Motion*, 12:261–279, 1990.

[46] M. J. Grote and J. B. Keller. Exact nonreflecting boundary condition for the time dependent wave equation. *SIAM J. App. Math.*, 55:280–297, 1995.

[47] M. J. Grote and J. B. Keller. Exact nonreflecting boundary condition for elastic waves. *SIAM J. App. Math.*, 60:803–819, 2000.

[48] M. J. Grote. Nonreflecting boundary conditions for elastodynamic scattering. *J. Comput. Phys.*, 161:331–353, 2000.

[49] E. Kausel and J. L. Tassoulas. Transmitting boundaries: A closed-form comparison. *Bull. Seis. Soc. Am.*, 71(1):143–159, 1981.

[50] J. Lysmer and R. L. Kuhlemeyer. Finite dynamic model for infinite media. *J. Eng. Mech.*, 95(EM4):859–877, 1969.

[51] W. White, S. Valliappan, and I. K. Lee. Unified boundary for finite dynamic models. *J Engng. Mech. Div., ASCE*, 103:949–964, 1977.

[52] H.-S. Ang and N.M Newmark. Development of a transmitting boundary for numerical wave motion calculations. Report to Defense Atomic Support Agency, 1972.

[53] B. Engquist and A. Majda. Absorbing boundary conditions for the numerical simulation of waves. *Math. Comput.*, 31(139):629–651, 1977.

[54] W. D. Smith. A non-reflecting plane wave boundary for wave propagation problems. *J. Comput. Phys.*, 15:492–503, 1974.

[55] P. A. Cundall, R. R. Kunar, P. C. Carpenter, and J. Marti. Solution of infinite dynamic problems by finite modelling in the time domain. *In Proceedings of the 2nd International Conference on Applied Numerical Modelling, Madrid, Spain*, pages 339–351, 1978.

[56] R. R. Kunar and J. Marti. A non-reflecting boundary for explicit calculations. *Computational methods for infinite domain media-structure interaction, AMD (Ed. A.J. Kalinowski)*, 46:183–204, 1981.

[57] P. Underwood and T. L. Geers. Doubly asymptotic boundary-element analysis of dynamic soil-structure interaction. *Int. J. Solid Struct.*, 17:687–697, 1981.

[58] R. Clayton and B. Engquist. Absorbing boundary conditions for acoustic and elastic wave equations. *Bull. Seis. Soc. Am.*, 67:1529–1540, 1977.

[59] Z. P. Liao and H. L. Wong. A transmitting boundary for the numerical simulation of elastic wave propagation. *Soil Dyn. Earthquake Engrg.*, 3:174–183, 1984.

[60] R. L. Higdon. Absorbing boundary conditions for difference approximations to the multi-dimensional wave equation. *Math. Comput.*, 176:437–459, 1986.

[61] R. L. Higdon. Numerical absorbing boundary conditions for the wave equation. *Math. Comput.*, 49:65–90, 1987.

[62] R. L. Higdon. Absorbing boundary conditions for accoustic and elastic waves in stratified media. *J. Comput. Phys.*, 101:386–418, 1992.

[63] C. L. Scandrett, G. A. Kriegsmann, and J. D Achenbach. Absorbing boundary conditions for the elastic wave equations. *SIAM J. Sci. Stat. Comput.*, 7:571–590, 1986.

[64] M. Cohen. Silent boundary methods for transient wave analysis. Earthquake Engineering Laboratories, Report No. EERL 80, 1980.

[65] S. H. Seale. *Dynamic loads in layered halfspaces*. PhD thesis, Massachusetts Institute of Technology, MA, 1985.

[66] J. Park. *Wave motion in finite and infinite media using the thin-layer method*. PhD thesis, Massachusetts Institute of Technology, MA, 2002.

[67] A. Bamberger, B. Chalinder, P. Joly, J. E. Roberts, and J. L. Teron. Absorbing boundary conditions for rayleigh waves. *SIAM J. Sci. Stat. Comput.*, 9:1016–1048, 1988.

[68] J. P. Wolf and C. Song. Doubly asymptotic multi-directional transmitting boundary for dynamic unbounded medium-structure-interaction analysis. *Earthquake Engrg. Struc. Dyn.*, 24:175–188, 1995.

[69] L. Kellezi. Local transmitting boundaries for transient elastic analysis. *Soil Dyn. Earthquake Engrg.*, 10:533–547, 2000.

[70] J.-P Berenger. A perfectly matched layer for the absorption of electromagnetic waves. *J. Comput. Phys.*, 114:185–200, 1994.

[71] F. D. Hastings, J. B. Schneider, and S. L. Broschat. Application of the perfectly matched layer PML absorbing boundary condition to elastic wave propagation. *J. Acoust. Soc. Am.*, 100:3061–3069, 1996.

[72] W. C. Chew and Q. H. Liu. Perfectly matched layers for elastodynamics: a new absorbing boundary condition. *J. Comp. Acous.*, 4(4):341–359, 1996.

[73] F. Collino and C. Tsogka. Application of the perfectly matched absorbing layer model to the linear elastodynamic problem in anisotropic heterogeneous media. *Geophysics*, 66:294–307, 2001.

[74] Y. Q. Zeng, J. Q. He, and Q. H. Liu. The application of the perfectly matched layer in numerical modeling of wave propagation in poroelastic media. *Geophysics*, 66:1258–1266, 2001.

[75] Y. Zheng and X. Huang. Anisotropic perfectly matched layers for elastic waves in cartesian and curvilinear coordinates. in: Earth Resources Laboratory 2002 Industry Consortium Meeting, Dept. of Earth, Atmospheric, and Planetary sciences, Massachusetts Institute of Technology, Cambridge, MA, USA, 2002.

[76] E. Becache, S. Fauqueux, and P. Joly. Stability of perfectly matched layers, group velocities and anisotropic waves. *J. Comput. Phys.*, 188:399–433, 2003.

[77] U. Basu and A. K. Chopra. Perfectly matched layers for time-harmonic elastodynamics of unbounded domains: theory and finite element implementation. *Comput. Methods Appl. Mech. Engrg.*, 192:1337–1375, 2003.

[78] U. Basu and A. K. Chopra. Perfectly matched layers for transient elastodynamics of unbounded domains. *Int. J. Numer. Meth. Engng.*, 59:1039–1074, 2004.

[79] U. Basu. Explicit finite element perfectly matched layer for transient three-dimensional elastic waves. *Int. J. Numer. Meth. Engng.*, 77:151–176, 2009.

[80] E. Kausel and J. M. O. Barbosa. PMLs: A direct approach. *Int. J. Numer. Meth. Engng.*, 90:343–352, 2012.

[81] J. F. Semblat, A. Gandomzadeh, and L. Lenti. A simple numerical absorbing layer method in elastodynamics. *Mecanique*, 338:24–32, 2010.

[82] M. N. Guddati and J. L. Tassoulas. Continued-fraction absorbing boundary conditions for the wave equation. *J. Comp. Acous.*, 8(1):139–156, 2000.

[83] D. Givoli and B. Neta. High-order non-reflecting boundary scheme for time-dependent waves. *J. Comput. Phys.*, 186:24–46, 2003.

[84] M. H. Bazyar and C. Song. A continued-fraction-based high-order transmitting boundary for wave propagation in unbounded domains of arbitary geometry. *Int. J. Numer. Meth. Engng.*, 74:209–237, 2008.

[85] C. Birk, S. Prempramote, and C. Song. An improved continued-fraction-based high-order transmitting boundary for time-domain analysis in unbounded domains. *Int. J. Numer. Meth. Engng.*, 89:269–298, 2011.

[86] I. C. Mathews and T. L. Geers. A doubly asymptotic, nonreflecting boundary for ground shock analysis. *J. Appl. Mech.*, 54:489–497, 1987.

[87] T. L. Geers and B. A. Lewis. Doubly asymptotic approximations for transient elastodynamics. *Int. J. Solid Struct.*, 34(11):1293–1305, 1997.

[88] Q. Qi and T. L. Geers. Application of the perfectly matched layer PML absorbing boundary condition to elastic wave propagation. *J. Acoust. Soc. Am.*, 102(3):1361–1371, 1997.

[89] R. F. Ungless. An infinite finite element. Master's thesis, M. A. Sc. Thesis, University of British Columbia, 1973.

[90] P. Bettess. Infinite elements. *Int. J. Num. Meth. Eng.*, 11:53–64, 1977.

[91] P. Bettess and O. C. Zienkiewicz. Differaction and refraction of surface waves using finite and infinite elements. *Int. J. Numer. Meth. Engng.*, 11:1271–1290, 1977.

[92] S. S. Saini, P. Bettess, and O. C. Zienkiewicz. Coupled hydrodynamic response of concrete gravity dams using finite and infinite elements. *Earthquake Engrg. Struc. Dyn.*, 6:363–374, 1978.

[93] Y. K. Chow and I. M. Smith. Static and periodic infinite solid elements. *Int. J. Numer. Meth. Engng.*, 17:503–526, 1981.

[94] Y. B. Yang, S. R. Kuo, and H. H. Hung. Frequency-independent infinite elements for analysis semi-infinite problems. *Int. J. Numer. Meth. Engng.*, 39:3553–3569, 1996.

[95] F. Medina and R. L. Taylor. Finite element techniques for problems of unbounded domains. *Int. J. Numer. Meth. Engng.*, 19:1209–1226, 1983.

[96] Z. Chuhan and Z. Chongbin. Coupling methods of finite and infinite elements for strip foundation wave problems. *Earthquake Engrg. Struc. Dyn.*, 15:839–851, 1987.

[97] Y. B Yang and H. H. Hung. A 2.5d finite/infinite element approach for modelling visco-elastic bodies subjected to moving loads. *Int. J. Numer. Meth. Engng.*, 51:1317–1336, 2001.

[98] Y. B. Yang, H. H. Hung, and L. C. Hsu. Ground vibrations due to underground trains considering soil-tunnel interaction. *Interaction & Multiscale Mech., an Int. J.*, 1(1):157–175, 2007.

[99] O. Laghrouche. *Numerical simulation of wave propagation in soil - Application to vibration isolation*. PhD thesis, Ecole Central De Nantes, France, 1996.

[100] O. Laghrouche and D. Le Houedec. Etude comparative de quelques moyens de réduction de vibrations dans le sol. *Mécanique Industrielle et Matériaux*, 47(2):35–37, 1994.

[101] S. L. Kramer. *Geotechnical Earthquake Engineering*. Prentice Hall Upper Saddle River, New Jersey, 1996.

[102] A. H. Hadjian. Fundamental period and mode shape of layered soil profiiles. *Soil Dyn. Earthquake Engrg.*, 22:885–891, 2002.

[103] C. Geuzaine and J. F. Remacle. Gmsh: A 3-D finite element mesh generator with built-in pre- and post-processing facilities. *Int. J. Numer. Meth. Engng.*, 79:1309–1331, 2009.

[104] S. W. Jones. *Ground vibration from underground railways: How simplifying assumptions limit predection accuracy*. PhD thesis, University of Cambridge, 2010.

[105] S. Jones and H. Hunt. Effect of inclined soil layers on surface vibration from underground railways using the thin-layer method. *J. Eng. Mech.*, 137(12):887–900, 2011.

[106] P. W. Andrade. *Implementation of second-order absorbing boundary conditions in frequency-domain computations*. PhD thesis, University of Texas at Austin, 1999.

[107] E. Kausel and J. M. Roësset. Stiffness matrices for layered soils. *Bull. Seis. Soc. Am.*, 71,(6):1743–1761, 1981.

[108] E. Kausel and R. Peek. Dynamic loads in the interior of a layered stratum: an explicit solution. *Bull. Seis. Soc. Am.*, 72(5):1459–1481, 1982.

[109] S. W. Hull and E. Kausel. Dynamic loads in layered halfspaces. *Proceedings of the Fifth Engineering Mechanics in Civil Engineering Division*, 1:201–204, 1984.

[110] A. M. Kaynia, C. Madshus, and P. Zackrisson. Ground vibration from high-speed trains: prediction and countermeasure. *J. Geotech. Geoenviron. Eng.*, 126(6):531–537, 2000.

[111] T. Maeda and E. Kausel. On the accuracy of some approximate antiplane half-space stiffnesses. *Bull. Seis. Soc. Am.*, 81(4):1340–1359, 1991.

[112] E. Kausel. Physical interpretation and stability of paraxial boundary conditions. *Bull. Seis. Soc. Am.*, 82(2):898–913, 1992.

[113] J. H. Lee, J. K. Kim, and J. L. Tassoulas. Implementation of a second-order paraxial boundary condition for a water-saturated layered half-space in plane strain. *Earthquake Engrg. Struc. Dyn.*, 40:531–550, 2011.

[114] J. H. Lee, J. K. Kim, and J. L. Tassoulas. Application of a second-order paraxial boundary condition to problems of dynamics of circular foundations on a porous layered half-space. *Soil Dyn. Earthquake Engrg.*, 31:291–305, 2011.

[115] MD. A. Zahid. *Efficient Absorbing Boundary Conditions for Modeling Wave Propagation in Unbounded Domains*. PhD thesis, North Carolina State University, 2005.

[116] S. Savadatti and M. N. Gudatti. Absorbing boundary conditions for scalar waves in anisotropic media. part 1: Time harmonic modeling. *J. Comput. Phys.*, 229:6696–6714, 2010.

[117] S. Savadatti and M. N. Gudatti. A fininte element alternative to infinite elements. *Comput. Methods Appl. Mech. Engrg.*, 199:2204–2223, 2010.

[118] J. H. Lee and J. L. Tassoulas. Consistent transmitting boundary with continued-fraction absorbing boundary conditions for analysis of soil-structure interaction in a layered half-space. *Comput. Methods Appl. Mech. Engrg*, 200:1509–1525, 2011.

[119] J. M. O. Barbosa, J. Park, and E. Kausel. Perfectly matched layers in the thin layer method. *Comput. Methods Appl. Mech. Engrg.*, 217-220:262–274, 2012.

[120] J. E. Luco and R. A. Westmann. Dynamic response of a rigid footing bonded to an elastic half space. *J. Appl. Mech. ASME*, 39:527–541, 1972.

[121] T.-J. Tzong and J. Penzien. Hybrid modeling of soil-structure interaction in layered media. Report No. UCB/EERC-83/22, Earthquake Engineering Research Center, University of California, Berkeley, CA, 1983.

[122] G. R. Liu and S. S. Quek. *The Finite Element Method: A Pratical Course*. Butterworth-Heinemann, Elsevier Science Ltd, 2003.

[123] Y. B. Yang and H. H. Hung. A Parametric Study of Wave Barriers for Reduction of Train Induced Vibrations. *Int. J. Numer. Meth. Engng.*, 40:3729–3747, 1997.

[124] D. E. Beskos, G. Dasgupta, and I. G. Vardoulakis. Vibration isolation using open or filled trenches, part1: 2-D homogeneous soil. *Computational Mechanics*, 1:43–63, 1986.

[125] S. Ahmad and T.M. Al-Hussaini. Simplified design for vibration screening by open and infilled trenches. *J. Geotech. Engrg.*, 117(1):67–88, 1991.

[126] A. Alzawi. *Vibration Isolation Using In-filled Geofoam Trench Barriers*. PhD thesis, The University of Western Ontario, London, Ontario, Canada, 2011.

[127] M. Cohen and P. C. Jennings. *Computational Methods for Transient Analysis, Chaper 7, Edited by T. Belytschko and T. J. R. Hughes*. Elsevier Science Publishers B. V., North-Holland, 1983.

[128] D. B. Meade. Applications of generalised stress in elastodynamics. *Quart. Appl. Math.*, XLIX(1):121–145, 1991.

[129] G. H. Yoon. Structural topology optimization for frequency response problem using model reduction schemes. *Comput. Methods Appl. Mech. Engrg.*, 199:1744–1763, 2010.

[130] O. A. López and M. Cruz. Number of modes for the seismic design of buildings. *Earthquake Engrg. Struc. Dyn.*, 25:837–855, 1996.

[131] N. Hamdan, O. Laghrouche, A. El Kacimi, and P. K. Woodward. Consistent transmitting boundary conditions with a reduced number of eigenmodes for wave propagation in elastic media. *Computters and Geotechnics*, 53:9–16, 2013.

[132] G. Segol, C. Y. Lee, and J. F. Abel. Amplitude reduction of surface waves by trenches. *J Eng. Mech. Div., ASCE*, 104(EM3):621–641, 1978.

[133] A. S. M. Israil and S. Ahmad. Dynamic vertical compliance of strip foundations in layered soils. *Earthquake Engrg. Struc. Dyn.*, 18:933–950, 1989.

[134] F. Cui and C. H. Chew. The effectiveness of flaoting slab track system-part I. receptance methods. *Appl. Acoust.*, 61:441–453, 2000.

[135] M. F. M. Hussein and H. E. M. Hunt. Modelling of foating-slab tracks with continuous slabs under oscillating moving loads. *J. Sound Vib.*, 297:37–54, 2006.

[136] T. Xin and L. Gao. Reducing slab track vibration into bridge using elastic materials in high speed railway. *J. Sound Vib.*, 330:2237–2248, 2011.

[137] M. A. Adam and G. Schmid. Investigation of ground vibrations in the vicinity of a train track embankment. *In Wave 2002, Okayama, Japan*.

[138] R. Penrose. A generalised inverse for matrices. *Proc. Cambridge Philos. Soc.*, 51:406–413, 1955.